OXIDATION OF Zr ALLOYS IN HIGH PRESSURE STEAM AND SOME RESULTS UNDER ATMOSPHERIC PRESSURE

G. Hache
Institut de Radioprotection et de Sûreté Nucléaire
Cadarache, B.P. 3,
13115 St-Paul-Lez-Durance Cedex, France
georges.hache@irsn.fr

ABSTRACT

Performance of high-burnup or new zirconium alloys under intermediate break loss-of-coolant-accident (LOCA) is not well understood at this time. The data for fresh Zircaloy-4 show a pressure enhancement effect below 1100°C, but moderate. The oxidation enhancement seems to be related to the tetragonal to monoclinic zirconia transformation. Limited published data for fresh E-110 alloy (Zr 1%Nb O-poor S-free) show a strong oxidation enhancement at 850°C, rapidly exceeding the 17%ECR embrittlement criterion. Data for M5 (Zr 1%Nb O-rich S-doped), ZIRLO alloys and high-burnup Zircaloy-4 are lacking. In the smaller second part of this paper, a simulation to calculate after Hobson's data what would have been the ECR value, if the U.S. Regulatory Staff had used in 1973 the Cathcart-Pawel correlation, gives the 14% ECR value. Finally, it is pointed out in this paper that, due to a compensation of approximations and system-effects, the Cathcart-Pawel weight gain correlation may be used for the calculation of chemical heat in a best-estimate methodology.

1. Introduction

Because of major advantages in fuel-cycle costs, reactor operation, and spent fuel management, the current trend in the nuclear industry is to increase fuel discharge burnup. At high burnup, fuel rods fabricated from conventional Zircaloys often exhibit significant degradation in microstructure. This is especially pronounced in pressurized-water reactor (PWR) rods fabricated from standard Zircaloy-4 in which significant oxidation, hydriding, and oxide spallation can occur. Thus, many fuel vendors have developed and proposed the use of new cladding alloys, such as low-tin Zircaloy-4, Zirlo, M5... Performance of these alloys under intermediate break loss-of-coolant-accident (LOCA) situations, especially at high burnup, is not well understood at this time. Therefore, it is important to verify the safety margins for high-burnup fuel and fuels clad with new alloys. Large break LOCA-related behaviour (under atmospheric pressure) of various types of fuel cladding has been and is being actively investigated in several countries [1-4]. However, the probability of intermediate break LOCA is higher [5-6]. For this purpose, the relevant databases (high pressure oxidation) were carefully examined in the main first part of this paper.

2. Breaks and transients

During intermediate break LOCA, steam pressure is higher when clad experiences oxidation; for example, during a 3-inch break calculation with the Appendix K to 10 CFR 50 [7] methodology, Peak Clad Temperature reaches about 1000°C, clad temperature remains above 800°C during more than 1000 sec (figure 1) and during this time pressure is about 35 bars (figure 2) [8]

Transients other than breaks occur under even higher pressure, and during some of them clad may experience oxidation. For PWR Design Basis Accidents the limiting case seems to be the single rod cluster control assembly (RCCA) withdrawal event. During one BWR ATWS calculation presented last year, Peak Clad Temperature reaches 1400°C, exceeding one fuel-shattering criterion [9].

This paper will focus on intermediate break conditions.

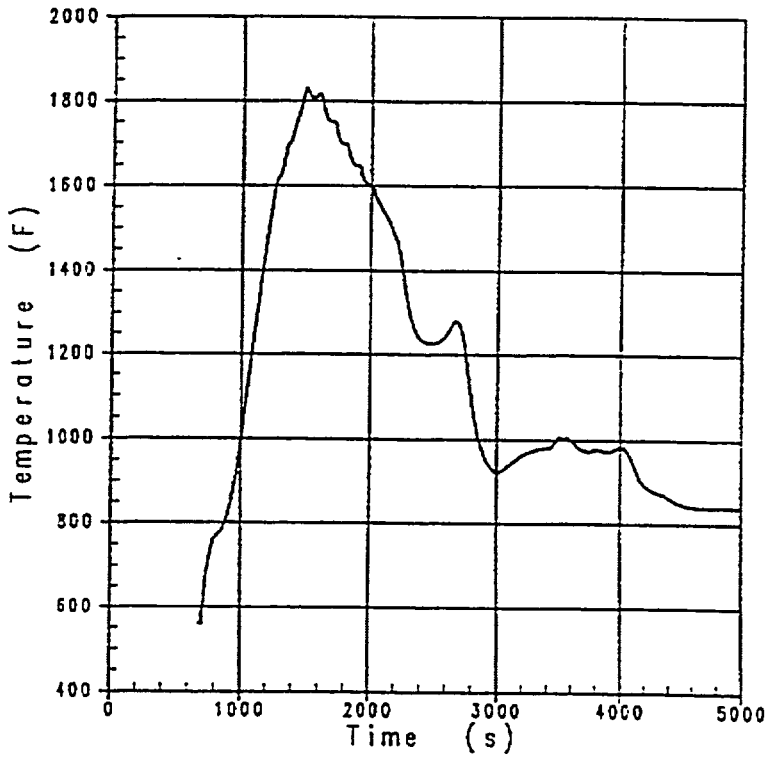

Figure 1

Westinghouse 3-loop plant Appendix K 3-inch break calculation for peak fuel - peak clad temperature (From Boyack et al., NUREG/CR-6744)

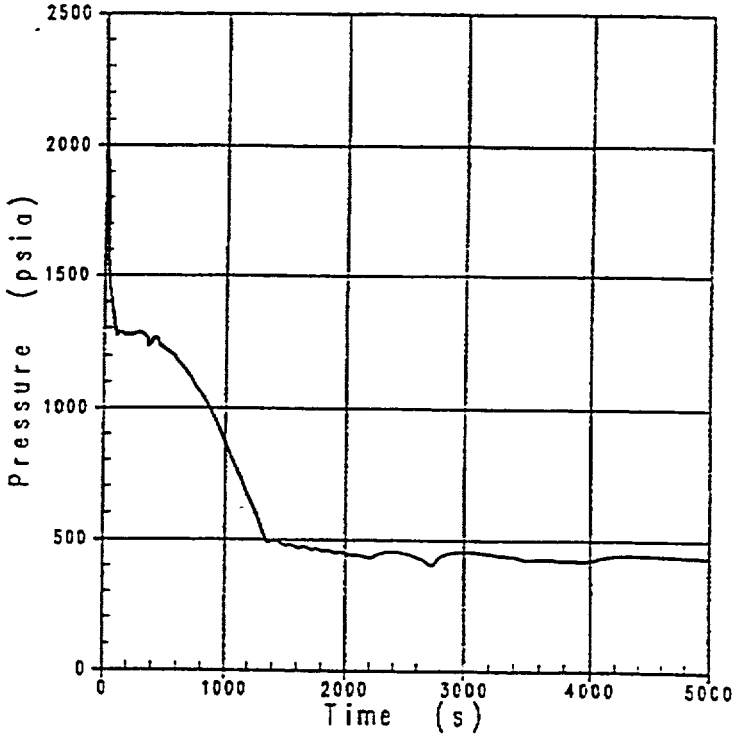

Figure 2

Westinghouse 3-loop plant Appendix K 3-inch break calculation for fresh fuel - pressurizer pressure (from Boyack et al., NUREG/CR - 6744)

3. Oxidation of fresh zircaloy under high-pressure steam

3.1 Experimental results

Scoping tests were performed by Pawel et al. (ORNL) at 900 and 1100°C [10]. Their results, bounded by the Baker-Just correlation [11], didn't lead to a modification of the Appendix K to 10 CFR 50, but were taken into account in the Regulatory Guide (RG) 1.157 § 3.2.5.1b [12] for best-estimate calculations. After this RG was issued, three other experiments were performed [13-15]. The main part of this paper will be devoted to the analysis of these data sets.

Some experimentalists measured only oxide layer growth [13, 15], others published only weight gain in open literature [14], reference Baker-Just correlation is also in weight gain [11]. Pawel et al. were alone to publish both oxide layer growth and weight gain [10], so we used Pawel et al.'s data to correlate weight gain and oxide thickness (figure 3).

Park et al. didn't publish full tabulated data in open literature [15], so we used their empirical model. Figure 4 shows that this model is correct for the highest temperatures (850 - 900°C) or the lowest pressures (below 100 bars); however, there is some overestimation for the configuration lowest temperatures (700 - 750°C) and highest pressures (100 bars and above).

Comparison of the four sets of results and of the Baker-Just correlation at 750, 800, 850 and 900°C is given in figures 5 to 8. The upper grey dotted line is adjustment of the temperature of the Baker-Just correlation to fit the highest point.

Figure 3 - correlation between weight gain and oxide thickness (Pawel's tests)

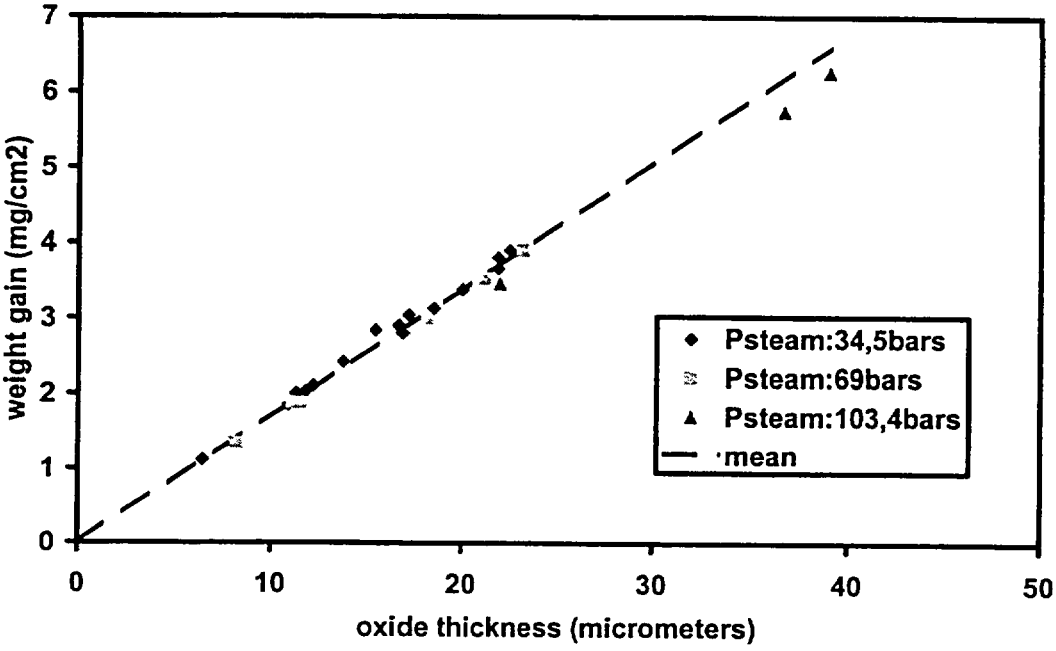

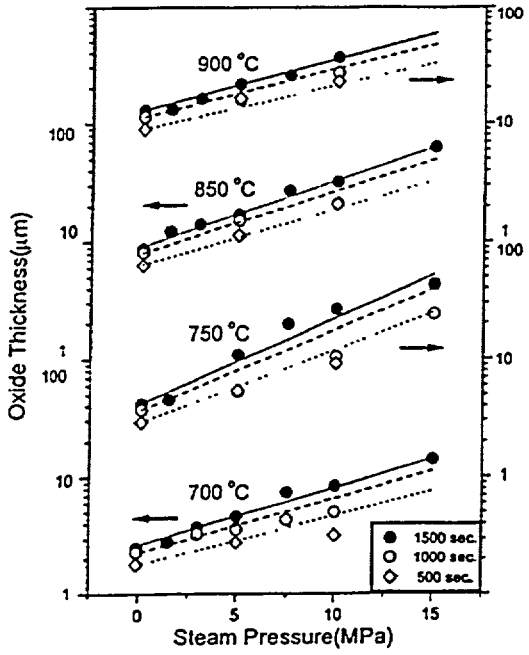

Figure 4

Comparison of Park's model to the Park's data (from Park et al., Park City (USA) 2000)

Figure 5 - Zry - oxide thickness at 750°C as a function of square root of time and steam pressure

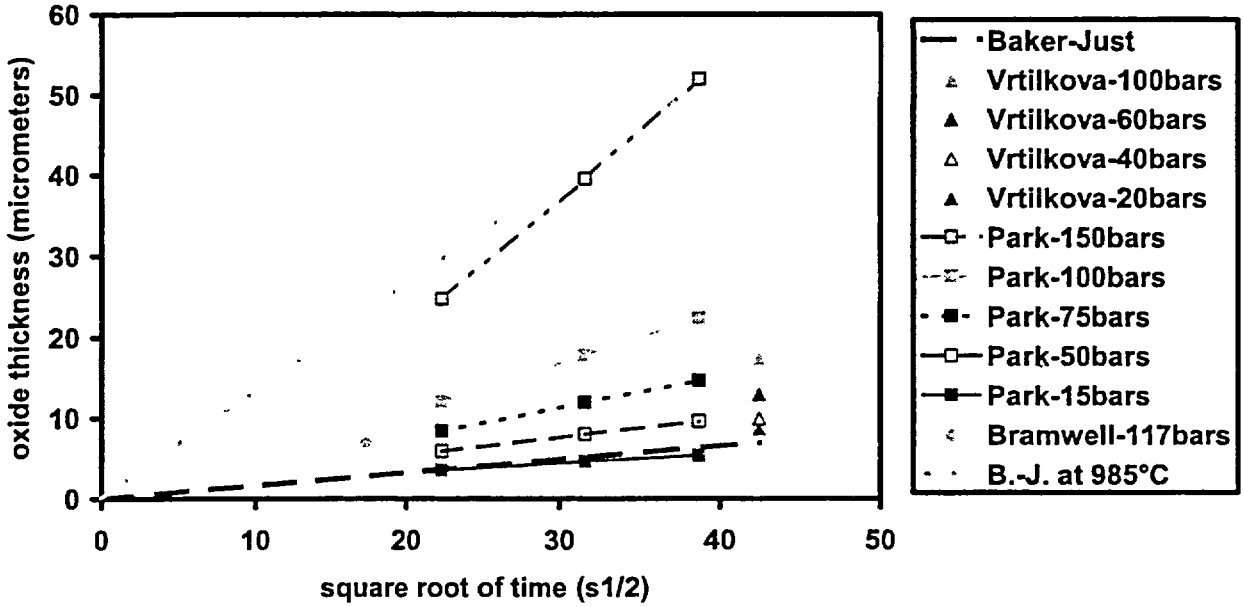

Figure 6 - Zry - oxide thickness at 800°C as a function of the square root of time and of steam pressure

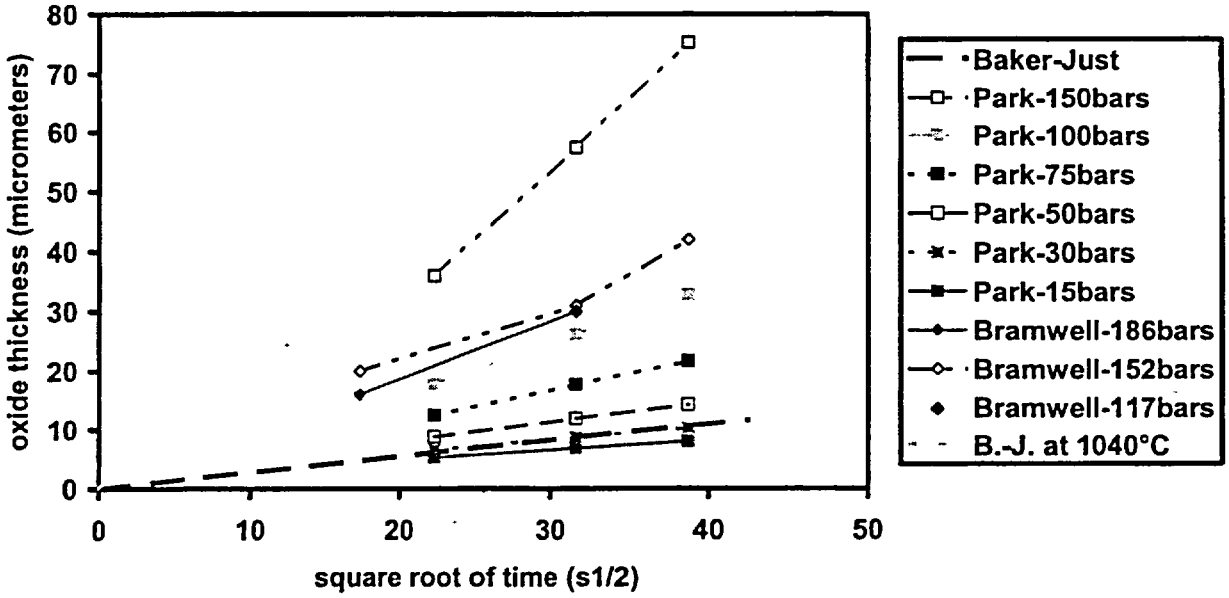

Figure 7 - Zry - oxide thickness at 850°C as a function of square root of time and steam pressure

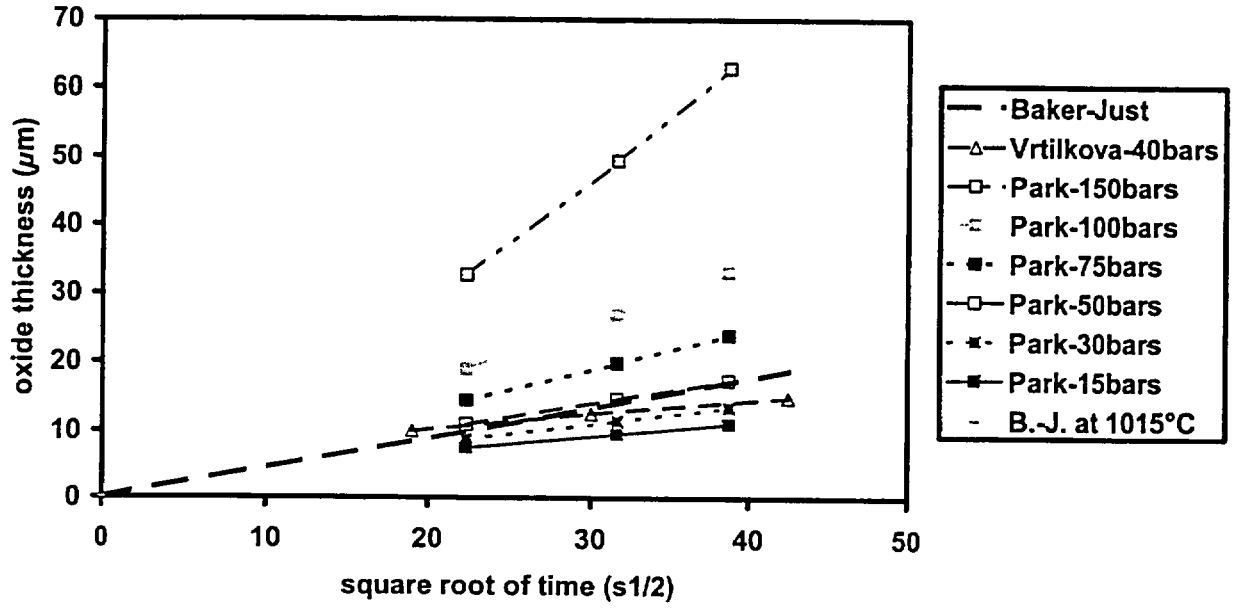

Figure 8 - Zry - oxide thickness at 900°C as a function of square root of time and steam pressure

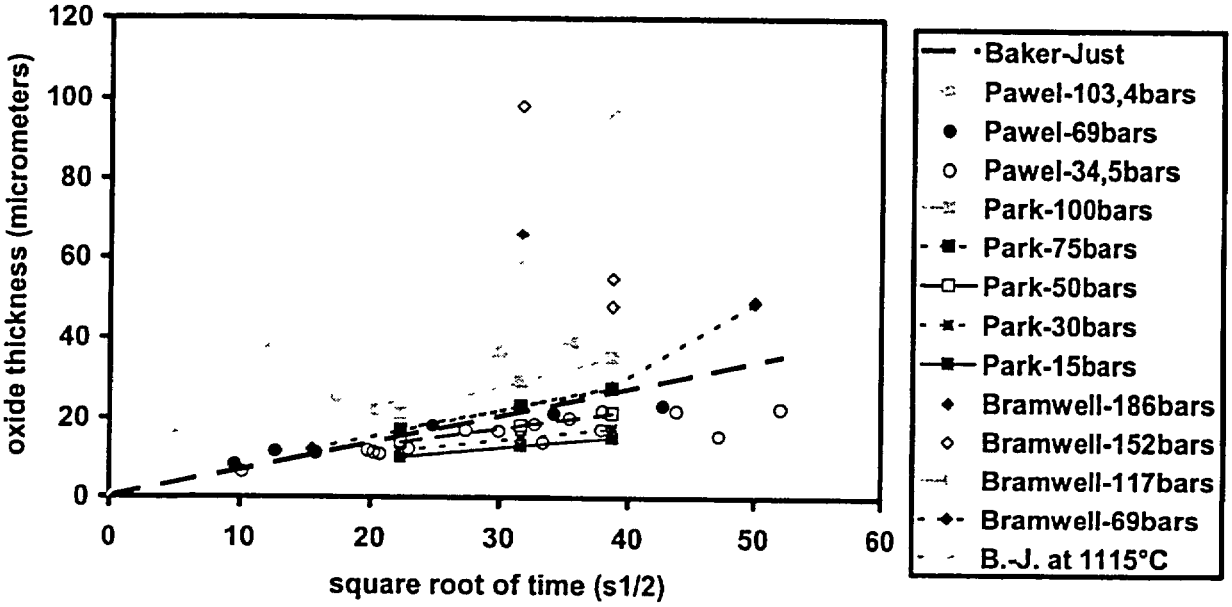

There is a good consistency between Bramwell, Pawel, Vrtilkova and Park results below 100 bars, that means that there is no effect of flowing steam (Bramwell, Pawel) versus stagnant steam (Park, Vrtilkova) below 100 bars: probably the high pressure enhances heat exchanges.

The pressure enhancement effect on the oxidation vanishes at 1100°C (figure 9).

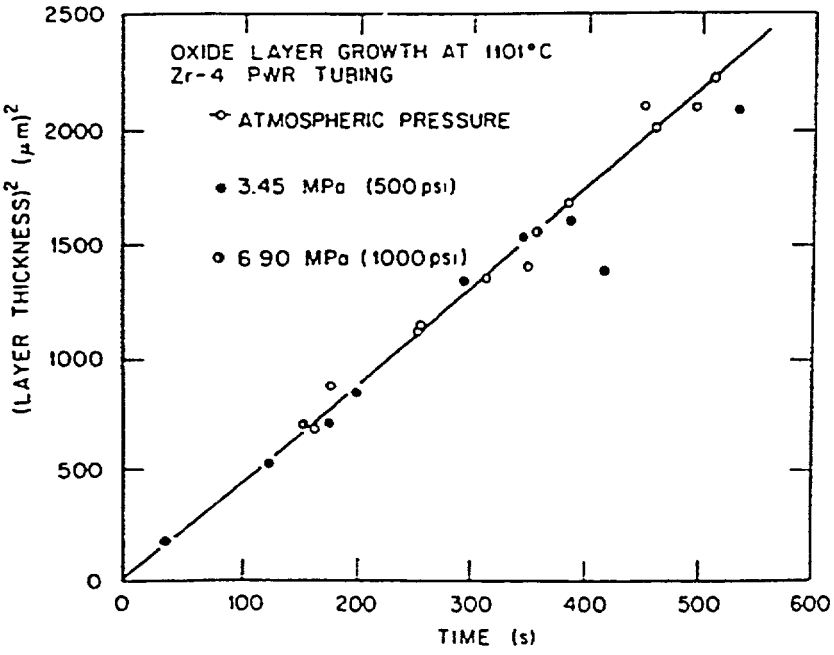

Figure 9

Oxide layer growth at 1101°C at 34,5 bars and 69 bars. Solid line represents data at atmospheric pressure (From Pawel et al., J. of Nucl. Mat. 82 (1979) p. 129-139)

3.2 Discussion

Cox suggests that porosity develops more rapidly in oxide at high pressure [16]. Pawel observes at 900°C a light external oxide layer, that he doesn't observe at 1100°C or at atmospheric pressure, associates this result with the oxide morphology (porosities, cracks). Bramwell finds also the light external layer at 900°C and 1000°C, but not at 800°C.

Pawel and Park associate their observations with the tetragonal/monoclinic transition of Zirconia. Below about 1100°C, the oxide formed at the metal/oxide interface is in the tetragonal form; this phase, normally not stable at this temperature, is metastabilized by the coupled effects of:

- compressive stresses in the oxide at the interface (due to the high Pilling-Bedworth ratio),
- small crystallite size in the oxide,
- substoichiometry of the oxide near the interface.

The pressure-temperature phase diagram of zirconia presented in figure 10 [17] shows that stresses of 2 GPa are sufficient to stabilize tetragonal zirconia at 800°C.

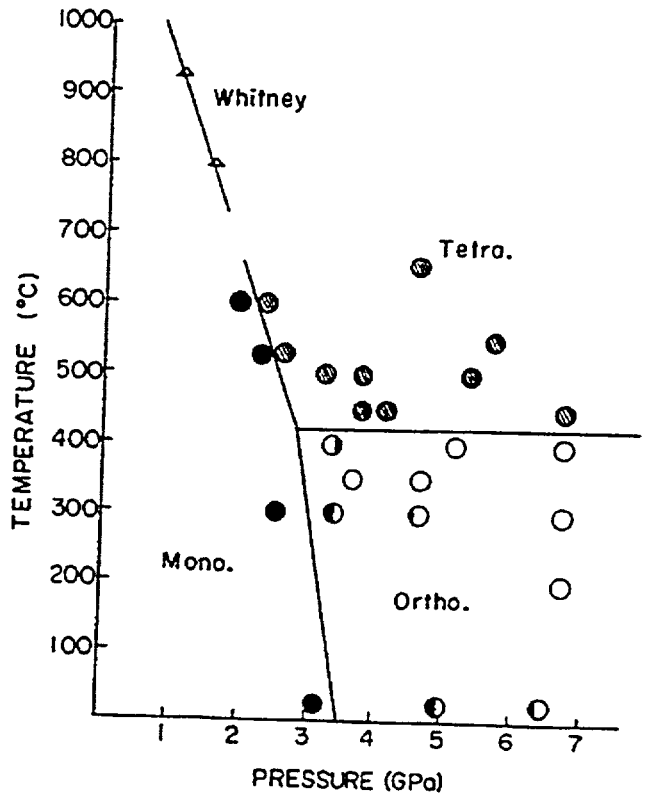

Figure 10

Pressure-Temperature phase diagram of zirconia (from Arashi et al., Tokyo (Japan) 1986)

Zirconia powder with crystallites of less than 15 nm is tetragonal [18]. Near the interface, oxide is at the oxygen potential in thermodynamic equilibrium with the metal.

During growing of the oxide scale, the same coupled effects induce transformation into monoclinic phase:

- stress relaxation in the oxide far from the metal/oxide interface,
- crystallite growth during annealing,
- evolution to stoichiometry.

When the stresses decrease below the dashed line in figure 10, stresses alone are no more able to stabilize tetragonal zirconia; spectacular experiments were done by Godlewski [19], in which the dissolution of the metal substrate caused, by suppressing the stresses, full transformation to monoclinic zirconia.

When small crystallite size tetragonal zirconia is annealed, crystallite size grows and tetragonal zirconia transforms into monoclinic zirconia (figure 11) [18].

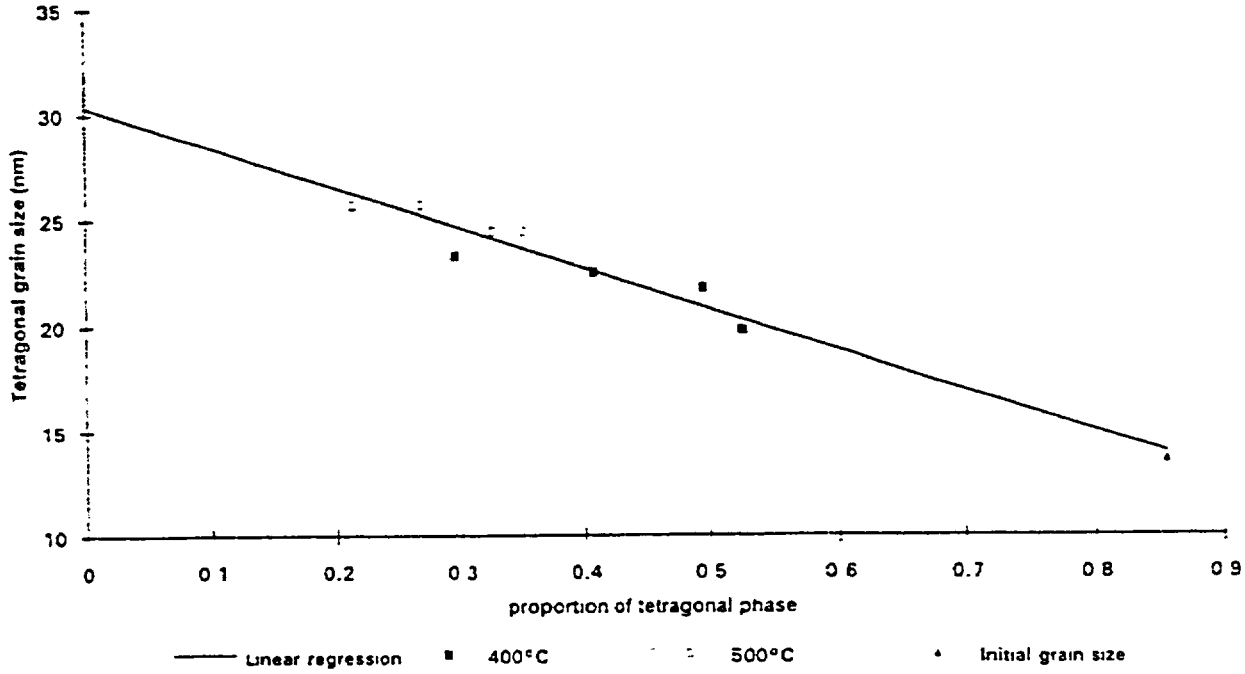

Figure 11

Annealed zirconia powder - Correlation between tetragonal crystallite size and content of tetragonal phase (from Barberis, J. of Nucl. Mat. 226 (1995) p. 34-43)

Barberis found again a critical crystallite size of 30 nm, that Garvie already found thirty years before [20]. Far from the metal/oxide interface, oxide oxygen potential approaches the thermodynamic equilibrium with steam.

This tetragonal/monoclinic transformation is thought by Pawel and Park to induce microporosities and microcracking. Their model is similar to Leistikow's breakaway model at atmospheric pressure. However, at atmospheric pressure, cracks formation needs times longer than the duration of Design Basis Accidents [21]. According to Park's tests with steam/argon mixtures, the pressure acceleration is due to steam partial pressure rather than total pressure. Murase and Kato have shown the crucial role of steam in crystallite growth and the tetragonal/monoclinic transformation, and that increasing the steam partial pressure accelerates this transformation [22].

Besides the common vanishing at 1100°C, Park made an interesting remark by observing that temperatures at which the pressure effect is maximal for Zry-4 (750-800°C) coincide with temperatures of Leistikow's first breakaway peak at atmospheric pressure and longer times (figure 12) [21].

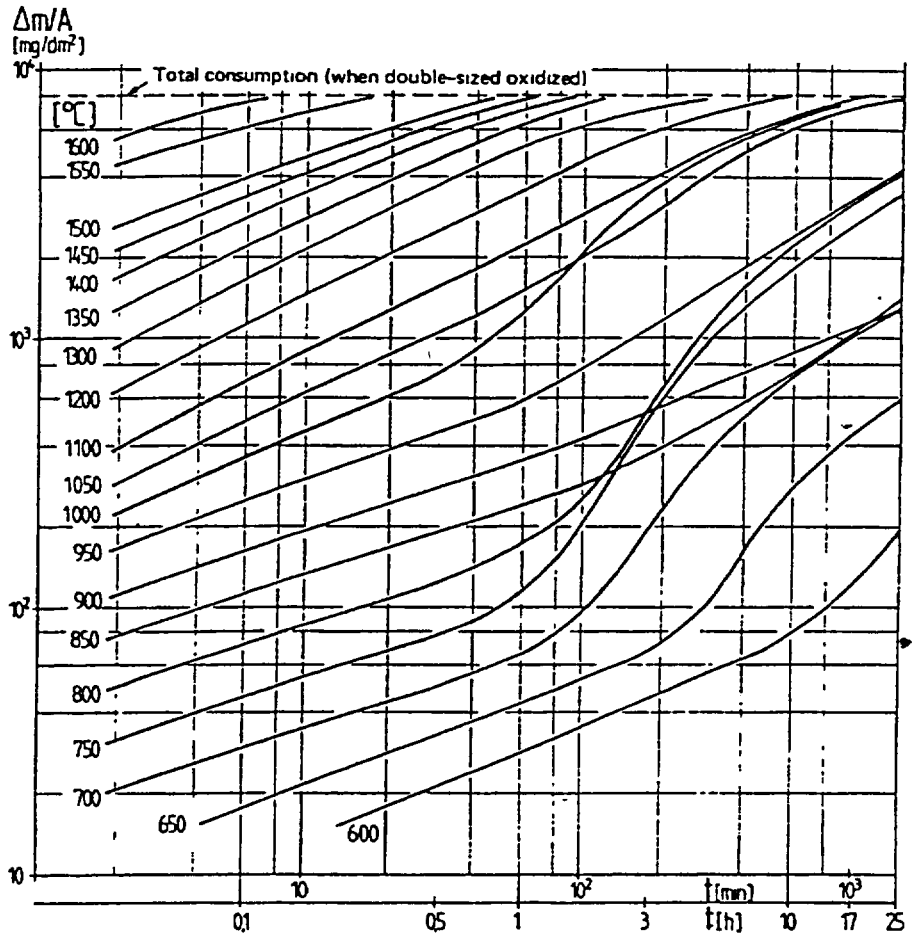

Figure 12

Isothermal oxidation of Zircaloy-4 as function of time. Long-term exposure to high temperature steam (≤ 25 h, 600-1600°C) (from Leistikow and Schanz, Nuclear Engineering and Design 103 (1987))

Another explanation is related to the electrical conductivity. According to the literature, zirconia is a mixed electronic/ionic conductor. When the kinetic is cubic (below 1000°C, range where oxide transforms to monoclinic), it is not governed only by oxygen ion diffusion, but also by electron transport [23]. According to Cox [16], zirconia electrical conductivity is strongly dependent on oxygen partial pressure. However, this explanation is only partial and cannot explain kinetics faster than the extrapolation of the higher temperature parabolic data, governed by oxygen ion diffusion alone (range where tetragonal oxide is always stable).

It is well known that large hydrogen uptake occurs during atmospheric breakaway [21]. Hydrogen uptake was not measured or not published in open literature by Bramwell, Vrtilkova and Park. Pawel performed a single measurement of Z-13 specimen oxidized at 905°C under 34,5 bars during 380 s [24]. However for this short duration, the pressure effect is not yet evident (Z-12 and Z-14 specimens: 10.9-11.8 μm [10], versus S-19, S-24 and Z-17 specimens: 11.2-11.5 μm [24] [10]. As hydrogen uptake impacts strongly the post-quench ductility [25], data on hydrogen uptake are insufficient.

3.3 Conclusion

For fresh Zircaloy-4, the kinetic is enhanced by pressure; it may exceed the Baker-Just correlation at 750-800°C even below 50 bars; however at these temperatures, the absolute values are limited, such that the pressure enhancement effect doesn't cause any actual safety problem for intermediate breaks with fresh Zircaloy-4, if hydrogen uptake is limited. However, data on hydrogen uptake are insufficient.

4. Oxidation of other Zr alloys under high-pressure steam

4.1 E-110 alloy (Zr 1%Nb O-poor S-free)

At 750°C, the pressure effect is lower than for Zircaloy-4 (figure 13) [14].

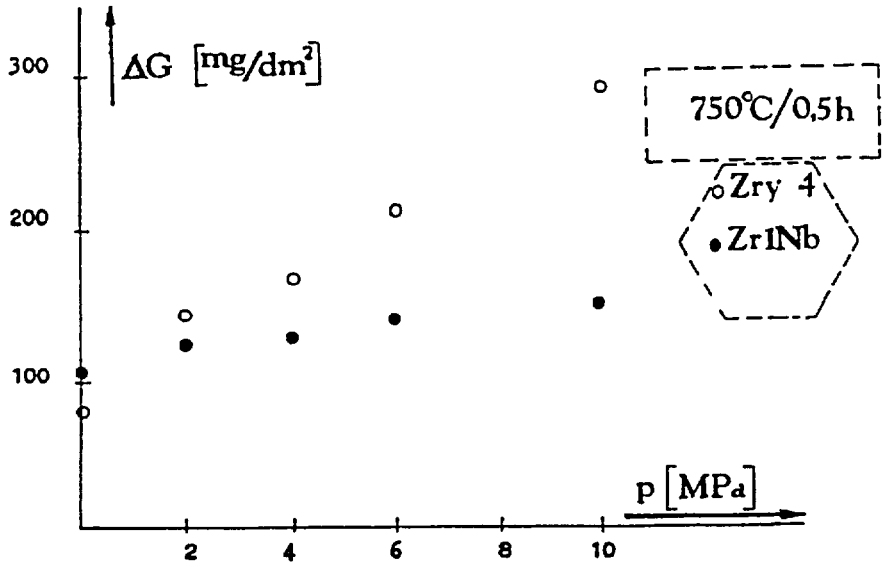

Figure 13

Dependence of the weight gains of Zr1Nb and Zry-4 alloys on steam pressure at 750°C (from Vrtilkova et al., REZ (Czech Republic), 1993)

However, at 850°C and 40 bars, the initial kinetic is strongly enhanced for E-110 alloy; it overcomes 17 % ECR (embrittlement criterion) under 2-side oxidation in about 200 s, even without wall thinning by ballooning, at 850°C it overcomes the Baker-Just Kinetic at 1204°C, the E-110 initial kinetic is about 10 times faster than the corresponding Zircaloy-4 kinetic (figure 14) [14].

Bibilashvili et al. published data in English only at 700°C [2]. However, they recognize that: "The effect of steam pressure on oxidation kinetics of Zr1%Nb alloy is marked at higher temperatures ... in contrast to Zry-4 alloy".

Pending to Park's remark, one may observe also that temperature at which the pressure effect is maximal for E-110 (850°C) is in the temperature range of the breakaway peak at atmospheric pressure and longer times (figure 15) [2].

Figure 14 - E110 / Zry - weight gain at 850°C as a function of square root of time and steam pressure

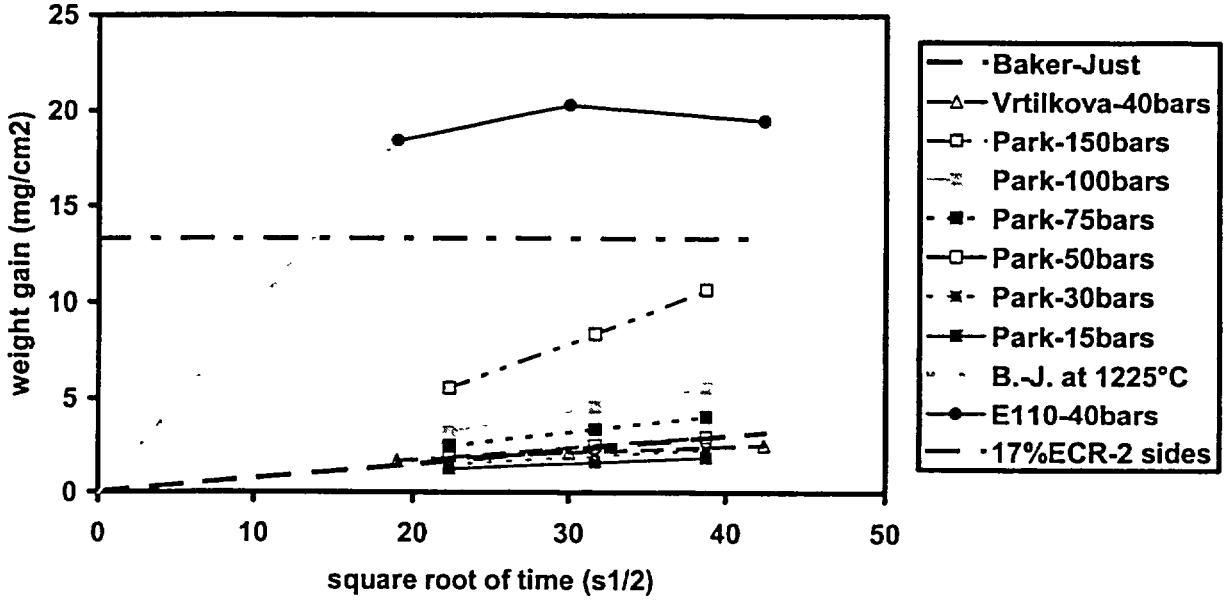

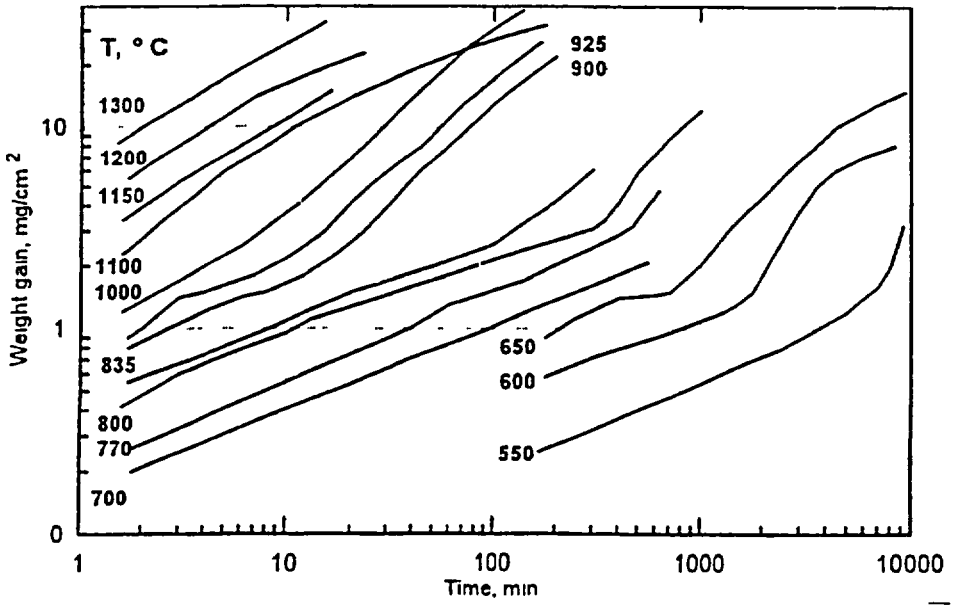

Figure 15

Weight gains of VVER-type claddings oxidized in steam at atmospheric pressure (From Bibilashvili et al., Dimitrovgrad (Russian Federation) 1995)

4.2. High-burnup Zircaloy-4

JAERI found that hydrogen modifies the tetragonal/monoclinic transition by the formation of a mixture of tetragonal and monoclinic oxides [26]. There is a lack of data for high burnup (hydrided) Zircaloy-4. It is desirable that experimental programs fill this gap.

4.3. Other alloys

Post-quench ductility cannot be extrapolated from one zirconium alloy to another one [25]. This is also the case for long-term breakaway at atmospheric pressure (figures 12 and 15) [21] [2]. On the contrary, short-term weight gain kinetic at atmospheric pressure can be extrapolated from one zirconium alloy to another one [27]. As we have seen in § 3 to 4.2, the case of high pressure steam oxidation behaviour is similar to post-quench ductility and long-term breakaway and dissimilar to short-term weight gain kinetic at atmospheric pressure .

There is a lack of data for M5 (Zr 1%Nb O-rich S-doped) and ZIRLO. It is desirable that experimental programs fill this gap.

5. 17 % ECR and the Baker-Just correlation

After this first main part, we will calculate after Hobson's data [28] what would have been the Equivalent Clad Reacted (ECR) value, if the U.S. Regulatory Staff had used in 1973 the Cathcart-Pawel weight gain correlation [24] instead of the Baker-Just Correlation [11]. The rationale and databases used to establish the 17 % maximum oxidation limit were presented two years ago [29]. We revisit hereafter this question for précising various aspects.

It has to be kept in mind that during the 1973 Emergency Core Cooling System (ECCS) Rule-Making Hearing, the U.S. Regulatory Staff suggested to consider a zero-ductility temperature (ZDT) no higher than 275° F (135°C), i.e. the saturation temperature during reflood. Based on Hobson's slow ring-compression tests, this was equivalent to a fractional thickness of the combined oxide and alpha layers (ξ_T/W_0) no higher than 0.44 (Reference 20 of [29]). Then, this threshold was replaced by the 17 % ECR limit calculated with the Baker-Just correlation through the rather complicated figure 8 of [29] (Reference 21 of [29]).

First of all, we have to point out a minor error in our figure 8 of [29], the mentions "from Hobson & Rittenhouse ORNL-4758, 1972, Fig. 5" and "Per Pawel, J. Nucl. Mater. 50 (1973) 247-258" were inverted: the two sinuous solid lines are running through points calculated after the least-square lines of ORNL-4758, Figure 5 ; the two smooth dashed-lines are calculated after the Arrhenius fit by Pawel of the same ORNL-4758, figure 5 data. Our inversion was copied from reference 21 of [29], page 89, first paragraph; no inversion exists in the other paragraph of this page or in the following pages.

Nevertheless, this error doesn't change the conclusion, simply the limiting line is the ORNL-4758, figure 5 - calculated one, not the Pawel's Arrhenius fit-calculated one. The 17 % ECR value was not measured but calculated with the Baker-Just correlation. Two years ago, we concluded: "The threshold equivalent cladding reacted (ECR) of 17 % is tied with the use of Baker-Just correlation. If a best-estimate correlation other than Baker-Just equation (e.g., Cathcart-Pawel correlation) had been used, the threshold ECR would have been < 17 %".

There is another way to illustrate this figure 8 of [29] calculation. In a first step, we draw the Hobson's slow ring-compression tests specimen ductility map as a function of deformation temperature and ξ_T/W_0 (figure 16), ξ_T/W_0 was calculated after least-square lines of ORNL-4758, figure 5, as for the limiting sinuous solid line of figure 8 of [29]; in order to show the number of Hobson's specimens, when they had same time at same oxidation temperature and same compression temperature, we performed an artificial displacement by 10°F, upwards for the (partially) ductile ones and downwards for the zero ductility ones. A very good straight line bounds the zero ductility points; this limiting line crosses 275°F at ~ 0.44.

In the next step, we draw the ductility map as a function of deformation temperature and ECR calculated after Baker-Just correlation, as for the figure 8 of [29] (figure 17). Again, a very good straight line bounds the zero ductility points; this limiting line crosses 275°F between 17 and 18 %; 17 % was chosen as rounded value at the left of the limiting line.

This procedure enables us to make a hypothetical step by drawing the ductility map as a function of deformation temperature and ECR calculated after Cathcart-Pawel correlation (figure 18). Again, a very good straight line bounds the zero ductility points and crosses 275°F between 14 and 15 % ; 14 % would have been chosen as rounded value at the left of the limiting line, if the Regulatory Staff would have had and used in 1973 the Cathcart-Pawel correlation. The value is 14 % and not 13 %, because Hobson's points oxidized at 2000°F on the sinuous solid line of figure 8 of [29] and on the figures 16 to 18 are more limiting than points at 2200°F.

Figure 16 - Hobson's slow ring-compression tests - Specimen ductility as a function of deformation temperature and ξ_T/Wo (Calculated after ORNL-4758, figure 5)

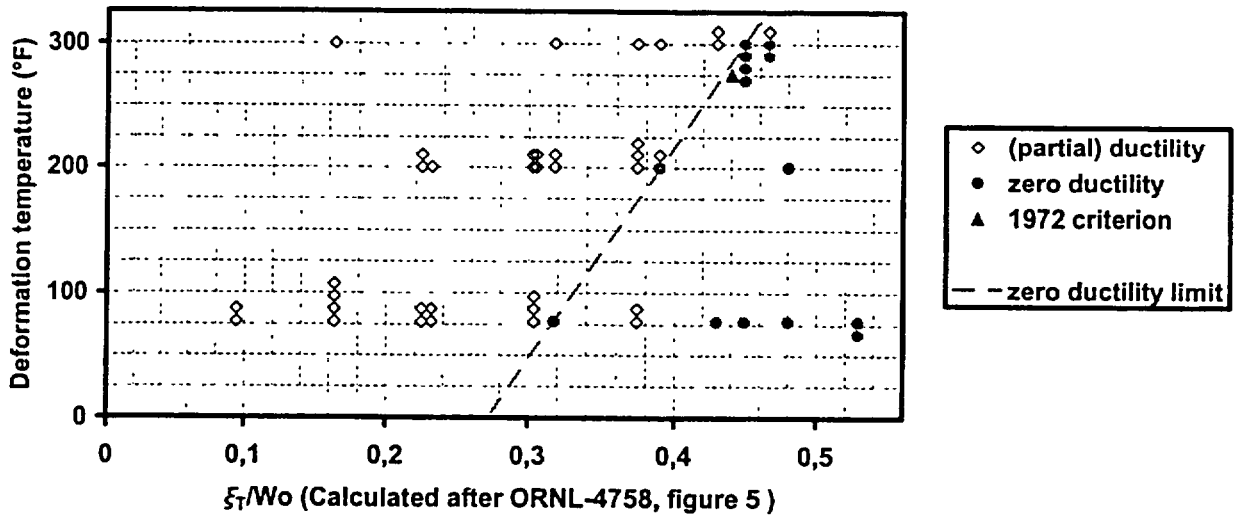

Figure 17 - Hobson's slow ring-compression tests - Specimen ductility as a function of deformation temperature and ECR (Calculated with Baker-Just)

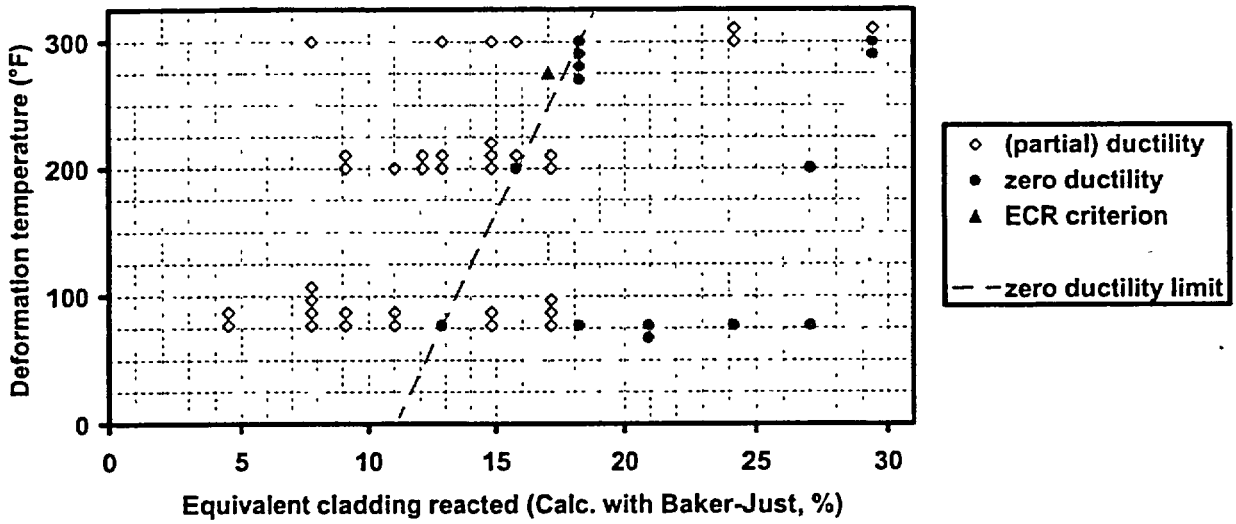

Figure 18 - Hobson's slow ring-compression tests - Specimen ductility as a function of deformation temperature and ECR (Calculated with Cathcart-Pawel)

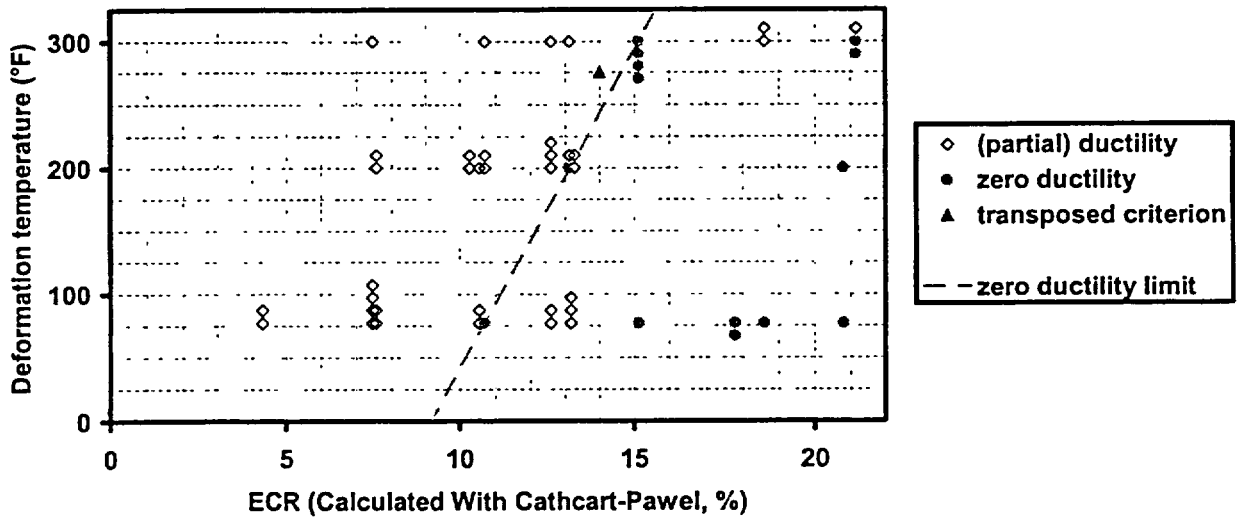

As a conclusion, Baker-Just correlation must be used for comparison with 17 %, but not necessarily for calculation of chemical heat.

6. Cathcart-Pawel correlation

Finally, as Cathcart-Pawel weight gain correlation [24] is used in RG 1-157 § 3.2.5.1 and recommended in Research Information Letter (RIL) 0202 [30], we will make some remarks on this correlation.

Oxidation was performed nominally only at the outer side. The MiniZWOK furnace had a low inertia, the transients were nearly purely isothermal, with fast heating and cooling ramps. There was a detailed Arrhenius-type correction of the heating and cooling ramps by the calculation of an equivalent isothermal time. Thermocouples were welded on the inner side, they measured directly nearly the metal/oxide interface temperature, the heat exchange between thermocouple and gas was low.

The weight gain was measured by the metallurgical method, oxide being supposed stoichiometric for the "classical" correlation. These tests looked apparently pretty good.

However, the reading of appendix B of [24] revealed a surprise: there was a high hydrogen uptake (up to 1096 wtppm). This was due to steam leaks at the inner side, this steam oxidized the tube entry and was transformed to hydrogen, which was absorbed near the tube center. Ignoring the hydrogen effect on the Zr(H)-0 phase diagram, in particular on the $\alpha Zr(0)/\beta Zr(H)$ border, Cathcart and Pawel thought that this hydrogen uptake was without impact on the kinetics.

Now we know that hydrogen stabilizes βZr, increasing the oxygen solubility, and destabilizes $\alpha Zr(0)$, a greater oxygen content being necessary to stabilize it in presence of hydrogen. This effect was confirmed by recent tests in France, sponsored by IRSN and EDF [31]: two specimens, one precharged at 1000 ppm hydrogen and the other without hydrogen, were charged at 0.5 wt % oxygen by 2-side oxidation and then annealed at 1100°C for 3 hours in order to dissolve the oxide layers up to the thermodynamic $\alpha Zr(0)/\beta$ equilibrium. Figure 19 shows that $\alpha Zr(0)$ thickness is reduced and β thickness enlarged for the hydrogen-containing specimen.

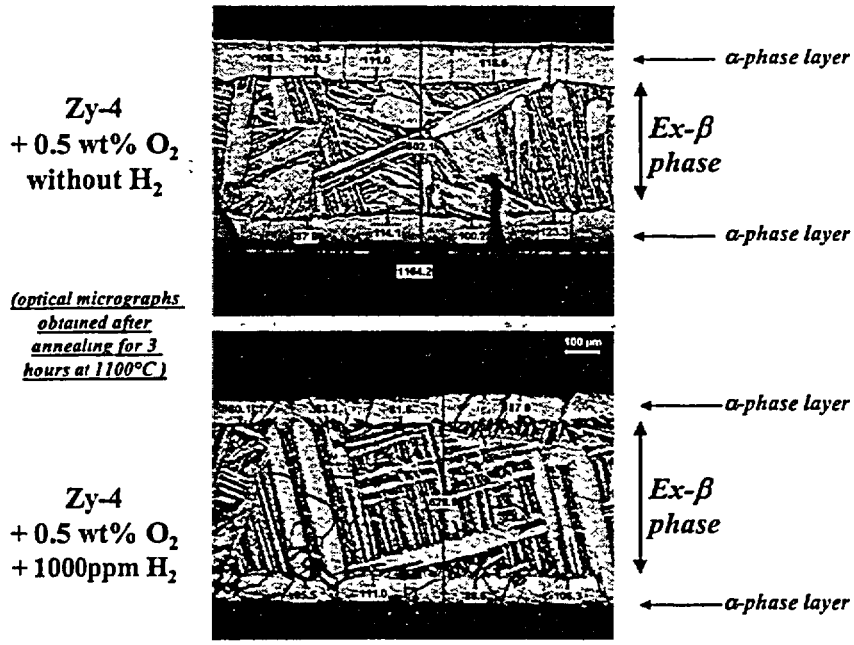

Figure 19

α and β fractions in 0.5 wt/% oxygen-containing specimens, as a function of hydrogen content (From Brachet et al., Stockholm (Sweden) 2002)

This explains why, despite the fact that Cathcart-Pawel weight gain and oxide layer growth correlations are nearly identical to Kawasaki ones [32] and higher than Leistikow ones [21] (figure 20), the alpha layer growth and even the combined oxide and alpha layer growth (ξ) are the lowest (figure 21).

Figure 20 - Parabolic rate constants for oxide layer determined in furnace-heated experiments as a function of temperature

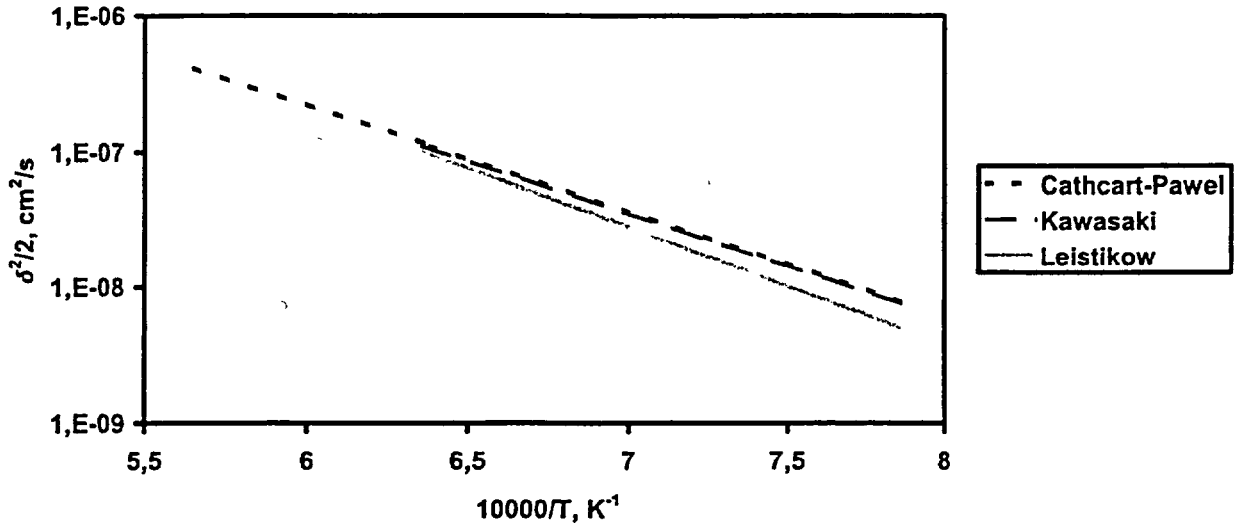

Figure 21 - Parabolic rate constants for oxide plus alpha layer (ξ) determined in furnace-heated experiments as a function of temperature

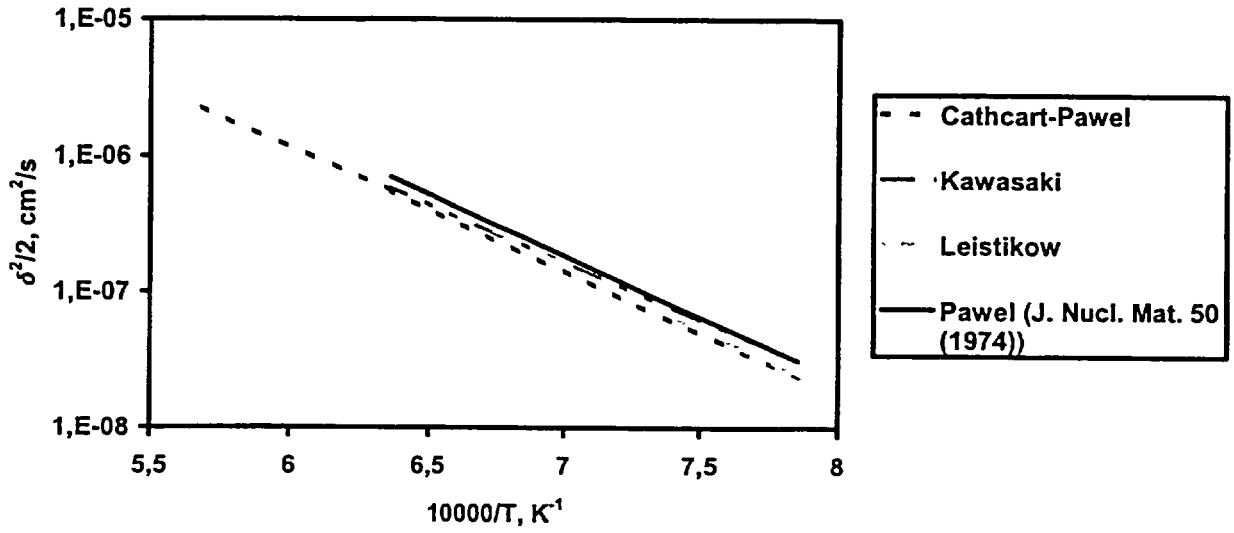

In Kawasaki experiments, oxidation was performed at both sides. There was no hydrogen uptake. His furnace had a higher inertia. Contrary to what is written by Williford [33], there was also a detailed Arrhenius-type correction of the heating and cooling ramps by the calculation of on equivalent isothermal time, see for example [34]. One thermocouple was welded on the outer side and another one placed inside the tube, they show good consistency during the isothermal plateau, the retained thermocouple was the outer one. Specimens were weighed.

In the metallurgical measure of the weight gain by Cathcart and Pawel, oxygen concentrations in the β and $\alpha Zr(0)$ phases are underestimated, $\alpha Zr(0)$ thickness is reduced, but this is compensated for by the oxide stoichiometry assumption, such that Cathcart-Pawel correlation coincides nearly perfectly with Kawasaki one.

As a conclusion, Cathcart-Pawel correlations cannot be used for the calculation of ξ (Supplemental Testimony criterion, reference 20 of [29]), relative β thickness (Scatena and Sawatzky criteria, reference 28 of [29]) or absolute β thickness (Chung and Kassner criteria, reference 17 of [29]). However, as Cathcart-Pawel weight gain correlation coincides nearly perfectly with Kawasaki one, it may be used for the calculation of chemical heat, provided that the uncertainties are taken into account (that is to say in a RG 1.157 methodology). By definition of a best-estimate correlation, as 50 % of the Cathcart-Pawel and Kawasaki experimental points oxidize faster than the weight gain correlation, it cannot be used in an Appendix K to 10 CFR 50 methodology.

Conclusions

1) For fresh Zircaloy-4 under intermediate break LOCA, there is a moderate pressure enhancement effect below 1100°C, this oxidation enhancement doesn't cause any actual safety problem for intermediate break LOCA, if hydrogen uptake is limited.

2) This oxidation enhancement seems to be related to the tetragonal to monoclinic zirconia transformation.

3) Limited published data show a strong oxidation enhancement at 850°C for fresh E-110 alloy, rapidly exceeding the 17%ECR embrittlement criterion under intermediate break conditions.

4) High pressure oxidation data for M5, ZIRLO alloys and high burnup Zircaloy-4 are lacking, and are insufficient for hydrogen uptake by fresh Zircaloy-4.

5) If the U.S. Regulatory Staff had had and used in 1973 the Cathcart-Pawel correlation, they would have calculated a 14 % ECR limit.

6) Due to a compensation of approximations and system-effects, the Cathcart-Pawel weight gain correlation may be used for the calculation of chemical heat in a best-estimate methodology, but not in an Appendix K to 10 CFR 50 methodology.

Références

1) Parsons, P.D. et al., The Deformation, Oxidation and Embrittlement of PWR Fuel Cladding in a Loss-of-Coolant Accident: A State-of-the-Art Report, CSNI Report 129, December 1986.

2) Bibilashvili, Yu.K. et al., High-temperature interaction of fuel rod cladding material (Zr1%Nb alloy) with oxygen-containing mediums, IAEA Technical Committee Meeting on Behavior of LWR Core Materials under Accident Conditions, Dimitrovgrad, Russian Federation, 9-13 October 1995, pp 117-128.

3) Le Bourhis, A., Justification of the M5 behavior in LOCA, OECD Topical Meeting on LOCA Fuel Safety Criteria, Aix-en-Provence, France, 22-23 March 2001, pp105-133.

4) Leech, W.J., Ductility testing of Zircaloy-4 and ZIRLO cladding after high temperature oxidation in steam, OECD Topical Meeting on LOCA Fuel Safety Criteria, Aix-en-Provence, France, 22-23 March 2001, pp 135-143.

5) French IPSN, Probabilistic safety assessment of the standard French 900 MWe Pressurized Water Reactors, Main report, April 1990.

6) U.S. NRC, Severe Accident Risk: An assessment for five U.S. Nuclear Power Plants, NUREG-1150, January 1991.

7) Emergency Core Cooling systems (ECCS) Evaluation Models, U.S. Code of Federal Regulations, Title 10, Part 50, Appendix K, 4 January, 1974, amended.

8) Boyack, B.E. et al., Phenomenon Identification and Ranking Tables (PIRTs) for Loss-of-Coolant Accidents in Pressurized and Boiling Water Reactors Containing High Burnup Fuel, NUREG/CR-6744, December 2001.

9) Valtonen, K. et al., FRAPTRAN Fuel Rod Code and its Coupled Transient Analysis with the GENFLO Thermal Hydraulic Code, First Nuclear Safety Research Conference, Washington, DC (USA), 22-24 October 2001, NUREG/CP-0176, pp 381-395.

10) Pawel, R.E. et al., The oxidation of Zircaloy-4 at 900 and 1100°C in high-pressure steam, Journal-of-Nuclear-Materials (Jun 1979), v. 82(1) pp 129-139.

11) Baker, L. and Just, L.C., Studies of metal-water reactions at high temperatures; III Experimental and theoretical studies of the zirconium-water reaction, ANL-6548, May 1962.

12) U.S. NRC, Office of Nuclear Regulatory Research, Best-estimate calculations of emergency core cooling system performance, Regulatory Guide 1.157, May 1989.

13) Bramwell, I.L. et al., An experimental investigation into the oxidation of Zircaloy-4 at elevated pressures in the 750 to 1000°C temperature range, 10. international symposium on zirconium in the nuclear industry, Baltimore, MD (USA), 21-24 June 1993, ASTM STP 1245, pp 450-465.

14) Vrtilkova, V. et al., Oxiding and hydriding properties of Zr-1Nb cladding material in comparison with zircaloys, Technical committee meeting on influence of water chemistry on fuel cladding behaviour, Rez (Czech Republic), 4-8 Oct 1993, IAEA-TECDOC--927 pp 227-251.

15) Park, K. et al., Pressure effects on high temperature Zircaloy-4 oxidation in steam, International topical meeting on LWR fuel performance, Park-City, Utah (USA), 10-13 April 2000, CD-ROM, poster presentations, pp 394-401.

16) Cox, B., Accelerated oxidation of Zircaloy-2 in supercritical steam, AECL-4448, April 1973.

17) Arashi, H. et al., P-T phase diagram of ZrO2 determined by in situ X-ray diffraction measurements at high pressures and high temperatures, Science and Technology of Zirconia III, Tokyo (Japan), 9-10 September 1986, pp 493-500.

18) Barberis, P., Zirconia powders and Zircaloy oxide films: tetragonal phase evolution during 400°C autoclave tests, Journal of Nuclear Materials 226 (1995), pp 34-43.

19) Godlewski, J. et al., Raman spectroscopy study of the tetragonal to monoclinic transition in zirconium oxide scales..., 9th international symposium on zirconium in the nuclear industry, ASTM STP 1132, pp 416-436.

20) Garvie, R.C., Zirconium dioxide and some of its binary systems, in Alper, A.M., High Temperatures Oxides Part II, Academic Press, 1970.

21) Leistikow, S. and Schanz, G., Oxidation kinetics and related phenomena of Zircaloy-4 fuel cladding exposed to high temperature steam and hydrogen-steam mixtures under PWR accident conditions, Nuclear Engineering and Design 103 (1987), pp 65-84.

22) Murase, Y. and Kato, E., Einfluss von Wasser auf die Kristallisation von ZrO2, Berichte der Deutsche Keramik Gesellschaft 57 (1980) Nr 4-5, pp 86-88 (in German).

23) Kofstad, P., High Temperature Corrosion, Elsevier Applied Science

24) Cathcart, J.V. et al., Zirconium metal-water oxidation kinetics IV. Reaction rate studies, ORNL/NUREG-17, July 1977.

25) OECD/NEA/CSNI, Proceedings of Topical Meeting on LOCA Fuel Safety Criteria, Aix-en-Provence, 22-23 March 2001, NEA/CSNI/R(2001)18.

26) Furuta, T. and Motohashi, H., Products at the surface of Zircaloy cladding under LOCA conditions, Journal of Nuclear Materials 95 (1980), pp 303-306.

27) Billone, M.C. et al., Steam oxidation kinetics of zirconium alloys, 11 June 2002, ADAMS accession number #ML021680052.

28) Hobson, D.O., Ductile-brittle behavior of Zircaloy fuel cladding, Proc. ANS Topical Mtg. on Water Reactor Safety, Salt Lake City, Utah (USA), 26 March, 1973, pp 274-288.

29) Hache, G. and Chung, H.M., The history of LOCA embrittlement criteria, 28th Water Reactor Safety Information Meeting, Bethesda, MD (USA), 23-25 October 2000, NUREG/CP-0172, pp 205-238.

30) Thadani A.C., Revision of 10 CFR 50.46 and Appendix K, Research Information Letter 0202, 20 June 2002, ADAMS accession number #ML021720690.

31) Brachet J.C. et al., Thermocalc/Zircobase calculations applied to Zircaloys; Influence of oxygen and hydrogen concentrations on the equilibrium α/β phases at high temperature, CALPHAD XXXI, Stockholm (Sweden), 5-11 May 2002.

32) Kawasaki, S. et al., Oxidation of Zircaloy-4 under high temperature steam atmosphere and its effect on ductility of cladding, Journal of Nuclear Science and Technology 15 (8), August 1978, pp 589-596.

33) Williford, R.E., An assessment of safety margins in Zircaloy oxidation and embrittlement criteria for ECCS acceptance, NUREG/CR-4412, April 1986.

34) Suzuki M. et al., Zircaloy-steam reaction and embrittlement of the oxidized zircaloy tube under postulated LOCA ; oxidation kinetics and embrittlement of zircaloy at above 1200°C, JAERI/M-6879, January 1977, English translation NUREG/TR-0014, November 1977.

This page left intentionally blank

INVESTIGATION OF THE IMPACT OF IN-REACTOR SHORT-TERM DRY-OUT INCIDENTS ON FRESH AND PRE-IRRADIATED FUEL CLADDING

M.A. McGrath, OECD Halden Reactor Project, Halden, Norway

B.C. Oberländer, Institutt for Energiteknikk, Kjeller, Norway

T. Anegawa and T. Hara, TEPCO, Tokyo, Japan

ABSTRACT

An instrumented fuel assembly (IFA), connected to a light water loop within the Halden reactor, has been designed for in-pile dry-out testing Two fresh fuel segments and six segments pre-irradiated to 22-40 MWd/kgU (Zry-2, Zyr-2 with liner and Zry-4) have been tested Each was instrumented with 2 or 3 Cr/Alumel thermocouples to monitor clad surface temperature and an elongation detector to monitor clad thermal expansion. Dry-out was initiated by reducing the coolant flow to an individual test rod channel until the uppermost clad thermocouple showed a significant increase. Flow was then re-established and the rod quenched. Multiple dry-out and quench events were used to accumulated the target time above temperature (10-15 s > 550 or 650°C) and the first six rods exposed were also operated under normal reactor conditions for a month after the final quench However, poor thermal contact between thermocouple and clad outer surface for the first six tested rods led to more severe dry-outs than planned. This was evident when clad from the upper regions of the rods was observed to have a grain structure consisting entirely of quenched former β-grains.

Extensive non-destructive and destructive testing of all the fuel segments were carried out in order both to assess the range of microstructural and mechanical changes induced in the fuel cladding due to the range of in-pile transient heating and to aid in the deduction of the peak clad exposure temperatures (PCTs). It was deduced that the first six rods had developed maximum PCTs in the range 950-1200°C, with oxide spalling, clad collapse and hydrogen pick-up adding to the quenched ex-β microstructure. Room temperature ductility was practically zero. It was thus significant that these rods had not failed in-pile either during quenching or subsequent normal reactor operation. There was significant improvement in room temperature ductility in all clad material where a small α-phase grain structure had been retained during the in-pile transient heating, indicating in-pile annealing of radiation damage.

1. INTRODUCTION

Light water reactor cores may be subjected to thermal-hydraulic transients resulting in inadequate core cooling for short periods of time. In PWRs this would result in departure from nucleate boiling (DNB) and in BWRs the result would be short term dry-out at the fuel rod surface. Both situations lead to transitory temperature increases of the cladding and it is a safety requirement that after such an event

reasonable fuel performance must be maintained up to the subsequent shutdown. In order to be able to assess post dry-out and quench fuel performance, it is necessary to know what effect in-pile transient heating has on the mechanical properties of irradiated cladding. In order to expand the database from out-of-pile experiments with pre-irradiated BWR fuel rod cladding [1], a series of in-pile dry-out experiments were carried out at the Halden Reactor Project. The aim was to expose fresh and pre-irradiated fuel rods to short-term in-pile dry-outs of the type anticipated after a pump trip in a BWR. This in-pile exposure was followed by post irradiation examination (PIE), directed at discovering any microstructural changes induced in the fuel rods and the consequence of these changes to fuel rod mechanical integrity.

Between July 1996 and January 1998 a total of eight rods were individually exposed to short-term dry-out in a series of three loadings of an experimental assembly (IFA-613). In assessing the consequences of dry-out for the rods, the first phase was to monitor fuel rod integrity post-transient and quench, for which six rods were operated under normal reactor conditions for a month after exposure to dry-out. The second phase of the assessment was to determine any changes induced in the microstructural and mechanical properties of the clad, for which a concurrent post-irradiation examination programme was conducted and concluded in 2000.

2. IN-PILE TESTING

2.1 Test Fuel Segments

A total of eight fuel segments were tested in three separate in-reactor loadings. Details of the test segments are given in Table 1.

Table 1. Fabrication and design details of the test fuel segments

IFA Loading	Rod No.	Burn-up (MWd/kg U)	Clad material	Clad ID/OD (mm)	Length (mm)	Fill pressure (bar)
IFA-613.1	DTC1406	29	Zry-2 non-liner	10 80/12.52	760	7.7
	DTC1404	24	Zry-2 non-liner	10.80/12.52	760	3.1
	613-1	0	Zry-2 non-liner	10.80/12.52	760	3.0
IFA-613.2	DTC1113	26	Zry-2 non-liner	10.80/12.52	760	16.6
	564-4	40	Zry-2 liner	10 64/12.27	300	3.0
	564-8	22	Zry-2 liner	10 64/12.27	300	4.5
IFA-613.3	N1310	29	Zry-4 non-liner	9.29/10.75	410	26.0
	613-7	0	Zry-4 non-liner	9.29/10.75	760	3.0

Six of the segments were pre-irradiated within the range 22 to 40 MWd/kgU whilst the other two segments were fresh. Segment length varied from 760 mm to 300 mm (the three shorter segments were attached to fresh fuel extension segments such that each test rod had approximately the same overall length in the test channel). Two thermocouples were attached to the clad surface of each test segment as

shown schematically in Figure 1. These were for monitoring the onset of and axial extent of the dry-out as well as the clad temperature reached Each rod was also equipped with a clad extensometer.

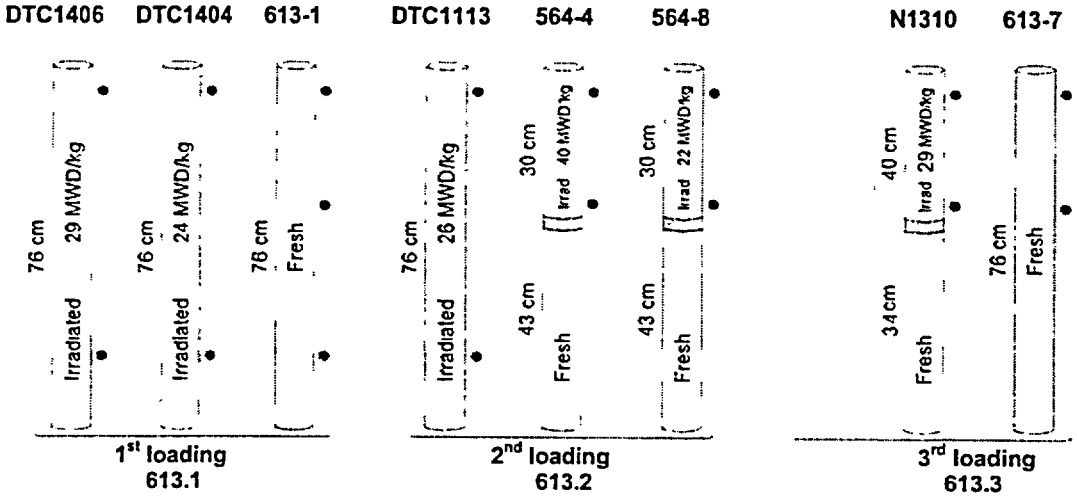

Figure 1. Schematic of the test fuel rods used for the three loadings of IFA-613.

2.2 Test Assembly

A schematic drawing of the test assembly, IFA-613, is given in Figure 2. The main feature of the rig is that it comprised three individual flow channels, each able to contain one instrumented test rod. The channels consisted of a stainless steel pressure tube, connected via a dedicated flow control system to a light water BWR type loop in the Halden Boiling heavy Water Reactor (HBWR) that allowed each rod to be exposed to dry-out on an individually controlled basis. The flow rate in the loop could be varied and an out-of-core electrical heater incorporated into the coolant loop system could be used at different settings. The loop was operated at 70 bar and with a hydrogen concentration of 450±50 ppb. In addition to the stainless steel pressure tube, each flow channel also comprised an outer stainless steel tube, the purpose of which was to ensure that under operating conditions an annulus of saturated steam formed around the pressure tube thereby thermally insulating it during the dry-out events from the low temperature (240°C) HBWR moderator. Other rig instrumentation included vanadium neutron detectors for determining the axial thermal flux profile, a typical example of which is shown in Figure 3, and thermocouples placed at the inlet and outlet of the channels to monitor the light water coolant temperature.

2.3 Dry-Out Test Procedure and In-Pile Operation

Possible procedures that could be used to effect dry-out under controlled conditions were evaluated during the first loading of the test assembly by using a fresh rod (613-1), which was thus repeatedly exposed to severe dry-out conditions, putting it outside of the actual test matrix. It was discovered that dry-out could be reached under three different conditions:

1. at very low flow rates (<20 l/h) without use of the out-of-core electrical heater in the loop

2. in the transient period after the electrical heater was turned off and the flow rate was reduced
3. at low flow rates (25 l/h) with constant use of the electrical heater

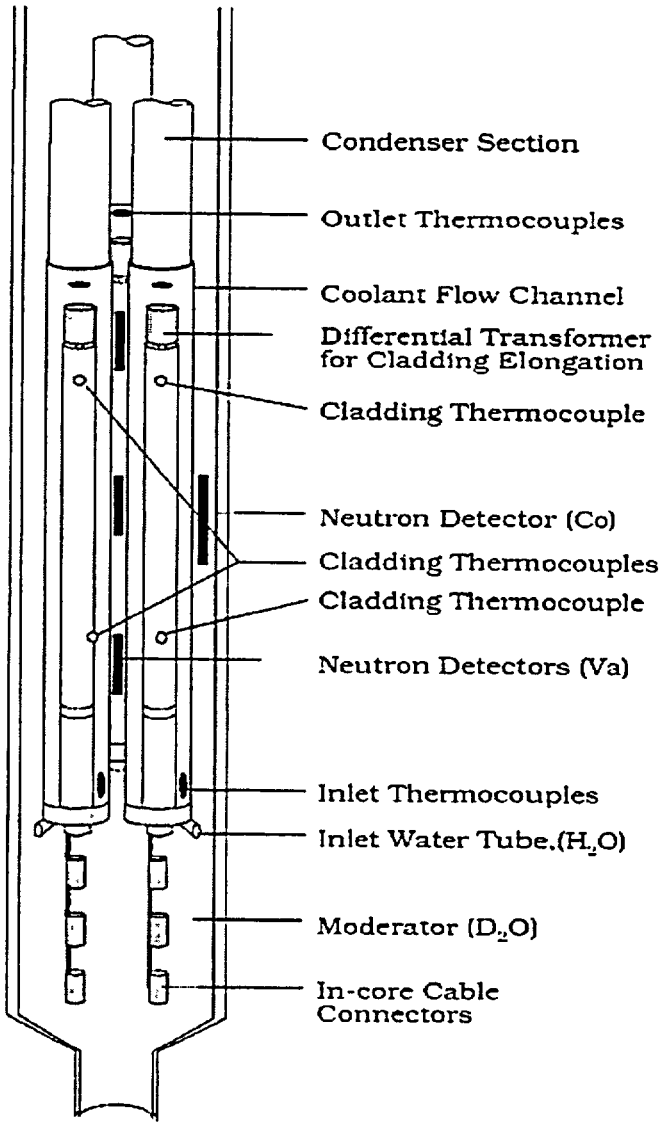

Figure 2. Schematic illustration of the Instrumented Fuel Assembly, IFA-613.

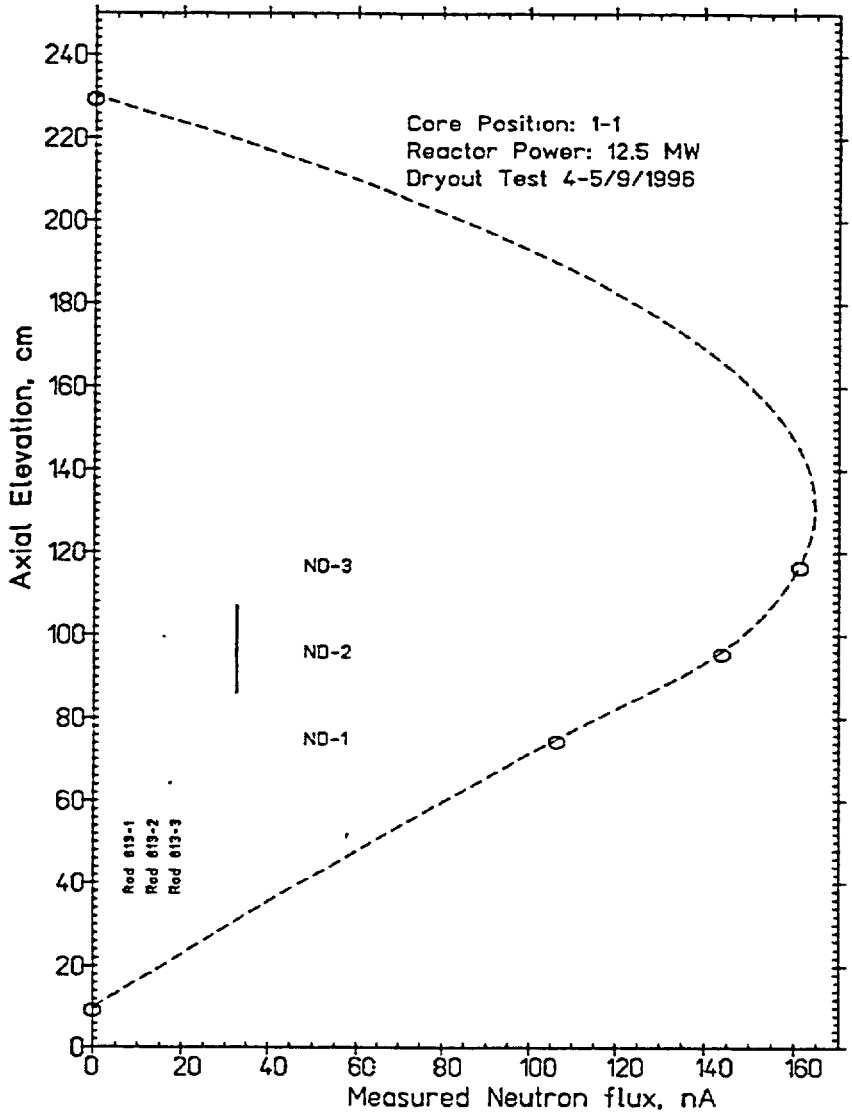

Figure 3. Typical axial power profile in IFA-613.

The dry-out event was more stable and easier to control without use of the electrical heater, hence the first method was used for most of the experiment. The target dry-out scenario as shown in Figure 4 was for the peak clad temperature (PCT) to reach or exceed 550°C or 650°C for approximately 10-15 s. Once dry-out was achieved and the target temperature, as indicated by the upper clad thermocouple, was exceeded the rod was quenched. If the time at target temperature was not long enough, further dry-out events were initiated until sufficient accumulated time above the target temperature was reached. Figures 5 and 6 show examples of the dry-out events accumulated by test rods from the first and final loading of IFA-613 (DTC1404 and N1310).

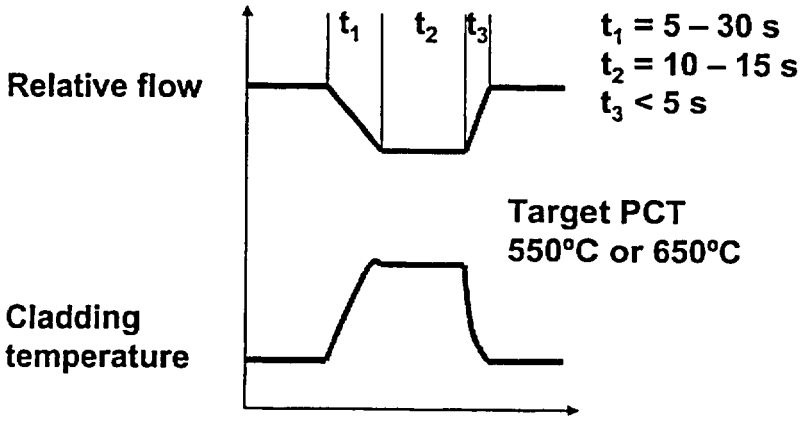

Figure 4. Target single in-pile dry-out scenario for testing rods in IFA-613.

For the first two loadings of the rig, the rods were operated under normal reactor conditions for approximately one month following dry-out. For the final loading, the rig was removed from the reactor immediately after the dry-out tests were completed in order that the "as-tested" fuel and clad properties could be observed in PIE. A summary of the tests carried out in the three loadings of the instrumented fuel assembly is shown in Table 2.

Table 2. Summary of in-pile dry-out exposures

Rod No.	ALHR during dry-out (kW/m)	Method to achieve dry-out	Recorded maximum PCT (°C)	Estimated* maximum PCT (°C)	Operation after dry-out (days)	ALHR after dry-out (kW/m)
DTC1406	12.2-13.2	1	570	1050 ±50	30	14.0
DTC1404	9.8-10.4	1	720	1000 ±50	30	19.3
613-1	8.6-14.7	1, 2, 3	780	1200 ±50	30	29.5
DTC1113	10.5-15.2	1	735	1100 ±50	23	19.7
564-4	10.0-11.4	1	800	950 ±50	23	13.4
564-8	18.4-19.6	2,3	750	1150 ±50	23	19.5
N1310	23.5-24.1	2	750	850 ±50	none	...
613-7	11.0-12.3	1	710	750 ±50	none	...

* see Section 2.4

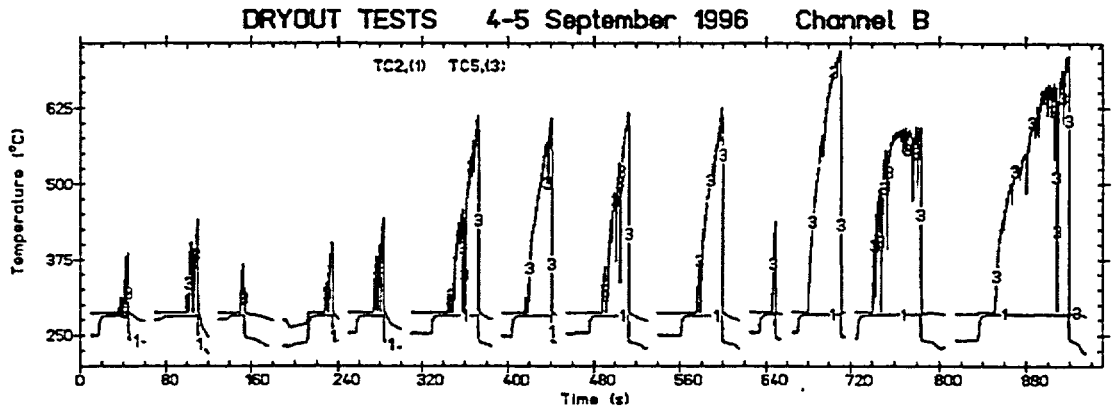

Figure 5. In-pile recorded cladding surface temperature for test rod DTC1404 exposed to repeated dry-out transients in IFA-613 1st loading

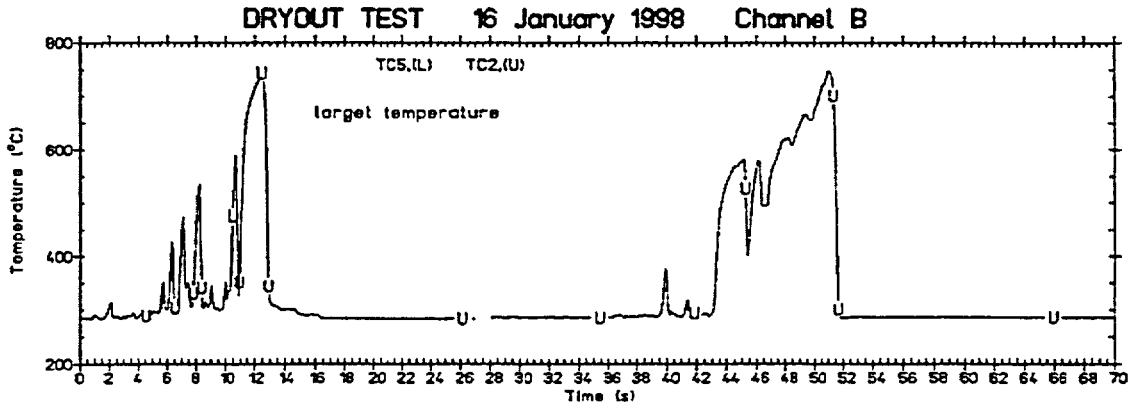

Figure 6 In-pile recorded cladding surface temperature for test rod N1310 exposed to two dry-out transients in IFA-613 3rd loading

2.4 In-Pile Results: Peak Clad Temperatures

According to the clad surface thermocouple readings, all rods received their target dry-out exposures. However, when cladding from the upper ends of rods from the first two rig loadings was observed during PIE to have a quenched, former β-grain structure, it was apparent that the maximum peak clad temperatures must have been substantially higher than the as indicated values of 570 to 800°C. Whilst it was apparent that such severe dry-out conditions would have affected the clad mechanical properties, these rods neither failed during the dry-out events nor the proceeding operation period.

The low temperature readings were attributed to insufficiently close thermal contact between thermocouple and cladding. As the surface thermocouples were used to monitor and control the dry-out events, this had allowed the more severe than planned dry-out exposures to occur, in terms of both accumulated time in dry-out (many transients) and peak temperature. A new thermocouple attachment was designed for the rods to be tested during the final loading of the rig. This proved satisfactory such that the target dry-out exposures for these rods were met without being significantly exceeded.

In order to estimate the clad exposure temperatures for the rods with under-reading thermocouples, the HECHAN code [2], used by Siemens/KWU for thermal-hydraulic pre-calculations for IFA-613, was used to define the shape of the axial temperature profile that would have developed along the cladding of a fuel rod during dry-out in IFA-613. Cladding temperature in the dry-out zone, T, can be described as follows:

$$T = T_o + (T_{peak} - T_o) \times (1 - \exp(-7 \times l_{DO} / L_{DO}))$$

Where:

T_o = clad temperature at boundary with wetted surface i.e. saturation temperature (285°C)

T_{peak} = peak clad temperature (PCT) in the dry-out zone

l_{DO} = axial elevation from the bottom of the dry-out zone (zero to L_{DO})

L_{DO} = total length of the dry-out zone i.e. where temperature > 285°C

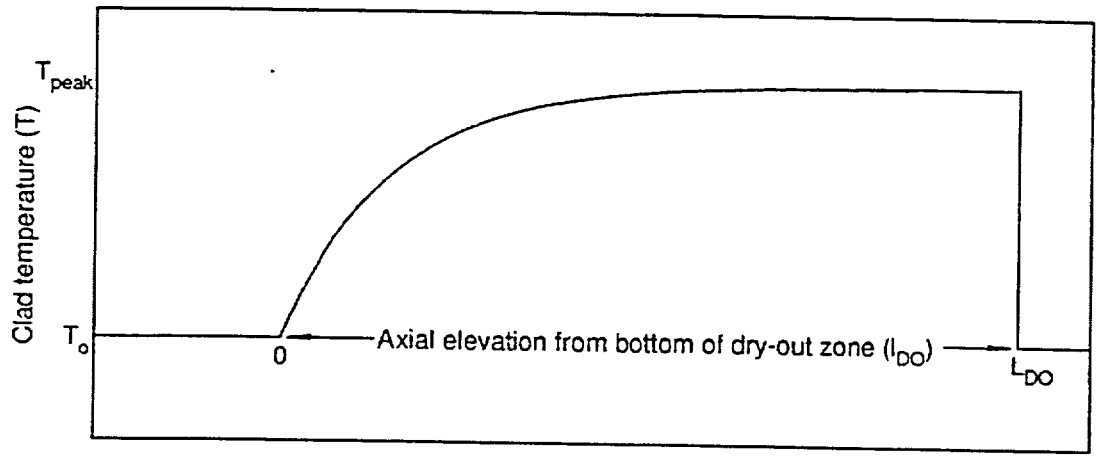

Figure 7. The axial temperature profile predicted by HECHAN to develop in the fuel rod cladding during dry-out transients performed in IFA-613.

The maximum peak clad exposure temperature for each rod was then estimated from the maximum clad elongation recorded during the dry-out transients, assessed in terms of Zircaloy thermal expansion and the axial temperatures profile predicted by HECHAN (see Figure 7). The length of the dry-out zone (L_{DO}) was estimated from the combined results from the PIE examination. For the first two loadings, PCTs of between 950 and 1200°C have been estimated with total hold times in dry-out varying from 5 to 80 s.

3. POST-IRRADIATION EXAMINATION (PIE)

Each rod was examined after in-pile testing with the aim of being able to document and quantify dry-out induced changes in the mechanical and microstructural properties of the clad. Non-destructive examination of the entire length of each rod was carried out to determine overall condition, used for assessing where the dry-out had occurred along the rods and to aid in making a cutting plan for the destructive PIE. The destructive examination and testing was carried out at selected axial positions according to the cutting plan. Sections were taken from the upper region of each rod, where the rods experienced short-term dry-out, with control samples being taken from the lower region of each rod where dry-out would not have occurred. Extra axial positions were also tested on some of the severely exposed rods with the aim of enabling an evaluation of the axial temperature profile assumed to have been induced in the clad during dry-out, and thus also the estimates for PCT.

The final aim was to allow rod overall condition, cladding mechanical properties and microstructure to be compared at various axial locations such that a comparative approach could be made to interpreting the PIE results. This resulted in four distinctive axial zones being identified· the unaffected zone; two transients zones; and a peak dry-out zone. These will be referred to as the results are given and again in a summary of the PIE results.

3.1 Visual Inspection and Profilometry

Rod overall condition was assessed by non-destructive PIE techniques. Visual inspections, recorded as photographic images, gave information about the surface oxide condition whilst profilometry gave information about changes to the diameter of the rods.

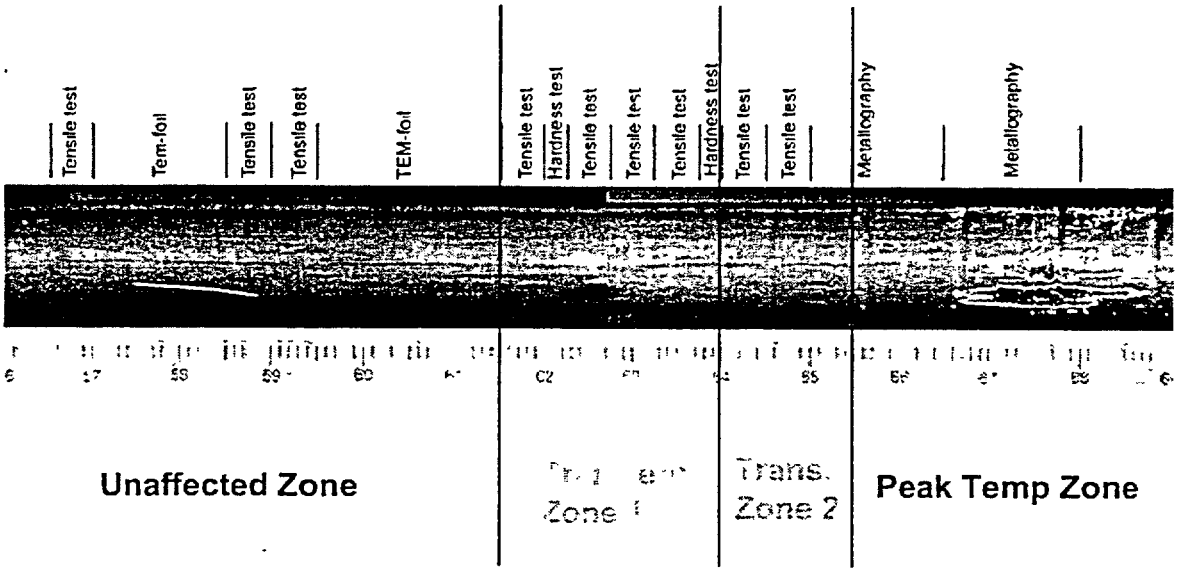

Figure 8(a). Results of the visual examination of the severely dry-out tested rod, DTC1404.

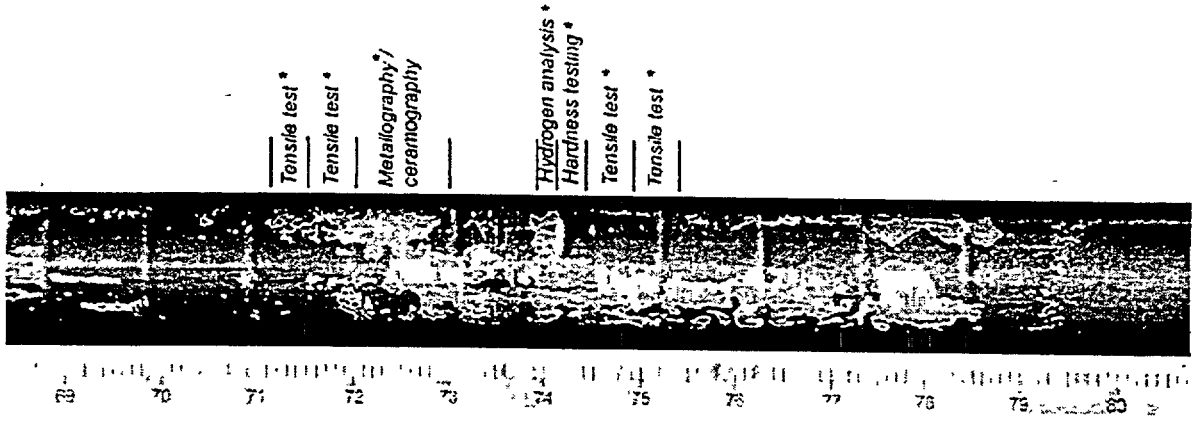

Figure 8(b). Results of the visual examination of the severely dry-out tested rod, DTC1404 (cont.).

Following in-pile testing, the rods were classed as either severely tested (DTC1406, DTC1404, 613-1, DTC1113, 564-4 and 564-8) or less severely tested (N1310, 613-7) and each severely tested rod showed basically the same surface characteristics, as typified by rod DTC1404. The results of both examinations for DTC 1404 are shown in Figures 8 and 9.

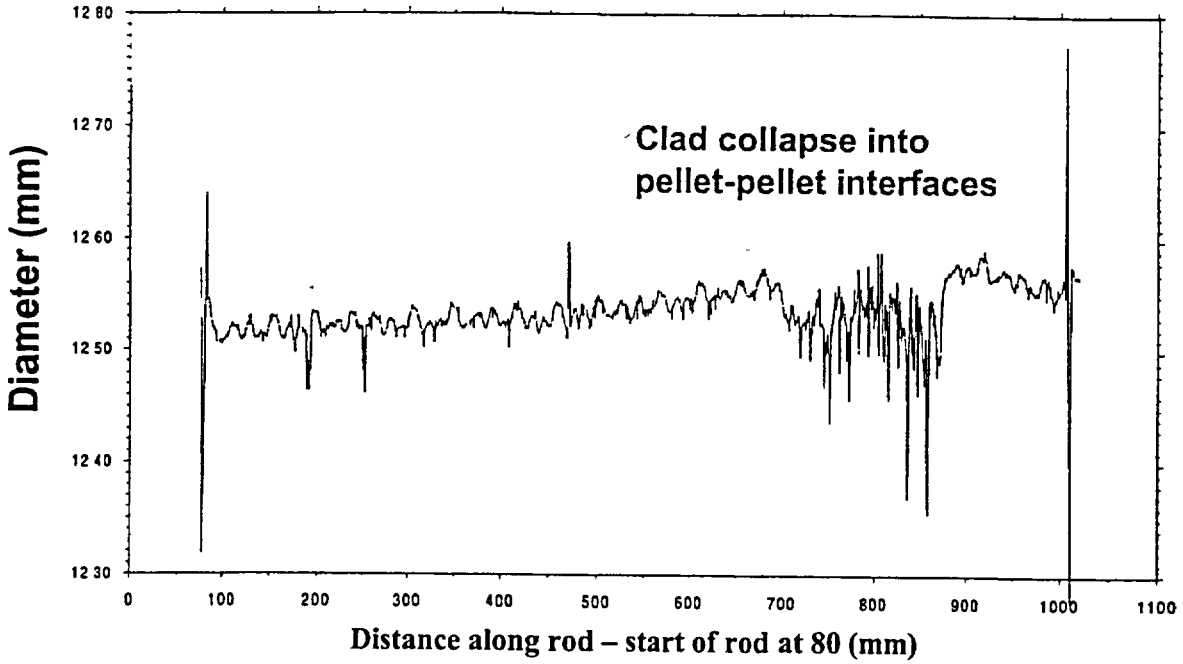

Figure 9. Results of the profilometry examination of the severely dry-out tested rod, DTC1404

From the bottom of the rod up to 655 mm, the surface is covered with a smooth, dark uniform oxide layer. A few white spots appear on the surface at 655 mm, indicating the start of oxide spalling and thus probably the onset of film boiling. These develop into a partial surface covering of white oxide, indicating substantial oxide spalling from about 665 mm up to the top of the active fuel stack (795 mm) At 610 - 620 mm, profilometry shows clad creepdown as a general reduction in diameter and regularly spaced surface depressions are visible from 625/635 mm to 795 mm. These coincide with pellet-pellet interfaces, indicating clad collapse between pellets

The less severely tested rods showed no evidence of oxide spalling or clad collapse, but did show a general reduction in diameter signifying clad creepdown.

3.2 Mechanical Testing and Fractography

The goal of this examination was to find dry-out induced changes in the mechanical properties of the cladding with respect to the rod axial elevation. Several 5 mm wide, transverse cross-sections were cut from upper, lower and intermediate locations of the rods and de-fuelled for tensile testing. Testing was performed at 20°C with an Instron 1115 Tensile Tester fitted with a specimen holder designed for testing ring samples in the hoop direction. Three holders were used, each consisting of two semi-circular cylinders with radii machined to match the inner diameter of the cladding being tested. The clad rings were placed over the holders and pulled in opposite directions at a cross-head speed of 2 mm/min. Gauge length was assumed to be 10% of the mean clad ring circumference, giving nominal strain rates of 0.55 to 0.63/min depending on clad ID. Values of ultimate tensile strength (UTS) and total plastic elongation to failure (TEL) were derived from load-displacement curves and the results from all the rods tested are given in Table 3. Examples of the load-displacement curves for one of the severely tested rods (DTC1404) and one of the less severely tested rods (N1310) are shown in Figures 10 and 11.

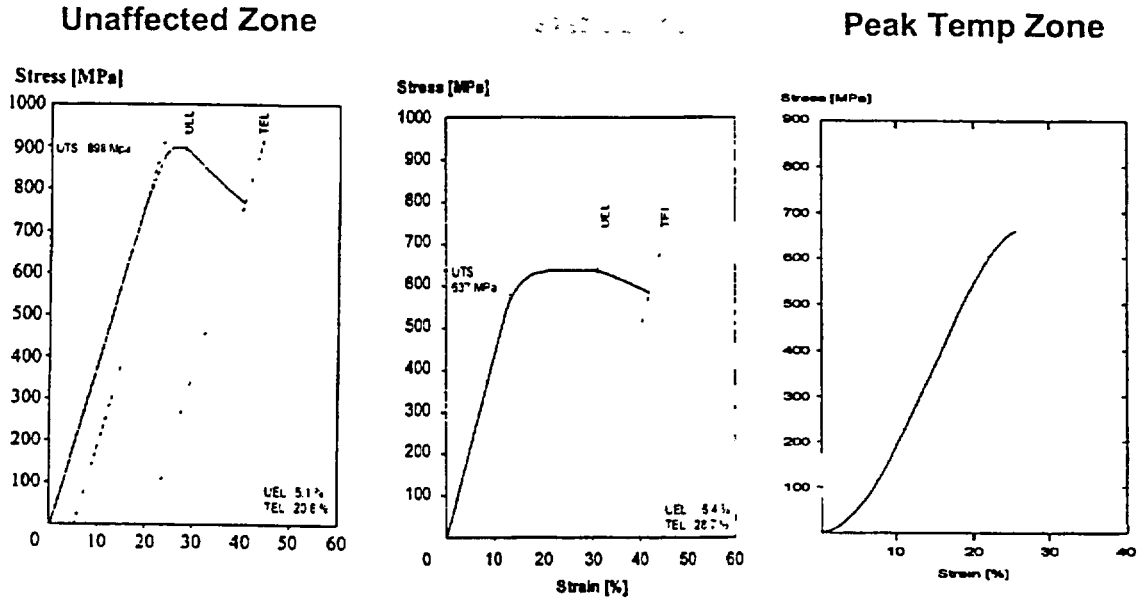

Figure 10. Example of the load-displacement curves generated from samples taken from three different axial locations on one of the severely tested rods (DTC1404)

Table 3. Results from ring tensile testing at room temperature

Rod No.	Unaffected zone		Transient zone 1		Transient zone 2		Peak dry-out zone	
	axial position (mm)	UTS/TEL (MPa/%)	Axial position (mm)	UTS/TEL (MPa/%)	Axial position (mm)	UTS/TEL (MPa/%)	Axial position (mm)	UTS/TEL (MPa/%)
DTC 1406	143 148 571 575 608	884 / 11.1 868 / 10.9 811 / 12.4 805 / 18.1 907 / 6.0	613 620 625 630 638 643	846 / 14.6 812 / 19.4 774 / 19.8 722 / 22.0 659 / 17.4 677 / 23.4	663 668	622 / 8.4 631 / 13.8	713 718 749 754 785	583 / 0.0 590 / 0.0 568 / 0.0 275 / 0.0 top
DTC 1404	149 154 168 568 588 593	870 / 12.5 847 / 14.6 898 / 20.6 866 / 17.3 852 / 15.7 888 / 14.0	618 625 635	749 / 21.8 700 / 25.8 637 / 28.7	643 648	663 / 24.4 667 / 21.7	713 718 747 752 795	695 / 4.1 740 / 4.1 662 / 2.3 620 / 2.0 top
DTC 1113	205	913 / 12.9	-	- / -	-	- / -	690 695 795	525 / 0.0 640 / 1.6 top
564-4	588	867 / 18.6	744	660 / 38.9	782	640 / 34.4	850	Top
564-8	594	827 / 21.0	-	- / -	714	754 / 15.8	777 850	743 / 7.0 top
N1310	512 522	925 / 5.1 827 / 1.3	780 790	759 / 12.0 737 / 15.1	-	- / -	-	- / -
613-7	89 119	738 / 39.1 732 / 39.3	694 724	638 / 54.7 647 / 44.3	-	- / -	-	- / -

The TEL and UTS results for one of the severely tested rods (DTC1404) and one of the less severely tested rods (N1310) are shown in Figure 12 and 13 as a function of axial location along each of the rods.

After mechanical testing, the fracture surfaces of the ring samples were examined in a scanning electron microscope (SEM) to determine the fracture mode and examples of these images for test rod DTC1404 are shown in Figure 14.

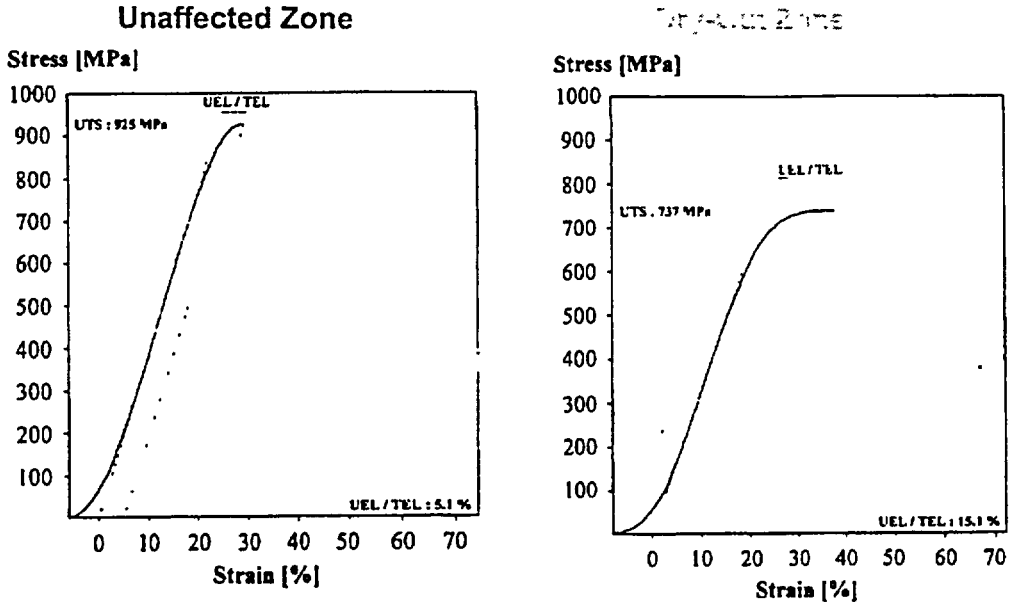

Figure 11. Example of load-displacement curves from one of the less severely tested rods (N1310).

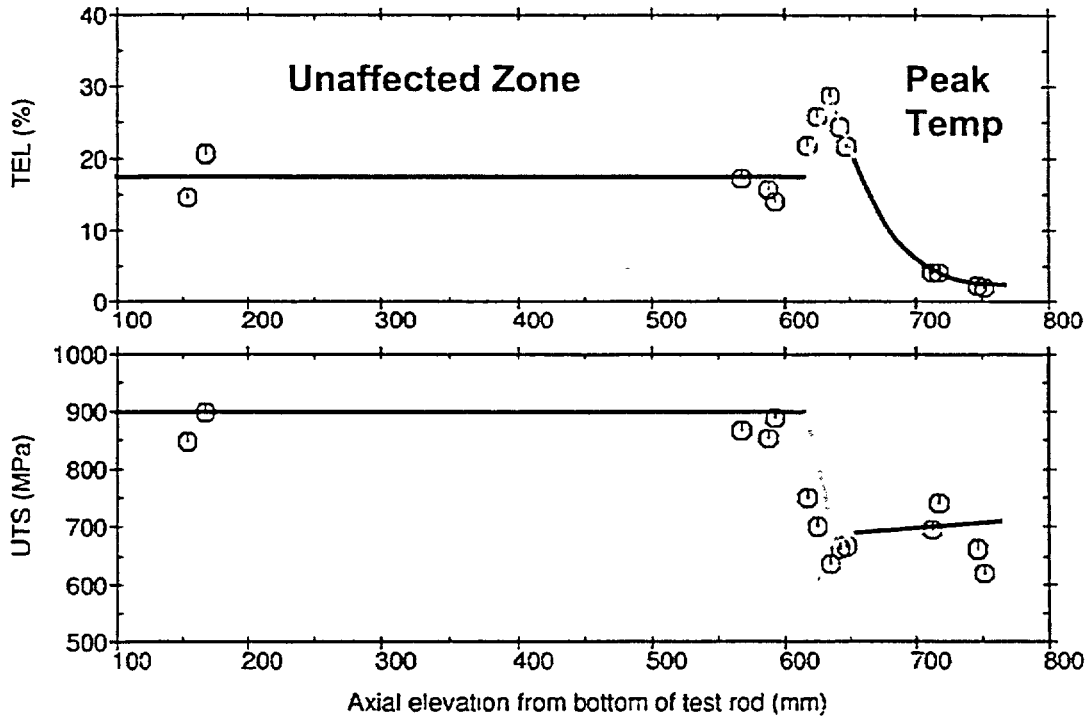

Figure 12. Mechanical testing results shown as a function of rod axial location for DTC1404.

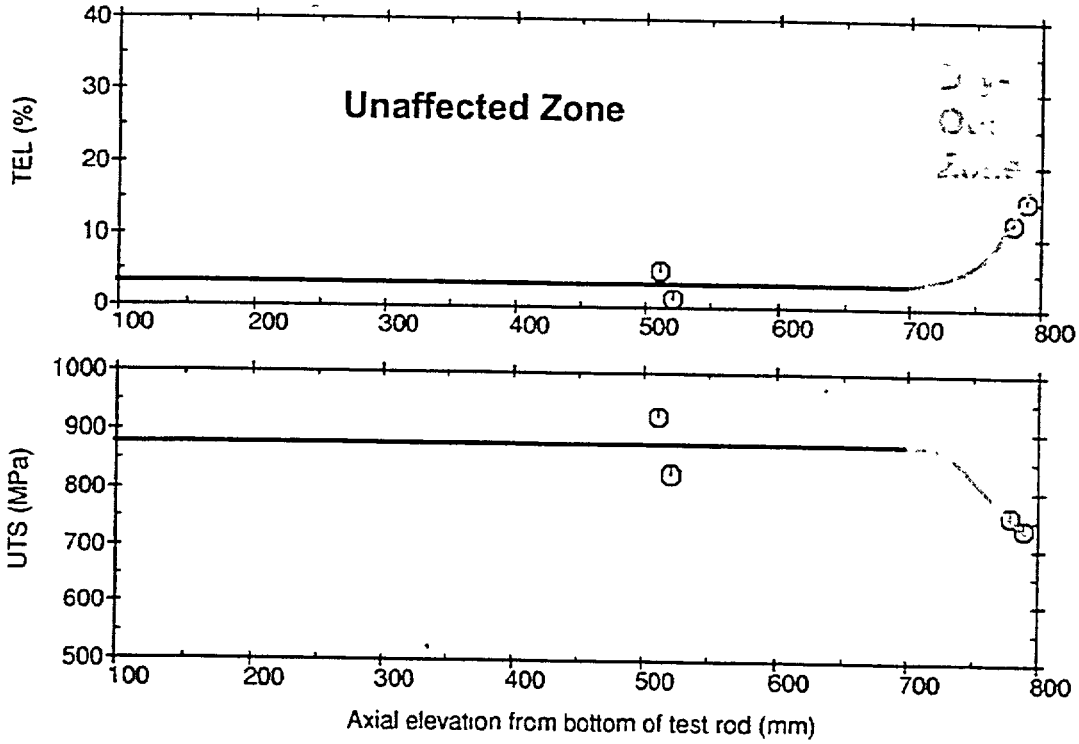

Figure 13. Mechanical testing results shown as a function of rod axial location for N1310.

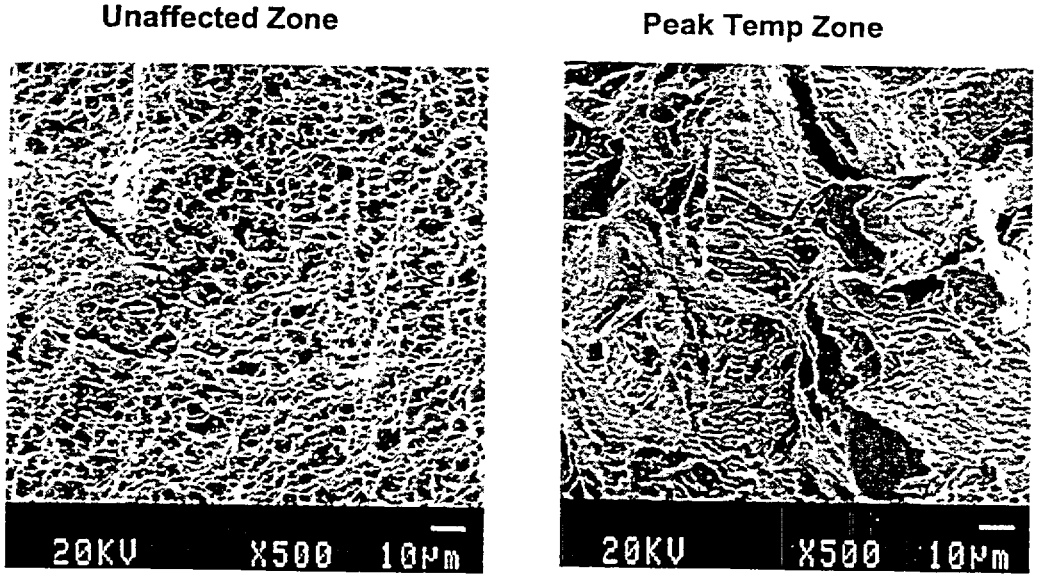

Figure 14. Scanning electron microscope images of DTC1404 ring tensile sample fracture faces.

3.3 Microstructural Investigation

Light microscopy was used to examine the microstructure of transverse and longitudinal samples of clad and typical microstructures from a severely tested rod (DTC1404) are shown in Figure 15. Transmission electron microscopy (TEM) samples were also prepared from two sections taken from rod DTC1404, for examination of the dislocation structure [3]. Total hydrogen content of the clad was determined by melt extraction of 1 mm thick transverse cross-sections.

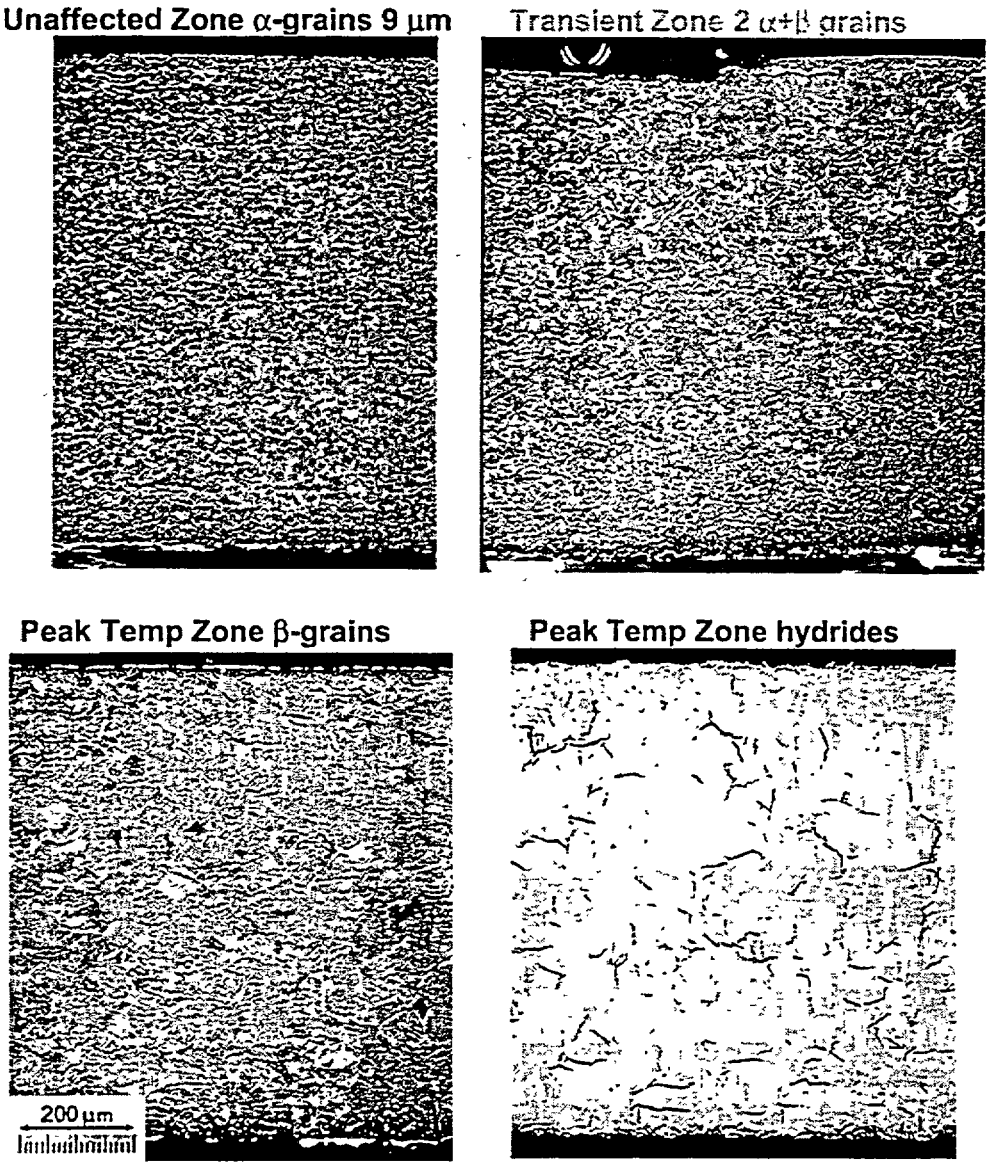

Figure 15. Light microscope images (all same magnification) of microstructure of DTC1404 clad at different axial locations.

3.4 Summary of PIE Results

The impact of in-reactor short-term dry-out incidents on fuel rods can be summarised with a combined description of the physical, mechanical and microstructural changes induced by the temperature transients. For severely tested rods (PCT > 1000°C), this combined description can be divided into four categories or four distinct axial zones. For the as-target dry-out tested rods (representative of a BWR pump trip), the combined description falls into two of these distinct axial zones. The results from a typical severely tested rod, DTC1404, are summarised below in terms of the four characteristic zones, with possible exposure temperatures given as a function of axial elevation:

- **Unaffected zone** (0 to 615 mm): this zone is characterised by an unchanging visual appearance and essentially constant values for ductility, strength and hardness (Figure 12) The fracture morphology is ductile (Figure 14) and the microstructure consists of equi-axed α-grains with an average diameter of 9 μm (Figure 15). TEM foils prepared from cladding taken from the top and bottom of the zone have been shown to have the same irradiation induced dislocation loop size distribution [3], indicating no significant recovery of the irradiation damage structure. Exposure temperatures are estimated as being from the coolant loop saturation temperature at the bottom of the zone (285°C) with a steep rise to about 550°C at the top of this zone.

- **Transient zone 1** (615 to 640 mm): this zone is characterised by increasing TEL concomitant with decreasing UTS (Figure 12), indicating thermal recovery of the irradiation induced damage structure. In comparison to the unaffected zone, TEL increases from 16% to about 30% and UTS decreases from 870 to 650 MPa. Fracture is ductile and the microstructure is similar to that in the unaffected zone: 9 μm diameter equi-axed α-grains i.e. no grain growth. Any significant annealing of irradiation damage loops within the short times of the in-pile dry-outs (tens of seconds) would probably require a minimum temperature of ~550°C [1], which is thus the exposure temperature attributed to the start of this zone. This is not inconsistent with the start of general clad creepdown which occurs at the start of this zone, given that the hoop stress exerted on the clad during operation would have been compressive but relatively low at 49 MPa. Rapid, high temperature creep must have occurred for the clad to collapse into pellet-pellet interfaces (observed in this zone), and an exposure temperature of 700-750°C (a temperature range at which the creep rate of Zry-2 increases rapidly [4]), is attributed to the axial region 625-635 mm. The maximum exposure temperature in this zone is estimated as 850°C, based on the start of the next zone.

- **Transient zone 2** (640 to 655 mm): this zone is characterised by a mixed grain structure and reducing ductility. In comparison to transient zone 1, UTS is little changed, but TEL decreases from 30% to about 20% (Figure 12) and the fracture morphology is both ductile and brittle. The microstructure consists of enlarged α-grains (8-15 μm) together with large former β-grains showing a typical quenched, Widmanstätten structure (Figure 15). The transition from one grain structure to another occurred between 642 mm and 655 mm, depending on radial and circumferential location within the cladding. The equilibrium temperature for the α to (α + β) phase transformation is 820°C and that for (α + β) to β is 960°C (both temperatures depend on oxygen content [4]). However, time at temperature is also required for phase transformation to occur and due to the rapid heating conditions of the dry-out transients, both temperatures would have been higher. Conservative estimates for the exposure temperatures at the bottom and top of transient zone 2 (640 and 655 mm respectively) are 850°C and 1000°C

- **Peak dry-out zone** (655 to 790 mm): this zone is characterised by a grain structure consisting entirely of a quenched Widmanstätten structure with a former β-grain size of 60-90 μm (Figure 15). The UTS is similar to that in transient zone 2 but the clad ductility is lower with TEL close to zero (Figure 12) and the fracture morphology shows features of brittle fracture (Figure 14). The hydrogen pick-up in this zone was about 90 ppm, insufficient in itself to significantly contribute to the embrittlement of this material, but the higher density of hydrides are in a random / radial orientation (Figure 15). This is due to precipitation having occurred at grain boundaries of the former β-grains and is thought to enhance the hydrogen embrittlement Oxide spalling occurs over this zone, indicating both rapid and significant oxide growth during dry-out, which could have lead to sufficient oxygen pick-up in the clad to enhance the embrittlement It is also taken to indicate a clad temperature of >1000°C for this zone.

The less severely tested rods both retained a clad microstructure of equi-axed α-grains throughout the in-pile dry-out testing, and only the characteristics of transient zone 1 (as described above) developed (Figure 13) e.g. for rod 613-7 a reduction in UTS from 735 to 640 MPa and an increase in the TEL from 40 to 50% indicating recovery of the radiation damage microstructure.

4. SUMMARY AND CONCLUSIONS

The in-pile dry-out transients, where an axial heat flux gradient would have existed, peaked towards the top of the rods, clearly induced dry-out over the upper regions of the rods with a fairly steep transient temperature gradient from the saturation to the peak dry-out temperature. Associated with this temperature profile, were a range of induced microstructural and mechanical property changes in the cladding, which could be characterised in up to four distinct axial zones.

Significant improvement in clad room temperature ductility occurs after in-pile dry-out transients where an exclusively small α-phase grain structure is retained i.e. maximum exposure temperature is 850°C.

Clad room temperature ductility is severely reduced after multiple exposures taking the clad to above 1000°C that result in a quenched, former β-Zr grain structure with hydrides oriented along former β-grain boundaries together with oxide spalling

As evidenced by six fuel rods that were operated without failure for 23-30 days post dry-out and quench, in-pile fuel rod integrity can still be retained even after in-pile dry-out transients that are sufficiently severe so as to induce the following: an α to β phase transformation; a significant reduction in clad room temperature ductility; clad collapse into pellet-pellet interfaces; and clad surface oxide spalling.

5. ACKNOWLEDGEMENTS

Acknowledgement is made of TEPCO's technical and financial backing of the entire dry- out test series. The TEM work was carried out under contract by AEA-T on behalf of the UK Industry Management Committee (IMC), financial assistance from whom is gratefully acknowledged.

6. REFERENCES

[1] Torimaru, T., Yasuda, T. and Nakatsuka, M., "Changes in Mechanical Properties of Irradiated Zircaloy-2 Fuel Cladding due to Short Term Annealing", Journal of Nuclear Materials, 238, pp. 169-174, 1996.

[2] Stosic, Z., "The Model HECHAN for Prediction of BWR Heating Channel Behaviour in Pre- and Post-Dryout Transient Regimes", Kerntechnik, Vol. 57, No. 6, 1992, pp-383-399.

[3] Dumbill, S. and Vatter, I. A., "Effects of Dry-Out on Microstructure of Irradiated Fuel Cladding", produced for British Energy Generation Limited under Project FC/PWR/5056, AEAT/ R/NS/0208, August 2000.

[4] "MATPRO - A Library of Materials Properties for Light Water Reactor Accident Analysis", SCDAP/RELAP5/MOD 3.1 Code Manual, NUREG/CR-6150 EGG-2720, Vol. 4, June 1995.

Main outcomes from the PATRICIA program on clad to coolant heat transfer during RIAs

Vincent BESSIRON

Institut de Radioprotection et de Sûreté Nucléaire (IRSN)
Centre d'Etudes de Cadarache
13115 Saint Paul lez Durance BP3 FRANCE
Tel : 33 4 42 25 66 19
Fax : 33 4 42 25 61 43
E-mail : vincent.bessiron@irsn.fr

ABSTRACT

In the frame of the studies on Reactivity Initiated Accidents (RIA), IRSN, with the support of EDF, has initiated an experimental program in order to investigate the clad-to-coolant heat transfer under fast transients. This program has been carried out in the PATRICIA loop of CEA, using single cladding tubes heated up by direct Joule effect. Both PWR and NSRR conditions have been simulated. The physical interpretation of the experiments led to assert the main characteristics of the clad-to-coolant heat-transfer on bare rods in PWR conditions at 280°C under very fast transients which are:

- *the boiling crisis is mainly governed by the flash boiling of a superheated liquid layer without sufficient time to get fully established nucleate boiling heat transfer,*
- *the critical heat-flux is of the order of 5-6 MW/m² and is reached when the clad outer temperature is around Tsat + 50°C,*
- *the fast crossing of transition boiling is followed by inverse annular film boiling with heat flux of the order of 1-2 MW/m².*

These results are intensively used for the development and the validation of the SCANAIR code and for the definition of the future CABRI tests in the Water Loop.

GENERAL CONTEXT

The French "Institut de Radioprotection et de Sûreté Nucléaire" (IRSN[1]), in collaboration with "Electricité de France" (EDF) and with the support of the Nuclear Regulatory Commission (NRC), has been studying Reactivity Initiated Accidents (RIAs) in PWRs for several years through the CABRI REP-Na experimental program.[1,2]

The interpretation of the CABRI experiments and the extrapolation to reactor conditions required the development of the SCANAIR computer code which is specifically designed to cope with the fast kinetics and the strong coupling between the phenomena taking place in the fuel rod (mechanics, thermics and fission gas behavior).[3,4,5,6]

One of the main concern about the behavior of high burnup fuel during RIAs deals with the ability of the cladding to withstand the mechanical loading during the transient. A key parameter governing the rod resistance to failure is the cladding temperature and much attention has to be put on the modelling of fuel-to-clad heat transfer on the one hand and on clad-to-coolant heat transfer on the other hand.

[1] Since March 2002 the former Institut de Protection et de Sûreté Nucléaire (IPSN) has been merged with the Office de Radioprotection contre les Rayonnements Ionisants (OPRI) in the newly created Institut de Radioprotection et de Sûreté Nucléaire (IRSN).

The PATRICIA experimental program described in this paper focused on the latter.

PRESENTATION OF THE PATRICIA-RIA EXPERIMENTAL PROGRAMME

Origin of the program

The calculation of some NSRR experiments with the SCANAIR code has shown that the usual pool boiling steady-state correlations are not adequate to simulate the clad-to-coolant heat-transfer during a RIA in NSRR conditions (stagnant water, atmospheric pressure).

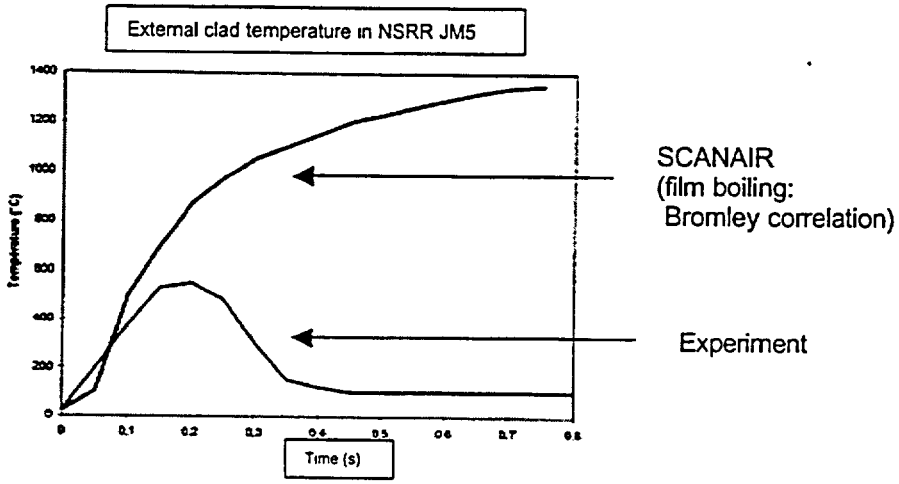

Figure 1 : Calculation of the NSRR JM5 test with usual correlations

These unexpected results have raised questions about the presence of kinetics effects in the heat-transfer phenomena. The transposition of these results to PWR conditions had to be investigated too.

The PATRICIA facility

The PATRICIA facility which is located at CEA/Grenoble consists in a water loop that can operate in PWR conditions (up to 15.5 MPa, 4 m/s, 280°C) and NSRR conditions (stagnant water, atmospheric pressure, 20°C). A tube (also referred to as "the clad" or "the rod") is located in the test section. The inner part of the tube is filled with air. The outer part is in contact with the water.

The geometry of the rod and of the test section is the following:

- rod length: 600 mm (nominal), possibility to use 140 mm or 1500 mm rods,
- outer rod diameter: 9.5 mm,
- inner rod diameter: 8.8 mm (thickness: 0.35 mm),
- cold wall diameter: 14.2 mm.

Compared to a PWR case:

- the flow cross section is conserved (S = 86.0887 mm²),
- the equivalent heated diameter is conserved (Deq=4 cross section / heated perimeter = 11.7 mm),
- the hydraulic diameter is not conserved (Dhyd=4 cross section / wetted perimeter = 4.7 mm instead of 11.77 mm in the reactor case).

The cladding is made of Inconel instead of Zircaloy 4 because of technological difficulties (welding of thermocouples on the inner clad surface).

The clad is electrically heated up by direct Joule effect.

Instrumentation and experimental procedure

Aim of the instrumentation

The objective of the PATRICIA-RIA program was to study the clad-to-coolant heat-transfer during a fast power transient.

In order to simulate the fast heating of the clad by the fuel pellet in a RIA, the test rod is electrically heated up with a representative transient (see next chapter).

The measurement of the clad temperature is needed to quantify the heat-transfer and for this purpose, thermocouples are welded on the clad inner surface at 4 different axial levels:

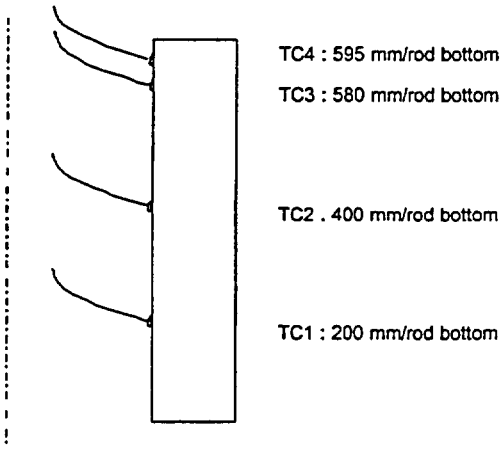

Figure 2:Position of the thermocouples

The estimation of the clad outer surface temperature together with the clad-to-coolant heat-flux from the measured inner-clad temperature can be divided in two steps:

- deconvolution of the inner surface temperature measured by the thermocouple in order to estimate the "real" inner surface temperature,
- inverse conduction calculation to estimate the temperature field in the cladding and in particular the outer clad surface temperature and the clad-to-coolant heat-flux.

Deconvolution

The temperature recorded by the inner surface thermocouple has to be deconvoluted in order to estimate the "real" inner surface temperature from the measured temperature.

For this purpose, "adiabatic tests" have been previously performed in order to determine the thermocouple transfer function. In these tests, quasi-adiabatic conditions are achieved by replacing the water by air. Therefore, the clad temperature is homogeneous in all the cladding and easily estimated by calculations. The temperature measured by the thermocouple is compared to the estimated adiabatic temperature and a transfer function is elaborated for each thermocouple.

The following figure shows an example of "adiabatic test":

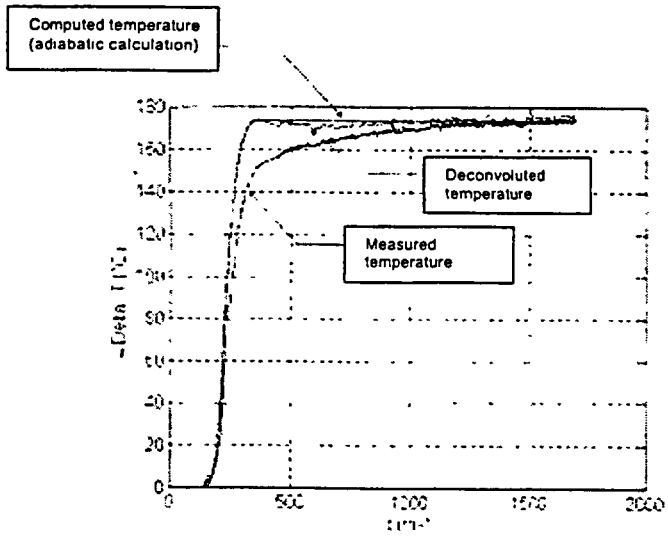

Figure 3: Adiabatic test

The adiabatic tests have been performed only once for each rod and the transfer function defined for each thermocouple is then applied to all the PATRICIA experiments using the same rod.

The deconvolution of the measured temperature is also associated with correction "overshoots" due to electric capacity effects.

Once this step is performed, the inverse conduction calculation has to be done in order to compute the temperature field in the rod.

Inverse conduction

The problem to solve is the following:

Boundary conditions:

$$T_{(r=r\,int)} = T\,\text{int}\,deconvoluated\,(t)$$

$$\frac{\partial T}{\partial r}_{(r=r\,int)} = 0$$

Fourier equation:

$$m\,Cp\frac{\partial T}{\partial t} - \lambda\ \frac{1}{r}\frac{\partial}{\partial r}\left(r\frac{\partial T}{\partial r}\right) = p$$

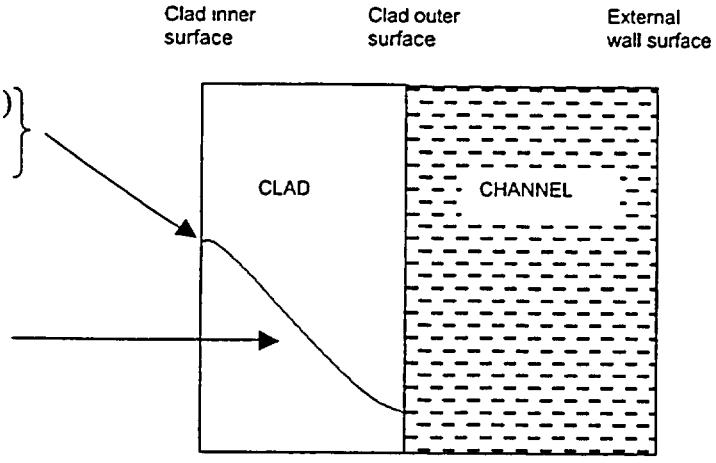

Figure 4: Inverse-conduction problem

From a mathematical point of view, this problem is "ill-posed" because the two kinds of boundary conditions (Neumann and Dirichlet) are set at the same location. It usually leads to instabilities when using a numerical method to solve this problem. A validated analytical method has been used and the absence of computational instabilities has been checked.

Once the temperature field is computed in the rod, both the clad outer surface temperature and the clad-to-coolant heat-flux ($= -\lambda \left(\frac{\partial T}{\partial r}\right)_{r=ext}$) are available for quantifying the heat-transfer.

Uncertainty analysis

An uncertainty analysis led to the following uncertainty ranges:

Heat flux: : ± 25%

Clad outer surface temperature: ± 30°C

Experimental matrix

Thermal-hydraulics conditions

PWR-like conditions at the inlet have been simulated (with small variations in order to study the influence of some parameters) : water at 15 MPa, 280°C, flowing at 4 m/s.

Heating kinetics

The clad is heated up by Joule effect with electrical power transients representative of the heating induced by the fuel during a neutronic power transient (although the clad heating is surfacic in a reactor case and volumic in the PATRICIA case).

In order to make the link with the existing data base on Critical Heat Flux (CHF) and post-BO heat-transfer in steady-state conditions, some experiments have been performed with a very slow increase of the power until the boiling crisis is reached ("steady-state" or "permanent" experiments PILMT). These experiments also allowed to check the instrumentation.

As regards the transient experiments, the width of the clad heating pulse has been determined through SCANAIR calculations and the following correspondence has been established:

	Neutronic pulse half-width	Clad heating transient half-width	PATRICIA expenments
"Slow" transient	300 ms	250 ms	750
"Fast" transient	30 ms	60 ms	150 and 112
"Ultra-fast" transient	10 ms	20-30 ms	065

Table 1: Correspondence between neutronic pulses and PATRICIA pulses

List of experiments

The list of the experiments is given hereafter:

Name	P (bars)	Te (°C)	Q (g/s)	Injected energy in the clad	Massic injected energy in the clad (J/g clad)	BOILING CRISIS
150.049	145.9	280	262	10183	201	
150.050	145.9	280	262	12078	238	✓
150.051	145.8	280	289	12480	246	✓
150.052	145.8	278	289	11911	235	✓
150.061	154.9	280	262	12529	247	✓
150.065	145.8	280	289	16784	331	✓
150.069	145	282	262	13315	263	✓
150.070	145	323	289	880	17	
150.072	145	325	289	3805	75	
150.074	145	324	289	13947	275	✓
750.055	145.6	320	289	3844	76	
750.058	145.5	280	289	18464	365	
750.059	145.5	280	262	18268	361	
750.060	156	280	262	15998	316	
750.063	146.1	280	289	27553	544	
750.064	146.1	280	289	25871	511	
750.067	145.1	282	289	18990	375	
750.068	145	282	262	19816	391	

Table 2: List of the PATRICIA experiments in PWR conditions

MAIN OUTCOME FROM THE PATRICIA EXPERIMENTS

Note: in the following, the words "Burn-Out (BO)", "Boiling crisis" or "Departure from Nucleate Boiling (DNB)" refer to the fast degradation of heat-transfer when a vapor film develops around the cladding. Tbo stands for the clad temperature at BO, *ie* "critical temperature". The "boiling curve" corresponds to the plot with clad temperature in abscissa and heat-flux in ordinate.

Steady-state experiments

Because of the slow evolution of the temperatures, no deconvolution has been applied on these experiments.

The power (55.5 kW) has been switched off 0.9 s after BO because the maximum authorized temperature had been reached (900°C internal clad temperature).

The critical heat-flux is 3.1 MW/m² (obtained at Tbo ~370°C *ie* Tsat + 25°C) and the film boiling flux is within the range 1-2 MW/m².

The corresponding boiling curve is given below together with a boiling curve based on usual correlations:

- forced-convection: Dittus-Boelter[8],
- critical heat-flux: Babcock and Wilcox[9],
- transition boiling: exponential fitting,
- film boiling: Bishop Sandberg Tong (BST)[8].

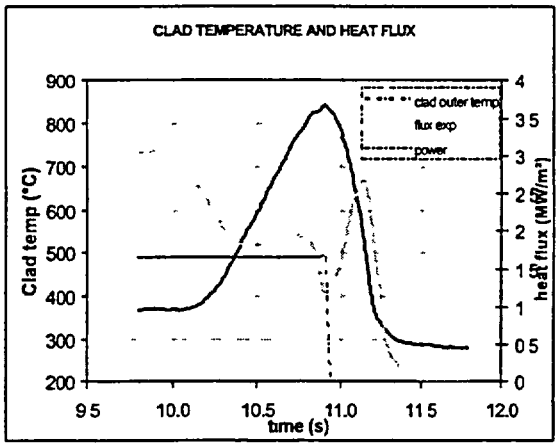

Figure 5: Clad temperature and heat flux, test PILMT 001

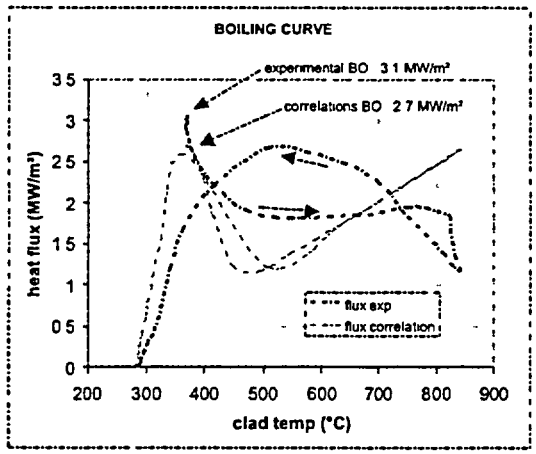

Figure 6: Boiling curve, test PILMT 001

Fast transients

Typical experimental curves and general considerations

The experiments exhibiting boiling crisis are characterized by two main features that can be clearly seen on the boiling curve (see Figure 8):

- presence of transition boiling: decrease of the flux with simultaneous increase of the clad temperature,
- presence of a rewetting peak.

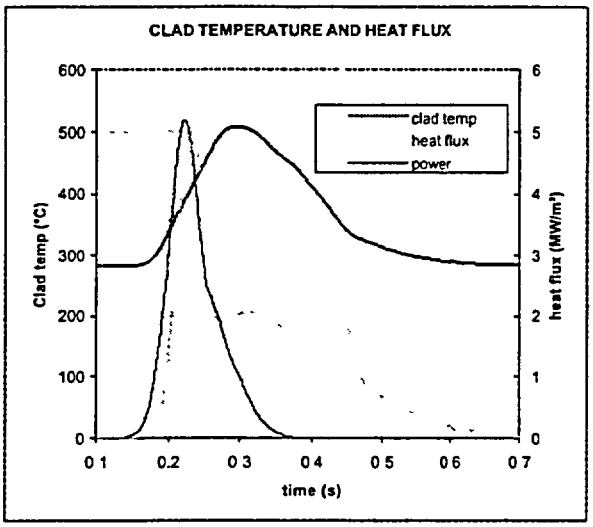

Figure 7: Clad temperature and heat flux, test 150_051

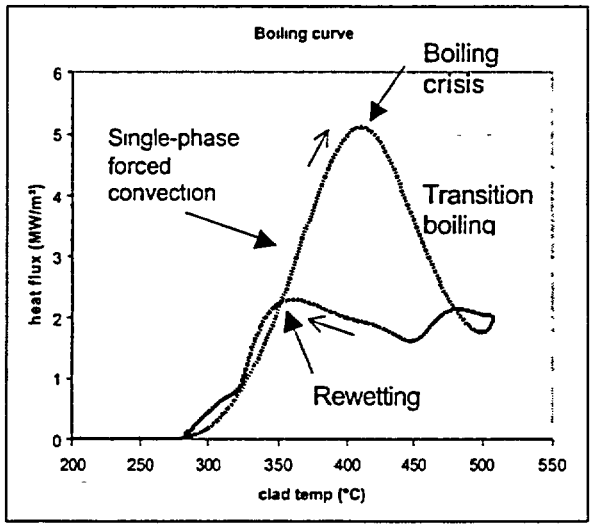

Figure 8: Boiling curve, test 150_051

In the case of experiments without boiling crisis, no crisis peak and no rewetting peak can be observed on the boiling curve (see Figure 10).

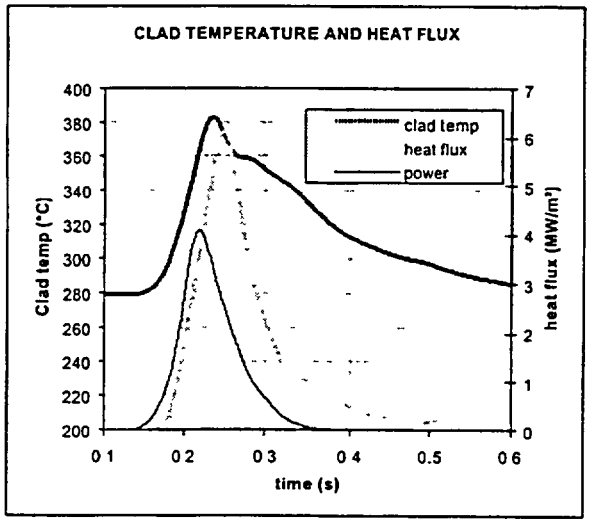

Figure 9: Clad temperature and heat flux, test 150_049

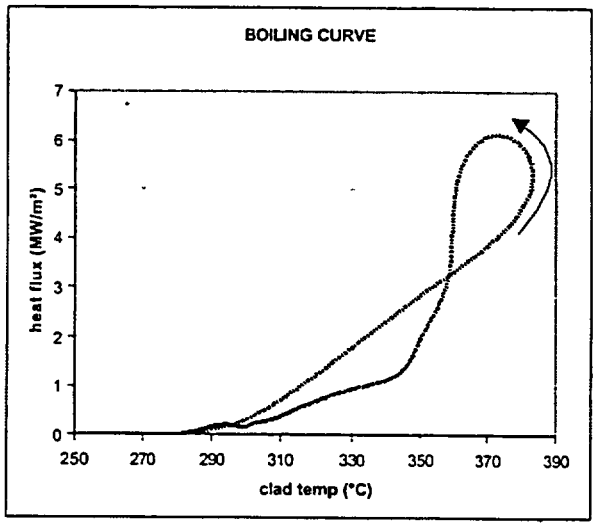

Figure 10: Boiling curve, test 150_049

Physical analysis

Single phase:

The pre-boiling phase is characterized by a simultaneous increase of the flux and of the clad outer temperature.

On the contrary to the transients without boiling crisis, there is no steep increase of the flux while the clad temperature overpasses the saturation temperature. This may indicate that the nucleation of bubbles does not have the time to fully develop and that the heat transfer is mainly controlled by single-phase forced-convection (see next section) although the clad temperature overpasses the saturation temperature.

Orders of magnitude:

- heat-flux: 0 to 5 - 6 MW/m²,
- heat-transfer coefficient: 20 000 - 50 000 W/m²/K

End of the single phase and boiling crisis

If the clad heating is going on, the flux suddenly decreases while the clad temperature increases very rapidly. the boiling crisis has been broken through. This occurs at clad outer temperatures of about Tsat + 50°C (Tbo: burn-out temperature).

The time during which the clad temperature is between Tsat and Tbo is only 20 ms and is lower than the time needed to obtain a fully established nucleate boiling heat transfer. The characteristic nucleation and detachment time in PWR conditions is of the order of some milliseconds[7] and a fully established nucleate boiling needs at least the detachment of some dozens of bubbles.

As the bubble nucleation is still very limited when the clad temperature reaches Tbo, the boiling crisis seems to be governed by single-phase conditions and it may correspond to the "flash boiling" of a superheated water layer.

The burn-out temperature is far higher than the usual BO temperatures in steady-state conditions (usually around Tsat + 15°C). The increase of the critical temperature with the kinetics is consistent with a fast non-equilibrium heat-transfer.

The level of the critical heat flux is about 5 - 6 MW/m. This value is about two times higher than in steady-state conditions because of predominant non-equilibrium phenomena. Before burn-out is reached, the fluid at the wall remains in single-phase and the rapid heating of the wall leads to twice as high enthalpy gradients as in steady-state conditions. As the heat flux is proportional to the enthalpy gradient in single-phase conditions, rapid transients induce higher heat fluxes, especially as the critical temperature is obtain for higher temperatures.

In the case of experiments without boiling crisis (e.g. Figure 10), the single phase heat transfer is the same as in the case of more energetic transients but the stopping of clad heating is reached before the crisis, allowing the bubble nucleation to develop: there is first a steep increase of the flux and then a decrease while the clad temperature remains close to Tsat.

Transition boiling and film boiling

If the boiling crisis has been broken through, then the flux suddenly decreases while the clad temperature significantly increases: the heat transfer is governed by transition boiling until the temperature reaches about 500°C.

For higher temperatures, the flux stabilizes and can slightly increase simultaneously with clad temperature: the heat transfer is governed by stable film boiling.

Orders of magnitude in stable film boiling:

- heat-flux: 1 - 2 MW/m²,
- heat-transfer coefficient: 3 000 – 5 000 W/m²/K.

Calculations with the TH2D computer code (two-phase and 2D code designed for computing thermal-hydraulics during a RIA, developed within an IRSN / Kurchatov Institute cooperation)[10] allows to estimate the topology of the flow during the transient. The Figure 11 shows that the bulk of the coolant is not affected by the clad heating: the thermal gradient only concerns a small fluid layer in the vicinity of the wall. The vapor film thickness reaches approximately 5% of the channel width.

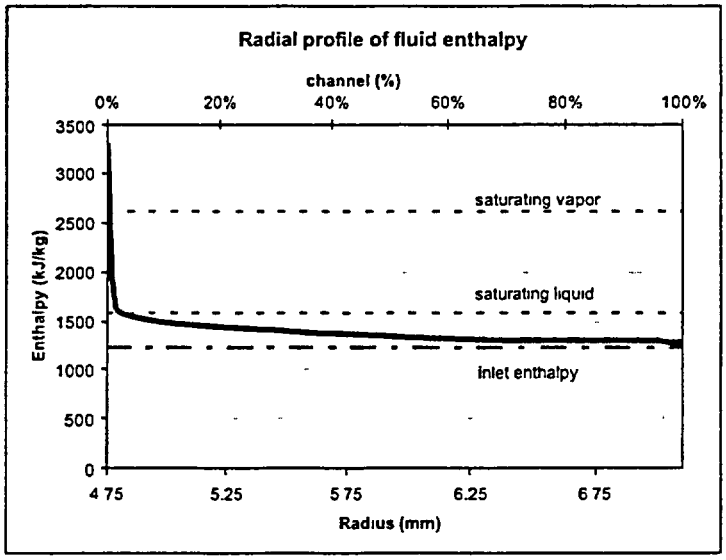

Figure 11: Profile of the fluid enthalpy in film boiling regime, test 150_065

Cooling down and clad rewetting

The heat transfer during the cooling down does not take the reverse path and remains lower than in the transition boiling phase. This could be due to a stabilization of the vapor film around the cladding.

The rewetting occurs around the temperature of minimum stable film (Tmsf ≈ 385°C in PWR conditions with Groeneveld's correlation) with fluxes typical of forced-convection heat-transfer.

Recommended correlations and parameters

- single phase:
  - Dittus-Boelter[8], up to the saturation temperature Tsat,
  - Linear interpolation up to the Burn-Out.
- Burn-Out:
  - critical heat-flux: Babcock and Wilcox[9],
  - temperature of critical heat-flux: Tbo = Tsat + 50°C,
- transition boiling: exponential fitting tending towards a film boiling correlation for high temperatures (T>500°C),
- film boiling (increasing clad temp.): Bishop Sandberg Tong (BST)[8],
- film boiling (decreasing clad temp.) : BST down to 500°C, linear interpolation to the forced convection at Tmsf below 500°C.

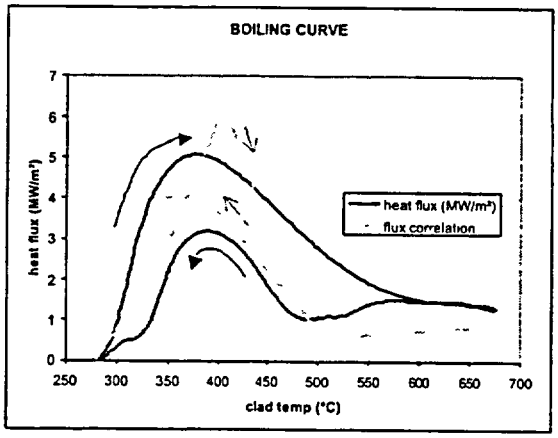

Figure 12: experimental boiling curve and recommended correlations (test 150_065)

APPLICATION WITH THE SCANAIR CODE

The results of the PATRICIA program are intensively used in the definition of the future experiments of the CABRI Water Loop Program with the SCANAIR code. This chapter describes the results obtained from the calculation of a 4-cycle UO_2 rod with a 50 µm zirconia layer submitted to a 30 ms half width neutronic pulse injecting 586 J/g (140 cal/g) in the fuel. The rod length is 0.8 m. The contribution of fission gases is taken into account in the computation of the gap conductance.

The dry-out zone corresponding to the axial extent where the BO has been reached is considerable and centered on the Peak Power Node because of the shape of the axial power profile of the CABRI reactor.

The radial-averaged fuel enthalpy at BO in this calculation is around 470 J/g (~113 cal/g) but it must be noticed that this value is very sensitive to the zirconia thickness and to the parameters having a significant influence on the fuel-to-clad heat-transfer modeling. In particular, a calculation with a very low zirconia thickness (simulating transient spalling) associated to a gap conductance based on solid-solid heat-transfer would lead to an enthalpy at BO around 355 J/g (85 cal/g).

In the dry-out zone, clad temperatures reach high values and remain above 600°C during approximately 3.5 s. Such thermal conditions may be appropriate for clad ballooning provided the rod internal pressure is high enough.

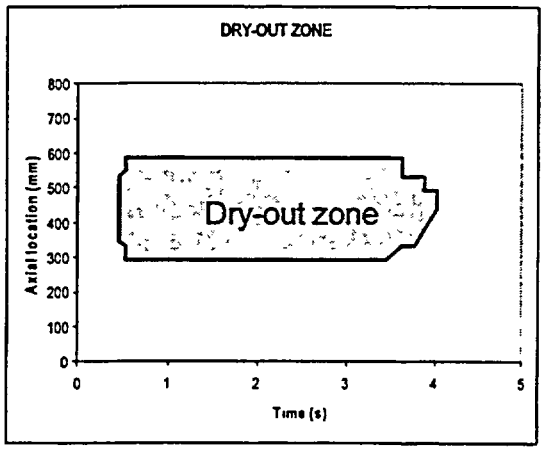

Figure 13: Dry-out zone

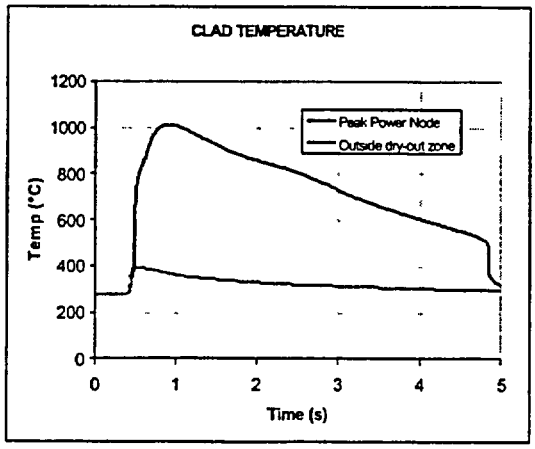

Figure 14: Clad temperature outside and inside the dry-out zone

CONCLUSION

The PATRICIA-RIA experimental program allowed to study thermal-hydraulics under fast transients and to recommend correlations for PWR conditions.

Steady-state experiments have been performed in order to make the link between the existing data base on CHF and post-BO heat-transfer in PWR conditions. They show a good agreement with the usual correlations.

The main characteristics of the clad-to-coolant heat-transfer on bare rods in PWR conditions (at 280°C) under very fast transients are:

- boiling crisis mainly governed by flash boiling of a superheated liquid layer without sufficient time to get fully established nucleate boiling heat transfer,
- critical heat-flux of the order of 5-6 MW/m² reached for clad outer temperature around Tsat + 50°C,
- fast crossing of transition boiling followed by inverse annular film boiling with heat flux of the order of 1-2 MW/m².

A boiling curve based on the outcomes of the PATRICIA program has been implemented in the SCANAIR code and is intensively used for the definition of the future experiments of the CABRI Water Loop Program.

As regards possible additional work on clad-to-coolant heat transfer during RIAs, experimental studies could complete the PATRICIA-RIA program by focusing on very fast transients (representative of 10 ms neutronic pulses) and on clad-surface roughness aspects.

ACKNOWLEDGMENTS

The author would like to thank Alain Memponteil, Géraud Cubizolles and Thierry Oulmann (CEA/Grenoble) for the achievement of the experiments and the processing of the experimental data. Their knowledge of two-phase thermal-hydraulics helped a lot for the interpretation of the tests.

Thanks are also due to Stefano Salvatores and François Tissier (EDF/SEPTEN) for the numerous and fruitful discussions we had on these topics.

REFERENCES

1 J. Papin, M. Balourdet, F. Lemoine, F. Lamare, JM. Frizonnet, F. Schmitz, *French studies on high-burnup fuel transient behavior under RIA conditions*, in *Nuclear Safety, Vol 37, N° 4, October-December 1996)*, pp. 289-327

2 JM. Frizonnet, JP. Breton, H. Rigat and J. Papin, *The main outcome from the interpretation of the CABRI REP-Na experiments for RIA studies, in* Proceedings of the International Topical Meeting on Light Water Reactors Fuel Performance, Portland, Oregon, March 2-6, 1997, American Nuclear Society.

3 J-C. Latché, F. Lamare, M. Cranga, *Computing Reactivity Initiated Accidents in PWRs,* in Proceedings of the ANS International Topical Meeting on Light Water Reactor Fuel Performance, Park City, UT (April 2000).

4 J. Papin, H. Rigat, F. Lamare and B. Cazalis, *The SCANAIR code for the description of PWR fuel rod behavior under RIA: Validation on experiments and extrapolation to reactor conditions, in* Proceedings of the International Topical Meeting on Light Water Reactors Fuel Performance, Portland, Oregon, March 2-6, 1997, American Nuclear Society.

5 E. Fédérici, F. Lamare, V. Bessiron, J. Papin, *Status of development of the SCANAIR code for the description of fuel behaviour under Reactivity Initiated Accident (RIA)*, in Proceedings of the ANS International Topical Meeting on Light Water Reactor Fuel Performance, Park City, UT (April 2000).

6 E. Fédérici, F. Lamare, V. Bessiron, J. Papin, *The SCANAIR code version 3.2 : main features and status of qualification*, in Proceedings of the IAEA Technical Committee Meeting on Fuel Behavior under Transient and LOCA conditions, Sept. 10-14, 2001, Halden, Norway.

7 Unal, HC, *Maximum bubble diameter during subcooled nucleate flow boiling of water* Int. Journal of Heat and Mass Transfer, Vol 19, p.p. 643-649

8 S.L. Tong, J. Weisman *Thermal analysis of pressurized water reactors* American Nuclear Society, 2nd edition, pp 279

9 J. Weisman, R. Bowring, *Methods for detailed thermal and hydraulic analysis of water-cooled reactors*, Nuclear Science and Engineering, 57, 255-276 (1975)

10 A. Sedov, V. Gagin, V. Bessiron, *Computing thermal-hydraulics in RIA conditions: the TH2D computer code,* to be published.

NSRR High Burnup Fuel Tests for RIAs and BWR Power Oscillations without Scram

Takehiko NAKAMURA*, Hideo SASAJIMA,
Jinichi NAKAMURA and Hiroshi UETSUKA

Department of Reactor Safety Research, Japan Atomic Energy Research Institute,
Tokai-mura, Ibaraki-ken, 319-1195, Japan

Abstract

In order to examine high burnup fuel performance under reactivity-initiated accidents (RIAs) and under unstable power oscillation conditions arising during an anticipated transient without scram (ATWS) in boiling water reactors (BWRs), fuel irradiation tests were conducted with irradiated fuels under the simulated power transient conditions in the Nuclear Safety Research Reactor (NSRR).

In the RIA simulating tests of BWR fuels at a burnup of 61 GWd/tU, cladding failure occurred in tests at fuel enthalpies of 260 to 360J/g (62 to 86cal/g) during an early phase of the transients, while the cladding remained cool. Transient hoop strain measurements of the cladding in the early phase of the transients indicated small deformation below 0.4%, suggesting that the deformation was caused mainly by thermal expansion of the pellets Hydride distribution in the BWR cladding was different from those observed in the PWR fuels failed in the earlier tests, which likely contributed to the BWR fuel failure at low hydrogen contents of about 150-200ppm.

In the power oscillation tests, irradiated fuels at burnups of 56 and 25GWd/tU were subjected to four to seven power oscillations, which peaked at 50 to 95kW/m at intervals of 2s. The power oscillation was simulated by quick withdrawal and insertion of six regulating rods of the NSRR. Deformation of the fuel cladding of the test rods was comparable to those observed in the RIA tests at the same fuel enthalpy level up to 368J/g. Cladding axial deformation due to pellet-cladding mechanical interaction (PCMI) was not enhanced due to the cyclic load. Fission gas release, on the other hand, was considerably smaller than in the RIA tests, suggesting different release mechanisms between the two types of transients.

*Corresponding author : take@fsrl.tokai.jaeri.go.jp
(phone): +81 29 282 6386, (fax): +81 29 282 5429

1. Introduction

Performance of high burnup fuel under accident conditions has become one of the key issues to be examined for the safety assessment of the on-going burnup extension worldwide. Pulse irradiation tests of high burnup light water reactor (LWR) fuels have been conducted in the Nuclear Safety Research Reactor (NSRR), in order to examine high burnup fuel performance and to clarify influence of burnups on failure threshold and its mechanism under reactivity-initiated accidents (RIAs)[1)-4)]. Consequences of the failure, such as fission gas release, fuel fragmentation, dispersal and mechanical energy generation, etc., have also been investigated to examine impacts of the failure[5)].

In addition to the RIA tests, a new type of tests was initiated in the NSRR to examine fuel performance under unstable power oscillation conditions arising during an anticipated transient without scram (ATWS) in boiling water reactors (BWRs). Power oscillation[6)] could be initiated by trip of recirculation pumps in BWRs due to their coupled instability of thermo-hydraulic/ nuclear characteristics under certain flow and power conditions, like an incident at the LaSalle County Unit #2 (LaSalle-2) BWR in the US in 1988[7)]. The reactor was shut down by scram, when the power reached to 118% nominal in a few minutes. The power oscillation with intervals of about 2s, however, could be developed further to reach peak powers of about an order of magnitude higher than the nominal without the scram[8)]. It is important to know behavior of high burnup fuels under such cyclic power conditions, in order to evaluate public risk of the events. Therefore, two tests were conducted with irradiated fuels under simulated power oscillation conditions.

2. Test matrix and procedure

A total of 67 tests of irradiated water reactor fuels have been conducted in the NSRR, as listed in **Table 1**. For RIA study, fifteen tests of BWR fuels at burnups from 26 to 61 GWd/t have been conducted[9), 3), 4)], in addition to twenty-four tests of pressurized water reactor (PWR) fuels at burnups from 38 to 50 GWd/t[1), 2)] and 21 tests of highly enriched fuels irradiated in the Japan Materials Testing Reactor (JMTR) to burnups from 13 to 38 GWd/t[10)]. In addition to these UO_2 fuel tests, five tests of MOX fuel irradiated in the Advanced Thermal Reactor (ATR) "Fugen" to a burnup of 20 GWd/t were conducted[11)]. Each fuel rod, contained in a stainless steel capsule filled with water at room temperature and at ambient pressure, was pulse irradiated at the center of the NSRR. Fuel enthalpies up to about 145 cal/g were promptly

Table 1 NSRR test fuels and their burnups for RIA and power oscillation tests

Test type	Fuel type		Burnup, GWd/t	Number of tests
RIA	UO_2	BWR	26-61	15
		PWR	38-50	24
		JMTR	12-38	21
	MOX	ATR	20	5
Power Osc.	UO_2	BWR	56	1
		JMTR	25	1

subjected to the rods within about 10ms in the RIA tests by the sharp pulsing power excursion achieved by quick pneumatic withdrawal of three transient rods.

In the power oscillation tests, on the other hand, irradiated BWR fuel at a burnup of 56 GWd/t and one irradiated in the JMTR to 25 GWd/t were subjected to four and seven power oscillations, which peaked at 50 to 95kW/m with intervals of 2s. The power oscillations were caused by quick withdrawal and insertion of six regulating rods of the NSRR with a computerized control[12].

3. RIA test results

In the RIA simulating tests of BWR fuels at a burnup of 61 GWd/t, cladding failure occurred in tests at fuel enthalpies of 260 to 360J/g (62 to 86cal/g) during an early phase of the transients, while the cladding remained cool. Longitudinal cracks showing brittle nature was seen in post-test examinations of the BWR fuels, as well as the PWR fuels failed in the earlier tests. Hydride distribution in the BWR cladding, however, was different from those observed in the PWR fuels (**Fig. 1**). Even though the hydrogen content was lower in the BWR cladding (about 150-200ppm), brittle fracture was seen over wider area than in the PWR cladding containing about 400ppm of hydrogen[1]. Hydrides in the BWR cladding precipitated in a wider area and oriented more randomly, while it was concentrated in a limited area close the outer surface and oriented circumferentially in the PWR cladding. Brittle fracture occurred only in the hydride rich area, which was often called "hydride rim", in the PWR cladding, while it propagated along the hydrides interconnecting circumferentially and radially oriented hydrides in most part of the cladding. Ductile fracture, which went 45 degrees perpendicular to the cladding radius, was seen only in the limited inner part next to Zr liner in the BWR cladding, while it was seen in about inner 2/3 of the cladding thickness in the PWR cladding.

Transient hoop strain measurements of the cladding in the early phase of the transients indicated small deformation below 0.4 % (**Fig. 2**), when the BWR cladding at a burnup of 61 GWd/t failed at a fuel enthalpy of 80 cal/g. Post-test diameter measurement and cross-section examination of the cladding tubes in other tests, which failed or survived at the comparable enthalpies, exhibited negligeable plastic hoop strains below 0.1%[4]. Magnitude of these deformation was comparable to those calculated with FRAP-T6 code[13), 14)] using only a thermal expansion model of the pellets. These results suggested that the small deformation resulting in the cladding fracture could be caused simply by thermal expansion of the pellets and influence of the fission gases in the pellets was quite limited in the early phase of the transient. It was known that plastic cladding deformation was caused mostly by the fission gases after the cladding temperature escalated to several hundreds degrees Celsius or higher later in the transients[3), 4), 14)].

From these high burnup fuel tests, it was understood that cladding embrittlement was more important for the fuel failure than enhanced pellet expansion due to accumulated fission gases in the course of burnup increase. Therefore, a series of separate effect tests of fresh fuels with hydrided cladding was conducted, in order to clarify the influence of the hydrides on the cladding fracture behavior. Fresh PWR

fuel rods with cladding, containing 200 to 1000ppm of hydrogen in a form of hydride rim similar to high burnup PWR cladding, was pulse irradiated in the NSRR in the same way with the irradiated fuel tests. Brittle fracture of the fresh hydrided cladding occurred in a similar way to those observed in high burnup PWR fuels. Appearance and a cross section of the cladding are shown in **Fig. 3**. The fresh fuel test results are plotted in **Fig. 4**, in a form of a failure/no-failure map for two parameters, i.e. hydrogen content and estimated peak cladding hoop strain. The peak hoop strain was calculated by FRAP-T6, taking account of thermal expansion of pellets. Rough idea of the failure thresholds in terms of the estimated peak strain and hydrogen content in the high burnup PWR and BWR fuel tests were indicated for comparison. Failure threshold of the hydrided cladding was larger than those of high burnup fuel claddings, suggesting influence of the other phenomena such as irradiation induced embrittlement.

Considerable transient fission gas releases were observed in the RIA tests. Fractional release rates varied from 3 to 23% depending on fuel enthalpies, burnups, and fuel types. In case of the BWR fuel for example, fission gas releases of the fuel at a burnup of 61GWd/t was about 12% at an enthalpy of 70cal/g, as shown in **Fig. 5**. The release increased to about 17% at an enthalpy of about 130cal/g. This tendency was seen also at lower burnups, but at lower release levels. Fission gas releases in the PWR fuel tests also show similar tendency, though they have more scatters. It should be noted that the BWR fuels at burnups above 56GWd/t had fission gas release of about 10% during steady state irradiation in commercial reactors. These steady state releases were not included in the figure. Therefore, the total that would be released at the failure could be close to 30% at the maximum in the tests[4].

4. Power oscillation test results

In the power oscillation tests, irradiated fuels at burnups of 56 and 25 GWd/t were subjected to four and seven power oscillations, which peaked at 50 to 95 kW/m at intervals of 2 s. Peak fuel enthalpies were estimated to be 256 J/g (61 cal/g) and 368 J/g (88 cal/g), respectively, in the two tests. Transient fuel rod behavior under the severer power oscillation condition is shown in **Fig. 6**. The cladding elongation increased as the power rose up, independent to the cladding temperature. The result suggested that pellet-cladding mechanical interaction (PCMI) caused the cladding deformation in the test. The cladding deformation was comparable to those observed in the RIA tests at the same fuel enthalpy level up to 368 J/g (88 cal/g). In other words, cladding axial deformation due to the PCMI was not enhanced due to the cyclic load.

Fission gas release, on the other hand, was considerably smaller than in the RIA tests, suggesting different release mechanisms between the two types of transients. **Figure 7** compares fission gas releases in the transient heating tests of high burnup BWR fuels. Fission gas release in the power oscillation test with a BWR fuel at an estimated peak fuel enthalpy of 256 J/g (61 cal/g) was much smaller than that in a comparable RIA test at a peak fuel enthalpy of 293 J/g (70 cal/g). High burnup BWR fuel from sibling segments were used in the two tests.

Departure from nucleate boiling (DNB), which would lead significant degradation of heat transfer from the cladding surface, did not occur in the two tests. Therefore, the cladding temperature remained about the saturation temperature of the water, which was 100 degrees Celsius. One other test is planned in Japanese FY2002 with a fuel at a burnup of 25GWd/t under a cooling condition with smaller sub cooling and power history similar to that in **Fig. 6**, in order to examine fuel rod behavior with the DNB causing elevated cladding temperature.

5. Summary

Brittle cladding failure occurred in high burnup PWR and BWR fuel tests at fuel enthalpies as low as 60 cal/g in series of RIA tests of high burnup PWR and BWR fuels conducted in the NSRR. Same type of failure occurred in fresh PWR fuel rods with hydrided cladding. The failure thresholds, however, was higher in fresh fuel tests than irradiated fuel tests, suggesting the irradiation effects for the cladding embrittlement. Recent RIA tests with transient cladding hoop strain measurement suggested that the PCMI failure was caused mainly by thermal expansion of pellets. Contribution of fission gases to the failure seems limited.

Considerable fission gas release and fine fuel fragmentation were observed in the tests. Consequence of the fuel failure would be influenced by these phenomena, which should depend on fission gases and fuel morphology at high burnups.

First two tests under conditions of BWR power oscillations without scram were conducted in the NSRR. Cladding deformation caused by PCMI was observed in the power oscillation tests. Magnitude of the deformation was comparable to those observed in the RIA tests and ratcheting effect of the cyclic load on the deformation was not observed. Fission gas release was smaller than that observed in RIA test at a comparable fuel enthalpy. One more test in FY 2002 is planned under a condition with expected DNB.

Acknowledgements

The authors are grateful to TEPCO for their supply of irradiated BWR fuel rods. They wish to thank colleagues in the NSRR Operation Division and Department of Hot Laboratories of JAERI for conducting the NSRR tests and pre/post-test examinations. They are grateful to H. Ikehata, M. Yoshinaga, K. Kusagaya and R. Hosoyamada for assisting data evaluation and analyses of the tests.

References

1) T. Fuketa, F. Nagase, K. Ishijima and T. Fujishiro, "NSRR/RIA Experiments with High-Burnup PWR Fuels," *Nucl. Safety,* 37, 4, Oct.-Dec. (1996).
2) T. Fukta, H. Sasajima and T. Sugiyama, "Behavior of High-burnup PWR Fuels with Low-Tin Zircaloy-4 Cladding Under Reactivity-Initiated-Accident Conditions," *Nucl. Technol.* 133, 50 (2001).
3) T. Nakamura, M. Yoshinaga, M. Takahashi, K. Okonogi and K. Ishijima, "Boiling Water Reactor Fuel Behavior Under Reactivity-Initiated Accident Conditions at Burnup of 41 to 45 GWd/tonne U," *Nucl. Technol.* 129, 141, (2000).
4) T. Nakamura, K. Kusagaya, T. Fuketa and H. Uetsuka, "High-Burnup BWR Fuel Behavior Under Simulated Reactivity-Initiated Accident Conditions," *Nucl. Technol.* 138, 246, (2002).
5) T. Sugiyama and T. Fukta, "Mechanical Energy generation during High Burnup Fuel Failure under Reactivity Initiated Accident Conditions," *J. Nucl. Sci. Technol.* 37, 10, 877-886, (2000).
6) B. E. Boyack, A. T. Motta, K. L. Peddicord, J. G. M. Anderson, C. A. Alexander, B. M. Dunn, T. Fuketa, L. E. Hochreiter, R. O. Montgomery, F. J. Moody, G. Potts, D. W. Preuitt, J. Rashid, R. J. Rohrer, J. S. Tulenko, K. Valtonen and W. Wiesenack, *Phenomenon Identification Ranking Tables (PIRTs) for Power Oscillations Without Scram in Boiling Water Reactors Containing High Burnup Fuel,* NUREG/CR-6743, LA-UR-00-5079, Los Alamos National Laboratory (2001).
7) USNRC, "AECD Concerns Regarding The Power Oscillation at LaSalle-2 (BWR-5)," AEOD Special Report S803, (1988).
8) W. Wulff, H. S. Cheng, A. N. Mallen and U. S. Rohatgi, B*WR Stability Analysis with the BNL Engineering Plant Analyzer*, NUREG/CR-5816, BNL-NUREG-52312, Brookhaven National Laboratory, (1992).
9) T. Nakamura, M. Yoshinaga, M. Sobajima, K. Ishijima, and T. Fujishiro, "Boiling Water Reactor Fuel Behavior at Burnup of 26GWd/tonne U Under Reactivity-Initiated Accident Conditions," *Nucl. Technol.* 108, (1994).
10) K. Ishijima, S. Tanzawa, T. Fuketa and T. Fujishiro, "Behavior of Preirradiated Fuels Under Simulated RIA Conditions," Proc. Topl. Mtg. Safety Thermal Reactors, Portland, Oregon, July 21-25, 1991, P.557, American Nuclear Society, (1991).
11) H. Sasajima, T. Fuketa, T. Nakamura, J. Nakamura and H. Uetsuka, "Behavior of Irradiated ATR/MOX Fuel under Reactivity Initiated Accident Conditions," *J. Nucl. Sci. Technol.* 37, 5, 455-464 (2000).
12) T. Nakamura, S. Katanishi, Y. Kashima, S. Yachi, M. Yoshinaga and Y. Terakado, "High Power Transient Characteristic and Capability of NSRR," *J. Nucl. Sci. Technol.* 39, 3, 264, (2002).

13) L. J. Siefken, C. M. Allison, M. P. Bohn, and S. O. Peck, "FRAP-T6: A Computer Code for the Transient Analysis of Oxide Fuel Rods," NUREG/CR-2148, EGG-2104, EG&G Idaho, Inc. (1981).

14) T. Nakamura, H. Sasajima, T. Fuketa and K. Ishijima "Fission Gas Induced Cladding Deformation of LWR Fuel Rods under Reactivity Initiated Accident Conditions," *J. Nucl. Sci. Technol.* 33, 12, 924, (1996).

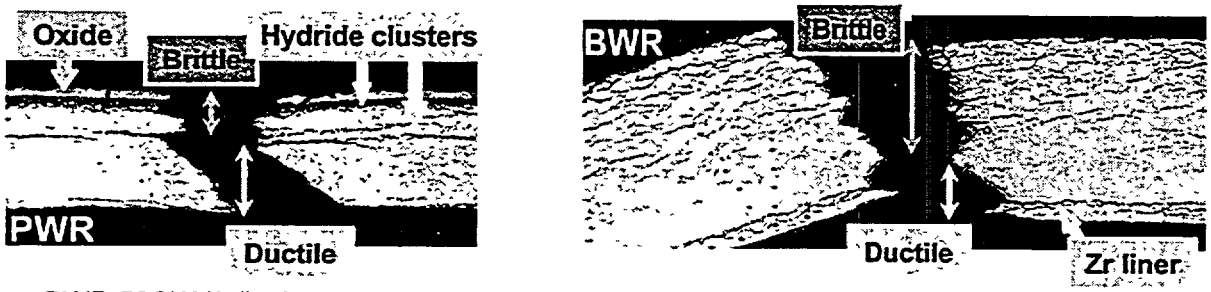

PWR 50GWd/t (hydrogen: about 400ppm) failed at 250J/g(60cal/g)

BWR 61GWd/t (hydrogen: about 200ppm) failed at 292J/g(70cal/g)

Fig. 1 Comparison of PWR and BWR cladding cross sections failed in RIA tests. Hydrides in the BWR cladding were oriented more randomly.

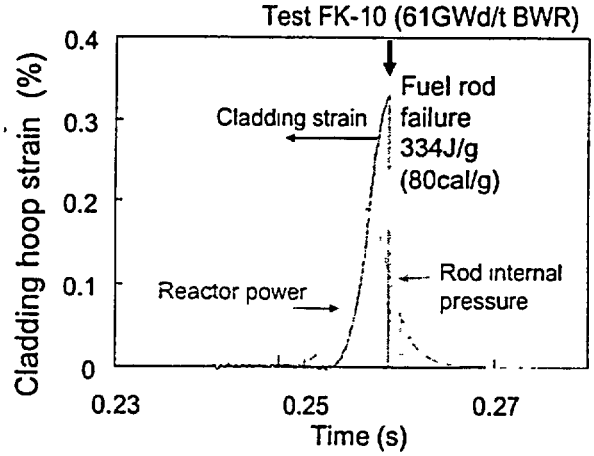

Fig. 2 Cladding deformation history measured in a RIA test with a high burnup BWR fuel rod. The rod failed at a fuel enthalpy of 80cal/g with cladding hoop strain below 0.4%.

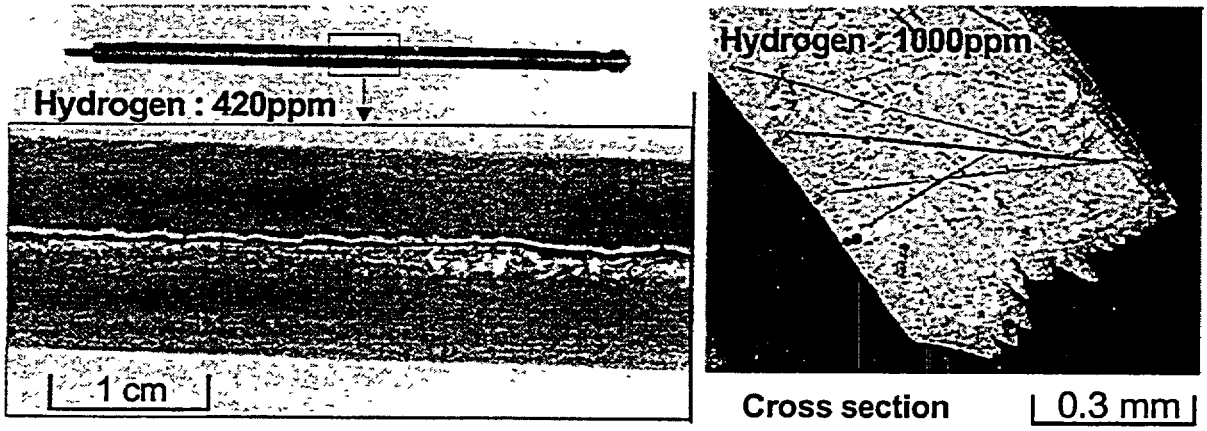

Fig. 3 Appearance and a cross section of fresh hydrided PWR fuel rod failed in RIA tests.

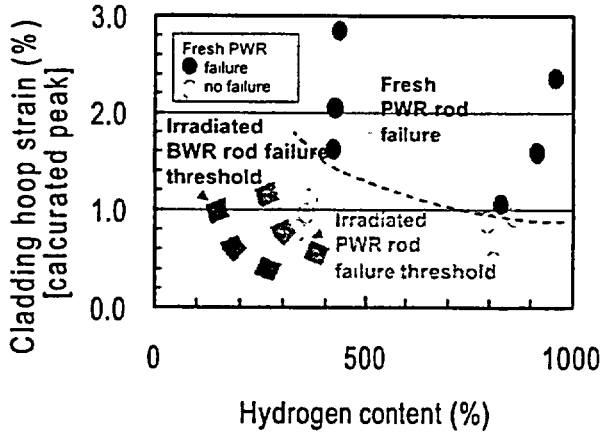

Fig. 4 Failure/no-failure map of fresh hydrided cladding tests. Estimated failure thresholds of high burnup fuels are indicated for comparison.

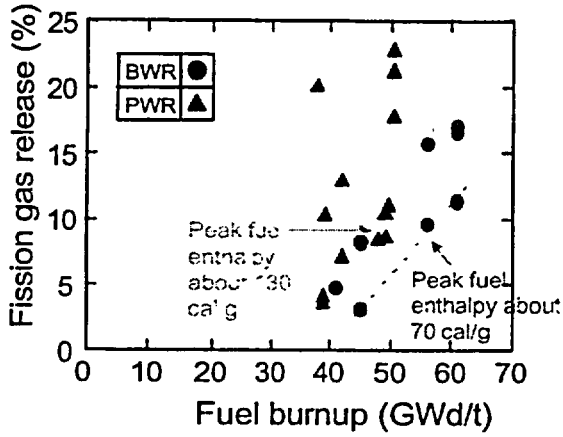

Fig. 5 Failure/no-failure map of fresh hydrided cladding tests. Estimated failure thresholds of high burnup fuels are indicated for comparison

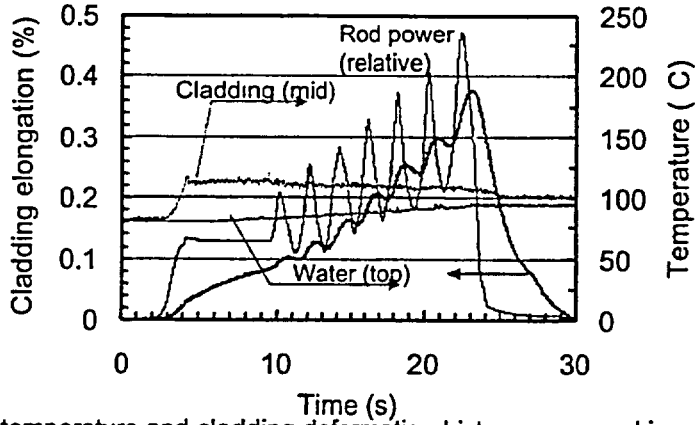

Fig. 6 Transient power, temperature and cladding deformation history measured in a power oscillation test with a fuel rod at a burnup of 25 GWd/t. The rod was subjected to seven power oscillations at linear heat rates up to 95kW/m and at an estimated peak fuel enthalpy of 368 J/g (88 cal/g).

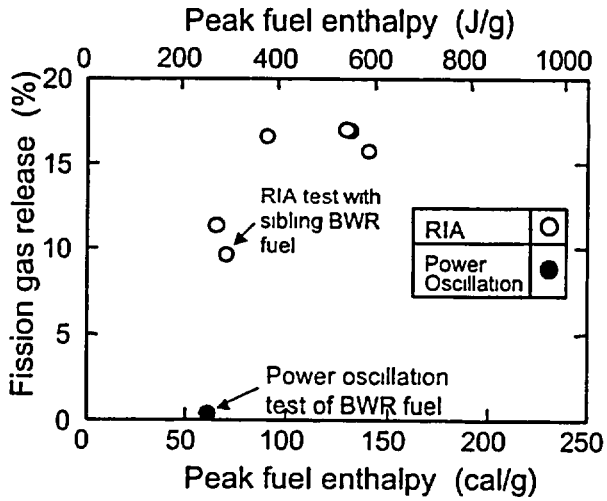

Fig. 7 Fission gas release observed in RIA and power oscillation tests of BWR fuel rods at burnups from 56 to 61 GWd/t as a function of peak fuel enthalpy.

FAILURE OF ZIRCALOY-4 SHEET CONTAINING HYDRIDE BLISTERS

O.N. Pierron[1], D.A. Koss[1], A.T. Motta[2], R.S. Daum[3], and K.S. Chan[4]
[1]Dept. Materials Science and Engineering, Penn State Univ., University Park, PA 16802
[2]Dept. Mechanical and Nuclear Engineering, Penn State University, University Park, PA 16802
[3]Argonne National Laboratory, Argonne, IL 60439
[4]Southwest Research Institute, San Antonio, TX
[Corresponding Author: Donald Koss, 202A Steidle Bdg., Penn State University, University Park, PA 16802, koss@ems.psu.edu, phone: 814 865 5447, Fax: 814 865 2917]

ABSTRACT

We have investigated the fracture behavior of unirradiated Zircaloy-4 sheet (0.64 mm thick) containing either model hydride blisters or a continuous hydrided layer "rim" at both 25° and 300°C and subject to the multi-axial stress state of near plane-strain tension. The blisters (either 2 or 3 mm in diameter) behave in a brittle manner, and the overall failure of the Zircaloy is controlled by fracture of the remaining "substrate" material. As a result, the fracture of the sheet is sensitive to the depth of the hydride layer/blister such that there is a significant decrease in ductility as the blister depth increases, up to a depth of about 100 μm. Beyond this value the ductility remains approximately constant. Importantly, moderate ductility is retained in the Zircaloy at 300°C for blisters of depths >200 μm, even though such blister depths severely limit room temperature ductility. In general, the ductility of a material with a continuous hydride rim is less than that of a material containing blisters of the same depth. Experimental evidence as well as analytical modeling indicates that, while substrate fracture is controlled by crack growth at 25°C, the inhibition of crack growth at 300°C results in eventual failure due to an onset of a shear instability process. As a result, the Zircaloy remains relatively "tolerant" of isolated hydride blisters at 300°C.

1. INTRODUCTION

The mechanical behavior of Zircaloy fuel cladding degrades during nuclear reactor operation due to a combination of oxidation, hydriding, and radiation damage [1]. As the cladding undergoes oxidation with the associated hydrogen pickup, the total amount of hydrogen increases, and hydride precipitates form preferentially near the outer (cooler) surface of the cladding, usually in the form of a continuous layer/rim containing a high concentration of discrete hydrided particles. Under conditions where oxide spallation occurs, hydride *blisters* may form. The blisters are often lens shaped (typically a few mm in major dimension) and consist of a very high hydride concentration and/or a solid hydride [2].

The influence of a *uniform* distribution of hydrides on the mechanical behavior of zirconium-based alloys has been studied extensively, usually under uniaxial tensile loading; see for

example refs.[2-12]. Recent studies have also examined the failure behavior of Zircaloy-4 cladding tubes for the case when hydrides are present in the form of a layer or rim [13]. These "hydride-rim" results, based on unirradiated cladding, indicate a significant loss of ductility with increasing hydrogen content and/or increasing hydride rim thicknesses [13] and suggest that a ductile-to-brittle transition occurs with increasing hydride rim thickness.

In addition to the presence of hydrides, a second condition that affects cladding failure is the stress state associated with in-service loading. For the case of recrystallized zirconium alloy sheet containing a uniform distribution of hydrides, increasing the biaxiality of the stress state increases the severity of the hydrogen embrittlement [14]. Such an effect becomes an issue for Zircaloy cladding subject to postulated reactor accidents such as the reactivity-initiated accident (RIA) [15]. In this case, the interaction between fuel pellets and the cladding tubes forces the cladding to deform under multiaxial stress states. Predicting a criterion for cladding failure thus requires a knowledge of the influence of the effects of irradiation, the specific hydride microstructure, and the stress state of loading. This study addresses the latter two issues.

The purpose of this study is to examine the influence of *hydride blisters* on failure behavior of unirradiated Zircaloy-4 under the multiaxial stress state associated with near-plane strain deformation. Our approach is to create a model system in which the effects of blisters on ductility can be studied separate from other parameters. Using a gas-charging procedure we introduced blisters of controlled depths in double notch tensile specimens that were specially designed to create biaxial tension and near plane-strain tension deformation within the gauge section . To study the influence of blisters it is necessary to have a gauge section that is large compared to the blister diameter (2-3 mm). Because of this we utilize flat Zircaloy-4 sheet with a crystallographic texture (and plastic anisotropy) similar to that of as-fabricated Zircaloy-4 cladding tubes. Both cold worked and stress-relieved as well as recrystallized conditions of the sheet are examined.

2. EXPERIMENTAL PROCEDURE

2.1 Materials Used

Zircaloy-4 sheet with a thickness of 0.64 mm was obtained from Teledyne Wah-Chang in the cold-worked, stress-relieved state (CWSR). Recrystallized (RX) material was obtained after annealing the as-received material at 650°C for 30 minutes in a vacuum of 10^{-5} Torr. The grain structure of the CWSR material, determined using polarized light microscopy, consisted of elongated grains, approximately 10 μm long and roughly 1-2 μm thick in the CWSR condition while equiaxed grains approximately 5 μm grain in diameter in were observed the RX condition.

Both the CWSR and RX conditions exhibited a strong crystallographic texture. The Kearns factors (resolved fraction of basal poles aligned with the three macroscopic directions, N=normal, L=longitudinal (rolling direction), T=transverse) [16], and measured by Teledyne Wah-Chang are shown in Table 1. The majority of the basal poles are aligned with the normal direction. Importantly, these values are similar to those reported for unirradiated CWSR Zircaloy-4 cladding tubes [17] if the hoop direction of the tube corresponds to the orientation transverse to the rolling direction of the sheet. Therefore, the texture of the sheets of Zircaloy-4 used in this study is similar to the typical texture of Zircaloy-4 cladding tubes, for which the basal planes tend to align with their poles inclined approximately ± 30° away from the normal of the tube surface and oriented towards the transverse direction [18].

Table 1. Kearns factors for both CWSR and RX Zircaloy-4 sheet and tubing.

	f_N	f_L	f_T
CWSR sheet (this work)	0.59	0.05	0.31
RX sheet (this work)	0.60	0.06	0.34
CWSR tubing [17]	0.58	0.10	0.32

The tensile properties of the Zircaloy-4 sheet used in this study are shown in Table 2 and are described in more detail elsewhere [19]. In comparing the behavior of the two material conditions, we see that the recrystallized (RX) condition exhibits a much higher strain hardening exponent ($n = d\ln\sigma/d\ln\varepsilon$, where σ is the stress and ε is the strain) but lower yield stress values. There is also a significant decrease of the yield stress as the temperature increases from 25° C to 300°C, as is the case for Zircaloy-4 cladding tube [20-22], In both conditions, the texture observed above causes the Zircaloy-4 sheet to be plastically anisotropic such that through-thickness deformation is difficult. Such behavior is apparent from the values of the plastic anisotropy parameter R' ($R' = \varepsilon_{width}/\varepsilon_{thickness}$, where ε_{width} and $\varepsilon_{thickness}$ are the width and thickness strains during uniform deformation in a tensile test); for the conditions listed in Table 2, R' is in the range of 1.6 to 5.2.

Table 2. Tensile Parameters of Zircaloy-4 sheet in either the recrystallized (RX) or cold worked and stress-relieved (CWSR) conditions at 25° and 300°C for uniaxial testing in the transverse direction of the sheet [19].

Condition	$\sigma_Y^{0.2\%}$ (MPa)	n-value	R'	Elongation to Failure (%)
RX/25°C	469	0.09	5.2	29
CWSR/25°C	573	0.01	2.2	19
RX/300°C	166	0.11	2.2	29
CWSR/300°C	318	0.03	1.6	16

2.2 Hydrogen charging

Hydrogen charging of the Zircaloy-4 sheet was performed by gas charging at 400°C using a Ni "window" whose geometry controlled the geometric shape of the hydride (i.e., blister or continuous layer). The Ni window consisted of a thin film of Ni (≈0.1μm thick) that was vapor deposited onto the specimen gauge section with the following geometries: (a) a 2 mm circle, (b) a 3 mm circle (for most of this study), and (c) a continuous layer over the whole gauge section. A short time period prior to vapor deposition, the surface of Zircaloy was cleaned using the ASTM procedure (G2-88) to remove the small oxide layer that is always present in Zr exposed to atmosphere. Uncoated regions of the Zircaloy quickly reformed the small oxide layer prior to exposure to the hydrogen/argon gas at the 400°C, inhibiting the diffusion of hydrogen and

restricting the hydride formation to regions below/near to the Ni coating. As described in detail elsewhere [23], hydrogen charging was performed at 400°C by exposing the coated specimen to a gas mixture of 12.5%H_2/argon at one atmosphere pressure and for charging times ranging from 30 s to 30 min. For a given material, it was observed that the depth of the blister was a linear function of the charging time. For the range of charging times used, cross-section metallography showed that the blister diameter corresponded to the Ni coating diameter. In addition, some hydrogen diffused throughout the sheet thickness to form discrete hydrides in the "substrate" region beneath the hydride blister. The resulting hydride distribution is illustrated schematically in Figure 1b with l being the blister width (2 or 3 mm) and d the blister depth.

2.3 Mechanical Testing

In-service loading of Zircaloy cladding tubes usually occurs under multiaxial tension with the maximum principal stress oriented in the hoop direction of the tube. Based on earlier studies [21], we have simulated such loading with a double edge notched tensile specimen, Figure 1a, designed to introduce a biaxial stress state in the specimen center such that near plane-strain tension is achieved (i.e., the minor strain component in the plane of the sheet is near zero). In the present study, 25.4 mm wide specimens (about 76mm long) with two 4.75 mm diameter notches, each of which was 6.35 mm deep, were tested. The resulting biaxial state of stress in the center of the specimen limits strain in the transverse direction of the specimen and induces the material near its center to a near plane-strain deformation path. Failure occurred in the specimen center, where a near plane-strain condition is met, and where the hydride blister was located.

The mechanical testing was performed at an approximate strain rate of 10^{-3} s^{-1}. In addition, the orientation of the tensile axis was chosen to be in the long transverse direction of the sheet (normal to the rolling direction) in order to obtain deformation behavior similar to that of unirradiated Zircaloy-4 cladding when tested in the hoop direction.

As will be shown later, the hydride blisters fractured at or shortly after yielding within the ductile substrate. In order to determine failure strains of the substrate material beneath the blister, we measured the *local* fracture strain $(\varepsilon_{frac})_{local}$ near, but not at, the fracture surface. After measurement of the initial specimen thickness, cross-section metallography of the fractured specimen was used to determine the specimen thickness at a location approx. 0.5 mm displaced from the fracture surface (to avoid a localized thickness reduction due to crack growth). Using this procedure, we calculated a local thickness strain that we interpret as that strain level at the onset of crack growth. This thickness strain value was then converted into a local failure strain $(\varepsilon_{frac})_{local}$ value by knowing the ratio of minor $(\varepsilon_2)_{blister}$ and major $(\varepsilon_1)_{blister}$ strains within the substrate beneath the blister (measured from the deformation of the circular Ni coating as in the first procedure) and using conservation of the volume. Thus,

$$(\varepsilon_{frac})_{local} = \frac{-\varepsilon_3}{1+\frac{(\varepsilon_2)_{blister}}{(\varepsilon_1)_{blister}}} \qquad (1)$$

For the case in which specimens were hydrided across the entire gauge length (a hydride rim), a microhardness indentation gridding procedure was used to determine the ratio $\varepsilon_2/\varepsilon_1$ on a local basis as done previously [21].

3. RESULTS AND DISCUSSION

3.1 Hydride Microstructure

As a result of the hydrogen charging procedure, the blisters were defined by the formation of a solid hydride to a near-uniform depth beneath the Ni coating, as is shown in Figure 2. In the present study, blisters with primarily a 3 mm diameter were formed with depths ranging from 5 to 250 μm. Based on previous studies [24, 25], we believe that the hydride that forms during charging is the δ-phase with a composition range from $ZrH_{1.64}$ to $ZrH_{1.96}$, but no direct confirmation was made. In our case, the kinetics of the blister formation suggest that once a very thin layer of δ-phase forms just below the Ni coating, subsequent hydrogen ingress tends primarily to cause further growth of the δ-phase.

In addition to the formation of a solid hydride blister, some of the hydrogen also forms individual hydride precipitates in the substrate below the hydride blister. As shown in Figure 2a, these hydride precipitates typically have a major dimension on the scale of 100 μm in the CWSR condition and tend to be aligned in the plane of the sheet, similar to the circumferential hydride microstructures in Zircaloy cladding tube. In contrast, the hydrides within the substrate in the RX material appear somewhat smaller (≈25 μm maximum dimension) but tend to have a stronger radial component to their orientation. The hydrogen contents in the ligament below the blister were measured as a function of blister thickness for both RX and CWSR conditions. Results from six different conditions (hydride depths ranging form 50 to 175 μm) show that the H content within the ligament increases from approximately 300 wt. ppm for the 50 μm blister depth to approximately 400 wt. ppm within the ligament below blisters with depth >100 μm.

In summary, the resulting microstructure, shown in Figure 2, consists of a combination of a hydrided substrate residing beneath a solid hydride blister whose width corresponds to the Ni coating dimension (typically 3 mm diameter) and whose depth is controlled by the charging time at 400°C (and, to some extent, by the time at the 300°C test temperature). It is useful to compare the microstructure shown in Figure 2a (the CWSR case) to that formed during service operation in *irradiated* Zircaloy-4 cladding. For example, Figure 3, which is based on high burn-up Zircaloy cladding, shows a solid hydride layer with a depth ~50 μm as well as the presence of a concentration of discrete, circumferential hydride precipitates. A comparison of Figures 2 and 3 shows that the morphology (shape, aspect ratio, orientation) of the hydrides in the substrate under the model blisters in this study is similar to that observed in the material hydrided in service; this irradiated cladding appears to have a higher density of hydride particles in the substrate beneath the hydride layer.

3.2 Effect of Blister Depth on Sheet Failure

Previous research has shown that the thickness of a continuous hydride rim has a strong influence on the failure of Zircaloy-4 cladding; specifically, increasing the thickness of the hydride rim decreases the ductility of the cladding [13, 26]. A similar effect is observed for the case of hydride blisters. The presence of the brittle blister causes the initiation of a crack that propagates to the depth of the blister, as described below. Failure of the sheet is then controlled by fracture of the ductile substrate beneath the blister, which fails at various strain levels, depending on the depth of the blister.

Based on the local fracture strain values, Figure 4 shows that ductility of the Zircaloy-4 sheet containing 3 mm blisters initially decreases rapidly with increasing hydride blister depth for both material conditions and at 300^0C as well as 25^0C. For all testing conditions, the rapid decrease in failure strain with increasing blister depth persists to about 100 μm depth. While there is little ductility (2-5%) beyond this value at 25^0C, moderate ductility (7 to 10% fracture strain for the cold worked material and 10 to 15% for recrystallized condition) is retained at 300^0C, even for blisters of depths > 200 microns. It is significant that our far-field ductility-values, $(\varepsilon_{frac})_{far}$, as measured over the scale of the 3 mm blister behave in a nearly identical manner to the local fracture strain values shown in Figure 4. Both the dependence of fracture strain on blister depth and the absolute magnitude of the fracture strain values are roughly identical between the two fracture strain procedures.

In addition to the depth of the blister, fracture of the sheet is also sensitive to temperature. Figure 4 also shows that, for a given blister depth, the material is significantly more ductile at 300°C than at 25°C. Although both the CWSR and the RX conditions show similar behavior at 25°C, the recrystallized condition shows significantly more ductility than the CWSR material at 300°C. This result is somewhat surprising since the RX condition contains a higher level of radial hydrides (known to promote fracture) within the substrate, as shown in Figure 2.

The influence of blister size, as opposed to blister depth, is illustrated in Figure 5, which shows that specimens with 2 mm diameter blisters exhibit approximately the same ductility as do 3 mm diameter blisters. Although no blister with a 2 mm diameter was tested at 300°C, we believe that the behavior at 300°C is similar to room temperature regarding the blister size. Therefore, these results indicate that the *ductility of specimens with hydride blisters depends mainly on the depth of the blister and not on its diameter* (either 2 or 3mm).

Figure 5 also compares the influence of blisters with that of a continuous hydride rim on fracture. In both the blister and rim cases, the ductility decreases rapidly with increasing hydride layer depth up to depths of ~ 100 μm. However, the decrease in fracture strain is more severe when the hydride layer is present in the form of a rim, especially at small blister/rim depths. For example, the fracture strain for a specimen with a 3-mm diameter and a 20 μm thick blister is about 0.24, while it is only about 0.12 for a specimen with a 20 μm continuous layer of hydride. Similar results, although not as complete as those in Figure 5, have been obtained for specimens tested at 300°C. Thus, the ductility of a material containing a continuous hydride rim is *less* than that of a material containing blisters of the same depth; this effect is most pronounced at small blister/rim depths.

Comparing to previous studies performed on tubing [13, 26], the fracture strains obtained in this study with *sheet material* containing a hydride rim are very similar to those obtained previously

on *tubing* with hydride rim. This supports our contention that the behavior of sheet material is a good model for that of tubing material with similar texture.

Finally, we note that, along with increased fracture strain at small blister depths, there is also a change in strain path. For thick blisters, the lateral constraint from the blister and the presence of cracks forces the Zircaloy substrate to a condition close to plane-strain deformation (i.e., referring to Figure 1, $\varepsilon_{yy} \approx 0$). Alternatively, the lack of transverse constraint from thin blisters as well as the high R-value of the substrate sheet metal results in a significantly larger minor strain in specimens with thin blisters. This change in strain path likely contributes to the observed increase in fracture strain at thicknesses below 50 microns (Figures 4 and 5). We offer this speculation on the basis that fracture of sheet metal usually depends on a critical thickness strain criterion [27]. Thus, any change in strain path in which the minor strain increases requires a compensating increase in major strain to achieve the critical thickness strain. In short, sheet metal ductility increases as the strain path deviates from plane-strain tension.

3.3 Mode of Failure: Fracture Profiles

While failure of the Zircaloy sheet initiates with cracking of the blisters both at 25° C and at 300°C, the mode of fracture of the substrate material (which determines the ductility of the hydrided sheet) depends on temperature. Figure 6 shows that the fracture profiles differ significantly between specimens tested at 25°C and 300°C. Independent of blister depth, the fracture profiles at 25°C are characterized by crack growth in the substrate along a path roughly *normal to the specimen surface* and therefore also normal to the maximum principal stress. Given the presence of 300-400 wt ppm hydrogen and the resulting hydride precipitates in the substrate, crack growth appears to result from damage accumulation within the substrate in the form of voids initiated by cracked hydrides, as shown in Figure 7. Thus, at 25°C, failure of the Zircaloy substrate occurs as a result of a crack growth process on a plane normal to the maximum principal stress and involving the growth and coalescence of voids formed by the cracked hydride precipitates.

In contrast to room temperature behavior, fracture of the substrate at 300^0C substrate occurs on a macroscopic plane inclined at ≈ 45° through the thickness, as also shown in Figure 6c and 6d. Such behavior suggests an alternate failure mode to crack growth. Specifically, we believe that the through-thickness shear failure evident in Figure 6c and 6d is a result of a deformation localization process on a plane of high shear stress, in the manner of localized necking of sheet metal [27, 28]. The pronounced crack blunting at 300°C indicates that cracks initiating within the blister are arrested by a very ductile, crack-resistant substrate. Significantly, the cracks appear to be more blunted in the RX condition than in the CWSR condition. This behavior is consistent with the increased ductility of the RX condition (see Figure 4), despite the presence of some radial hydrides in the RX material.

3.4 Fracture of Hydride Blisters

The failure behavior of Zircaloy sheet with hydride blisters (and, we believe, Zircaloy cladding tubes with hydride blisters) can be understood as a sequential process of crack initiation within the hydride blister and the subsequent failure of the substrate material beneath the blister.

In the present study, both acoustic emission results at room temperature and tests performed at temperatures up to 400^{0}C and interrupted at small strains ($\varepsilon \leq 0.02$) show the blister cracks at small plastic strains ($\varepsilon \leq 0.02$) within the substrate beneath the blister. In all cases, cross-section metallography shows the cracks are oriented normal to the blister surface and extend through its depth, consistent with their brittle behavior; i.e. the cracks arrest at the ductile substrate. Thus, we conclude that the hydride blisters are brittle at temperatures $\leq 400°$ C. Because the blisters are not only brittle but also reside on a ductile substrate, multiple cracks (all of which extend the width of the blister) form during deformation of the sheet, as illustrated in Figure 9. The crack spacing decreases roughly linearly with blister depth. A detailed analysis of the fracture behavior of hydride blisters is described elsewhere [28].

4. FRACTURE MECHANICS ANALYSIS

The results described above indicate that the fracture behavior is sensitive to blister depth as well as temperature. In all cases, the hydride blisters crack at small strains and fracture of the sheet is controlled by failure of the ductile substrate beneath the blister. While substrate failure at 300^{0}C appears to result from a shear instability, room temperature fracture has the characteristics of crack growth (i.e., fracture along a plane normal to σ_1 accompanied by comparatively little local necking). As described elsewhere [23,28], it is possible to use an elastic-plastic analysis to predict fracture *strains* necessary to propagate the crack within a blister of a given depth and to cause sheet fracture.

We assume that the hydride blister/rim of depth a is equivalent to a crack of the same initial depth a (a consideration of the presence of parallel cracks and crack-tip shielding indicates that the single crack assumption is reasonable [23,28]) and that the geometries for both hydride rim and blister configurations correspond to a semi-infinite surface crack or a semi-elliptical surface crack, respectively. In both cases, the cracks reside in a sheet of finite thickness, and we assume plane-stress conditions through the thickness. Because of the large amount of plastic yielding that occur during crack growth, the J-integral procedure is used, as is described below.

In order to account for plasticity, the material is assumed to follow the Ramberg-Osgood equation:

$$\frac{\varepsilon}{\varepsilon_0} = \frac{\sigma}{\sigma_0} + \alpha\left(\frac{\sigma}{\sigma_0}\right)^{n'} \qquad (2)$$

where σ_0 is the yield stress, $\varepsilon_0 = \frac{\sigma_0}{E}$, E is the elastic modulus, n' is the inverse of the strain-hardening exponent ($n' = \frac{1}{n}$), and $\alpha = \frac{{\sigma_0}^{n'-1}E}{k^{n'}}$ and where k is given by the equation:

$$\sigma_{eq} = k(\bar{\varepsilon}_N)^n \qquad (3)$$

where σ_{eq} is the equivalent stress and ε_N is the void nucleation strain.

Therefore, the plastic strain at the crack tip will be equal to:

$$\varepsilon_n^p = \alpha \frac{\sigma_0}{E}\left(\frac{\sigma_n}{\sigma_0}\right)^{n'} \qquad (4)$$

where σ_n is the net-section stress, $\sigma_n = \frac{\sigma}{1-a/t}$.

where t is the thickness. Fracture occurs when the driving force for the crack propagation, $J(a_e, \sigma)$, reaches the critical value J_c; and so the condition for crack propagation can be expressed as

$$J(a_e,\sigma) = J_c = \frac{K_c^{\,2}}{E} \qquad (5)$$

where K_c is the plane-stress fracture toughness of the sheet. The J-integral may be separated into elastic $J_e(a_e,\sigma)$ and plastic $J_p(a_e,\sigma)$ components and then is equal to:

$$J(a_e,\sigma) = J_e(a_e,\sigma) + J_p(a_e,\sigma) = J_e(a_e,\sigma)\left[1+\alpha\left(\frac{\sigma_n}{\sigma_0}\right)^{n'-1}\right] \qquad (6)$$

where $J_e(a_e,\sigma) = \frac{K_e^{\,2}}{E}$ for plane-stress conditions. Substituting (4) into Equation (2) leads to the following relationship for the fracture plastic strain:

$$\varepsilon_n^p = \alpha \frac{\sigma_0}{E}\left\{\frac{1}{\alpha}\left(\frac{K_c^{\,2}}{K_e^{\,2}} - 1\right)\right\}^{\frac{n'}{n'-1}} \qquad (7)$$

Equation 12 permits us to predict the fracture strain provided that we know the stress-intensity factor K_e for the crack geometries. In all cases, we apply the "plastic zone correction" procedure by considering a hypothetical crack of length $a_e = a + r_{0\sigma}$, where $r_{0\sigma}$ is half of the plastic zone size in plane-stress conditions or

$$r_{0\sigma} = \frac{1}{2\pi}\left(\frac{K_e}{\sigma_0}\right)^2 \qquad (8)$$

The plastic zone $2r_{0\sigma}$ is obtained by first calculating K_e with a_e=a; then K_e is recalculated using $a_e = a + r_{0\sigma}$.

In order to determine the stress intensity parameter for the case of the cracked hydride blisters, the crack geometry correction factor for a semi-elliptical crack in a strip of finite thickness was employed [36]. For the case of the continuous hydride rim, the correction factor was that for a semi-infinite surface crack in a strip of finite thickness. These correction factors are based on the presence of a single crack in the material.

In order to apply the crack-growth analysis described, the fracture toughness, K_c, must be known. For Zircaloy-4 cladding tubes, previous studies show K_c-values to depend on H content and temperature. K_c-values in the range of 120-150 MPa.m$^{1/2}$ are common for unhydrided Zircaloy-4 at

both room temperature and 300°C. At room temperature, Grigoriev et. al. [29] found K_c-values about 104 MPa.m$^{1/2}$ for H contents 400-600 wt. ppm (assuming the following relationship: $K_c = \sqrt{J_{max} E}$, with J_{max} the J_I-integral for the maximum load point, and E the elastic modulus). Based on data from Huang [30], Kuroda et. al. assumed K_{IC}-values of 73 MPa.m$^{1/2}$ in their fracture mechanics analysis of hydrided Zircaloy-4 cladding at room temperature[31]. At 300°C, the H content does not appear to influence the fracture toughness [29], in which case $K_c \cong$ 120-150 MPa.m$^{1/2}$ [32]; Grigoriev et. al. report a J_{max}-value that indicates $K_c \cong$ 117 MP.m$^{1/2}$ at 300^{0}C for 400 wt. ppm H [29] . In addition, the nominal stress σ was calculated using Hill's original yield function for plane-strain condition and the constitutive stress-strain relation expressed in Equation 6 with the equivalent strain being given by Equation 4. An iterative calculation was then made to obtain the fracture strain ε_n^p. The material properties used in the analysis for both temperatures and materials (CWSR and RX) are given in Table 3.

Table 3. Material properties used in the fracture mechanics analysis.

Property	CWSR		RX	
	25°C	300°C	25°C	300°C
n	0.01	0.025	0.087	0.112
n'	100	40	11.5	8.9
E (GPa)	100	75	100	75
σ_0 (MPa)	573	318	469	166

Figure 9 shows the comparison between the fracture mechanics predictions and the observed dependences of fracture strain on blister/rim depth. As shown in Figure 9a, the agreement between experimental results and crack growth predictions are quite good assuming K_c = 70 MPa.m$^{1/2}$, which is a value close to that (73 MPa.m$^{1/2}$) assumed by Kuroda et. al. [31]. Bearing in mind that our substrate material contains 300-400 wt ppm hydrogen, the 70 MPa-value is similar but somewhat less than that (90 MPa.m$^{1/2}$) observed by Grigoriev et. al. [39]. In addition, close inspection of Figure 9a shows that the calculated fracture strains for the two blister diameters (2mm and 3mm) are superimposed on each other. This supports our earlier conclusion, based on experimental observations, that the blister diameter (2 or 3 mm) has no significant effect on the failure of Zircaloy-4.

Figure 9b shows that the influence of the continuous hydride rim on fracture can also be predicted by our crack growth analysis, also on the basis of $K_c \cong$ 70 MPa.m$^{1/2}$. Reasonable agreement between the predicted and observed dependences is obtained. The predicted fracture mechanics results also confirm the earlier experimental observation that, compared to a hydride blister, a continuous hydride rim is more deleterious to ductility at a given hydride depth.

For the case of the recrystallized materials, the crack growth analysis fits experimental observations, Figure 9c, using a K_c-value between 100 and 150 MPa.m$^{1/2}$. While somewhat surprising, the increased K_c-value of the RX material is consistent with its lower flow stress and increased tensile ductility. For example, an unhydrided plane strain specimen was tested as well as a sister sample hydrided in the form of discrete hydride precipitates through the whole thickness below the Ni coating (no solid hydride blister was present) at a H concentration similar to that of the

hydrided substrates, both at room temperature and in the RX condition. Very similar average strains were found. Those results show that the tensile ductility of the hydrided substrate is similar to that of the unhydrided material and, importantly, significantly higher in the RX compared to the CWSR condition. Thus, it is reasonable the RX material exhibits more crack growth resistance than the CWSR material.

5. DISCUSSION

The experimental results presented here represent a reasonably complete picture of the behavior of Zircaloy sheet containing blisters at room temperature and at 300^{0}C. The model developed in the previous section accounts well for the fracture strains observed at 25 C, but at 300^{0}C, a different failure process is operative, and the model is no longer applicable. Earlier experimental observations, Figure 6, indicated a transition in failure mode from crack growth at room temperature to shear instability at 300^{0}C. Such a transition is consistent with our observation that the strains to nucleate voids at cracked hydride particles increase markedly with increasing temperature [28]. It is also consistent with the observation of a much reduced level of hydrogen embrittlement in Zircaloy-4 at 350^{0}C [7]. Thus, we expect a significant increase in fracture strain within the crack-tip process zone and therefore higher fracture toughness at 300^{0}C, consistent with experimental observations [29]. As shown in Figure 9d, the elevated values of the fracture toughness result in a significantly over-prediction of the experimentally observed fracture strains. Thus, we conclude that our unirradiated Zircaloy-4 containing hydride blisters does not fail by crack growth, but rather by a competing mechanism: a deformation localization process in which failure occurs by shear localization. An alternate failure model should be used to predict the experimental data at 300°C, but an adequate analysis is not currently available.

The current experiments were undertaken as a model study to identify the influence of model hydride blisters on Zircaloy ductility. As such, this model does not reproduce exactly the failure conditions of hydrided cladding in the reactor. In addition to the other parameters present in the reactor environment that also influence failure, such as radiation damage, there are additional factors that make the present tests different. When blisters form in fuel cladding, they often do so on top of an existing hydride rim, which may or may not be partially dissolved. Such a configuration should have a more severe impact on ductility than the isolated blister configuration used in our work.

Because of the above reasons, the absolute values of ductility do not necessarily correspond to the ductility that would be exhibited by Zircaloy cladding in a reactor. Nevertheless, this study does provide a systematic identification of the effects of hydride blisters on ductility under deformation conditions that are similar to those that would be expected during a reactivity initiated accident, especially if little friction exists between fuel and cladding. In particular, the temperature dependence of the effects should also be useful for understanding in-reactor behavior. For the case where fuel/cladding friction is very high, equal biaxial behavior should be prevalent and studies are ongoing to determine Zircaloy ductility under those conditions.

6. CONCLUSIONS

Both cold-worked and stress-relieved (CWSR) and recrystallized (RX) Zircaloy-4 sheet specimens were hydrided to form either 2 mm or 3 mm solid hydride blisters of controlled depths residing on a substrate that contains ~300-400 wt. ppm hydrogen in the form of discrete hydride particles. Limited tests were also performed on material with a continuous hydride layer. The fracture behavior of these materials were studied (primarily at 25° and 300°C) using double edge notched tensile specimens designed to induce near plane-strain deformation. The main conclusions are as follows:

1. In all cases, the hydride blisters are brittle even at 400^0C. A population of cracks forms and propagates through the blisters soon after the yielding of the plastic substrate beneath the hydride blister. The crack spacing in the blisters decreases with blister thickness.
2. Fracture of the sheet is controlled by the crack growth resistance of the substrate, such that the fracture strains decreases with increasing hydride blister/layer depth to levels of about 100 μm deep, above which the ductility remained constant. At 300^0C, both CWSR and RX Zircaloy-4 retain moderate ductility (7-10% fracture strain for CWSR and 10-15% for the RX condition), even for blister depths > 200 micron, which is close to one third of the sheet thickness.
3. The material is significantly more ductile at 300^0C than at room temperature. Also, the sheet is somewhat more ductile if the hydride is present as a blister rather than as a continuous layer. Blisters with 2 mm or 3 mm diameter have the same effect on sheet ductility.
4. An examination of the fracture profiles indicates a transition in failure mode within the substrate from crack growth on a plane normal to the maximum principal stress at 25^0C to a shear instability process on an inclined plane at 300^0 and 400^0C. At room temperature, the cracks that initiate within the hydride blisters (as well as in the continuous layers) propagate in a manner that can be predicted using elastic-plastic fracture mechanics. The observed fracture strains and their dependence on hydride blister depth can be well predicted using this model.

ACKNOWLEDGMENTS

We would like to thank Dave Green at Penn State for many technical discussions and Ralph Meyer at the NRC for his continued encouragement. This research has been supported by the Fermi Consortium at Penn State (ONP) and by the Southwest Research Institute (KSC).

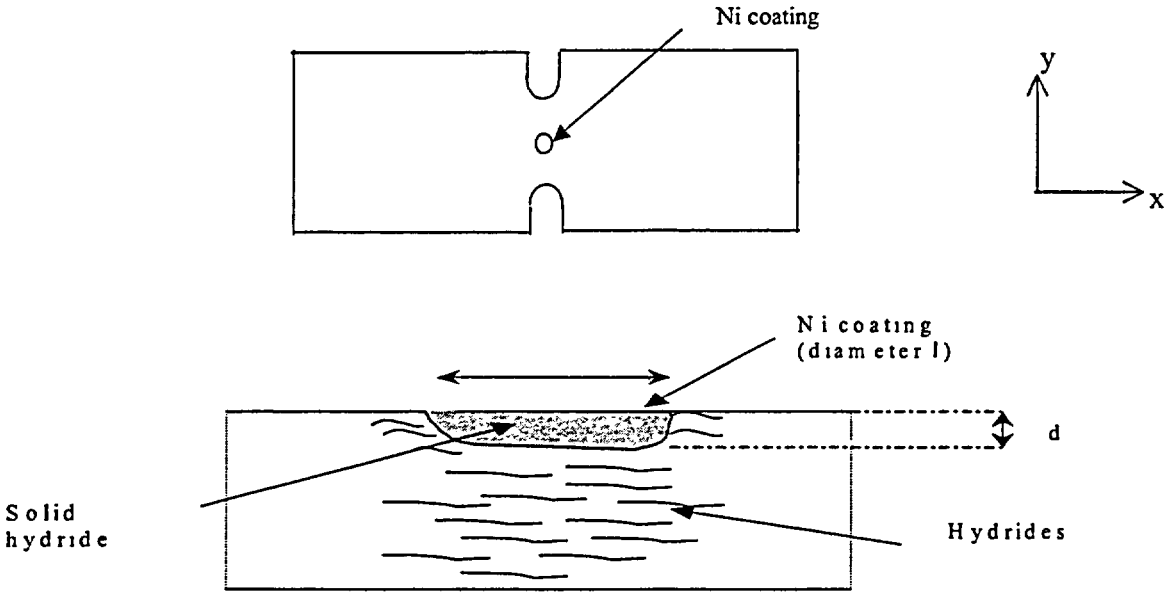

Figure 1. A schematic of (a) a double edge notched tensile specimen with a Ni coating/hydride blister in its center and (b) hydride blister made by hydrogen charging through a Ni coating with diameter *l*. The y direction is parallel with the rolling direction.

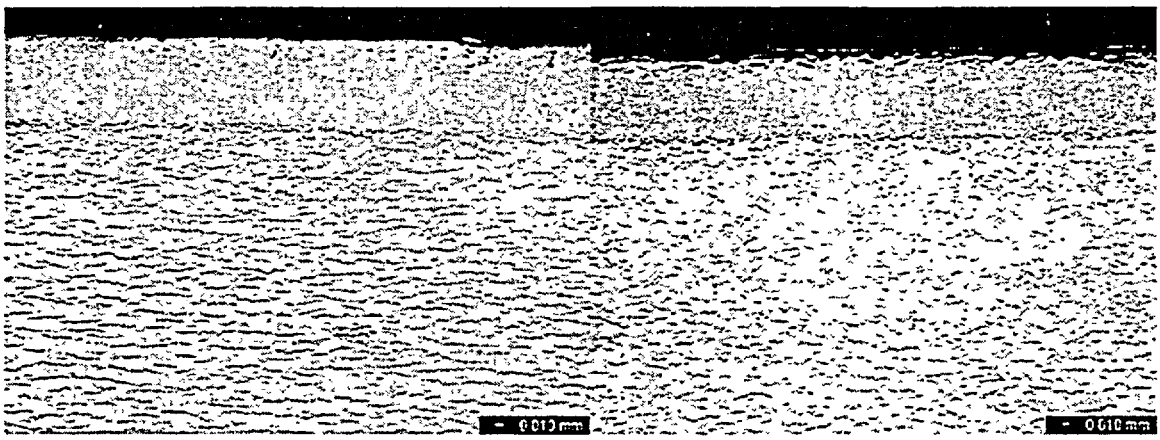

(a) (b)

Figure 2. Light micrographs of a transverse section of Zircaloy-4 sheet showing hydride blister and discrete hydride precipitates within the substrate beneath the blister in (a): CWSR specimen and (b): RX specimen.

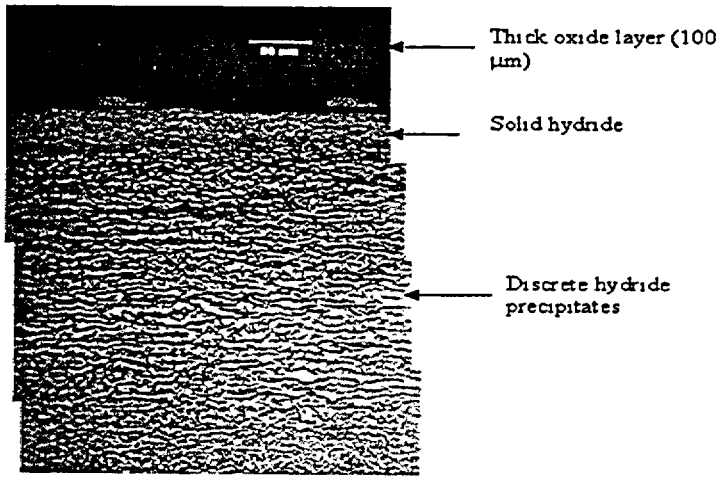

Figure 3. A light micrograph showing a hydride layer and associated hydrides in the substrate beneath the layer in irradiated Zircaloy-4 cladding tube (average fuel burnup of 67 GWd/t and fast fluence of 1.3×10^{22} n/cm^2).

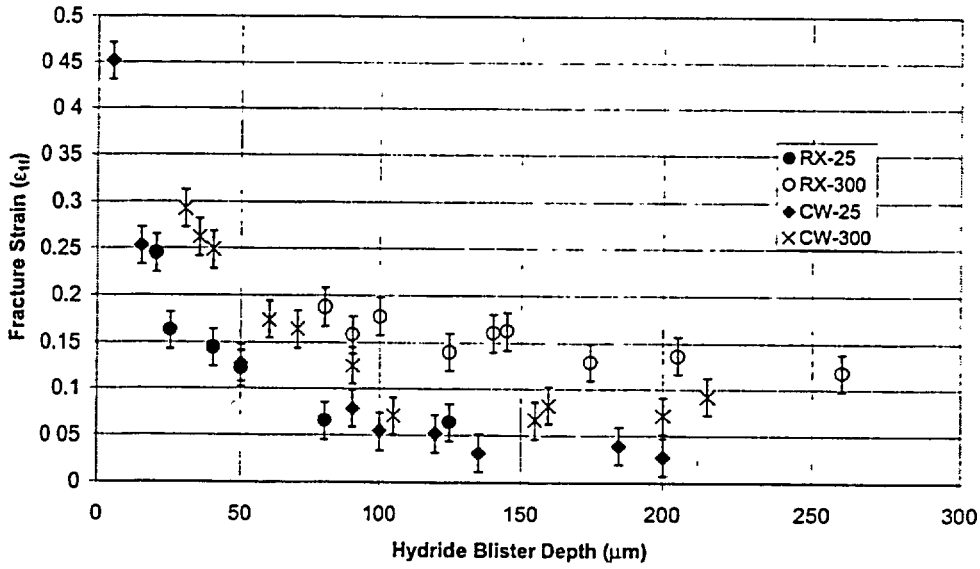

Figure 4. Local fracture strain versus hydride blister thickness for both cold worked and stress relieved (CWSR) and recrystallized (RX) Zircaloy-4 sheet tested at either 25^{0}C or 300^{0}C. All data are for 3 mm blisters.

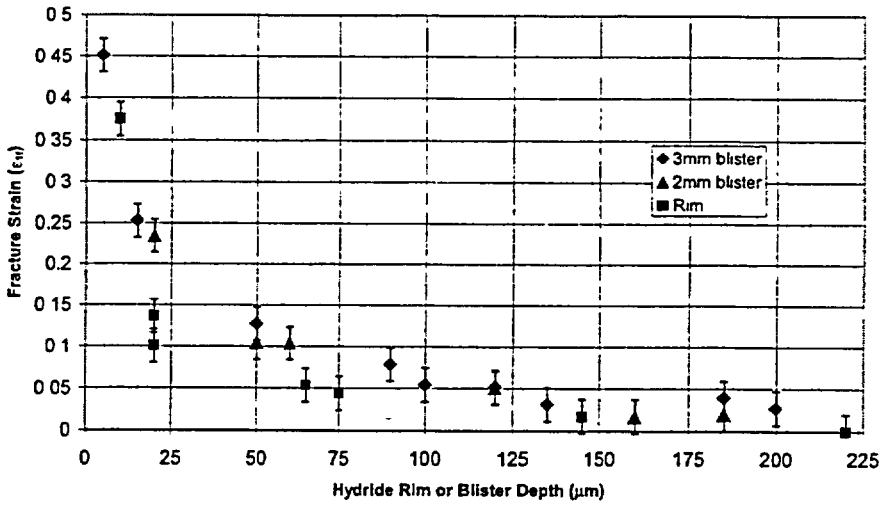

Figure 5. Local fracture strain versus blister or rim depth for either 3 mm or 2 mm diameter hydride blisters or a continuous rim of hydrides (25^0 C).

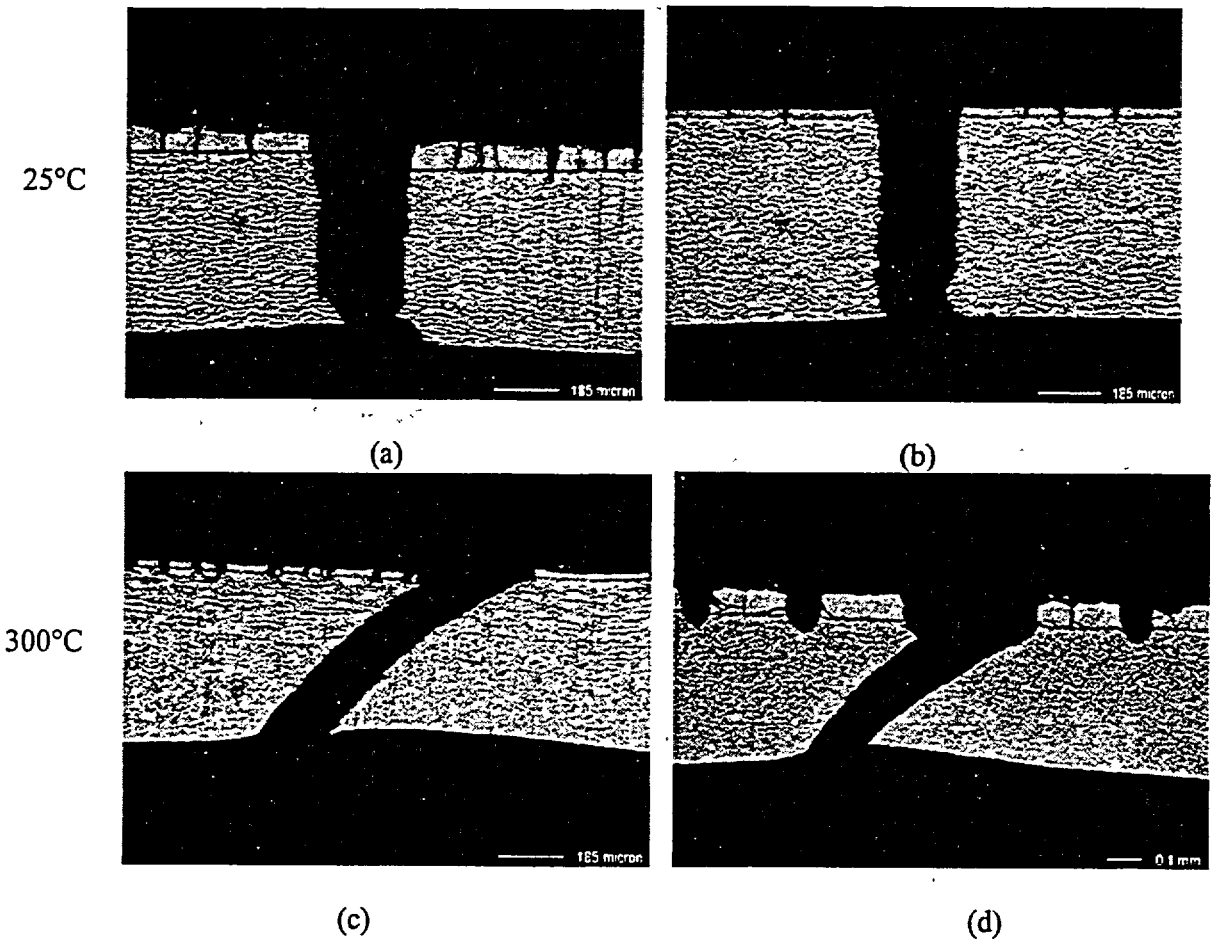

Figure 6. Fracture profiles of (a) CWSR sheet with a 100 μm blister, (b) RX with 40 μm blister, (c) CWSR with 35 μm blister, and (d) RX with 80 μm blister. Test temperatures are indicated.

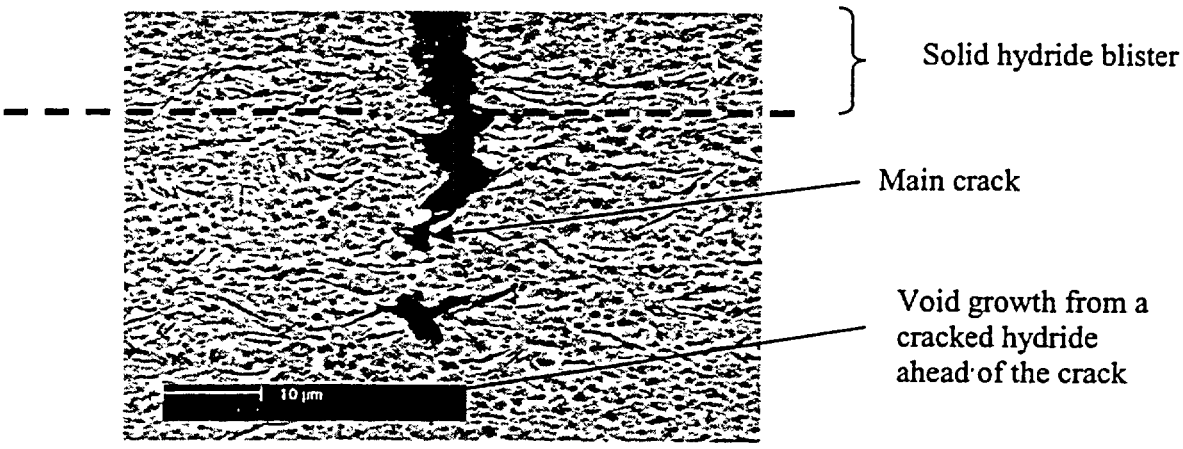

Figure 7. A light micrograph showing fractured hydrides and void nucleation near the tip of a crack beneath a 200 µm blister in CWSR Zircaloy-4 deformed at room temperature

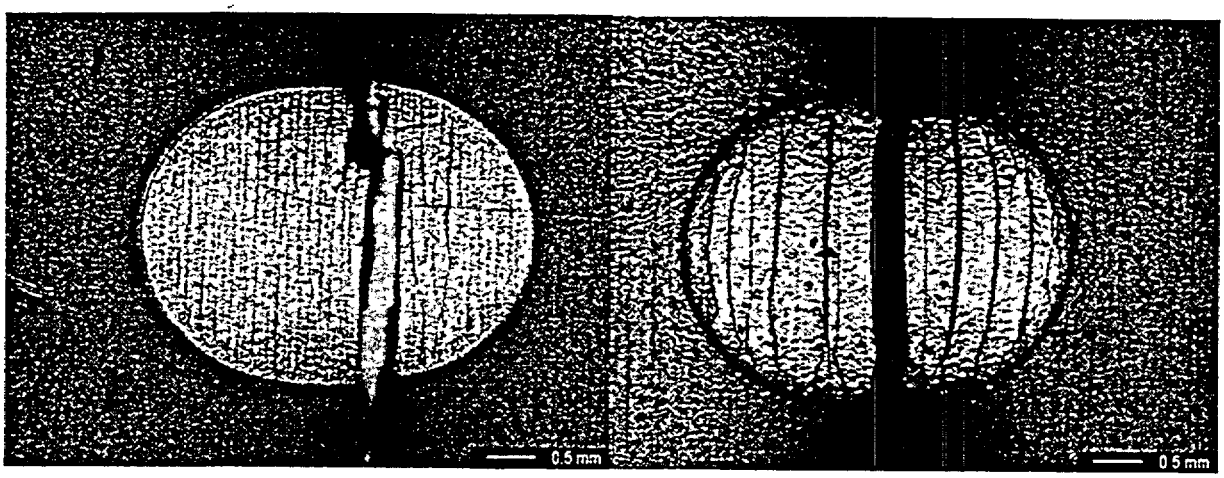

(a) (b)

Figure 8. Macrographs of cracked blisters in CWSR material failed at (a) 25^0C and with a 50 µm deep blister and (b) 300^0C with a 105 µm deep blister.

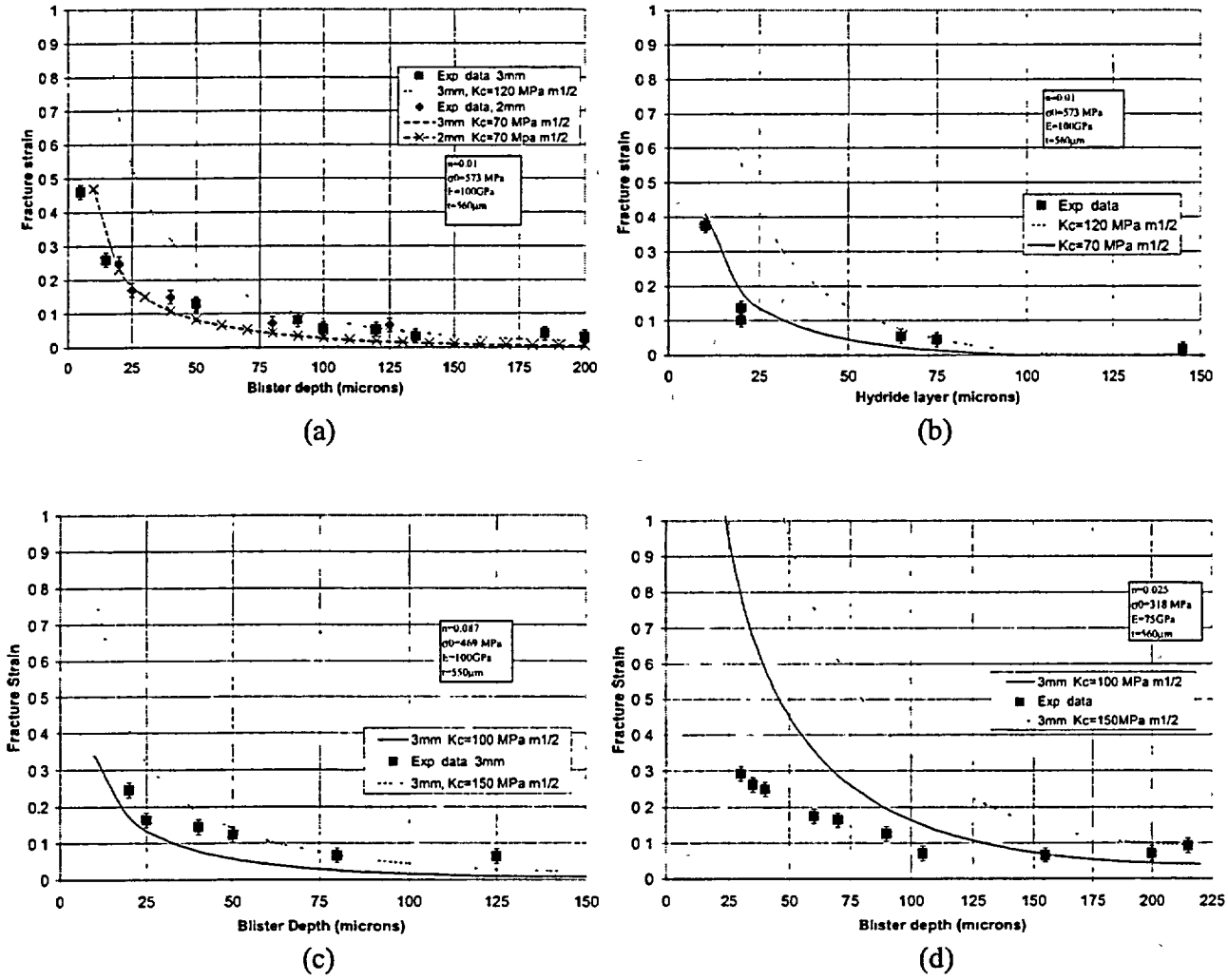

Figure 9. The dependence of observed and predicted fracture strain strains for (a) CWSR Zircaloy-4 with hydride blisters at 25^{0}C, (b) CWSR Zircaloy-4 with a hydride rim at 25^{0}C, (c) RX Zircaloy-4 with blisters at 25^{0}C, and (d) CWSR material with hydride blisters at 300^{0}C.

REFERENCES

[1] C. Lemaignan and A. T. Motta, "Zirconium in Nuclear Applications," in *Nuclear Materials*, vol. 10B, B.R.T.Frost, Ed. New York: VCH, 1994, pp. 1-52.

[2] A. M. Garde, G. P. Smith, and R. C. Pirek, in *11th International Symposium on Zr in the Nuclear Industry*, vol. STP 1295. American Society for Testing and Materials, West Conshohocken, PA, (2002) pp.407-430.

[3] C. E. Coleman and D. Hardie, *J. Less-Common Metals*, **2**, 1966, 168-185.

[4] C. E. Ells, *J. Nucl. Mater.*, **28**, 1968, 129-151.

[5] L. A. Simpson, *Metall. Trans.A,*, **12A**, 1981, 2113-2124.

[6] S. Yamanaka, M. Kuroda, D. Setoyama, M. Uno, K. Takeda, F. Nagase, and H. Uetsuka, *J. Alloys and Compounds*, **330-332**, 2002, 400-403.

[7] J. B. Bai, C. Prioul, and D. Francois, *Metall. and Mater. Trans.A*, **25A**, 1994, 1185-1197.

[8] F. Prat, M. Grange, J. Besson, and E. Andrieu, *Metall. and Mater. Trans.A,*, **29A**, 1998, 1643-1651.

[9] M. Grange, J. Besson, and E. Andrieu, *Metall. and Mater. Trans.A,*, **31A**, 2000, 679-690.

[10] M. Kuroda, K. Yoshioka, S.Yamanaka, H. Anada, F. Nagase, and H. Uetsuka, *J. Nucl. Sci. Tech.*, **37**, 2000, 670-675.

[11] M. Kuroda, S. Yamanaka, D. Setoyama, M. Uno, K. Takeda, H. Anada, F. Nagase, and H. Uetsuka, *J. Alloys Compounds*, **330-332**, 2002, 404-407.

[12] S. I. Hong, K. W. Lee, and K. T. Kim, *J. Nucl. Mater.*, **303**, 2002, 169-176.

[13] Daum, R. S., S. Majumdar, M. C. Billone, D. W. Bates*, D. A. Koss and A. T. Motta, 13th International Symp. on *Zirconium in the Nuclear Industry*, ASTM STP 1423, (2002) pp. 696-713.

[14] F. Yunchang and D. A. Koss, *Metallurgical Transactions A*, **16A**, 1985, 675-681.

[15] R. O. Meyer, R. K. McCardell, H. M. Chung, D. J. Diamond, and H. H. Scott, *Nuclear Safety*, **37**, 1996, 872-387.

[16] J. J. Kearns and C. R. Woods, *J. Nucl. Mater.*, **20**, 1966, 241.

[17] P. Delobelle, P. Robinet, P. Bouffioux, P. Greyer, and I. LePichon, 11th International Symposium on Zr in the Nuclear Industry, 1996; ASTM STP 1295; Garmisch-Partenkirchen, .373-393.

[18] E. Tenckhoff, *Deformation Mechanisms, Texture and Anisotropy in Zirconium and Zirconium Alloys*, vol. 966. Philadelphia: ASTM, 1988.

[19] O. N. Pierron, D. A. Koss, and A. T. Motta, *accepted for Journal of Nuclear Materials*, 2002.

[20] T. M. Link, "Failure of Zircaloy Cladding under Severe Loading Conditions," M.Sc. thesis; in *Materials*. Penn State University, University Park, PA; 1997.

[21] T. M. Link, D. A. Koss, and A. T. Motta, *Nuclear Engineering and Design*, **186**, 1998, 379-394.

[22] SCDAP/RELAP5/MOD2, *Code Manual volume 4: MATPRO: "A Library of Materials Properties for Light Water Reactors Accident Analysis", NUREG/CR-5273, EGG-2555, chapter 4.9.*, 1990.

[23] O. N. Pierron, "Influence of Hydride Blisters on Failure of Zircaloy-4 Sheet," M.Sc. thesis; in *Materials*. Penn State University, University Park; 2002.

[24] G. E. Fernandez and G. Meyer, *J. Nuc. Mater.*, **279**, 2000, 167.

[25] J. Bloch, I. Jacob, and M. H. Hintz, *Journal of Alloys and Compounds*, **191**, 1993, 179-186.

[26] Daum, R. S., S. Majumdar, H. Tsai, T. S. Bray, D. A. Koss, A. T. Motta and M. C. Billone, *Small Specimen Test Techniques: Fourth Volume*, ASTM STP 1418, M. A. Sokolov, J. D. Landes, and G. E. Lucas, Eds., American Society for Testing and Materials, West Conshohocken, PA, (2002) pp.195-210

[27] K. S. Chan, D. A. Koss, and A. K. Ghosh, *Metallurgical Transactions A*, **15A**, 1984, 323-329.

[28[O.N.Pierron, D.A.Koss, A.T.Motta and K.S.Chan, submitted to the J. of Nuclear Materials, 2002.

[29] V. Grigoriev, B. Josefsson, and B. Rosborg, 11th ASTM International Symposium on Zr in the Nuclear Industry, 1996; ASTM STP 1295; Garmisch-Partenkirchen, Germany, 431-447.

[30] F. H. Huang, *J. Nucl. Mater.*, **207**, 1993, 103-115.

[31] M. Kuroda, S. Yamanaka, F. Nagase, and H. Uetsuka, *Nucl. Eng. Des.*, **203**, 2001, 185.

[32] Asada, T., Kimoto, H., Chiba, N., and Kasai, Y., 9th Zirconium in the Nuclear Industry, ASTM STP 1132, C.M.Eucken and A.M.Garde eds., Philadelphia 1991, 99-118.

Thermal Creep of Dry-Cask-Stored Surry PWR Cladding

H. Tsai and M. C. Billone

Argonne National Laboratory
Argonne, Illinois 60439 U.S.A.

Abstract

Thermal creep tests of irradiated Zircaloy-4 cladding have been conducted under conditions relevant to spent-fuel dry-cask storage. The test samples were from medium burnup (≈36 GWd/MTU) Surry-2 Pressurized Water Reactor (PWR) fuel rods after having been stored in a dry cask for 15 years. Sample internal pressure loading was achieved with actively regulated argon gas. Five tests have been completed with hoop stress ranging from 190 to 250 MPa and temperature from 360 to 400°C. All samples were intact at the end of the prescribed test duration of ≈2000-3000 h. Two of them, C8 (220 MPa and 380°C) and C9 (190 MPa and 400°C), reached >1% creep strain at ≈2000 h. The stress level for C9 was subsequently increased from 190 to 250 MPa, resulting in a sharply increased creep rate. Significantly, the C9 sample remained intact with a creep strain of 5.8% at the end of the incremental ≈700 h. These results indicate the Surry-2 cladding retained substantial residual creep ductility after 15 years of dry-cask storage.

Introduction

Because of the limited storage capacity in spent-fuel pools, some spent-fuel assemblies have to be relocated into dry casks for interim storage until long-term geological repositories are available [1]. Some of the original licenses issued by the United States Nuclear Regulatory Commission (NRC) for 20 years of dry-cask storage of spent fuel up to 45 GWd/MTU burnup are coming up for renewal shortly.

Thermal creep of spent-fuel cladding is an important consideration in assessing the viability of extended dry-cask storage [2]. Upon discharge from the reactor, the fuel rod cladding can experience a significant hoop stress loading due to the rod's internal gas pressure. At elevated temperatures, the hoop stress may induce outward thermal creep of the cladding. The vacuum drying operation can elevate the cladding temperature to ≈400-500°C for many hours. Transfer and transport operations can also result in elevated temperatures for periods of minutes to hours. Once the spent fuel is dried and relocated in the storage cask, the temperature will decrease from initial storage temperatures of 300-400°C. Thermal creep of the cladding under these conditions may impact the fission product release within the cask and the integrity of the spent fuel rods during repository transfer operations following dry-cask storage.

The present work is related to an activity initiated by the U.S. Department of Energy (DOE) in the mid-1980s [3]. At that time, DOE procured a Castor-V/21 dry-storage cask for benchmarking computer codes by measuring the thermal and radiological characteristics of the cask. The cask was loaded with irradiated assemblies from the Surry-2 Nuclear Station and then tested in a series of configurations using a variety of cover gases, including vacuum. After the benchmark tests, the cask was

undisturbed for 15 years with the fuel in an essentially inert atmosphere (He/<1% air). Under the sponsorship of the U.S. NRC, the Electric Power Research Institute, and DOE-RW, twelve rods were retrieved from the cask for post-storage characterization. These twelve rods had the highest combined burnup and storage temperature among all the rods in the cask. Cladding from two of the rods was subsequently prepared for thermal creep testing described here. The burnup of the two fuel rods is ≈36 GWd/MTU.

In addition to generating creep rate data for predictive modeling, a key objective of the present effort is to evaluate residual creep ductility of the cladding after the 15-y dry-cask storage. A significant residual creep strain (>≈1%) would suggest that the rods may be suitable for further storage in the cask and may survive creep during transportation, reconsolidation and final repository conditions. As the Surry rods are not the limiting case for 45 GWd/MTU, demonstration of residual creep life can be used to argue that higher burnup rods with thicker oxide layers, higher hydrogen content and higher storage temperatures would also have survived 20 years of dry cask storage without creep failure.

Test Matrix

The test series consists of five tests, as shown in Table 1. The test conditions were selected to yield data on secondary (steady-state) creep rates after the primary-to-secondary creep transition. Three of the tests, with slightly more aggressive conditions, were aimed at demonstrating residual ductility of >~1% within the allocated test durations.

Table 1. Test Matrix for Post-Storage Thermal Creep Tests of Surry-2 Cladding

Test	Temp. (°C)	Hoop Stress (MPa)	Duration (h)	Objectives
C3	360	220	>≈2000	Secondary Creep Rate
C6	380	190	>≈2000	Secondary Creep Rate
C8	380	220	>≈2000	2nd Creep Rate and Creep Ductility
C9	400	190	≈2000	2nd Creep Rate and Creep Ductility
C9(1)	400	250	≈700	2nd Creep Rate and Creep Ductility

(1) Same sample but with the stress increased from 190 to 250 MPa.

Test Conduct

Thermal creep tests were performed with sections of defueled Surry-2 rod cladding internally pressurized with argon gas. Periodically, the samples were depressurized and removed from the furnace for diametral and length measurements. The measurements were made at room temperature with a precision laser profilometer. To inhibit possible hydride reorientation [4,5] in the cladding, the samples were depressurized first before cooling and removal from the furnace. Thus, each test consisted of multiple runs.

Test Samples

Test samples were prepared from two Surry-2 rods, H9 and G6, with identical design and comparable irradiation/storage histories [3]. The nominal outside diameter (OD) and wall thickness of the cladding were 10.72 and 0.62 mm, respectively. Each sample was a 76-mm-long defueled cladding specimen. Sample locations and the estimated oxide layer thickness and hydrogen content are shown in Table 2. The estimates were made by interpolation and extrapolation of measurement data from nearby sibling samples. All samples were from the flat-power region of the rods just above and below Grid Spacer No. 4.

Table 2. Surry Post-Storage Thermal Creep Samples

Sample	Source	Axial Location[1]	Oxide Thickness (μm)[2]	H content (wppm)[2]
C3	Rod H9	-38	23	230
C6	Rod H9	76	25	240
C8	Rod G6	254	23	260
C9	Rod H9	330	30	265

(1) mm above fuel column midplane measured from center of the sample.
(2) Estimated based on characterization data of sibling samples.

The samples were defueled by dissolution with nitric acid and cleansed with alcohol and water in an ultrasonic cleaner. To minimize the volume of pressurized gas in the systems, the inside of the samples was filled with slightly undersized Zr-702 pellets. The end fittings for the samples, made also of Zr-702, were attached by welding for improved hermeticity. Whereas the bottom end fitting was a solid plug, the top end fitting was a single machined piece with a thick-wall extension tube. The extension allowed the mechanical connection to the pressurization system to be made outside the furnace, also for improved hermeticity. To overcome the softening effect of welding, reinforcing hose clamps were applied to the welded ends.

Test Chambers

To mitigate sample oxidation and possible spread of loose contamination in case of a sample rupture, test chambers purged with high-purity argon gas were used. The test chambers were equipped with multiple thermocouples with hot junctions positioned near, but not touching, the sample. The thermocouples and the temperature recording systems were calibrated against standards traceable to National Institute of Standards and Technology (NIST) prior to the start of the tests.

Pressurization Systems

Five pressurization systems were constructed. Instead of the conventional pumps and accumulators, microprocessor-based pressure controller and regulators were used to maintain the sample pressure steady during the tests. This approach resulted in systems that are physically compact, as shown in Fig. 1. The pressure source was commercial cylinders capable of producing hoop stresses of ≈320 MPa max. in the Surry-2 cladding. Each system contained a solenoid valve, which, in case of a sample rupture, would close and isolate the sample from the pressure source. The pressure transducers and the

associated measurement and recording systems were calibrated against standards traceable to NIST prior to the tests.

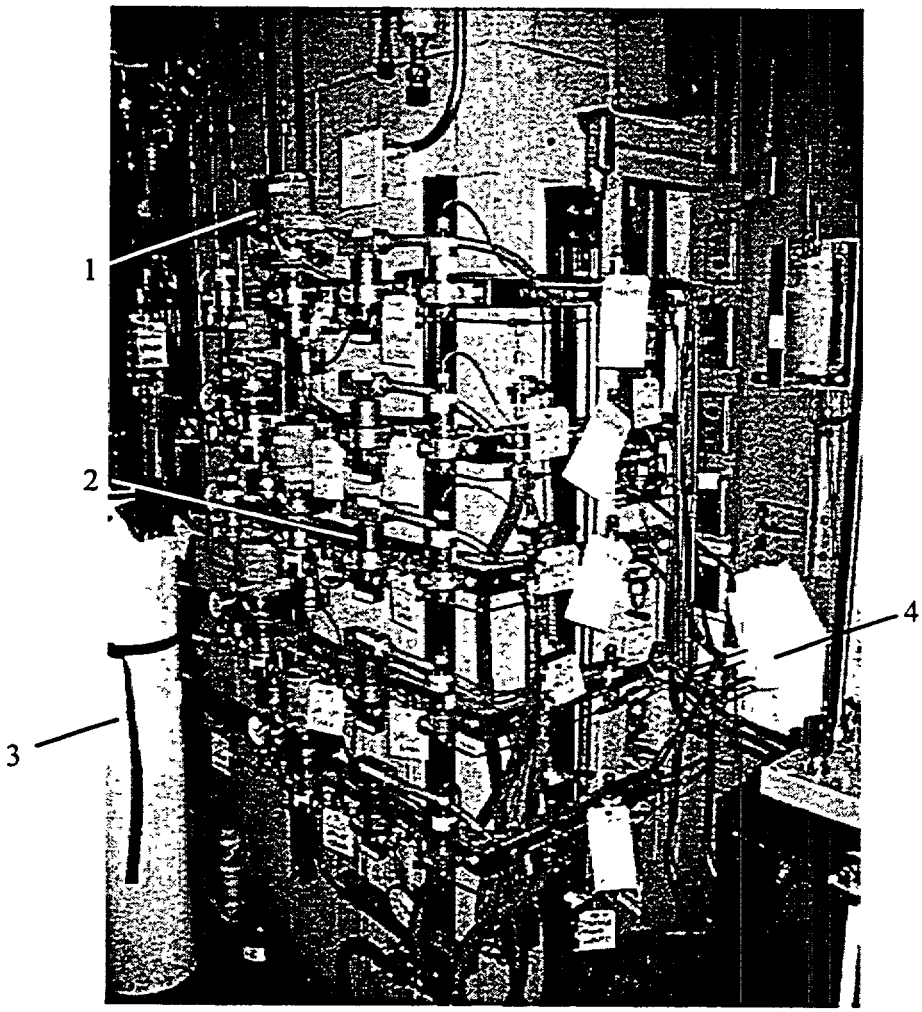

Fig. 1. Pressurization systems for the Surry-2 thermal creep tests. 1: pressure controllers/regulators; 2: solenoid valves; 3: pressure source (argon cylinders); 4: line penetrations into the hot cell.

Profilometry

A laser profilometer was used to measure the sample diameter and length before the test and after each run. The stage mechanism of the profilometer provided accurate rotational and linear positioning capability to allow repeated measurements of sample dimensions at the same locations after every run. The diametral measurement accuracy is $\approx 5 \times 10^{-4}$ mm, corresponding to a strain accuracy of $\approx 0.005\%$ for the Surry samples.

Sample diameters were measured every 9° azimuthal at 7.6-mm longitudinal intervals. The 19 azimuthal readings were averaged to yield the sample OD for that axial location. The ODs of the middle 5 axial locations were then averaged to yield the sample diameter for strain determinations. The length of the sample was measure by profiling the lower end plug from a fixed top-end reference position. A shifting of the profile would be an indication of sample length change.

Test Results

All samples were confirmed to be intact at the end of the tests. Summary pressure and temperature histories are shown in Table 3. Also shown are wall-average hoop strains at the end of the tests. (Accounting for the Surry-2 cladding geometry, wall-average hoop strain was determined to be 1.13 times the measured OD strain.) As described previously, for the C9 sample, there were two stress settings – the initial 1873 h was 190 MPa and the subsequent 693 h was 250 MPa. It should be noted that the reported hoop stresses are engineering stresses, not true stresses. No efforts were made during the tests to adjust the gas pressure to keep the hoop stress constant to account for wall thinning. Rather, the internal pressure was maintained constant over the entire test duration.

Table 3. Summary Test Conditions and Results

Sample	Time-Avg. Temp. (°C)		Time-Avg. Gas Pressure (MPa)		Time-Avg. Hoop Stress (MPa)		Test Duration (h)	Wall-avg. Hoop Strain (%)
	Actual	Target	Actual	Target	Actual	Target		
C3	360.4	360	27.99	28.06	219.4	220	3305	0.22
C6	381.0	380	24.28	24.23	190.4	190	2348	0.35
C8	381.0	380	28.09	28.06	220.2	220	2180	1.10
C9	399.6	400	24.20	24.23	189.8	190	1873	1.04
	399.5	400	31.80	31.88	249.4	250	693	5.83

Measured creep deformations as a function of time for the five tests are summarized in Fig. 2. All samples were in the secondary (steady-state) creep regime at the time of test termination. Calculated steady-state creep rates from the straight portion of the curves are shown in Table 4. The data suggests a strong temperature and pressure dependency of steady-state creep rates in the regime tested. For instance, a 20°C difference in the C3 and C8 tests resulted in a ten-fold difference in the creep rates. Likewise, a 30 MPa difference in the C6 and C8 tests resulted in a five-fold difference in creep rates.

Radial plots depicting the cross-sectional profiles of the samples were evaluated after every run. The data are useful to detect localized bulging, which may be a precursor of imminent burst rupture. All results indicate the deformation to be azimuthally uniform, even for the C9 sample with a hoop strain of 5.83% at the end of test. The C9 data are shown in Fig. 3.

There were no discernible sample length changes in any of the tests. These results suggest that the creep deformation was isotropic. Figure 4 shows the result for the C9 sample. The fact that the end-fitting diameter stayed unchanged before and after the test is also indicative that sample oxidation was negligible during the test.

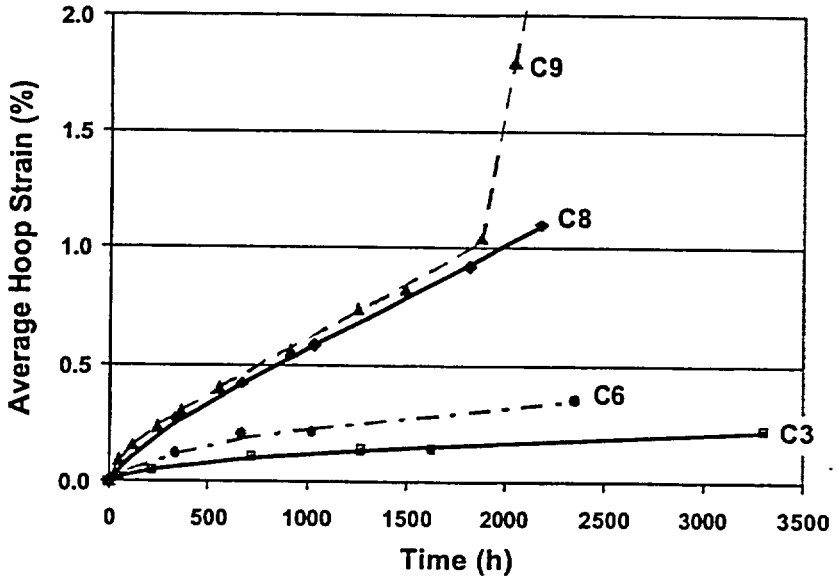

Fig. 2. Creep deformation histories for the Surry-2 tests. For the C9 test, the stress loading was increased from 190 to 250 MPa at 1873 h, resulting in the sharp change of the creep rate. Not shown in this chart is the hoop strain of 5.83% at the conclusion of C9 test at 2566 h.

Table 4. Secondary Creep Rates for Post-Storage Surry-2 Cladding

Sample	Nominal Temp. (°C)	Nominal Hoop Stress (MPa)	Secondary Creep Rate (%/h)
C3	360	220	4.2×10^{-5}
C6	380	190	8.8×10^{-5}
C8	380	220	4.5×10^{-4}
C9	400	190	4.9×10^{-4}
C9	400	250	$>4.9 \times 10^{-3}$

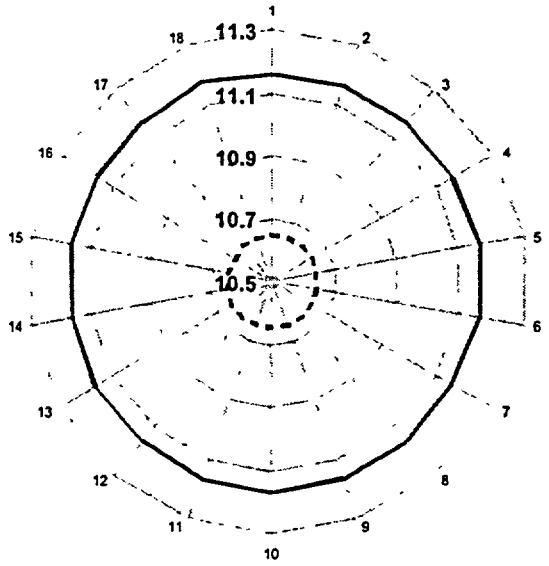

Fig. 3 Cross-section profiles of the C9 sample at the axial midplane before (dashed line) and after the test. The dimensional unit is mm.

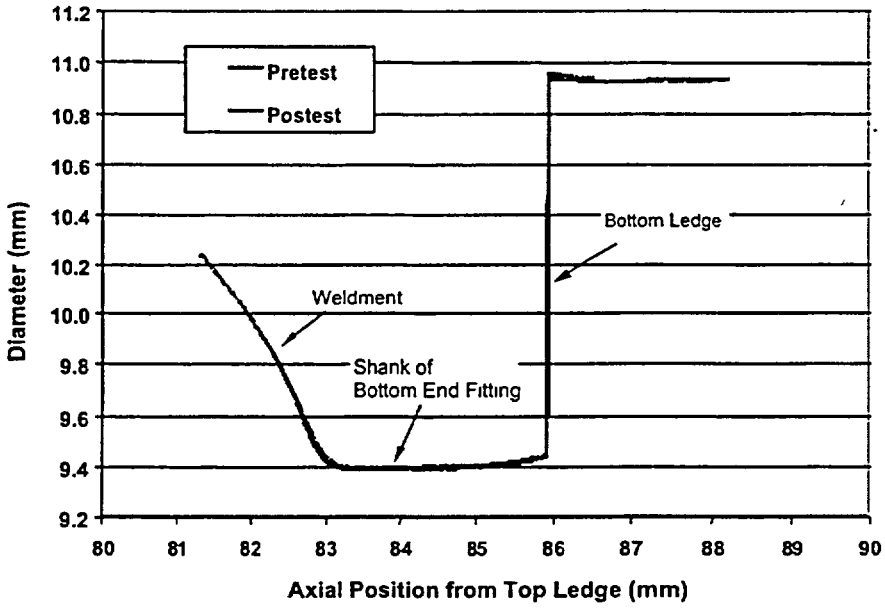

Fig. 4 Near-identical position of the lower end fitting of the C9 sample before and after the creep test (as measured from the top of the sample) indicates there was no change in the sample length.

Conclusions

Steady-state creep rate and residual ductility in temperature and hoop stress regimes of 360 – 400°C and 190 – 250 MPa, respectively, have been measured for post-storage Surry-2 PWR cladding. None of the samples ruptured in the tests. The Surry-2 cladding has residual creep strain >1% for thermal creep temperatures of 380°C (220 MPa) and 400°C (190 MPa). A residual strain of >5.8% was achieved in the 400°C sample after raising the stress level to 250 MPa for ≈700 h. Wall thinning undoubtedly contributed to the increased creep rate during the ≈700 h. Significantly, the deformation was uniform around the circumference of the cladding. No localized bulging, a precursor to burst rupture, was observed in this 250-MPa sample. Secondary creep rates spanning two orders of magnitude were measured in the five tests. The data, showing strong dependency to both temperature and stress, are valuable for code benchmarking and model improvement.

Acknowledgments

The authors sincerely appreciate the support provided by NRC, EPRI, and DOE-RW for the project. The authors would like to acknowledge Dr. B. Hilton and the excellent team at ANL-West for the nondestructive examination of the Surry fuel rods. Mr. A. McArthur, Mr. D. McGann and Mr. J. Dobrzynski of ANL-East contributed significantly to the conduct of the creep tests.

References

1. R. E. Einziger, et al. "Data Needs for Long-Term Dry Storage of LWR Fuel," EPRI Report 108757, April 1998.
2. US NRC Interim Staff Guideline ISG-11, Revision 1.
3. M. A. McKinnon and V. A. Deloach, 'Spent Nuclear Fuel Storage – Performance Tests and Demonstration," PNL-8451, Pacific Northwest Laboratory, 1993.
4. M. Leger and A. Donner, "The Effect of Stress on Orientation of Hydrides in Zircaloy Alloy Pressure Tube Materials," Canadian Metallurgical Quarterly 24, 235-243 (1985).
5. R. P. Marshall and M. R. Louthan, Jr., "Tensile Properties of Zircaloy with Oriented Hydrides," Trans. ASM, 56, 693 (1963).

DROP IMPACT ANALYSES OF SPENT FUEL DRY CASK STORAGE SYSTEMS

J.I. Braverman, R.J. Morante, J. Xu, C.H. Hofmayer
Brookhaven National Laboratory, Upton NY
S.K. Shaukat
United States Nuclear Regulatory Commission

ABSTRACT

A series of analyses were performed to assess the structural response of spent nuclear fuel dry casks subjected to various handling and storage related loading events. The results of these analyses are being used by the Nuclear Regulatory Commission (NRC) to perform a probabilistic risk assessment (PRA). Although the PRA study is being performed for a specific nuclear plant, the PRA study is also intended to provide a framework for a general methodology that could also be applied to other dry cask systems at different plant locations.

The dry cask system analyzed consists of a transfer cask, used for handling and moving the multi-purpose canister (MPC) that contains the fuel, and a storage cask, used to store the MPC and fuel on a concrete pad at the site. This paper describes the refined analyses of the dry casks for two loading events. The first loading consists of dropping the transfer cask in the reactor building while it is lowered by the crane to the concrete floor at ground elevation. The second loading consists of dropping the storage cask while it is being transferred from the reactor building to the concrete storage pad outdoors.

Three dimensional finite element models of the transfer cask and storage cask, containing the MPC and fuel, were utilized to perform the various drop analyses. These models were combined with finite element models of the target structures being impacted. The transfer cask drop analyses considered various drop heights for the cask impacting the reinforced concrete floor at ground level. The finite element model of the target included a section of the concrete floor and concrete wall supporting the floor. The storage cask drop analyses evaluated a 30.5 cm (12 in.) drop of the cask impacting three different roadway surfaces: reinforced concrete, asphalt, and gravel.

1 INTRODUCTION

The NRC is currently performing a probabilistic risk assessment (PRA) for storing spent nuclear fuel in dry casks at nuclear power plants. To support the PRA study, the structural response of a dry cask storage system subjected to various mechanical loads needs to be assessed. The loads requiring evaluation include accidental loading events resulting from the handling, on-site transfer, and on-site storage of the cask system, and the effects of natural phenomena such as wind, flood, and earthquake. In an effort to screen out some of the non-significant loading events, simplified analyses were performed. On the basis of these prior analyses, it was determined that more refined analyses were warranted for certain loading events in order to obtain more realistic results. This paper describes the refined analyses performed on a spent nuclear fuel transfer cask and storage cask, subjected to two loading events identified by the screening process.

2 PURPOSE

The purpose of this study is to perform nonlinear impact analyses of the Holtec International nuclear spent fuel cask system. The specific loading events analyzed were (1) a drop of the HI-TRAC transfer cask from various heights up to 30.5 m (100 ft) onto a concrete floor in the reactor building and (2) a 30.5 cm (1 ft) drop of the HI-STORM storage cask onto a concrete pad, asphalt surface, and gravel surface.

3 APPROACH

Existing computer models of the HI-TRAC transfer cask and HI-STORM storage cask, containing the sealed multi-purpose canister (MPC) and fuel, were utilized to perform the various drop analyses. These models were obtained from Holtec International and were combined with newly developed finite element models of the various targets. A number of different load cases were analyzed for the transfer cask drop and the storage cask drop accidents. For the transfer cask drop case, a vertical drop and horizontal drop of the HI-TRAC cask onto the concrete floor were evaluated. For the storage cask drop case, a vertical drop of the HI-STORM cask onto three types of surfaces (concrete, asphalt, and gravel) were evaluated.

The LS-DYNA computer code was used to perform the nonlinear impact analyses. LS-DYNA is a general purpose finite element code for analyzing the large deformation dynamic response of structures. The main solution methodology is based on explicit time integration. The program is particularly suited to analyze complex impact type problems. LS-DYNA is the same program utilized by HOLTEC in developing the HI-TRAC and HI-STORM cask models and used by HOLTEC to obtain NRC certification of the HI-STORM Cask System.

4 ANALYTICAL MODELS

4.1 HI-TRAC Transfer Cask Drop on a Concrete Floor

The HI-TRAC model used in this analytical study is the 125 ton HI-TRAC transfer cask, loaded with the MPC-68 full of fuel, and with the bottom transfer lid in place. The transfer cask outside diameter is 2.39 m (94 in.) and the height is 5.12 m (201 1/2 in.). The transfer cask, fully loaded with the MPC and fuel, weighs approximately 110,200 kg (243,000 lb). The cask is constructed using inner and outer cylindrical stainless steel shells, filled with lead shielding material in the annular space between the shells. The target that the cask impacts is a reinforced concrete floor supported by a wall beneath the floor. Due to symmetry in a vertical plane, a half model representation of the HI-TRAC cask containing the MPC and fuel, concrete floor, and concrete wall beneath the floor was developed. The concrete floor model dimensions are 3.96 m x 17.2 m x 0.61 m thick (156 in. x 678 in. x 24 in.). The concrete wall model is 13.1 m x 17.2 m x 0.381 m thick (516 in. x 678 in. x 15 in.). The concrete compressive strength is 29.0 MPa (4,200 psi). Appropriate boundary conditions were applied to the concrete floor and wall, to represent the support provided by the adjacent shear walls and foundation mat.

The HI-TRAC transfer cask model received from Holtec and utilized in this study represents the combined MPC/fuel as equivalent solid elements. The model does not include a separate shell for the MPC. Therefore, for the vertical end drop case, a series of vertical "truss elements" were added to represent the MPC shell. This provided a means of obtaining the vertical response of the MPC directly from the LS-DYNA analysis. Some additional modifications were made to the transfer cask model to improve the accuracy for the type of impact problem being analyzed.

The LS-DYNA model of the HI-TRAC cask and concrete floor/wall used for the vertical end drop case is shown in Figures 1 and 2. For the horizontal drop case, the same HI-TRAC cask model was utilized; however, the cask model was rotated ninety degrees.

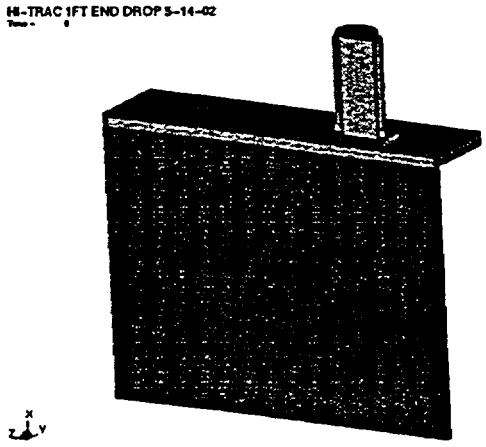

Figure 1 HI-TRAC Vertical End Drop Model With Concrete Floor/Wall

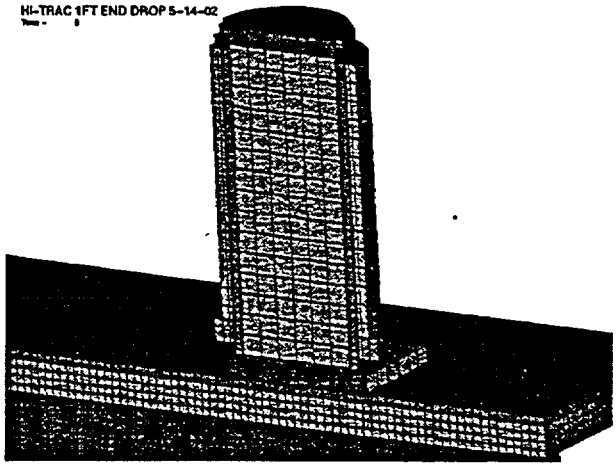

Figure 2 HI-TRAC Finite Element Model

The LS-DYNA model considered the various nonlinear effects important to this type of impact problem. In addition to large deformation capability, the analytical model included many contact surfaces between the various components, such as the fuel region to MPC bottom plate and the bottom transfer lid plate to the concrete floor surface. Material nonlinear behavior was represented using an elasto-plastic material with nonlinear stress-strain curves for the steel elements. For the solid brick concrete elements, a constitutive model with concrete damage and failure capability was used.

4.2 HI-STORM Storage Cask Drop on Concrete Pad, Asphalt, and Gravel

The HI-STORM model used in this analytical study is the HI-STORM 100 storage cask loaded with the MPC-68 full of fuel. The storage cask outside diameter is 3.37 m (132 1/2 in.) and the height is 5.87 m (231 in.). The storage cask, fully loaded with the MPC and fuel, weighs approximately 163,300 kg (360,000 lb). The cask is constructed using inner and outer cylindrical stainless steel shells, filled with concrete in the annular space between the shells. The three roadway surfaces that are modeled for the drop analyses are concrete, asphalt, and gravel. All of the surfaces rest on a soil sublayer. Due to symmetry in a vertical plane, a half model representation of the HI-STORM cask containing the MPC and fuel, roadway surface, and underlying soil was developed.

The LS-DYNA model of the HI-STORM cask, concrete pad, and soil used for the vertical drop case is shown in Figures 3 and 4. This model was also used for the other two cases: the vertical drop onto the asphalt layer and the vertical drop onto the gravel layer. However, the thickness of the pad, material model, and material properties were modified to represent the asphalt and gravel materials at the subject facility.

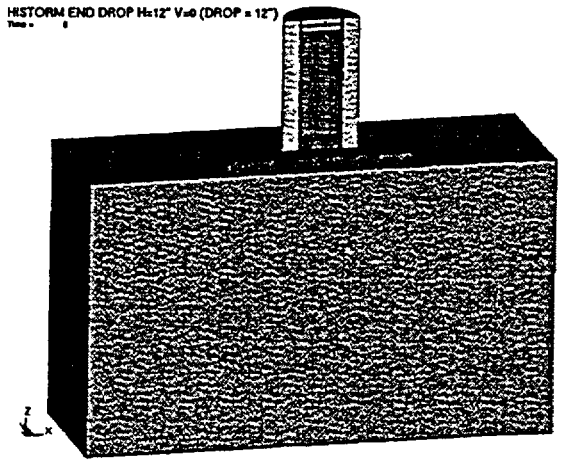

Figure 3 HI-STORM Model With Concrete Pad And Soil

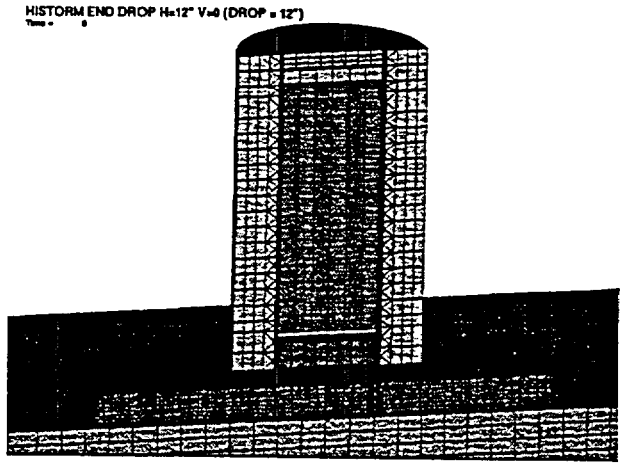

Figure 4 HI-STORM Finite Element Model

The LS-DYNA model for the HI-STORM storage cask drop analyses considered the various nonlinear effects described above for the HI-TRAC transfer drop model. The Mohr-Coulomb material model was utilized for asphalt and gravel, which can be defined by a friction angle and cohesion value.

5 CASES ANALYZED

5.1 Drop of HI-TRAC Transfer Cask

This case considers the drop of the HI-TRAC cask in the reactor building while it is lowered by the crane to the concrete floor at ground elevation. Various drop heights of the cask were considered up to 30.5 m (100 ft). The drop heights selected for analysis were 0.305 m, 7.62 m, 24.4 m, and 30.5 m (1, 25, 80, and 100 ft), which permits interpolation of the results at any other drop height. Two drop orientations were analyzed for the cask impact on the concrete floor; the cask in an upright position (vertical end drop) and the cask in a horizontal orientation.

5.2 HI-STORM Storage Cask Drop on Concrete Pad, Asphalt, and Gravel

The HI-STORM storage cask is transported from the reactor building to a reinforced concrete storage pad outdoors. Therefore, three accidental drop cases of the storage cask are analyzed corresponding to the three different surfaces that the transport vehicle travels over. A drop of the storage cask onto concrete, asphalt, and gravel surfaces is analyzed. For all three cases a drop height equal to 30.5 cm (12 in.) was utilized, which corresponds to the height the storage cask is held above the ground while it is being transported from the reactor building to the reinforced concrete storage pad.

5.2.1 Drop Onto Reinforced Concrete Storage Pad

For this case, a 30.5 cm (12 in.) vertical end drop of the storage cask impacting a 61 cm (24 in.) thick reinforced concrete pad, resting on soil was analyzed. Three analyses were performed corresponding to the lower bound, best estimate, and upper bound elastic soil moduli, which are equal to 324 MPa, 641 MPa, and 1,579 MPa (47 ksi, 93 ksi, and 229 ksi), respectively. Poison's ratio is equal to 0.4 and the soil density is 2,003 kg/m^3 (125 lbs/cubic ft).

5.2.2 Drop Onto Asphalt Surface

For this case, a 30.5 cm (12 in.) vertical end drop of the storage cask impacting a 30.5 cm (12 in.) thick layer of asphalt resting on soil was analyzed. Because asphalt material properties are sensitive to temperature, three loading cases were considered. The three cases correspond to material properties of asphalt at 4.4 °C, 23.9 °C, and 43.3 °C (40 °F, 75 °F, and 110 °F). This approximates the expected average temperature at the subject facility corresponding to winter, spring/fall, and summer.

The properties for the asphalt layer were determined from a literature review of available information for a "good" asphalt mix. The best estimate values for the elastic modulus of asphalt are 10,342 MPa at 4.4 °C (1,500 ksi at 40 °F), 4,482 MPa at 23.9 °C (650 ksi at 75 °F), and 1,379 MPa at 43.3 °C (200 ksi at 110 °F).

5.2.3 Drop Onto Gravel Surface

Two cases were evaluated for the storage cask drop on a gravel surface: a 30.5 cm (12 in.) thick gravel layer and a 61 cm (24 in.) thick gravel layer, both resting on soil. The 61 cm (24 in.) layer corresponds to the gravel region surrounding the concrete pad where the storage casks are stored, while the 30.5 cm (12 in.) layer corresponds to the gravel region away from the concrete pad where the gravel layer tapers to smaller thicknesses.

The properties for the gravel layer were determined from a literature review of available information on "well graded" crushed stone aggregate. The best estimate value of 345 MPa (50 ksi) for the elastic modulus would tend to be somewhat higher than what might be expected at the subject facility. This would be conservative because a higher modulus would result in higher impact forces and accelerations. To gauge the effect of varying the modulus of the gravel material, an analysis was performed for the best estimate value (345 MPa (50 ksi)) and for the upper bound estimate (689 MPa (100 ksi)) for the 30.5 cm (12 in.) thick gravel layer case.

6 ANALYTICAL RESULTS

The primary results of interest for the various drop cases analyzed are the maximum accelerations of the MPC and fuel, the maximum stresses/strains in the MPC, and relative deformations between the MPC and the HI-TRAC or the HI-STORM cask. It is acceptable for the HI-TRAC or HI-STORM casks to undergo permanent deformation, provided that the MPC maintains leaktight integrity.

The results presented in this paper are due to the cask impact forces, and thus do not include pressure or dead weight loads. The effects due to internal MPC pressure would be additive to the stresses and strains presented below for impact forces. For the vertical drop case, the internal positive pressure would reduce the vertical stresses and strains in the MPC shell. The

effects due to dead weight (1 g) acting downward would cause a negligible increase in the total response.

6.1 Drop of HI-TRAC Transfer Cask

6.1.1 Vertical End Drop Onto Concrete Floor

The structural response of the MPC for the vertical end drop of the HI-TRAC transfer cask onto the concrete floor is summarized in Table 1. For each drop height, the MPC maximum acceleration corresponding to the top of the MPC is presented. The maximum axial stress in the MPC is shown in the next column followed by the maximum axial strain. The maximum acceleration of the fuel is also provided.

Table 1. HI-TRAC Drop Analyses

HI-TRAC Drop Orientation	Drop Height (ft)	Multi- Purpose Canister (MPC)			Fuel
		Max Acceleration (g)	[1] Max Stress (ksi)	[1] Max Strain (%)	[2] Max Acceleration (g)
Vertical End Drop	1	56.9	7.47	0.03	38.8 x DLF[3]
	25	170	20.7	0.7	149 x DLF[3]
	80	177 8	21 8	1.6	190 x DLF[3]
	100	178.2	22 2	2.0	198 x DLF[3]
Horizontal Drop	1	37	> yield	0.47	37
	25	122	> yield	3	122
	80	230	> yield	3	230
	100	264	> yield	3	264

Note: 1 ft = 30.48 cm; 1 ksi = 6.895 MPa

1 Maximum stresses & strains:
For the end drop case - are based on maximum axial forces at the bottom of the MPC.
For the horizontal case - stresses are principal stresses and strains are effective plastic strain based on HI-TRAC inner shell.

2 Accelerations are based on combined MPC/fuel model.

3. All fuel accelerations must be multiplied by the appropriate dynamic load factor (a maximum of 1.52).

The maximum acceleration of the MPC is 56.9 g, 170 g, 177.8 g, and 178.2 g, corresponding to the 0.305 m, 7.62 m, 24.4 m, and 30.5 m (1, 25, 80, and 100 ft) drop heights. A representative plot of the MPC maximum acceleration time history for the 7.62 m (25 ft) drop height is presented in Figure 5. As expected, with increasing drop heights the acceleration increases; however, the relationship is nonlinear. This occurs because the structural properties of the MPC and other HI-TRAC members are nonlinear and some of these members deform into the plastic region. The MPC shell deformed into the plastic region at approximately the 7.62 m (25 ft) drop height. Once the MPC deforms into the plastic region, its acceleration will not increase significantly as the drop height is increased; however, the plastic strain will continue to increase.

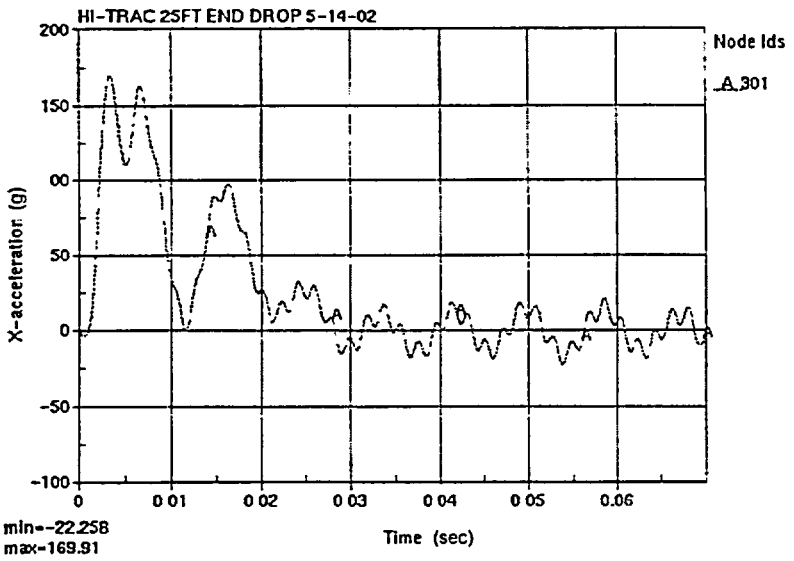

Figure 5 MPC Acceleration Time History - 7.62 m (25 Ft) Vertical Drop On Concrete Floor

The maximum axial stress in the MPC for the 0.305 m (1 ft) drop is 51.5 MPa (7.47 ksi). For this drop height the MPC remains in the elastic range of the material property. For drop heights of 7.62 m (25 ft) and more, the stresses rise above 143 MPa (20.7 ksi) which is slightly above the yield stress of the MPC shell (139 MPa (20.1 ksi) at 232 °C (450 °F)). Even though these stresses are above the yield of 139 MPa (20.1 ksi), the stresses are well below the ultimate stress value of 441 MPa (64.0 ksi) for the type of stainless steel material used for the MPC shell. A plot of the force time history for the 7.62 m (25 ft) drop height is presented in Figure 6.

The maximum total strain in the MPC shell is 0.03% for the 0.305 m (1 ft) drop and rises to 2.0% strain for the 30.5 m (100 ft) drop. The maximum strain of 2.0% is well below the 40% ultimate strain limit typical for the MPC stainless steel material.

The relative deformation between the HI-TRAC top lid and the top of the MPC was reviewed to ensure that there is no contact/impact between the HI-TRAC and the MPC. A review of the relative displacement, throughout the time history for the 30.5 m (100 ft) drop (worst) case, demonstrated that a gap is maintained, and therefore, the HI-TRAC top lid does not impact the top of the MPC.

For accelerations of the fuel, Table 1 provides the maximum vertical "rigid body" acceleration at various drop heights. However, these accelerations must be multiplied by a dynamic load factor (DLF) to account for the dynamic amplification within the fuel region. An upper bound estimate of the DLF, to be applied to the tabulated fuel accelerations in Table 1, is 1.52. This is based on the maximum DLF for a triangular load pulse, as documented in standard texts on structural dynamics (e.g., Biggs, 1964). The DLF of 1.52 is based on a one degree-of-freedom elastic response. If the fuel region is modeled more realistically in the future, the maximum acceleration can be obtained directly from the fuel finite elements. This would most probably reduce the maximum acceleration response of the fuel.

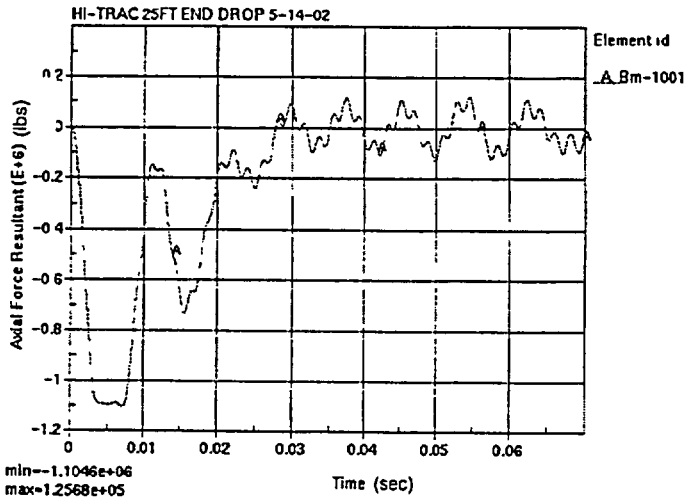

Figure 6 MPC Force Time History - 7.62 m (25 Ft) Vertical Drop On Concrete Floor

6.1.2 Horizontal Drop Onto the Concrete Floor

The structural response of the MPC for the horizontal drop of the HI-TRAC cask onto the concrete floor is also summarized in Table 1. For each drop height, the MPC/fuel maximum acceleration from the time history is presented. This acceleration corresponds to the maximum predicted acceleration obtained from the bottom, middle, or top of the MPC/fuel region.

As indicated in Table 1, the maximum acceleration of the MPC/fuel is 37 g, 122 g, 230 g, and 264 g, corresponding to the 0.305 m, 7.62 m, 24.4 m, and 30.5 m (1, 25, 80, and 100 ft) drop heights. A representative plot of the MPC maximum acceleration time history for the 7.62 m (25 ft) drop height is presented in Figure 7. As expected, with increasing drop heights the acceleration increases; however, the relationship is nonlinear. As in the vertical end drop case, this occurs because the structural properties of the MPC and other HI-TRAC members are nonlinear and some of these members deform into the plastic region.

As described earlier, the HI-TRAC model obtained from the cask vendor does not include the MPC as a separate discrete shell. To obtain an estimate of the stresses/strains in the MPC shell, the stresses and strains calculated in the HI-TRAC inner shell were utilized. This assumes that the maximum deformation of the MPC shell would correspond to the deformation of the HI-TRAC inner shell that supports the MPC.

From the LS-DYNA analysis, the maximum principal stress in the HI-TRAC inner shell was calculated to be somewhat higher than the yield point, indicating that some plastic deformation occurs. From the computer analysis, the maximum effective plastic strain in the HI-TRAC inner shell was calculated to be less than 3% for the worst case, which is well below ~40% strain limit for the HI-TRAC stainless steel material.

The deformation of the HI-TRAC inner shell relative to the MPC shell was reviewed. The maximum change in the diametrical dimension was determined at the top, bottom, and mid point along the height of the HI-TRAC inner shell. The maximum change in diametrical dimension is less than the nominal available gap. Thus, there is no permanent deformation that would cause the HI-TRAC inner shell to impinge the MPC shell.

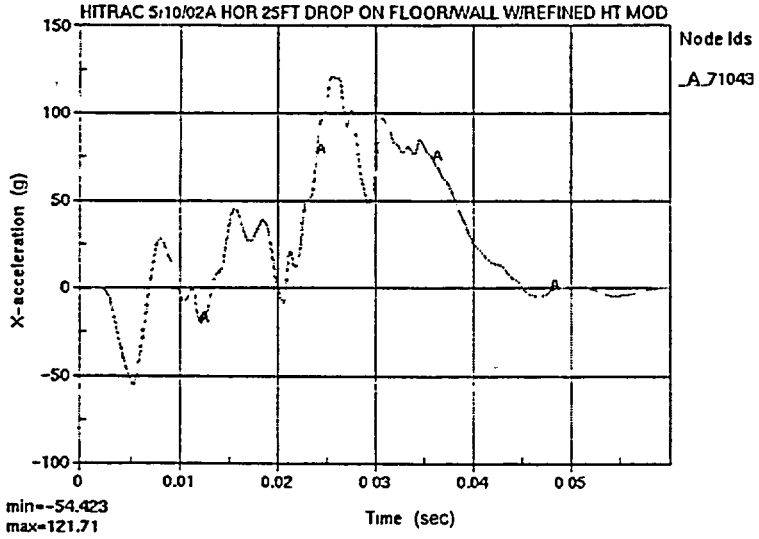

Figure 7 MPC Acceleration Time History – 7.62 m (25 ft) Horizontal Drop On Concrete Floor

6.2 HI-STORM Drop on Three Different Surfaces

6.2.1 Drop on Concrete Pad

The maximum acceleration values for the 30.5 cm (12 in.) drop of the HI-STORM cask system onto the 61 cm (24 in.) concrete pad resting on soil are shown in Table 2. The maximum acceleration at the bottom center of the HI-STORM cask is 41.2 g's for the best estimate soil property. The acceleration time history at this location is shown in Figure 8. The acceleration time history plot is initially flat at 1.0 g for a period of time because the HI-STORM cask was dropped from 30.5 cm (12 in.) height above the concrete pad and then impacted the pad at about 0.248 seconds. As shown in Table 2, the variation in soil property does not have a significant effect on the maximum acceleration of the cask for the configuration and parameters defined for this load case.

Since the MPC shell was not discretely modeled, the stresses in the MPC were calculated using the stresses determined by the cask vendor from previous calculations (HI-STORM 100 Cask System Topical Report, 1999) and scaling the results in proportion to the new calculated g values. Using this approach and the appropriate dynamic load factor, the stresses in the MPC shell were calculated to be - 53.3 MPa (- 7,732 psi). This stress value is well below the elastic buckling stress and yield for the MPC stainless steel material.

Table 2. HI-STORM Drop Analyses

Impact Surface	Thickness of Target Layer (in.)	Elastic Soil Modulus* (ksi)	Max Acceleration (g)	Comment
Concrete	24	47	40.4	Lower bound soil property
		93	41.2	Best estimate soil property
		229	44.5	Upper bound soil property
Asphalt	12	93	25.4	Best estimate asphalt property at 4.4 °C (40 °F) and best estimate soil property
		93	23.2	Best estimate asphalt property at 23.9 °C (75 °F) and best estimate soil property
		93	Bounded by 23.9 °C (75 °F) Case	Best estimate asphalt property at 43.3 °C (110 °F) and best estimate soil property
Gravel	24	93	21.9	Best estimate gravel property and soil property
	12	93	15.8	Best estimate gravel property and soil property
			19.0	Upper bound gravel property and best estimate soil property

Note: 1 in. = 2.54 cm; 1 ksi = 6.895 MPa

* Elastic soil modulus was based on the shear modulus calculated from the shear wave velocity of the free field

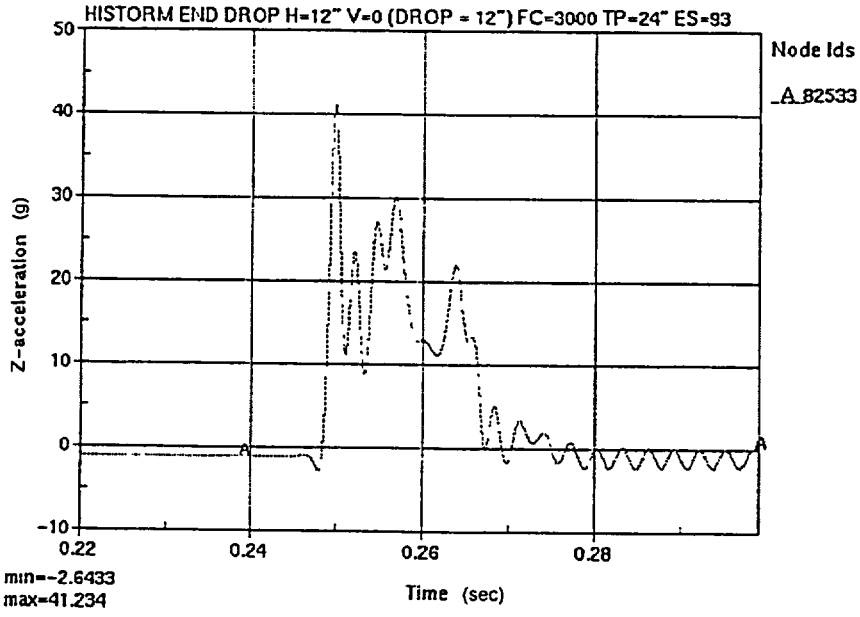

Figure 8 HI-STORM Acceleration Time History - 30.5 cm (12 in.) Vertical Drop On Concrete Pad

6.2.2 Drop on Asphalt Layer

Three basic cases were evaluated corresponding to material properties of asphalt at 4.4 °C, 23.9 °C, and 43.3 °C (40 °F, 75 °F, and 110 °F), which approximates the expected average temperature at the subject facility corresponding to winter, spring/fall, and summer. The maximum acceleration values for a 30.5 cm (12 in.) drop of the HI-STORM cask for the 4.4 °C and 23.9 °C (40 °F and 75 °F) are shown in Table 2. The 43.3 °C (110 °F) drop case was not analyzed because at this high temperature, the acceleration would be lower than the 23.9 °C (75 °F) case.

The maximum accelerations at the bottom center of the HI-STORM cask, for the best estimate asphalt property are 25.4 g's and 23.2 g's for the 4.4 °C and 23.9 °C (40 °F and 75 °F) cases, respectively. The acceleration time history for the 4.4 °C (40 °F) case is shown in Figure 9.

Since the MPC shell was not discretely modeled, the stresses in the MPC were calculated using the stresses determined by the cask vendor from previous calculations and scaling the results in proportion to the new calculated g values. Using this approach and the appropriate dynamic load factor, the vertical stresses in the MPC shell were calculated to be - 50.0 MPa (- 7,245 psi) and - 45.6 MPa (- 6,618 psi) for the 4.4 °C and 23.9 °C (40 °F and 75 °F) cases, respectively. Both of these stress values are well below the elastic buckling stress and yield for the MPC stainless steel material.

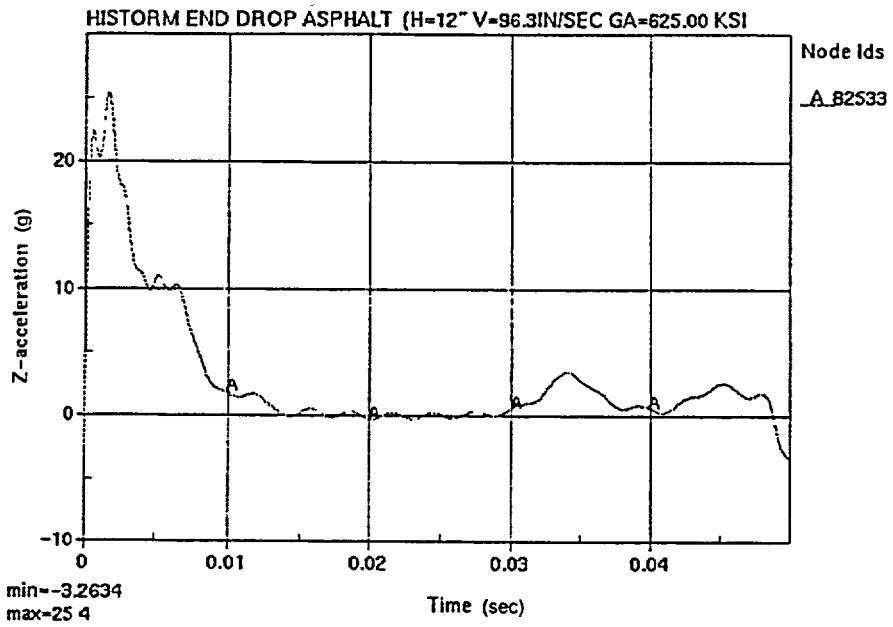

Figure 9 HI-STORM Acceleration Time History - 30.5 cm (12 in.) Vertical Drop On Asphalt at 4.4 °C (40 °F)

6.2.3 Drop on Gravel Layer

Two cases were analyzed corresponding to a 61 cm (24 in.) layer of gravel and a 30.5 cm (12 in.) layer of gravel. The maximum acceleration values for a 30.5 cm (12 in.) drop of the HI-STORM cask onto the 61 cm and 30.5 cm (24 in. and 12 in.) gravel layers are shown in Table 2.

The maximum accelerations at the bottom center of the HI-STORM cask, for the best estimate gravel property are 21.9 g's and 15.8 g's for the 61 cm and 30.5 cm (24 in. and 12 in.) gravel layer cases, respectively. As a measure of the sensitivity of the gravel material property, an upper bound case for the gravel property was performed for the 30.5 cm (12 in.) gravel layer. The maximum acceleration for this upper bound gravel property was 19.0 g's. The acceleration time history for this case (30.5 cm (12 in.), upper bound gravel property) is shown in Figure 10. This represents a 20% increase in acceleration from the best estimate gravel property.

The stresses in the MPC were calculated using the stresses determined by the cask vendor from previous calculations and scaling the results in proportion to the new calculated g values. Using this approach and the appropriate dynamic load factor the vertical stresses in the MPC shell, for the 30.5 cm (12 in.) drop case, were calculated to be - 39.7 MPa (- 5,754 psi) and - 28.6 MPa (- 4,151 psi) for the 61 cm (24 in.) and 30.5 cm. (12 in.) gravel layers, respectively. Both of these stress values are well below the elastic buckling stress and yield for the MPC stainless steel material.

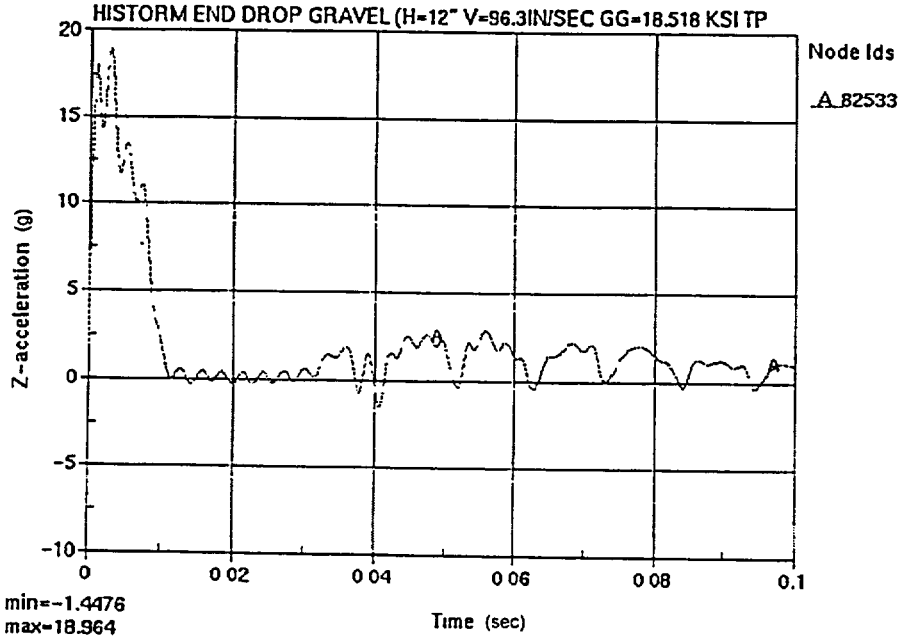

Figure 10 HI-STORM Acceleration Time History - 30.5 cm (12 in.) Vertical Drop On 30.5 cm (12 in.) Gravel Layer

7 CONCLUSIONS/RECOMMENDATIONS

This study evaluated the structural response of the HI-TRAC fuel transfer cask and the HI-STORM storage cask to various drop scenarios. The analyses for the HI-TRAC transfer cask considered vertical and horizontal drop cases onto a reinforced concrete floor due to drops at various heights. For the HI-STORM storage cask drop scenarios, analyses were performed for a 30.5 cm (12 in.) drop of the cask onto three different surfaces (concrete, gravel, and asphalt). The LS-DYNA analyses and the evaluations reported herein focus on the structural adequacy of the MPC shell and the fuel response.

7.1 HI-TRAC Drop Cases

The analyses for the HI-TRAC end drop onto the concrete floor provided maximum acceleration values for the MPC at 0.305 m, 7.62 m, 24.4 m, and 30.5 m (1, 25, 80, and 100 ft) drop heights. The results of the analyses demonstrate that for the 0.305 m (1 ft) drop, the vertical stresses in the MPC shell are in the elastic range (below yield) of the material. For the 7.62 m (25 ft) up to 30.5 m (100 ft) drop cases, the stresses in the MPC shell exceed yield but the strains are well below the ultimate strain value, and therefore, the materials will not rupture. In addition, the deformations between the HI-TRAC top lid and the MPC top lid remain within the available nominal gaps.

Although the MPC ultimate stress or strain values were not reached for any of these cases, a check on the buckling strength is recommended to determine whether it would govern the capacity of the MPC shell. Resistance to buckling is provided by the close proximity of the HI-TRAC inner shell, the fuel basket supports attached vertically to the MPC shell wall, and the fuel basket grid structure.

7.2 HI-STORM Drop Cases

The analyses for a 30.5 cm (12 in.) drop of the HI-STORM cask provided maximum acceleration values for impact on concrete, gravel, and asphalt surfaces. Stresses in the MPC were calculated using the stresses determined by the cask vendor from previous calculations and scaling the results in proportion to the new calculated g values.

For the HI-STORM drop onto the concrete floor, the maximum compressive stress in the MPC shell was calculated to be - 53.3 MPa (- 7,732 psi). For the HI-STORM drop onto the asphalt layer, three temperature conditions for the asphalt were considered. The maximum vertical stress in the MPC shell was calculated to be - 50.0 MPa for the 4.4 °C (- 7,245 psi for the 40 °F) governing case. The results for the HI-STORM drop onto gravel show that the maximum stresses are - 39.7 MPa (- 5,754 psi) and - 28.6 MPa (- 4,151 psi) for the 61 cm (24 in.) and 30.5 cm (12 in.) gravel layers, respectively. All of the calculated stresses are well below yield and below the elastic buckling stress. Therefore, it can be concluded that the MPC shell would not fail or rupture during the 30.5 cm (12 in.) drop onto all three surfaces.

7.3 RECOMMENDATIONS

As a result of performing the various analyses described in this report, a number of technical refinements have been identified which are recommended for future analyses. These technical refinements will improve the analytical models used for the dry casks, verify some of the assumptions made, determine the sensitivity to variation of key parameters, and obtain additional information that was not available from the existing analytical models. These refinements will also eliminate some of the conservatisms that were inherent in the existing analyses. Some of the refinements that are recommended in future studies are:

1) Refine the HI-TRAC finite element model to include the MPC vertical shell and top lid so that accelerations, stresses, and strains can be obtained directly from the MPC model rather than scaling prior results.
2) Refine the fuel model representation in the current HI-TRAC model to more accurately represent the fuel and fuel baskets.
3) Evaluate alternative concrete material models to determine whether alternative models would provide more accurate results. The current concrete material model utilized,

appears to be stiffer than expected, and therefore probably produces overly conservative results.

4) Perform analyses for an accidental drop of the HI-TRAC cask onto the HI-STORM cask resting on the concrete floor at ground level. This would require including the actual model of the HI-STORM cask in the existing HI-TRAC drop model shown in Figures 1 and 2.
5) Determine the vertical buckling strength of the MPC shell to confirm that it would not govern the capacity of the MPC.

8 REFERENCES

Biggs, J.M., "Introduction to Structural Dynamics," McGraw Hill Book, Company, New York, 1964.

LS-DYNA Computer Code and associated manuals, Version 960, March 2001, Livermore Software Technology Corporation.

Topical Safety Analysis Report for the Holtec International Storage and Transfer Operation Reinforced Concrete Module Cask System (HI-STORM 100 Cask System), NRC Docket No. 72-1014, Holtec Report HI-951312, Volumes I and II, Revision 8, June 25, 1999.

DISCLAIMER

Evaluation of Seismic Behavior of HI-STORM 100 Casks at Private Fuel Storage Facility[a]

V. K. Luk[1], D. A. Aube[1], S. K. Shaukat[2], I. P. Lam[3], and R. A. Dameron[4]

1) Sandia National Laboratories, Albuquerque, NM, USA
2) United States Nuclear Regulatory Commission, Washington, D.C., USA
3) Earth Mechanics, Inc., Fountain Valley, CA, USA
4) ANATECH Corporation, San Diego, CA, USA

Abstract

Sandia National Laboratories conducted a research project to develop a comprehensive methodology for the seismic evaluation of spent fuel dry cask storage systems for the Office of Nuclear Regulatory Research of the U.S. Nuclear Regulatory Commission (NRC). This paper documents the development of coupled finite element models and the analysis results to examine the seismic behavior of cylindrical HI-STORM 100 casks to be installed on concrete pads at the proposed Private Fuel Storage (PFS) Facility in the state of Utah. The ABAQUS / Explicit code was used to develop coupled models that consist of a cylindrical cask, a flexible concrete pad, soil-cement layers under and adjacent to pad, and an underlying soil foundation. Nonlinear contact elements were used at the interfaces of cask/pad, pad/soil-cement layer, and soil-cement layer/soil foundation in order to examine the dynamic and nonlinear behavior of the model including the soil-structure-interaction effects during a seismic event.

1. Introduction

The Spent Fuel Project Office (SFPO) in the Office of Nuclear Material Safety and Safeguards (NMSS) at the Nuclear Regulatory Commission (NRC) is involved in investigating technical issues concerning the dry storage and transportation of spent nuclear fuel. Sandia National Laboratories (SNL) was contracted by the Office of Nuclear Regulatory Research (RES) at the NRC for establishing criteria and review guidelines for the seismic behavior of dry cask storage systems (DCSS). The results of this research are expected to aid the NMSS staff in performing the safety review of licensing applications of DCSS.

One type of Independent Spent Fuel Storage Installations (ISFSI) licensed under 10 CFR Part 72 [1] consists of array(s) of freestanding storage casks resting on a concrete pad constructed on a natural sub-grade or engineered fill soil. In the safety review process of these cask systems, their seismically induced horizontal displacements and angular rotations must be quantified to determine whether casks will overturn or neighboring casks will collide during a seismic event. The research project focused on evaluating the seismic behavior of a freestanding DCSS by performing site-specific and parametric analyses in order to support the NRC in establishing seismic acceptance criteria and safety review guidelines for licensing applications of these storage systems.

[a] *This work is sponsored by the U.S. Nuclear Regulatory Commission Sandia is a multiprogram laboratory operated by Sandia Corporation, a Lockheed Martin Company, for the United States Department of Energy under Contract Number DE-AC04-94AL85000*

2. Background

The Private Fuel Storage (PFS), L.L.C. submitted an application to the NRC for a license to install cylindrical HI-STORM 100 casks on the Reservation of the Skull Valley Band of Goshute Indians, a federally recognized Indian Tribe [2]. Sandia National Laboratories was tasked to conduct a research project to pursue the following objectives:

1. To investigate the dynamic responses of freestanding cylindrical HI-STORM 100 casks subjected to a prescribed site-specific seismic excitation through:
   a) Developing a coupled finite element model consisting of a cylindrical cask, a concrete pad, soil-cement layers under and adjacent to pad, and an underlying soil foundation,
   b) Applying sets of properly prescribed seismic time histories to the coupled model, and
   c) Applying appropriately selected material properties to the submodels and physical parameters at their interfaces.
2. To provide support to the NRC in revising the Regulatory Guidelines for the dry cask storage systems.

The NMSS staff provided the project team with the basic information on cask design, pad dimensions, soil-cement layers under and adjacent to the pad, site-specific soil profile, and time histories of seismic accelerations. Two sets of seismic excitations specific to the PFS site were considered in the seismic analyses of PFS casks using seismic input time-histories, based on a 2,000-year and a 10,000-year return period. A sensitivity analysis was also performed using the 1971 San Fernando Earthquake, Pacoima Dam record [3]. Each set has one vertical and two horizontal components of statistically independent seismic accelerations. In each case of seismic excitations, a deconvolution procedure was used to adjust the amplitudes and frequency contents of the surface defined accelerations before applying them simultaneously at the base of soil foundation in the coupled model.

The coupled model has three interfaces at cask/pad, pad/soil-cement layer, and soil-cement layer/soil foundation. Different combinations of coefficients of friction were used at these interfaces. According to the analysis results on rectangular and cylindrical casks obtained by Luk, et al [4 and 5], the cask usually experiences higher sliding displacements with a lower coefficient of friction at the cask/pad interface and higher angular rotations with respect to the vertical axis for a higher coefficient of friction. A lower bound coefficient of friction of 0.20 (for investigating cask sliding) and an upper bound coefficient of friction of 0.80 (for examining cask tipping-over) were used at the cask/pad interface. Coefficients of friction of 1.00 and 0.31 were also assumed at the other two interfaces. Three sets of soil profile data (the best estimate, the lower bound and the upper bound) were used separately in seismic analyses of PFS casks.

3. Finite Element Analysis Modeling Approach

A coupled 3D finite element model was developed to investigate the dynamic response of freestanding Holtec HI-STORM 100 casks subjected to prescribed seismic excitations. The coupled model consists of a cylindrical cask, a flexible concrete pad, soil-cement layers under and adjacent to pad, and an underlying soil foundation. The analysis results from the model address the dynamic coupling among these structural subsystems, in particular, the soil-structure-interaction effects.

The analysts and engineers at SNL, Earth Mechanics, and ANATECH worked jointly in developing the coupled model. The model development effort involved two separate investigations. The first one focused on defining the material properties and investigating the size of soil foundation submodel, which was calibrated by exercising the 1D SHAKE [6] and 2D DYNA-FLOW [7] simulations. The second one was to address the dynamic and nonlinear response of the cylindrical cask in terms of its wobbling and sliding by examining closely the nonlinear contact behavior at the cask/pad, pad/soil-cement layer, and soil-cement layer/soil foundation interfaces in the coupled model.

There are many factors influencing the dynamic response of casks in an earthquake event. This project focused on performing sensitivity studies on the cask response with three key factors. They are: 1) prescribed seismic loading, 2) coefficients of friction at the interfaces in the coupled model, and 3) soil profile data.

A total of three sets of seismic loading were used as input excitations to the coupled model. A prescribed time history of seismic accelerations with a duration of 30 seconds, which is based on the design basis response spectra of the PFS site for a 2,000-year return period, was used to generate the design basis response of the cask [2]. A similar site-specific time history of seismic accelerations for a 10,000-year return period was used to provide a limiting case assessment of cask response. A sensitivity study was also performed using the 1971 San Fernando Earthquake, Pacoima Dam record [3], which is an actual earthquake record. Each set of seismic loading has one vertical and two horizontal components of statistically independent accelerations. Each one of the three seismic acceleration components was treated with a deconvolution procedure to produce a modified time history of deconvoluted accelerations with properly adjusted frequencies and magnitudes. All three components of deconvoluted accelerations were applied simultaneously at the base of soil foundation in the coupled model. The concept of deconvolution is a mathematically rigorous solution process that applies the wave propagation equation of the free-field surface along with the boundary conditions. It has been proven that the solution would be unique and rigorously correct for a linear representation of the soil mass (that is, linear shear modulus and viscous damping model). Idriss and Seed [8] and Schnabel, et al. [9] provided detailed discussions on the deconvolution procedure.

The coupled model has three interfaces at cask/pad, pad/soil-cement layer, and soil-cement layer/soil foundation. Different combinations with upper and lower bound coefficients of friction were used at these interfaces in search of governing cases for maximum horizontal sliding displacement or angular rotation of the cask. A lower bound coefficient of friction of 0.20 (for investigating cask sliding) and an upper bound coefficient of friction of 0.80 (for examining cask tipping-over) were used at the steel-to-concrete cask/pad interface. Bounding coefficients of friction of 1.00 and 0.31 were also assumed at the other two interfaces.

There are three sets of soil profile data (the best estimate, the lower bound and the upper bound) for the PFS site. Each set of soil profile data was used separately in the seismic analyses of PFS casks. Different soil profile data were used for the seismic events with 2,000-year and 10,000-year return periods and the 1971 San Fernando Earthquake, Pacoima Dam record. For the seismic event with the 10,000-year return period, the shear modulus and damping of each layer of the soil foundation are adjusted for shear strains while for the seismic events with the 2,000-year return period the low strain shear modulus and damping were used.

3.1 Description of Analysis Model

The three-dimensional coupled models were developed using the ABAQUS / Explicit code, Version 5-8.19 [10]. The layout of the entire model is shown in Figure 1. The directional views of the model in three orthogonal axes are illustrated in Figures 2, 3, and 4, respectively. The coupled model consists of a HI-STORM 100 overpack cask with MPC-68 option freestanding on a full-sized concrete pad that is designed to hold 8 (2x4) casks, as shown in Figure 5. There is a shallow layer of compact aggregate and soil-cement, acting as a passive constraint, adjacent to the concrete pad. This shallow surface layer and the concrete pad are placed on a continuous soil-cement layer that is on top of the soil foundation. Figure 6 shows a detailed surface layout above the soil foundation.

All elements of the coupled model are of the type "C3D8R", which is a three-dimensional continuum/solid of 8-nodes, with reduced (one Gauss point) integration and built-in hourglass control. The cask is modeled as a solid cylindrical body partitioned into four horizontal sections with six radial rows of solid elements in each section and 64 elements around the outside perimeter. The density of solid elements in each horizontal section is calculated and distributed in such a manner that the center of gravity of the cask is located at the correct design position. The cask, the concrete pad, the compacted aggregate, and the soil-cement layers are modeled as elastic bodies.

In the coupled model, contact elements are used at the three interfaces of cask/pad, pad/soil-cement layer, and soil-cement layer/soil foundation. At the two top interfaces involving the pad, the pad surface is designated as the "master' surface and the "slave" option is assigned to its interacting partner. At the third interface, the underside of the soil-cement layer is designated as the "slave" surface and the top of the soil foundation as the "master" surface. Different combinations of upper bound and lower bound interfacial coefficients of friction were selected in the seismic analyses of casks to search for the governing cases of maximum horizontal sliding displacement or angular rotation of casks.

In order to simulate semi-infinite boundary conditions, the outside layer of elements on the four vertical sides of soil foundation submodel are represented by edge columns that allow only horizontal shear deformation. The input motion of deconvoluted seismic accelerations is applied to all nodes at the base of soil foundation submodel.

Figure 1. The layout of entire 3D coupled model at PFS Facility

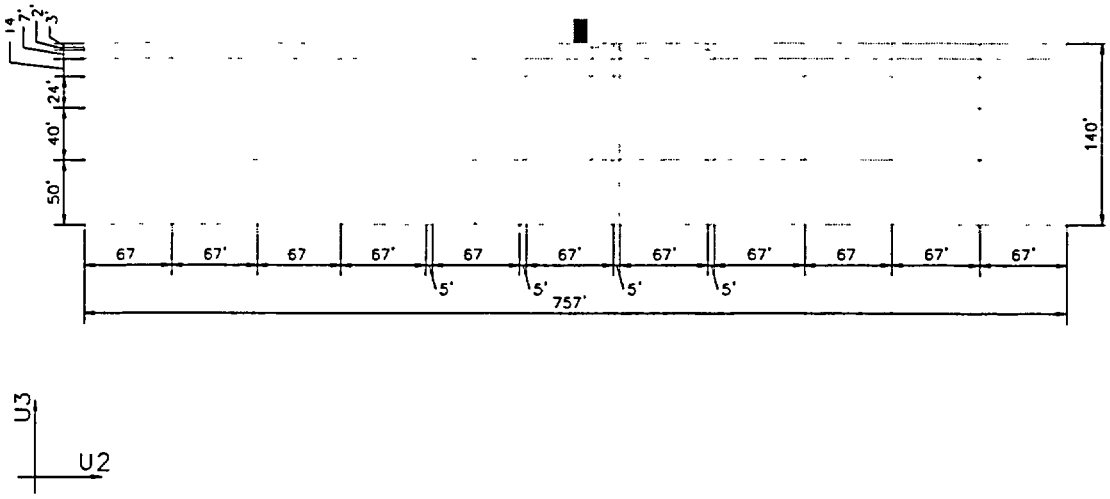

Figure 2. Model layout viewed in U1 direction

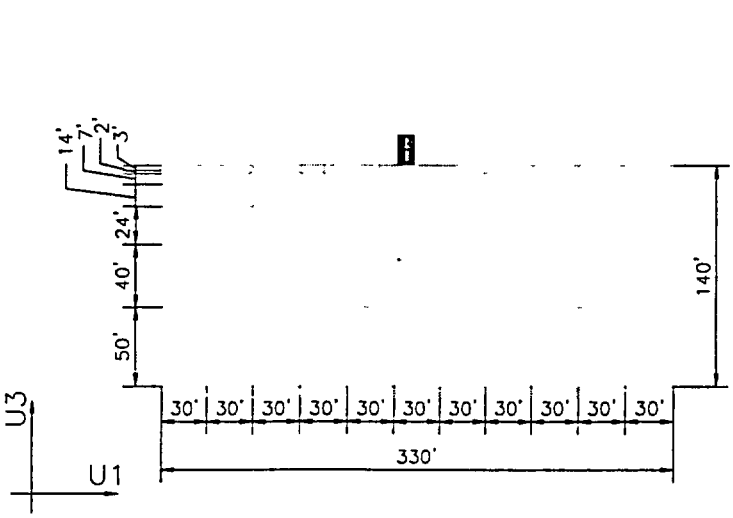

Figure 3. Model layout viewed in U2 direction

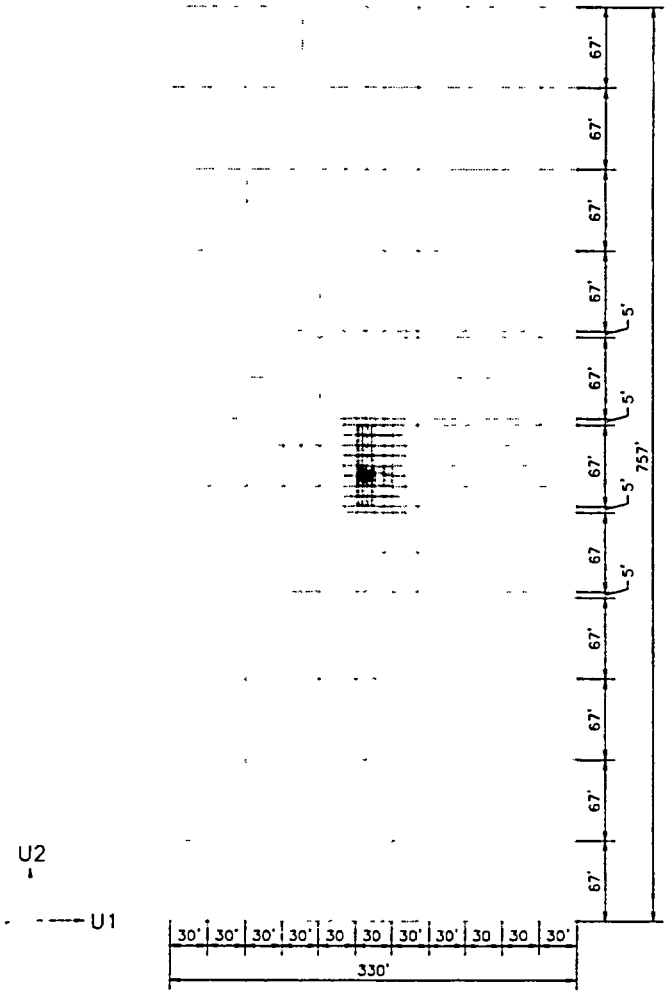

Figure 4. Model layout viewed in U3 direction (plan view)

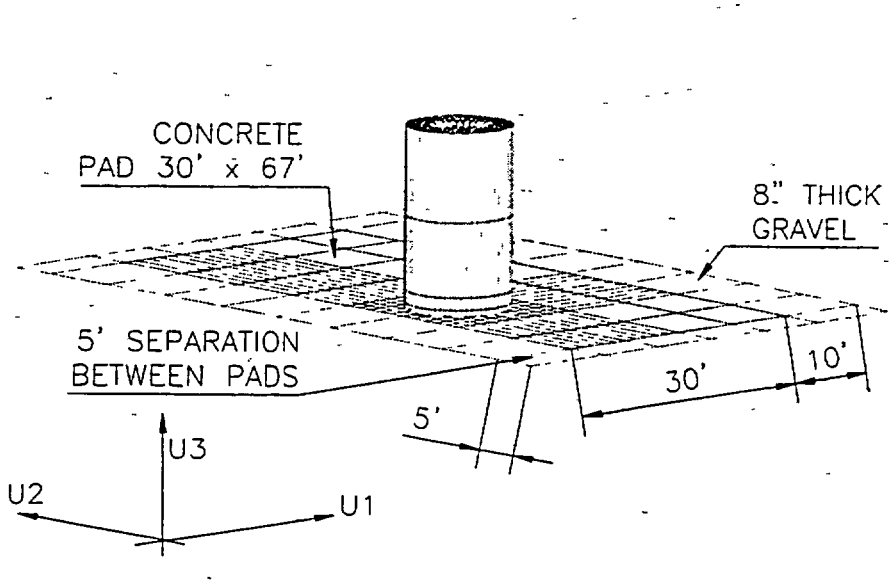

Figure 5. A cylindrical HI-STORM 100 cask on a full-sized concrete pad

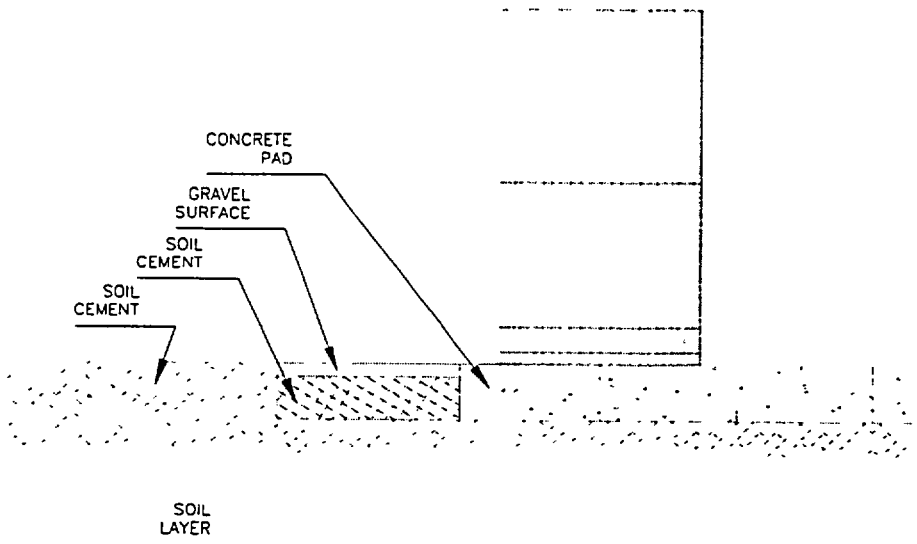

Figure 6. A detailed surface layout above soil foundation

3.2 Model Details

The coupled model consists of four structural components: a single cylindrical HI-STORM 100 cask, a flexible full-sized concrete pad, soil-cement layers under and adjacent to the pad, and a soil foundation. The modeling details of each submodel are described in the following subsections.

3.2.1 Cask Submodel

The HI-STORM 100 overpack casks with MPC-68 option were used at the PFS Facility. The cask geometry has an outside diameter of 132.5 inches and a height of 231.25 inches. The center of gravity of cask is 118.38 inches above pad. An overpack cask with fully loaded MPC-68 weighs 360,000 lbs.

3.2.2 Concrete Pad Submodel

A continuous concrete pad (30' x 67' x 3') holding 2x4 HI-STORM 100 casks was designed for the PFS Facility. This full-sized pad was used in the coupled model.

3.2.3 Soil-cement Layers and Compact Aggregate

There is a shallow layer of compact aggregate (8") and soil-cement (2'-4"), acting as a passive constraint, adjacent to the concrete pad. The compact aggregate layer, which was only used in a narrow band around the concrete pad, is 10' and 5' wide in U1 and U2 directions, respectively (see Figure 5). This surface layer and the concrete pad are placed on a continuous soil-cement layer of 2' that is on top of the soil foundation.

3.2.4 Soil Foundation Submodel

The size of soil foundation submodel plays an important role in assessing the soil-structure-interaction (SSI) effect. Sensitivity studies on the submodel size were performed to demonstrate that its chosen model size could simulate the behavior of a semi-infinite soil foundation underneath the 2' thick soil-cement layer. The lateral dimensions of the soil foundation submodel are finalized as 330' in U1 direction and 757' in U2 direction (see Figure 4), which are either equal or slightly larger than eleven times the pad size in the corresponding directions. It should be noted that the outside layer of elements on the four vertical sides of soil foundation submodel, with widths equal to the pad dimensions, are represented by edge columns that allow horizontal shear deformation only in order to simulate semi-infinite boundary conditions. This model configuration indicates that the nodes at the inner row of the set of edge columns define the true model size with their degrees of freedom constrained to those at the outside row. Therefore, the actual geometry of the soil foundation submodel is only nine times (or slightly larger) the pad dimension. This selection of the lateral dimension of soil foundation submodel exceeded the recommended minimum as defined by the US Corps of Engineers soil-structure-interaction modeling guidelines [11].

In addition, a depth of 140', which was partitioned into six horizontal layers as shown in Figure 2, was selected for the soil foundation submodel. The 140' depth was chosen to reach a level below that the soil stiffness increases monotonically with depth. In addition, it was also based on satisfying the guidelines in American Society of Civil Engineers (ASCE) Standard [12]. In the

close vicinity of the concrete pad, the top surface is further divided into compact aggregate and soil-cement layer, as illustrated in Figure 6.

3.3 Material Properties of Cask and Pad

The cask and the concrete pad are assumed to behave elastically when subjected to seismic excitations. Therefore, their elastic material properties were chosen in the model as shown in Table 1. The cask and pad moduli are based on assumed concrete strengths of 5,000 psi and 4,000 psi, respectively. The cask and pad are modeled as elastic bodies with zero damping.

Table 1. Elastic material properties of cask and pad

Structural Element	Young's Modulus, E (psi) (x 10^6)	Poisson's Ratio, ν	Density, ρ (lb-s^2/in.^{4})
Cask	4.0305	0.2	0.000318496 (Section 4)*
			0.000243043 (Section 3)*
			0.000243043 (Section 2)*
			0.000599072 (Section 1)*
Pad	3.6050	0.2	0.00022465

* Geometry definition of horizontal sections of the cask:

Section 1: from cask base to 8" above base
Section 2: from 8" above base to 24" above base
Section 3: from 24" above base to 118.38" above base
Section 4: from 118.38" above base to cask top

3.4 Soil Foundation

The site-specific soil profile data at the PFS Facility are categorized in terms of best estimate, lower bound and upper bound to provide a broad range of variation. For each set of soil profile data, the soil foundation was partitioned into thirteen horizontal layers to a depth of 700 feet. In the 3D coupled model, it was decided to use six horizontal layers to a depth of 140 feet to represent the soil foundation. Sensitivity studies were performed to demonstrate the adequacy of using this discretization scheme to incorporate the depth variation of soil properties such as shear wave velocity and damping profiles in the soil foundation submodel.

The same soil profile data (best estimate, lower bound and upper bound) were used in performing the cask analyses for the seismic event with a 2,000-year return period and the 1971 San Fernando Earthquake, Pacoima Dam record. However, different soil profile data were used for the seismic event with a 10,000-year return period in which the shear modulus and damping factor of the soil foundation are dependent on its shear strains.

3.4.1 Soil Material Properties

The 140-foot depth of the soil foundation was partitioned into six horizontal layers. With these graduations, the best estimate, the lower bound, and the upper bound strain-compatible soil properties for different seismic events were averaged for each horizontal layer. Damping is one

of the key soil material properties. The damping ratio (%) is the material damping from free field site response analyses using the SHAKE program [9] reflecting the strain dependent soil property for the specific soil layer. These damping ratios were then used to represent the target damping value for the 3D coupled model solutions using the ABAQUS code [10], which utilizes the classical Rayleigh damping algorithm. Only the mass proportional damping response was implemented in the coupled analyses. The mass related damping parameters were chosen such that the resultant damping matches the tabulated target damping value at the overall fundamental period of the soil foundation model. The stiffness proportional damping terms were not implemented (i.e. set to zero) to avoid very severe computational penalty associated with developing the very large stiffness matrix in the 3-D coupled model. This limitation, which is regarded as conservative, tends to over predict the high frequency response of the soil/pad/cask system. The project team conducted some sensitivity studies using smaller 2-D models to evaluate potential errors introduced in the one parameter Rayleigh damping approach and found that the approach provides reasonable solutions.

3.5 Seismic Input at Base of Soil Foundation

Three sets of seismic loading were used as input excitations to the coupled model in performing dynamic analyses of casks. A seismic event with a duration of 30 seconds, which is based on the response spectra specific to the PFS site for a 2,000-year return period, was used to generate the design basis response of casks. This seismic event is prescribed by one vertical component and two horizontal components of statistically independent accelerations. The three components of peak ground accelerations are 0.728 g (horizontal, east - west), 0.707 g (horizontal, north - south), and 0.721 g (vertical) [2]. The original time histories of seismic accelerations for this event provided by the NRC are shown in part (a) of Figures 7-9.

A sensitivity study on the cask response was also performed using the 1971 San Fernando Earthquake, Pacoima Dam record whose time histories of the three components of accelerations are shown in part (a) of Figures 10-12. The peak ground accelerations for the two horizontal components are 0.641 g and that for the vertical component is 0.433 g [3]. The earthquake record indicates that there are very low levels of seismic excitations after the first 20 seconds of this 41.8-second event, therefore the time histories of the first 20 seconds only are plotted in these figures and used in the dynamic analyses.

A similar site-specific time history of seismic accelerations for a 10,000-year return period was used to provide an upper bound assessment of cask response. The peak ground accelerations for the three components, which envelop the PFS earthquake hazard spectra [2], are 1.25 g (horizontal, east - west), 1.23 g (horizontal, north - south), and 1.33 g (vertical). Part (a) of Figures 13-15 shows the original time histories of seismic accelerations for this event that were provided by the NRC.

In every set of seismic loading, each one of the three acceleration components was treated with a deconvolution procedure to produce a modified time history of deconvoluted accelerations with properly adjusted frequencies and magnitudes. The net outcome is that when all three components of deconvoluted accelerations are applied simultaneously at the base of soil foundation in the coupled model, the dynamic characteristics of the original seismic motions is preserved and the desired surface shaking intensity can be achieved. The deconvoluted accelerations for the three seismic events, which were used in the analyses, are shown in part (b) of Figures 7-15. The analysis results of the free-field surface accelerations, which are plotted in part (c) of these figures, indicated that they are very similar to the original seismic surface accelerations.

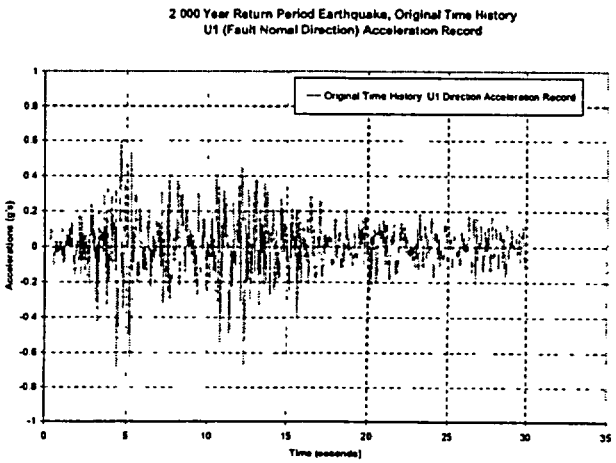

(a) Original time histories

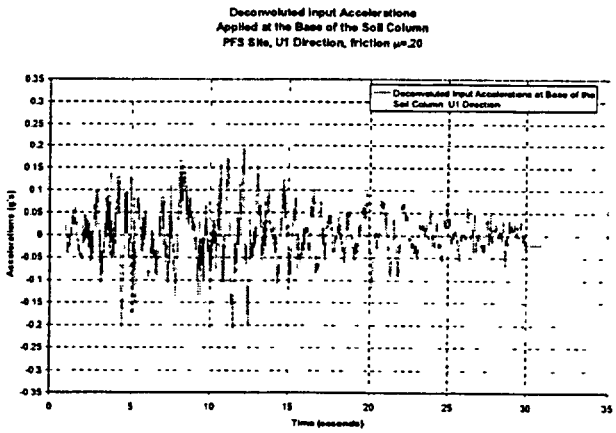

(b) Deconvoluted base input time histories

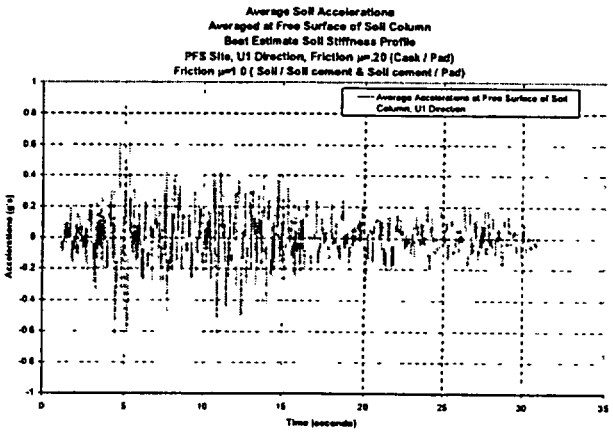

(c) Time histories of free-field analysis results

Figure 7. PFS accelerations for seismic event with 2,000-year return period in the horizontal U1 direction for best estimate soil profile data

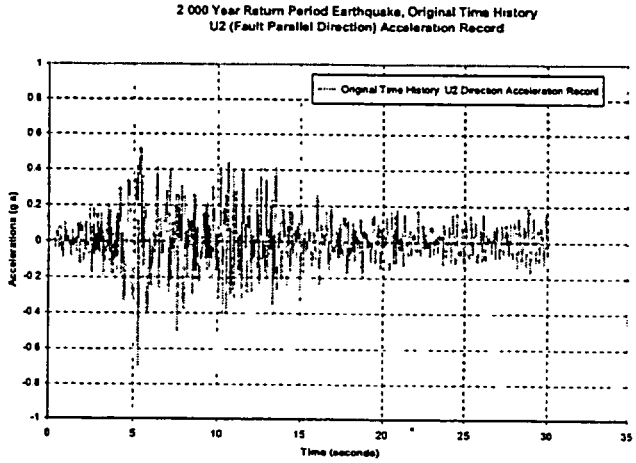

(a) Original time histories

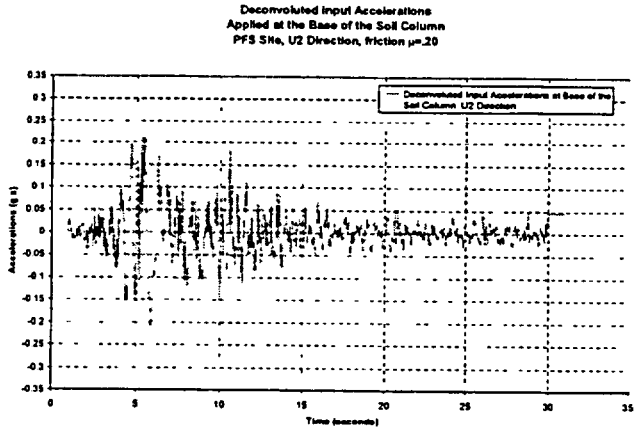

(b) Deconvoluted base input time histories

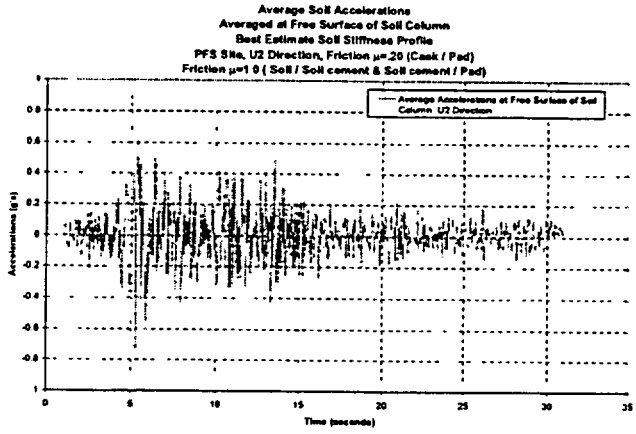

(c) Time histories of free-field analysis results

Figure 8. PFS accelerations for seismic event with 2,000-year return period in the horizontal U2 direction for best estimate soil profile data

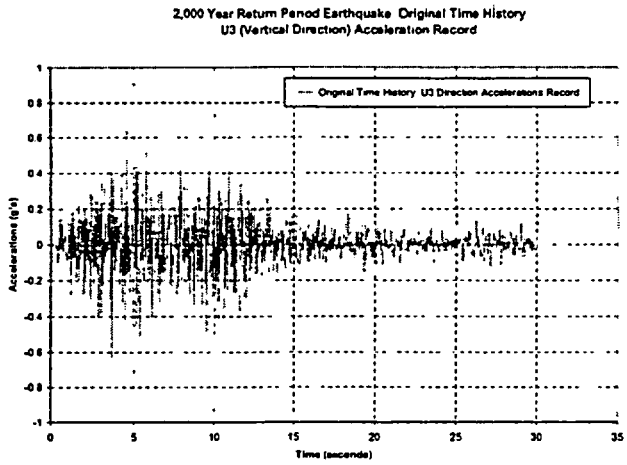

(a) Original time histories

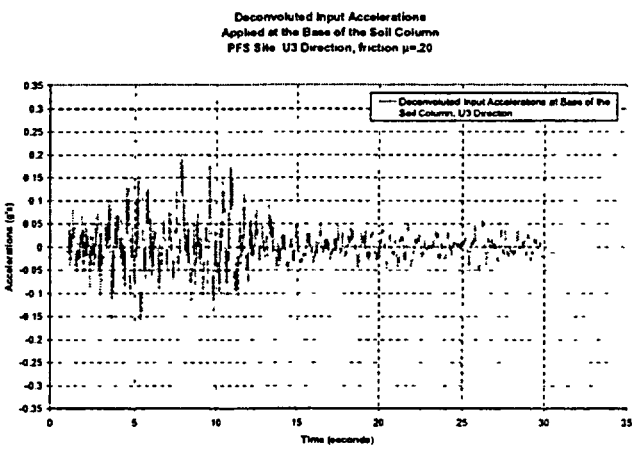

(b) Deconvoluted base input time histories

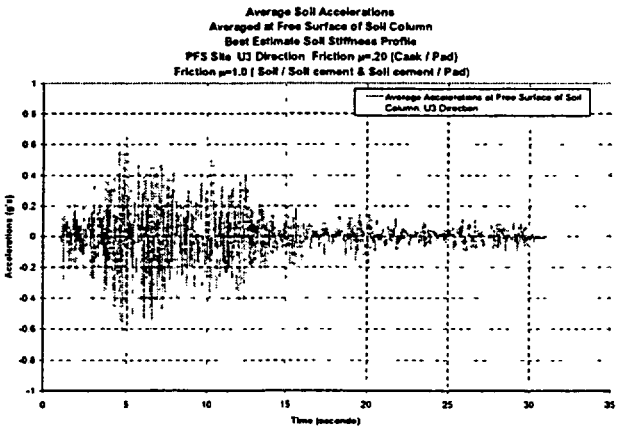

(c) Time histories of free-field analysis results

Figure 9. PFS accelerations for seismic event with 2,000-year return period in the vertical U3 direction for best estimate soil profile data

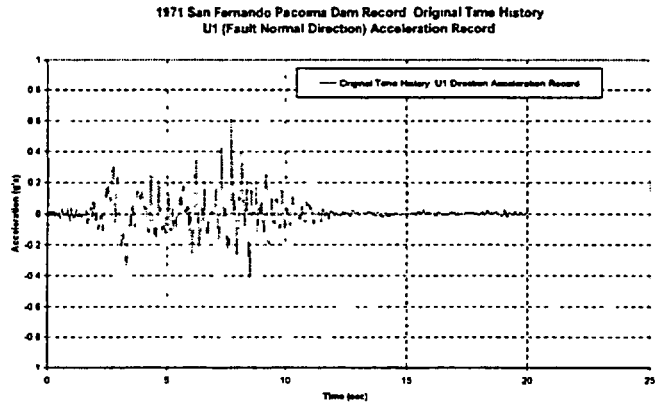

(a) Original time histories

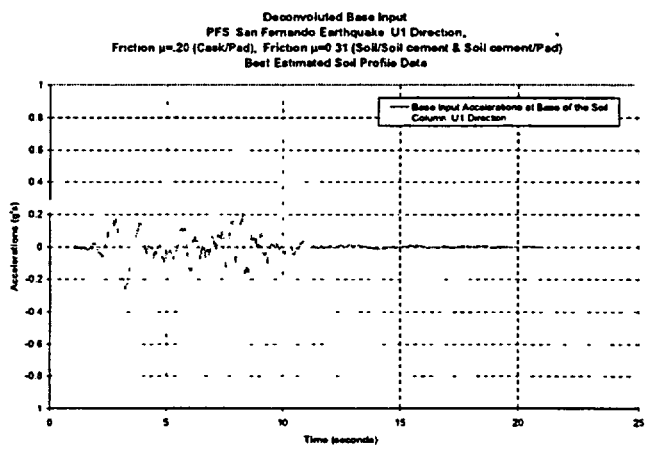

(b) Deconvoluted base input time histories

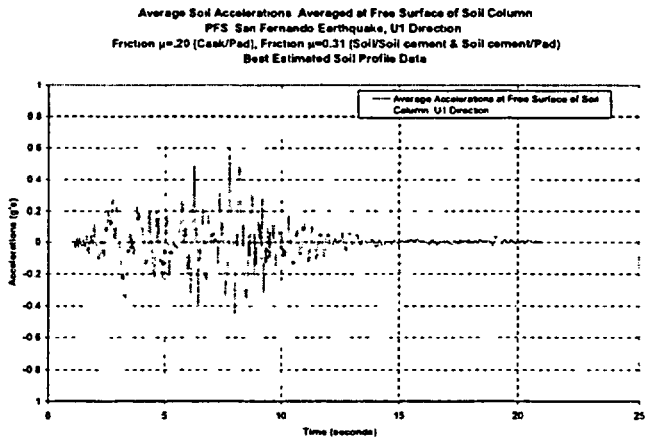

(c) Time histories of free-field analysis results

Figure 10. Accelerations for 1971 San Fernando Pacoima Dam record in the horizontal U1 direction for best estimate soil profile data

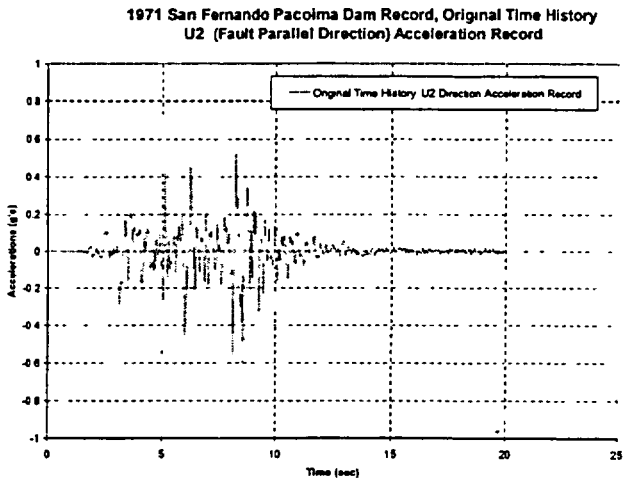

(a) Original time histories

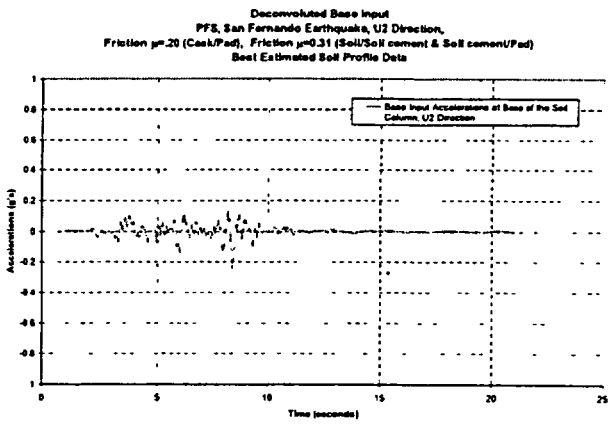

(b) Deconvoluted base input time histories

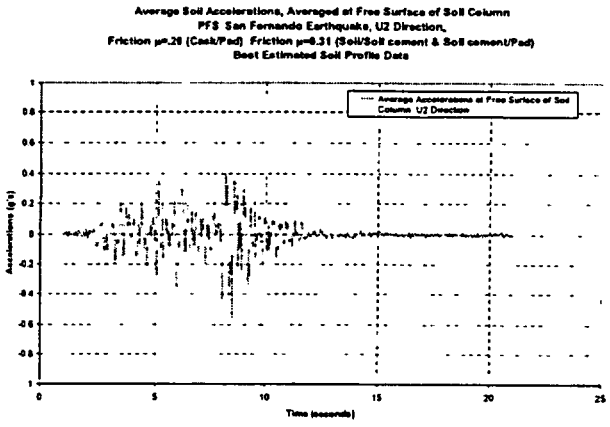

(c) Time histories of free-field analysis results

Figure 11. Accelerations for 1971 San Fernando Pacoima Dam record in the horizontal U2 direction for best estimate soil profile data

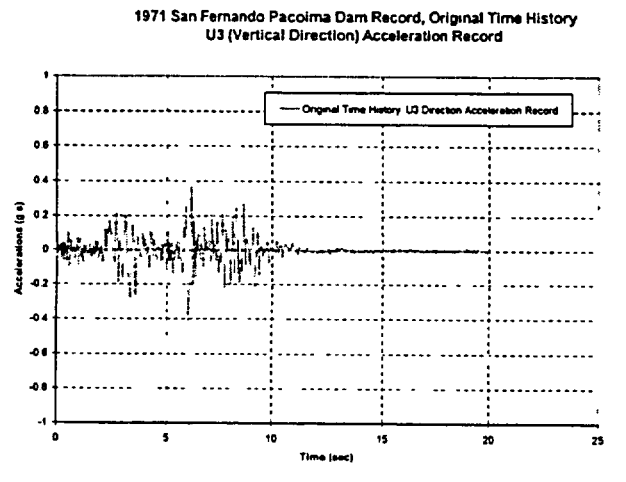

(a) Original time histories

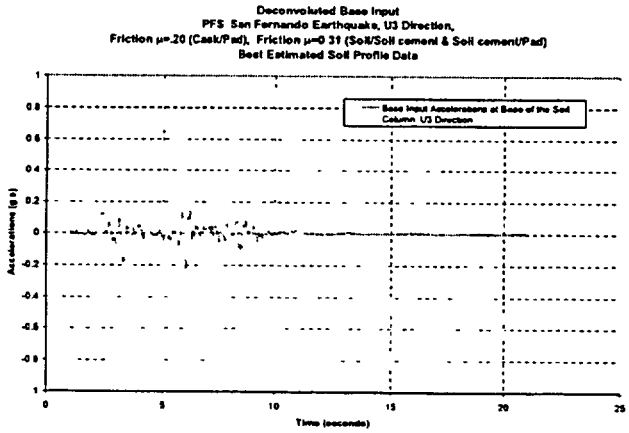

(b) Deconvoluted base input time histories

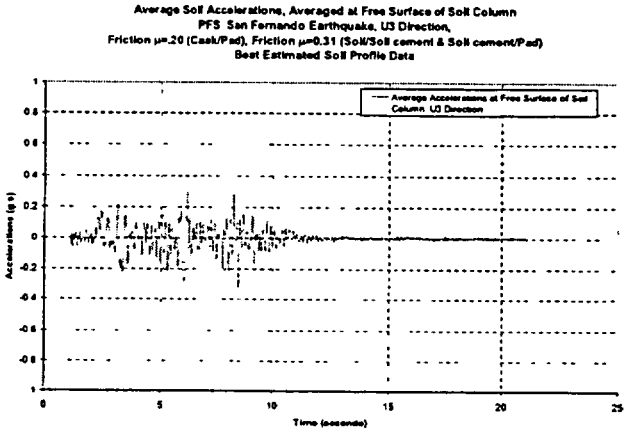

(c) Time histories of free-field analysis results

Figure 12. Accelerations for 1971 San Fernando Pacoima Dam record in the vertical U3 direction for best estimate soil profile data

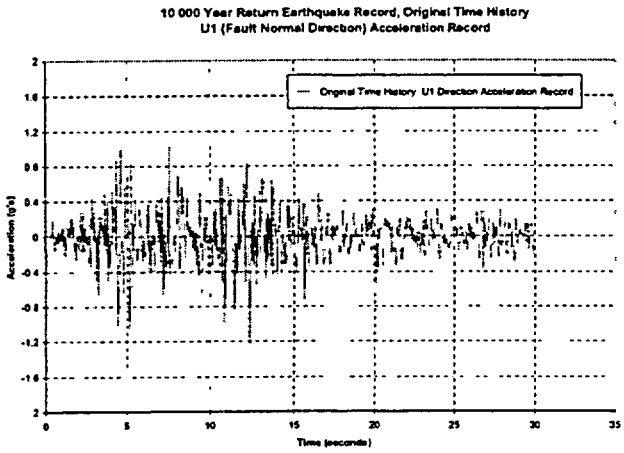

(a) Original time histories

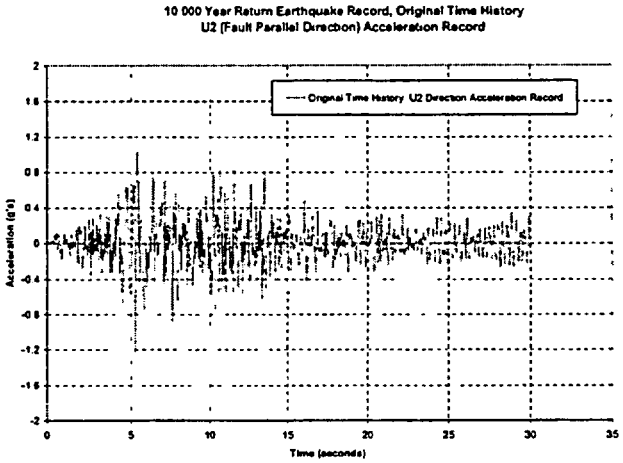

(a) Original time histories

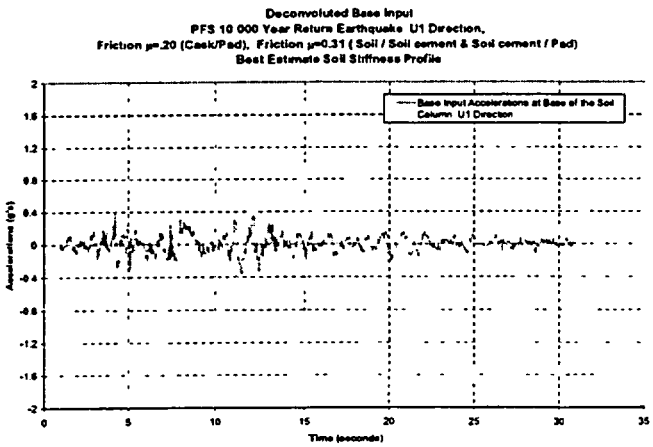

(b) Deconvoluted base input time histories

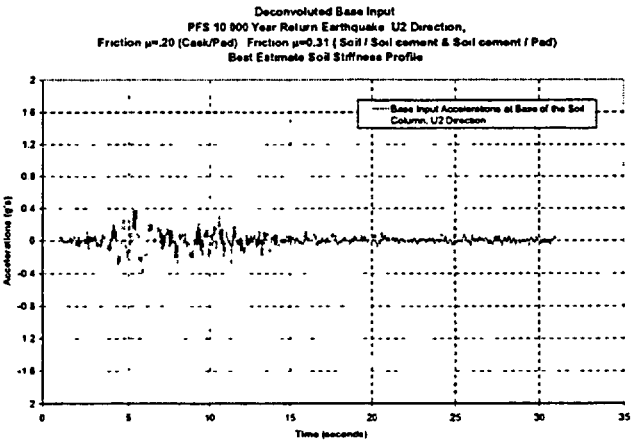

(b) Deconvoluted base input time histories

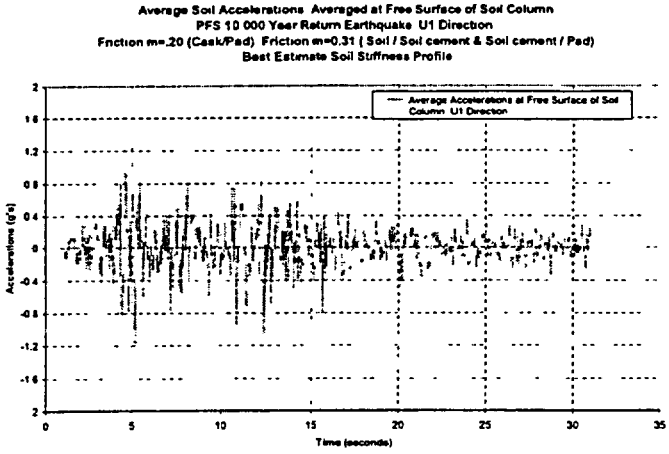

(c) Time histories of free-field analysis results

Figure 13. PFS accelerations for seismic event with 10,000-year return period in the horizontal U1 direction for best estimate soil profile data

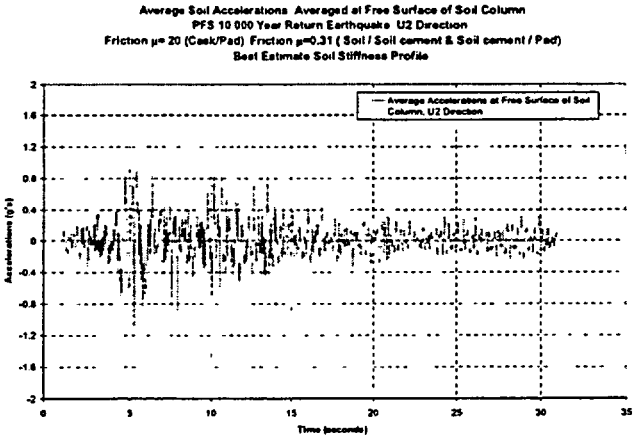

(c) Time histories of free-field analysis results

Figure 14. PFS accelerations for seismic event with 10,000-year return period in the horizontal U2 direction for best estimate soil profile data

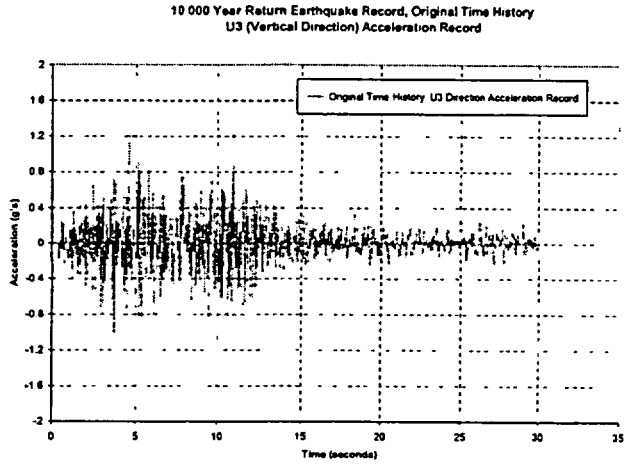

(a) Original time histories

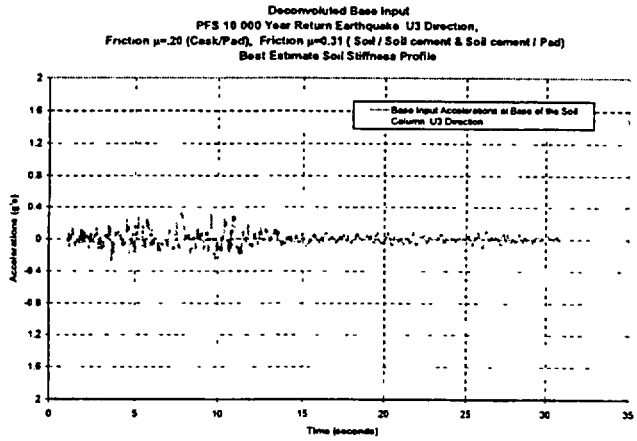

(b) Deconvoluted base input time histories

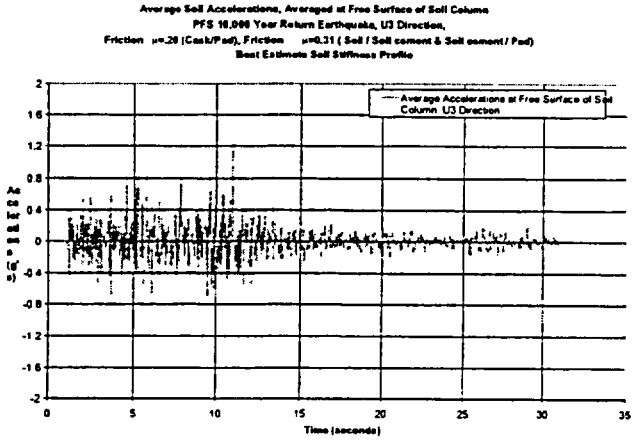

(c) Time histories of free-field analysis results

Figure 15. PFS accelerations for seismic event with 10,000-year return period in the vertical U3 direction for best estimate soil profile data

4. Analysis Results from Coupled Model

The coupled model has three interfaces at cask/pad, pad/soil-cement layer, and soil-cement layer/soil foundation. Analysis results indicate that the friction at these interfaces plays a dominant role in the dynamic cask response in a seismic event. This report documents analysis results for various selected cases with different combinations of lower and upper bounds of coefficients of friction at these interfaces. The cask response is found to be very sensitive to the coefficient of friction at the cask/pad interface. A lower bound coefficient of friction of 0.20 (for investigating cask sliding) and an upper bound coefficient of friction of 0.80 (for examining cask tipping-over) were used at this interface. Coefficients of friction of 1.00 and 0.31 were also assumed at the other two interfaces. The analysis results from the coupled model with different combinations of interfacial coefficients of friction are compiled in Tables 2-4 for the three sets of seismic excitations.

Before executing the explicit dynamic calculations for each loading configuration, a static load of all submodels was applied for duration of one second to perform implicit calculations in order to create initial conditions of the finite element model for subsequent dynamic computations. Therefore, there is a one-second shift in the analysis results of seismic response of the cask. In addition, a zero displacement boundary condition was assumed in U1 and U2 directions at the cask base in the static load initialization step. The coupled model would not be properly executed without this assumption because of the huge memory required to perform the implicit calculations with this complicated model. This assumption was then removed at the start of dynamic computations.

The seismic responses of the cask are expressed in terms of three components of displacements and two components of rotations. The two horizontal displacements, U1 and U2, and the vertical component, U3, which are referenced to the top surface of concrete pad, describe the translational movements of the cask. The rotational movements of the cask are measured by the two rotational angles with respect to the vertical axis in U1 and U2 directions, respectively.

The analysis effort was started by investigating the dynamic cask response using different interfacial coefficients of friction for a seismic event with a 2,000-year return period and the best estimate soil profile data. The analysis results in Table 2 indicate that the maximum horizontal displacements of the cask are obtained for the case with a coefficient of friction of 0.20 at the cask/pad interface and that of 0.31 at the interfaces of pad/soil-cement layer and soil-cement layer/soil foundation. This combination of interfacial coefficients of friction was then chosen as the governing case for all subsequent seismic analyses to investigate the maximum horizontal displacements of casks. Table 2 also indicates that the combination of interfacial coefficients of friction of 0.80 and 1.00 generates the maximum rotational angles of the cask with respect to the vertical axis and was therefore selected for all subsequent analyses for this investigation.

The maximum horizontal sliding displacements at the top and base of cask and its maximum rotational angle with respect to the vertical axis in U1 and U2 directions for the three seismic events are listed in Tables 2-4. A detailed evaluation of these tables indicate that the case of using the lower bound soil profile data and the interfacial combination of 0.20 and 0.31 produces a higher cask rotational angle in Table 4 for the seismic event with a 10,000-year return period, and therefore, this soil profile data was selected to investigate the maximum cask rotational angle. For the 1971 San Fernando Earthquake, Pacoima Dam record in Table 3, the results of cask rotation angle are very similar for all three cases of soil profile data, and the best estimate soil profile data was selected in investigation.

The cask does not experience much vertical displacement in all three seismic events. The cask base is never entirely lifted off the top surface of pad throughout the seismic event with a 2,000-year return period and the 1971 San Fernando Earthquake, Pacoima Dam record. However, during the seismic event with a 10,000-year return period, the analysis results reveal that the entire cask base lifts off the top surface of pad 0.26 inches maximum for a total duration of less than 0.30 seconds and that the maximum vertical displacement at any point along the perimeter of the cask base is less than 2.7 inches above the pad top surface. Therefore, the analysis results of the cask vertical displacements are not included in Tables 2-4.

In Table 2, analysis results from three different types of models are included for sensitivity evaluation of cask response. Model type 1 consists of the standard coupled model as illustrated in Figure 1. Model type 2 represents the coupled model without compacted aggregate and soil-cement layers (that is, concrete pad sits directly on soil foundation). For model type 3, the coupled model includes one live cask, seven dead casks (simulated by their dead weights), and dead weights of fully loaded neighboring concrete pads. Analysis results in Table 2 indicate that the maximum horizontal sliding displacements of cask for both model types 2 and 3 were lower than those for model type 1, which has been regarded as the governing configuration of the coupled model.

The dynamic coupling or the soil-structure-interaction (SSI) effect of the cylindrical cask with the soil foundation was examined in detail using the acceleration results in U1 direction for the combination of interfacial coefficients of friction of 0.20 and 0.31. Figure 16 shows the analysis output locations at A' and B' on the free surface, and D' on the top of soil-cement layer. In addition, there are analysis output locations at four points, A, B, C, and D on the soil surface, and four points, D, E, F, and G at various depths along the central axis of the pad for demonstration purposes. The SSI effect is demonstrated in Figure 17 with the acceleration results at A' and D'. The acceleration results at four locations on the soil surface and at various depths along the central axis of the pad are shown in Figures 18 and 19, respectively. Noticeable differences in accelerations are observed in these figures to demonstrate the presence of the SSI effect and to justify the development of the coupled finite element model in the research effort. The SSI effect was further investigated by plotting the corresponding response spectra in Figures 20 - 22.

As indicated in Table 4, the maximum horizontal sliding displacement of cask occurs in the seismic event with a 10,000-year return period, with a lower bound soil profile data, and a combination of coefficients of friction of 0.20 at the cask/pad interface and 0.31 at the other interfaces. The detailed analysis results for this case are therefore chosen to be included in the report. The time histories of relative displacements between concrete pad and top of cask in U1, U2, and U3 directions are shown in Figures 23, 24, and 25, respectively. The time histories of cask rotational angles in U1 and U2 directions relative to the vertical axis are plotted in Figure 26. Figure 27 shows an interesting trajectory of relative displacements between concrete pad and top of cask.

Table 2. Summary table of seismic analysis results for Private Fuel Storage (PFS) casks in the seismic event with a 2,000-year return period

Soil Profile Data (Model Type)	Interfacial Coefficient of Friction: μ1 at cask/pad and μ2 at pad/soil-cement layer and soil-cement layer/soil foundation	Location on Cask	Maximum Horizontal Sliding Displacement / Time				Maximum Rotational Angle (degrees)	
			U1		U2			
			in.	sec.	in.	sec.	East-West U1	North-South U2
Best Estimate (Model Type 1)	μ1 = 0.20 μ2 = 1.00	Top	**3.01**	11.9	**2.85**	14.2	0.02	0.01
		Base	2.99	11.9	2.84	14. 2		
	μ1 = 0.20 μ2 = 0.31	Top	**3.93**	12.9	**3.98**	14.2	0.02	0.01
		Base	3.92	12.9	3.96	14.2		
	μ1 = 0.80 μ2 = 1.00	Top	**1.97**	11.0	**2.35**	5.6	0.22	0.40
		Base	1.46	7.9	1.10	5.7		
Best Estimate (Model Type 2)	μ1 = 0.20 μ2 = 0.31	Top	1.28	5.3	**1.76**	13.84	0.03	0.01
		Base	**1.30**	5.3	1.75	13.8		
Best Estimate (Model Type 3)	μ1 = 0.20 μ2 = 0.31	Top	**3.20**	12.9	**3.61**	11.8	0.03	0.01
		Base	3.11	12.9	3.59	11.8		
Lower Bound (Model Type 1)	μ1 = 0.20 μ2 = 0.31	Top	**2.34**	11.4	**1.85**	11.7	0.02	0.01
		Base	2.31	11.4	1.84	11.8		
Upper Bound (Model Type 1)	μ1 = 0.20 μ2 = 0.31	Top	**2.35**	5.3	**3.92**	13.6	0.01	0.01
		Base	2.34	5.3	3.91	13.7		

Table 3. Summary table of seismic analysis results for Private Fuel Storage (PFS) casks for the 1971 San Fernando Earthquake, Pacoima Dam record

Soil Profile Data	Interfacial Coefficient of Friction: μ1 at cask/pad and μ2 at pad/soil-cement layer and soil-cement layer/soil foundation	Location on Cask	Maximum Horizontal Sliding Displacement / Time				Maximum Rotational Angle (degrees)	
			U1		U2			
			in.	sec.	in.	sec.	East-West U1	North-South U2
Best Estimate	μ1 = 0.20 μ2 = 0.31	Top	**3.00**	6.3	**1.64**	8.7	0.01	0.01
		Base	3.00	6.2	1.64	8.7		
Lower Bound	μ1 = 0.20 μ2 = 0.31	Top	**2.75**	6.2	**2.30**	8.7	0.02	0.01
		Base	2.73	6.2	2.29	8.8		
Upper Bound	μ1 = 0.20 μ2 = 0.31	Top	**2.62**	6.2	**1.12**	8.2	0.01	0.01
		Base	2.62	6.2	1.12	8.2		
Best Estimate	μ1 = 0.80 μ2 = 1.00	Top	**0.57**	8.8	**0.59**	8.6	0.06	0.07
		Base	0.43	8.8	0.35	8.7		

Table 4. Summary table of seismic analysis results for Private Fuel Storage (PFS) casks in the seismic event with a 10,000-year return period

Soil Profile Data	Interfacial Coefficient of Friction: μ1 at cask/pad and μ2 at pad/soil-cement layer and soil-cement layer/soil foundation	Location on Cask	Maximum Horizontal Sliding Displacement / Time				Maximum Rotational Angle (degrees)	
			U1		U2			
			in.	sec.	in.	sec.	East-West U1	North-South U2
Best Estimate	μ1 = 0.20 μ2 = 0.31	Top	**9.80**	11.4	**6.78**	10.2	0.03	0.01
		Base	9.79	11.4	6.78	10.2		
Lower Bound	μ1 = 0.20 μ2 = 0.31	Top	**15.94**	11.5	**6.84**	9.2	0.10	0.05
		Base	15.82	11.5	6.80	9.2		
Upper Bound	μ1 = 0.20 μ2 = 0.31	Top	**12.19**	11.4	**6.00**	9.8	0.06	0.04
		Base	12.19	11.4	5.97	9.8		
Lower Bound	μ1 = 0.80 μ2 = 1.00	Top	**7.20**	11.7	**7.39**	14.3	0.65	1.16
		Base	5.11	8.1	7.08	14.3		

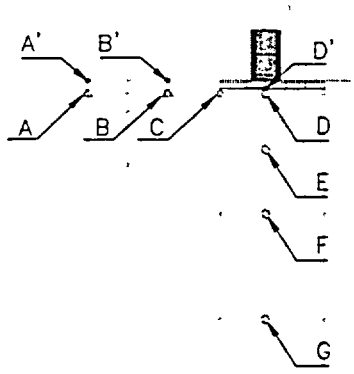

Designation	Description
A	Point at free field location (top of soil surface)
B	10' from edge of pad (top of soil surface)
C	Edge of pad (top of soil surface)
A'	Point at free field location (free surface)
B'	10' from edge of pad (free surface)
D'	Center of pad (top of soil-cement layer)
E	Depth of 12' below free surface
F	Depth of 26' below free surface
G	Depth of 50' below free surface

Figure 16. Location definition of designation points

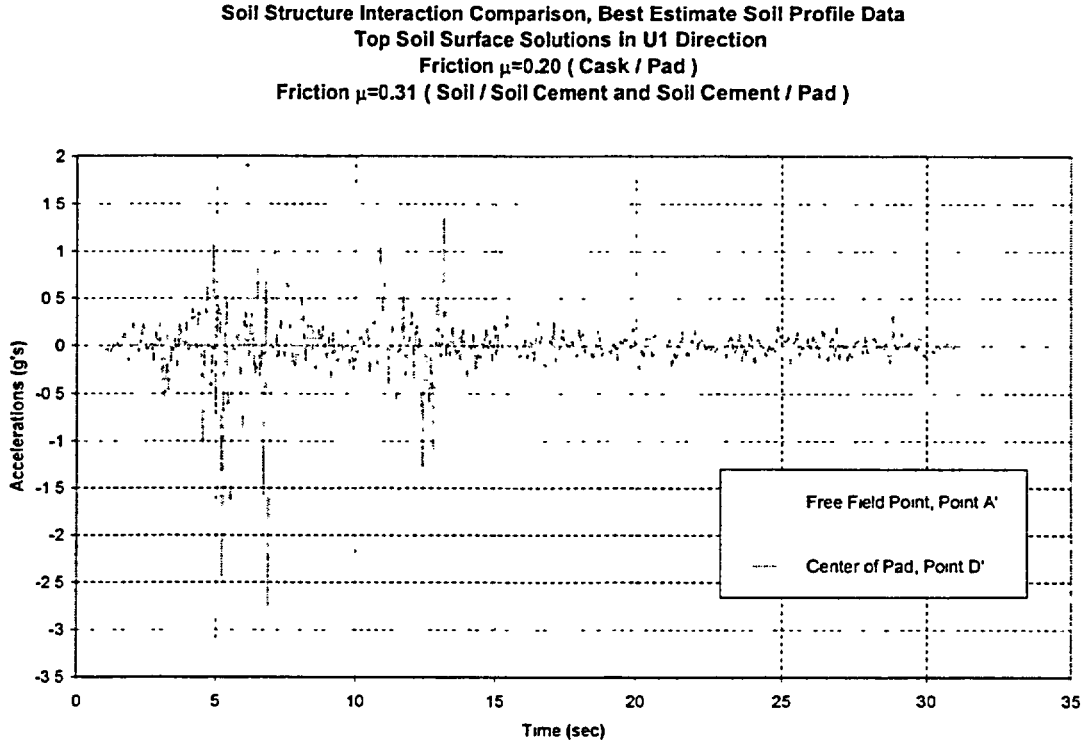

Figure 17. Time histories of accelerations in U1 direction at points A' and D' to demonstrate the SSI effect

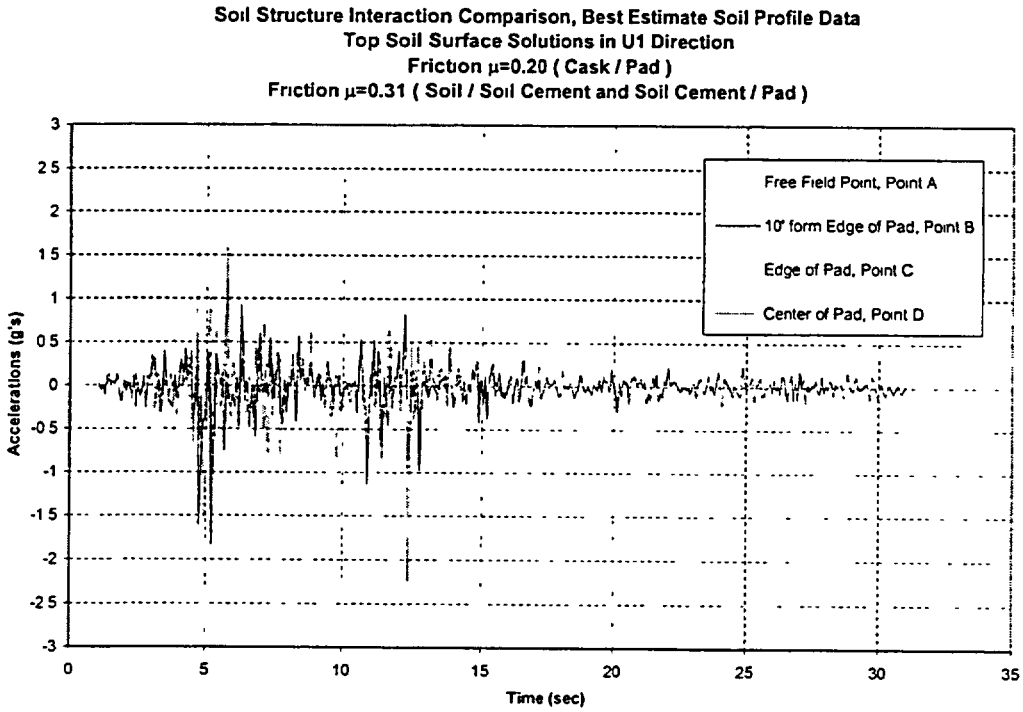

Figure 18. Time histories of U1 accelerations at four locations on top of soil surface to demonstrate the SSI effect

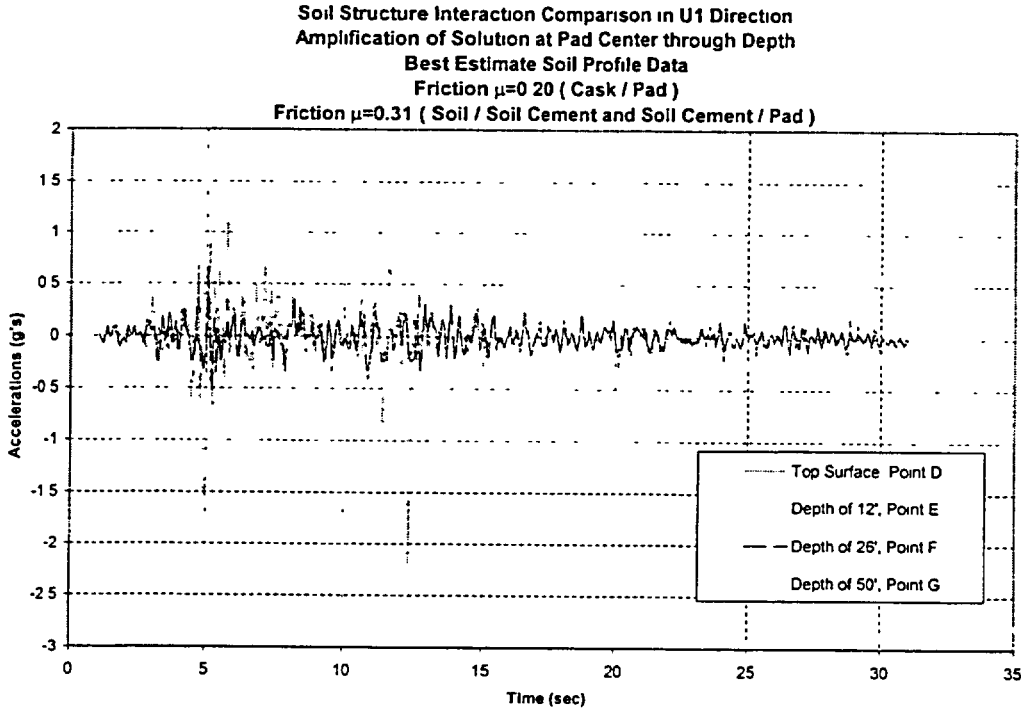

Figure 19. Time histories of U1 accelerations at four depths along the central axis of pad to demonstrate the amplification effect

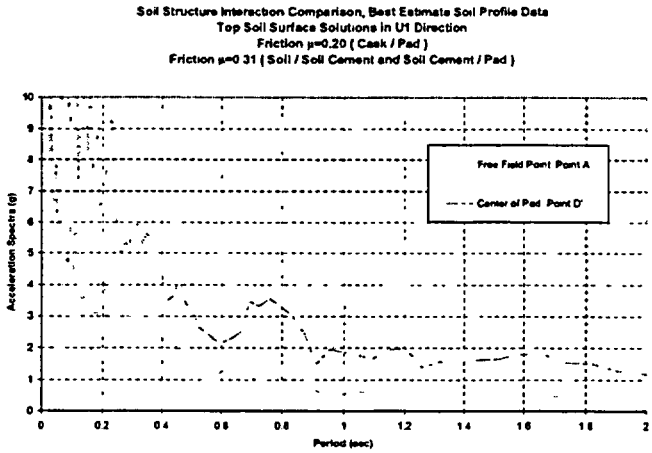

Figure 20. Response spectra in U1 direction at points A' and D' to demonstrate the SSI effect

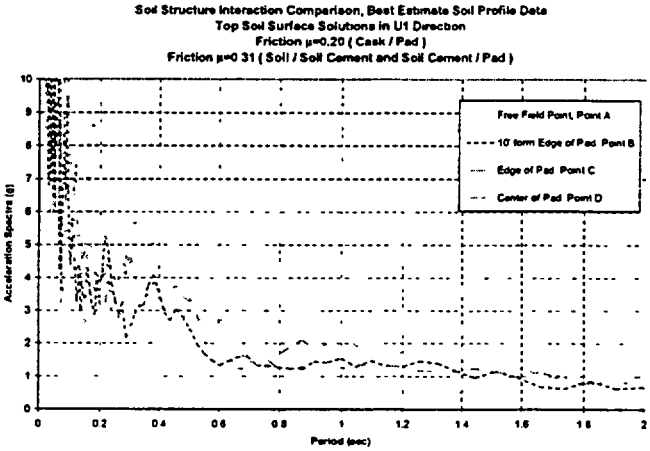

Figure 21. Response spectra in U1 direction at four locations on top of soil surface to demonstrate the SSI effect

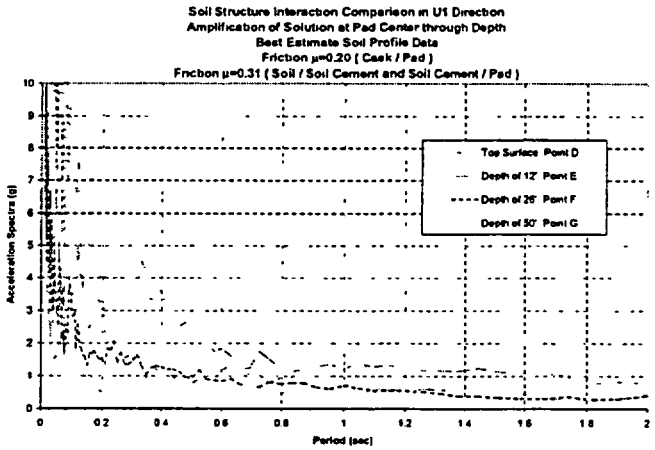

Figure 22. Response spectra in U1 direction at four depths along the central axis of pad to demonstrate the amplification effect

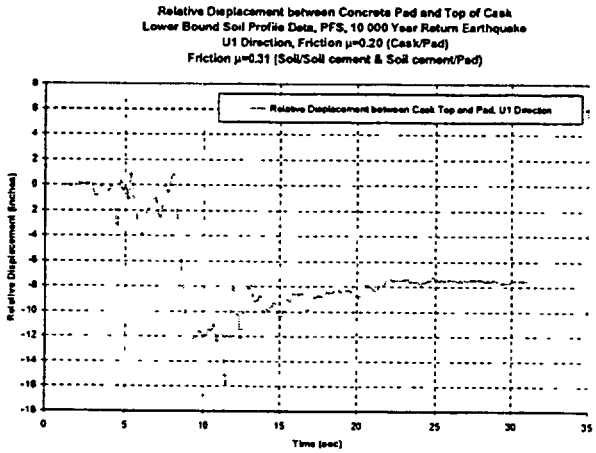

Figure 23. Time history of relative displacement between concrete pad and top of cask, lower bound soil profile data, U1 direction, μ=0.20 (cask/pad), μ=0.31 (soil/soil cement and soil cement/pad)

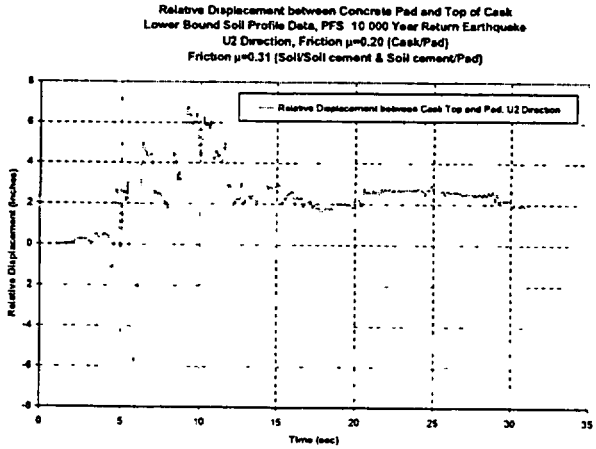

Figure 24. Time history of relative displacement between concrete pad and top of cask, lower bound soil profile data, U2 direction, μ=0.20 (cask/pad), μ=0.31 (soil/soil cement and soil cement/pad)

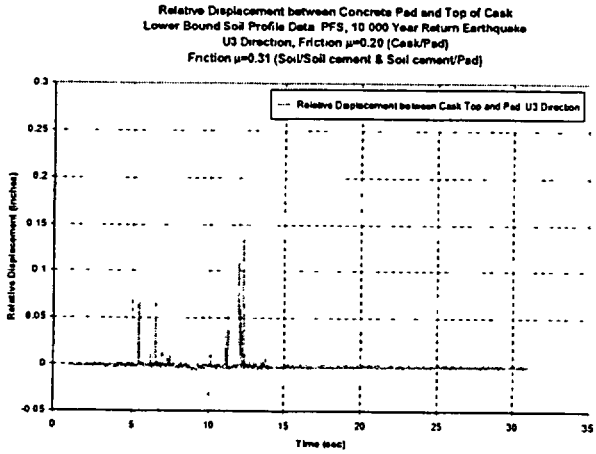

Figure 25. Time history of relative displacement between concrete pad and top of cask, lower bound soil profile data, U3 direction, μ=0.20 (cask/pad), μ=0.31 (soil/soil cement and soil cement/pad)

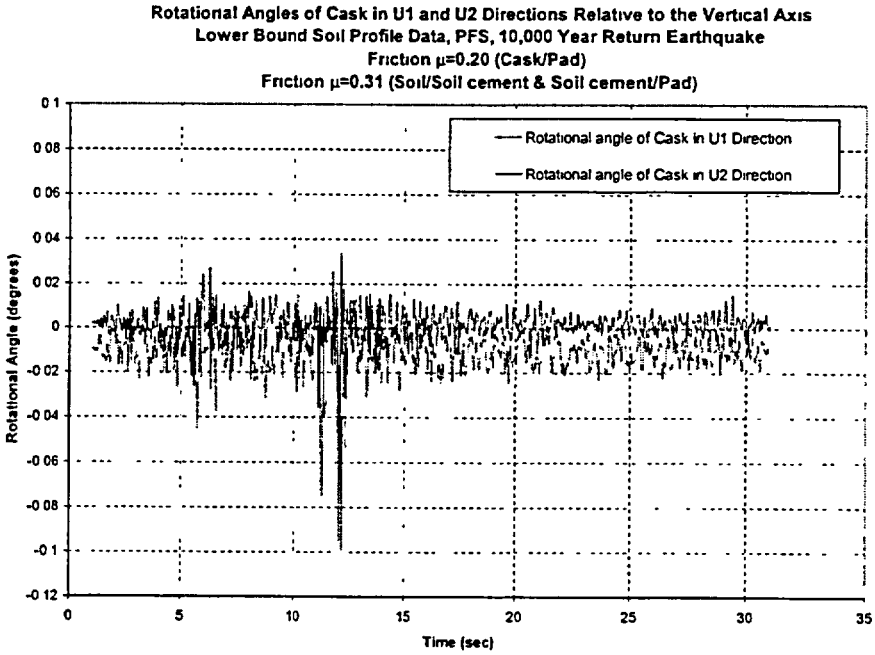

Figure 26. Time history of rotational angle of cask in U1 and U2 directions relative to the vertical axis, lower bound soil profile data, μ=0.20 (cask/pad), μ=0.31 (soil/soil cement & soil cement/pad)

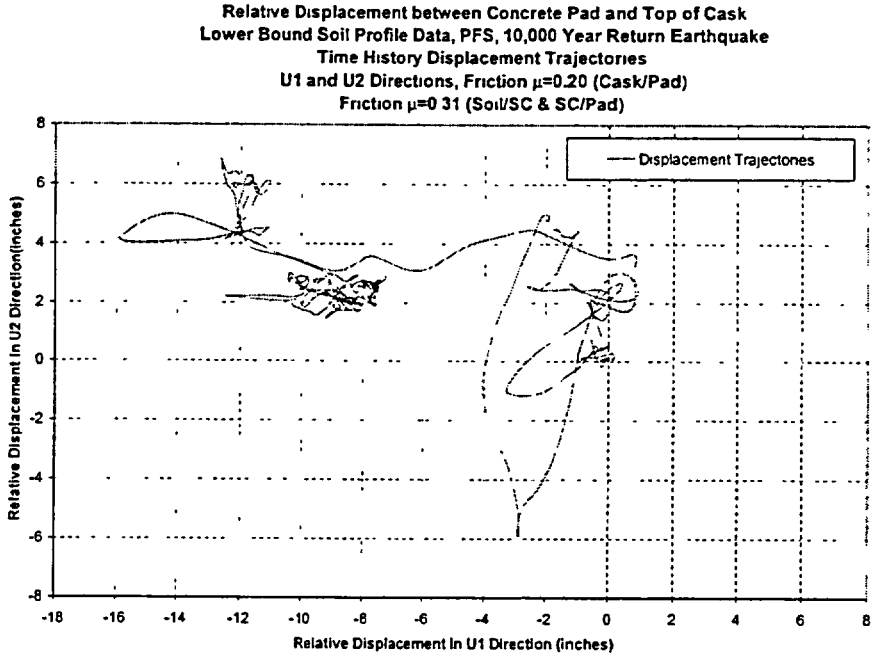

Figure 27. Relative displacement between concrete pad and top of cask, lower bound soil profile data, time history displacement trajectories, U1 & U2 directions, μ=0.20 (cask/pad), μ=0.31 (soil/soil cement & soil cement/pad)

5. Summary

The research project investigates the seismic response of freestanding dry cask storage systems. This report documents the seismic analysis results for cylindrical HI-STORM 100 casks at the Private Fuel Storage (PFS) Facility. The research team consisting of analysts and engineers at Sandia National Laboratories (SNL), Earth Mechanics, and ANATECH developed the three-dimensional coupled finite element model, using the ABAQUS / Explicit code, to examine the dynamic and nonlinear behavior of the cask and to simulate the effect of soil-structure-interaction. The coupled model consists of a cylindrical cask, a flexible concrete pad, soil-cement layers under and adjacent to the pad, and a soil foundation whose material properties are based on the site-specific soil profile data.

A total of three sets of seismic loading were used as input excitations to the coupled model. Two artificial seismic time histories of accelerations, which are based on the response spectra specific to the PFS site for a 2,000-year and a 10,000-year return period, were used to calculate the dynamic response of the cask. A sensitivity study was also performed using the actual 1971 San Fernando Earthquake, Pacoima Dam record. Each set of seismic loading has one vertical and two horizontal components of statistically independent accelerations. Each one of the three seismic acceleration components was treated with a deconvolution procedure to produce a modified time history of deconvoluted accelerations with properly adjusted frequencies and magnitudes in order to preserve their dynamic characteristics and to achieve the desired surface shaking intensity. All three components of deconvoluted accelerations were applied simultaneously at the base of soil foundation in the coupled model.

The coupled model has three interfaces at cask/pad, pad/soil-cement layer, and soil-cement layer/soil foundation. The horizontal sliding displacements and the rotational angles of casks are found to be dependent on the selection of coefficient of friction at these interfaces. Sensitivity studies of cask response were therefore performed with different combinations of lower and upper bound interfacial coefficients of friction for the seismic event with a 2,000-year return period and the best estimate soil profile data. The results of sensitivity studies indicate that the combination of coefficients of friction of 0.20 at the cask/pad interface and 0.31 at the other two interfaces generates the maximum horizontal sliding displacements of the cask, and the corresponding combination of interfacial coefficients of friction of 0.80 and 1.00 produces the maximum cask rotational angles. These two combinations were used to investigate the dynamic behavior of casks for the all three sets of seismic loading and the three cases of soil profile data.

The results from all seismic analyses of coupled models indicate that the maximum horizontal cask sliding displacements are 15.94 inches (for the seismic event with a 10,000-year return period), 3.98 inches (for the seismic event with a 2,000-year return period), and 3.00 inches (for the 1971 San Fernando Earthquake, Pacoima Dam record). According to the design installation configuration at the PFS site, the separation distance between neighboring casks is 47.50 inches. Therefore, the issue of probable cask collision can be properly addressed based on this set of information. In addition, the analysis results show that the maximum cask rotation with respect to the vertical axis in either horizontal direction is less than 1.5 degrees, which is significantly less than the cask rotation for tipping over (approximately 29 degrees). Therefore, the PFS casks are not anticipated to tip over during an earthquake with a return period of either 2,000 years or 10,000 years.

6. References

1. Title 10, The Code of Federal Regulation, January 1, 2001.

2. NRC Safety Evaluation Report Concerning the Private Fuel Storage Facility, Docket No. 72-22, September 29, 2000, including Supplement No. 1, November 13, 2001, and Supplement No. 2, December 21, 2001.

3. Pacoima Dam Recording: 1971 San Fernando Earthquake, California, Magnitude 6.4, Date: 2/9/1971, Time: 0600 Pacific Time.

4. Luk, V. K., Smith, J. A., Aube, D. A., and Dameron, R. A., "NRC Project on Seismic Behavior of Spent Fuel Storage Cask Systems - Final Report on Seismic Analysis of Three-Module Rectangular Transnuclear West Module/Cask," dated December 21, 2001.

5. Luk, V. K., Smith, J. A., Aube, D. A., Dameron, R. A., and Lam I. P., "NRC Project on Seismic Behavior of Spent Fuel Storage Cask Systems - Final Report on Seismic Analysis of HI-STORM 100 Casks at Hatch Nuclear Power Plant," dated June 28, 2001.

6. Idriss, I.M., and Sun, J.I., User's Manual for SHAKE91, University of California, Davis, November 1992.

7. Prevost, J. H., DYNAFLOW: Finite Element Analysis for the Static and Transient Response of Linear and Nonlinear Two and Three Dimensional System, Princeton University, 1996.

8. Idriss, I. M. and Seed, H. B., "Seismic Response of Horizontal Layers," Journal of the Soil Mechanics and Foundation Division, ASCE, Vol. 94, No. SM 4, July 1968.

9. Schnabel, P. B., Lysmer, J., and Seed H. B., "SHAKE: A computer Program for Earthquake Response Analysis of Horizontally Layered Sites," Report No. UCB/EERC-72/12, Earthquake Engineering Research Center, University of California, Berkeley, December 1972, 102 p.

10. ABAQUS / Explicit: User's Manual, Version 5.8-19, 1998, Pawtucket, RI, Hibbitt, Karlsson, and Sorensen, Inc.

11. US Army Corps of Engineers, Engineer Technical Letter No. 1110-2-339, March 1993.

12. Seismic Analysis of Safety-Related Nuclear Structures and Commentary, ASCE 4-98, American Society of Civil Engineers, New York, NY, 1998.

This page left intentionally blank

FINALIZATION OF INVENTORY REPORT: MATERIALS HAVING POSSIBILITIES FOR VERY LOW LEVELS OF RADIOACTIVITY THAT ARE POTENTIALLY CLEARABLE

Carl Feldman (U.S. Nuclear Regulatory Commission)
William Thurber (SC&A), et al.

Finalization of the inventory report is near completion. The report provides information on the amounts, types, and associated low levels of radioactive solid materials released from NRC licensed facilities whose dispositions might be considered for clearance. While the report focuses on identifying potentially clearable materials from NRC licensees, it also provides overview and perspective information on inventories most likely considered for disposition to low-lever radioactive waste facilities (LLW), and also disposition inventories from non-NRC licensed facilities such as from DOE, DOD, and unlicenced commercial industries that process materials resulting in technically enhanced, naturally occurring radioactive materials (TENORM).

The information found in developing this inventory information strongly indicated a large difference in radioactivity levels between materials segregated for clearance and those more likely to be sent to LLW facilities for disposal. All the materials considered for clearance were found to contain none to very low levels of radioactivity (measurement uncertainties were within background noise). All the other materials were found to have significantly higher radioactivity levels which clearly categorized them for LLW disposal. High confidence levels for accomplishing the segregating these materials into two distinct disposition categories critically depended on establishing proper procedures to perform and implement the screening process. Also, incorporation of a good quality control program into the overall process, was essential.

This page left intentionally blank

Surveys of Volumetric Contamination and Difficult Geometries

G. Powers, NRC

NUREG-1761: Radiological Surveys for Controlling Release of Solid Materials

E.W. Abelquist, T.J. Bower, ORISE
R. Coleman, ORNL
C.V. Gogolak, P.Shebell, EML

The U.S. Nuclear Regulatory Commission (NRC) is developing a basis to support a rulemaking that would set specific requirements on controlling licensees' releases of solid materials. Specifically, the solid materials being evaluated are metals, building concrete, onsite soils, equipment, furniture, etc., which are present at, and/or used in, licensed nuclear facilities during routine operations. Historically, licensees have released solid materials on a case-by-case basis, without a consistent approach to designing and conducting clearance surveys. Therefore, only information about measuring residual radioactivity in materials that are to be cleared from nuclear facilities, including guidance about designing, performing, and documenting radiological surveys of solid materials to address the need for consistency in the surveys will be discussed. It is irrelevant that dose limits have not yet been defined since only the techniques of measurement and analysis may change in complexity and effort.

A Data Quality Objectives (DQO) Process (discussed in Section 3 of NUREG-1761) is the foundation for designing and implementing surveys of solid materials. In other words, a licensee, before beginning to plan for the survey, must decide whether to dispose of the solid material as radioactive waste or perform surveys to determine whether the material can be released. That is. it may be more cost-effective to simply dispose of the material as radioactive waste, rather than performing clearance surveys. Solid materials that have a limited potential to be contaminated would likely be surveyed for clearance, while those materials that are known (or likely) to have contamination in excess of the release criteria, which would therefore require cleaning and reevaluation prior to release, would probably be disposed of as radioactive waste.

After determining that clearance is the preferred option, the licensee would again use the DQO Process to determine the most advantageous survey protocol based on the solid material being released which may include; the available survey instrumentation, the need for laboratory analyses, and the applicable release criteria. Effective survey design should consider the available process knowledge of the solid materials and the need for additional characterization of the material. Characteristics that impact the release of solid materials include their physical description, potential for contamination, nature of the contamination, and degree of inaccessible areas.

Again, it should be noted that this report does not provide release criteria, but does presume that criteria have been obtained prior to survey design. Specifically, this report assumes that derived concentration guideline levels for clearance ($DCGL_C$) are available for use, and focuses on how those release criteria can be applied when multiple radionuclides may be present.

This report also describes a number of different survey approaches, including conventional scanning, automated scanning using a conveyorized survey monitor, and *in toto* techniques, such as *in situ* gamma spectrometry and tool monitors. In addition, because detection limits for survey instrumentation are an important criterion for selecting a particular approach, this report addresses the measurement of contamination for each survey approach considered. This report also stresses the use of situation-specific measurement sensitivity of scanning to release solid materials whenever the minimum detectable concentration (MDC) of the scan is less than the $DCGL_C$. Statistical survey designs, such as those discussed in NUREG-1575, "Multi-Agency Radiation Survey and Site Investigation Manual" (MARSSIM), Rev. 1, are recommended in cases where the scan MDC is greater than the $DCGL_C$.

Survey approaches discussed were determined using the DQO Process, giving due consideration to two major requirements. Specifically, (1) the survey result must be able to demonstrate that clearance criteria have been met within predetermined confidence levels, and (2) the survey unit size must be sufficiently evaluated to develop a technically defensible approach for area or volume averaging.

The general release survey approaches identified include (1) surveys using conventional instruments that incorporate both scanning and statistical designs for determining sample sizes; (2) automated scanning surveys (conveyorized survey monitors); (3) *in toto* surveys performed using gamma spectrometers, bag monitors, tool monitors, and portal monitors; and (4) analytical methods and laboratory analyses on representative samples based on statistical sampling designs. A section is provided on guidance of reducing survey data, demonstrating compliance with clearance release criteria, and documenting results. Appendixes provide a primer on the basic radiation properties, which are relevant to the measurement of radioactivity in and on solid materials and also addresses some of the fundamental principles of radiation detection and measurements. additional information on advancements in general radiation detectors and survey instruments that utilize new detection materials and software.

One of the technical challenges is defining a "survey unit" for clearance surveys of materials. The material survey unit (or batch) concept is at the core of statistical designs for release surveys. In the MARSSIM, the survey unit represents a specific land area or building surface area. For clearance of solid materials, the survey unit may consist of equipment surface area, volume of bulk material (soil or rubblized concrete), number of small items, lengths of pipe, etc. Like the survey unit concept in the MARSSIM, any relationship between the survey unit size (i.e., batch size) and the modeling input used to establish the $DCGL_C$ should be adhered to. Thus, the definition of a material survey unit (or batch) for solid materials released using a conveyorized survey monitor (CSM) may relate to the amount of material scanned as it passes under the detector(s) for a specified observation interval and given belt speed. Based on the material's classification, 10 to 100 percent of the material might be selected for analysis on the CSM. Another example might include a few large pieces of equipment. In this case, the survey unit might consist of the entire piece itself, such as a large electrical panel. Therefore, material survey unit selection is ultimately based on the DQO Process, consistent with the nature of the material, the clearance survey technique selected, and the material's potential for contamination.

A question that often arises is how to handle the release of materials that have inaccessible areas that may have contamination. If the material surfaces are inaccessible, then by definition, it is not possible to demonstrate that release criteria have been satisfied using conventional survey activities. In such cases, a couple of options exist. First, the material might not be released for unrestricted use; that is, the surveyor

might conclude that since surfaces are not accessible, they must be assumed to have contamination at levels greater than the release criteria. Thus, the materials might be disposed of as radioactive waste. In fact, this approach has been used to deal with materials that have inaccessible surfaces.

A second alternative might be to make the surfaces accessible, either by cutting or dismantling the material, or by using specialized survey equipment (e.g., small detectors). This option requires additional resources beyond those required for conventional clearance surveys.

Other techniques that may be considered is the use of thermoluminescent dosimeters (TLDs) or small detectors to measure surface activity levels within buried and embedded piping systems, small detectors, such as miniature GM detectors, and other "pipe-crawling" detector systems have been used to assess surface contamination in pipe systems. Nondestructive assay (NDA) is another quantitative technique that does not require sampling or sample preparation, and will not alter the physical or chemical state of the object being measured. NDA techniques have been developed and used on nuclear fuel materials, transuranic waste, soils, and scrap metal. The two basic approaches to NDA involve passive and active techniques. A passive technique involves directly measuring the spontaneous decay of nuclear material, while an active technique attempts to excite atoms and molecules to emit characteristic radiation that can be measured and used for identification and quantification. With the exception of nuclear activation analysis, active techniques cannot distinguish between nuclear isotopes like some passive techniques. In general, NDA techniques are less sensitive than laboratory techniques.

This page left intentionally blank

Fire Risk Research Program: Addressing Key Uncertainties

J.S. Hyslop, Senior Reliability and Risk Analyst
Office of Nuclear Regulatory Research
U.S. Nuclear Regulatory Commission

Fire can be a significant or even dominant contributor to the overall plant risk of a nuclear power plant. Furthermore, many key components of a fire risk analysis (FRA) suffer from significant uncertainty. The U.S. NRC Office of Nuclear Regulatory Research (RES) is making significant headway into addressing these uncertainties in FRA through implementation of its Fire Risk Research Program. Specifically, three areas of uncertainty; circuit analysis, human reliability analysis, and early fire effects; are addressed in this paper. Progress in addressing uncertainty in these areas is related to developing a more mechanistic understanding. In particular, RES is improving the understanding of factors that underlie the FRA methods, participating in testing to collect new data, and reviewing and analyzing new data. It is important to note that the treatment of uncertainty in the Fire Risk Research Program extends across the spectrum of technical areas in FRA, beyond those areas discussed in this paper.

I. Introduction

Depending upon plant configuration and design, fire can be a significant or even dominant contributor to the overall risk from accidents in a particular nuclear power plant. Reviews of some Individual Plant Examinations of External Events (IPEEEs) have identified situations where variations in FRA analytical assumptions can lead to significant variations in estimates of fire-induced core damage frequency (CDF) [1]. In particular, these variations can be attributed to significant uncertainties in key components of FRA.

The U.S. NRC Office of Nuclear Regulatory Research (RES) is making significant headway into addressing these uncertainties in FRA through implementation of its Fire Risk Research Program[1]. The Fire Risk Research Program was developed by RES in 1998 and has the following broad objectives: (1) improve qualitative and quantitative understanding of the risk contribution due to fires in operating nuclear power plants (NPPs) and other facilities regulated by the NRC, (2) support ongoing or anticipated fire protection activities in the NRC program offices, including the development of risk-informed, performance based approaches to fire protection for operating NPPs, and (3) evaluate current FRA methods and tools and develop improved tools. These objectives involve multiple activities which will address uncertainty.

The overall quantification approach for fire-induced CDF has not changed from earliest commercial NPP FRAs. The equation remains:

$$CDF = \sum_{i} f_i \left(\sum_{j} p_{ed,j|i} \left(\sum_{k} p_{CD,k|i,j} \right) \right)$$

where the fire-induced CDF is a function of a set of fire scenarios, i, with their respective frequencies, f_i; the probability of damage to equipment j in each fire scenario, p_{ed}; and the probability of core damage p_{CD} for those set of sequences k for each fire scenario. Fire protection defense-in-depth elements; prevention of fires, prompt detection and suppression, and protection of structures, systems, and components important to post fire safe shutdown; are modeled directly in this equation. Fire prevention is related to the frequency of fires; detection and suppression, as well as protection of structures, systems, and components by barriers and spacing, are related to the probability of equipment damage; and post-fire safe shutdown is related to the likelihood of core damage following a fire event. Uncertainty in all three terms of this equation is being addressed in the Fire Risk Research Program.

II. Discussion of Key Issues

This paper focuses on a number of issues that are poorly understood, and are potentially very large contributors to risk. This paper does not attempt to address a complete set of uncertainties in FRA. Uncertainties to be addressed are in the areas of circuit analysis, human reliability analysis (HRA), and early fire effects. Before discussing uncertainties, an introduction into these issues will be provided without addressing risk specifically.

Circuit Analysis

The circuit analysis issue is primarily concerned with the likelihood of fire-induced spurious actuation of systems or components, e.g. a pump or valve, and inaccurate instrumentation readings, due to cable failure and circuit faults. Most postulated spurious actuations are associated with specific type of cable failures, namely hot shorts. A hot short occurs when an energized conductor contacts a non-energized, non-grounded conductor. These hot shorts may occur between conductors in the same cable, or between conductors in neighboring cables. In order for a spurious actuation to occur, the conductors involved in this shorting behavior must be configured in the circuit such that an unplanned or undesired operation of the component can occur. Spurious actuations can manifest themselves in unplanned starting of a component, losing control of the component, opening a diversion path, or blocking a flow path, for example.

Corrupted indication and instrumentation signals may mislead operators. Inaccurate instrumentation readings can occur with cable failures where electrical isolation is degraded, but a short circuit is not formed, i.e. a loss of insulation resistance. Such a condition can substantially bias an instrumentation readout. Various failures, generally in the control cables, can also cause misleading or conflicting status indications. A valve, for example, might indicate open when it is actually closed.

HRA

Fire effects on manual actions as well as potentially demanding manual actions specific to post-fire safe shutdown must be analyzed in an FRA. Examples of fire effects are smoke, toxic gases from burning specific combustibles, and high temperatures. Examples of potentially demanding manual actions are those challenged by stress, time, complexity of

actions, availability of staged equipment, and environmental factors such as noise and lighting. Demanding manual actions may be required by remote shutdown from outside the control room for fires in a control room and a cable spreading room containing redundant trains. Remote shutdown can transfer control to a remote shutdown panel, or to numerous local control areas requiring potentially demanding manual actions to electrically isolate the safe shutdown equipment from the fire. Manual actions may also be complicated by misleading instrumentation readings which may occur from specific cable failures and circuit faults as described above.

Early Fire Effects

The early fire stage in this paper is defined as the fire development from ignition through the challenge of secondary combustibles. For cabinet fires, it may involve an over-current condition in a cable in a cabinet which produces a fire that spreads to other cabinet combustibles, and may breach the cabinet. For a pump, the early fire stage involves ignition and fire spread, which may include fire from oil deposited outside the pump assembly.

III. Addressing Uncertainty

This section will consist, for each key issue, of a description of the existing FRA treatments, research advances to understanding these issues (including goals and challenges), future plans, and any expected remaining issues. The common theme of the research activities in each of these areas is to develop a better mechanistic understanding. Generally, the Fire Risk Research Program is developing this better understanding by improving the understanding of factors that underlie the FRA methods, participating in testing to collect new data, and reviewing the latest data to improve estimates. RES is also performing analyses which directly include uncertainty estimates, as well performing basic research into assessing and integrating different types of uncertainty. Uncertainty will also be treated more comprehensively in pilot plant FRAs via the Fire Risk Requantification Studies [1]. These studies are being conducted as a joint NRC(RES)/EPRI program, and represent a major milestone in ongoing efforts to improve FRA methods, and implement those improvements through updating a number of licensee FRAs. RES advances in the key areas of circuit analysis, HRA, and early fire effects will be discussed under the context of the general improvements described above.

Circuit Analysis

IPEEEs at most utilized a single probability for spurious actuation. In some cases, large screening failure probabilities were used, and in other cases a generic mean value was utilized [2]. This generic value was conditioned upon cable failure, and had a relatively broad distribution. Generally, all spurious actuations were considered to be statistically independent of one another in the IPEEEs, which potentially decreases the significance of multiple spurious actuations.

RES advances have occurred via a broad study in circuit analysis [3] including examination of plant-specific and scenario-specific factors which could influence the likelihood of spurious actuations, acquiring new data from participating in tests with EPRI and international organizations, and participating in assessing the data from these tests. Influence factors fall in four general categories: cable physical properties, cable routing and installation factors, circuit factors, and fire exposure factors. Examples of influence factors for cable physical properties

are insulation type, armoring, and shielding. Examples of cable routing and installation factors are cable tray type, use of conduits, types of air drops, and bundling of cables. Examples of circuit factors are circuit current, voltage, and wiring configuration. Influence factors may increase or decrease the likelihood of spurious actuations. Influence factors such as armoring and shielding expand the ground plane and make shorts to ground more likely, decreasing the probability of spurious actuations. Also, different types of insulation will tend to either melt (thermo-plastics) or char (thermo-sets) under high temperature, impacting the likelihood of cable to cable hot shorts.

Also, RES has participated in joint NRC/EPRI tests for spurious actuations conducted at Omega Point Laboratories in Texas[4]. The EPRI portions of the test focused upon the response of a surrogate MOV control circuit to cable failure. Under NRC sponsorship, insulation resistance was measured to determine the shorting behavior of each conductor in a small bundle of cables, providing new data on the cable failure modes [5]. RES also participated in an EPRI-sponsored expert elicitation to interpret the data from the joint NRC/EPRI tests on spurious actuations [6]. A major conclusion from the entire set of circuit analysis tests and analyses is that the likelihood of spurious actuation is condition dependent, as supported by influence factors. In particular, the likelihood of spurious actuations is higher than previously thought for certain cable configurations, i.e. for multi-conductor cables. RES has plans to conduct experiments on circuit analysis with its international partners in the Cooperative PRA (COOPRA) international group, including members from IRSN, GRS, and Canada, to expand our knowledge on circuit analysis.

The ultimate goal of the circuit analysis work is to develop a practical analysis method for quantifying the significance of circuit issues. Since much work is involved in tracing cables and performing circuit analysis, key in this practical approach is to identify important cables and circuits, eliminating unnecessary cable tracing and circuit analysis. A proposed approach has been developed on circuit analysis [3], but the practicality of the approach must be determined through actual applications. (Also, the approach involves screening to identify important circuits, and the rules for such screening need to be worked out through exercising against practical applications.) The joint NRC/EPRI Fire Risk Requantification Studies will enable RES to refine our approach on circuit analysis, with the goal of developing a process that will give assurance that the primary circuit failure modes and effects issues have been captured within a reasonable work scope compatible with efforts in the balance of the FRA.

Potential follow up research may involve examination of dependency for multiple spurious actuations. The dependency of multiple spurious actuations can be significant in assessing the risk of draindowns, or diversions where, for example, multiple valves in series or in parallel must spuriously operate in order to constitute a sufficient flow to be challenging to safe shutdown. The issue of multiple spurious operations can also be important in assessing existing procedures for operator response to fire events. As noted above, we also anticipate continued efforts in concert with international partners to gather additional data on cable failure modes and effects. Such efforts might ultimately lead, for example, to a combinatorial model that could be used to support the estimate of spurious operation likelihood.

HRA

The approach adopted in many IPEEEs for characterizing human reliability was highly simplified, and perhaps overly simplistic. Often the Individual Plant Examination (internal events) human error probability was applied; however, in some cases simple adjustments to

those values based upon judgement were made. Many challenges exist in advancing the state-of-art in HRA for FRA. Examples of challenges are to incorporate smoke effects on operator performance, and to model control room abandonment and remote shutdown operations. Also as indicated in the previous discussion, cable and circuit failure can produce false instrumentation readings and indications, and treating this potential in FRA is also a challenge.

Much new effort is to be directed in this area in the Fire Risk Requantification Studies. Namely, RES plans to utilize ATHEANA, a technique for human event analysis [7]. This technique will take into account stress, timing, and other typical HRA concerns, but also will evaluate specific plant conditions much more explicitly. Typical HRA considers a representative sequence of events when developing human error probabilities; the ATHEANA approach will search for those conditions that significantly increase the likelihood of human error and then quantify the likelihood of those conditions. EPRI plans to utilize alternative HRA analysis techniques in the Fire Risk Requantification Studies.

Early Fire Effects

It is often observed that not all fires represent a challenge to nuclear safety. The current approach to quantify the percentage of fires which may challenge secondary targets uses severity factors. Severity factors have been developed [8], for example, for cabinet fires in switchgear rooms, for pumps, and for transformers. These factors are generic in nature, and do not distinguish between different cabinet configurations, different pumps, or different types of transformers (oil versus air-cooled). They also are based on generic industry-wide fire experience, and do not account for case specific variations in the fire conditions (e.g., proximity of a fire ignition source to secondary combustibles or cables).

Since severity factors are developed generically, initial fire conditions for growth beyond the source component for a specific scenario are highly uncertain. Yet, the characteristics of the early fire stage will drive the extent of fire damage [9]. As can be imagined, a high voltage transformer (480V/4160V) which has oil as a cooling medium most probably has a much higher likelihood of developing a propagating fire than one absent of oil. Also, a fire in an electrical cabinet vented in the bottom and top can develop a chimney effect, enhancing the likelihood of a severe fire much more than a fully sealed cabinet.

RES has supported the development of a mechanistic framework [10] to describe fire development and propagation on a step-by-step basis. This approach is based upon developing fire initial phase scenarios, or FIPS. For example, a fire begins with the joining of an ignition source and some initial combustible material in the presence of oxygen. To become challenging, the fire must generally spread to some secondary fuels, and ultimately grow large enough to damage the plant component targets of interest. The FIPS describes the development of the fire scenario through this process of fire growth and spread to secondary combustibles This approach can help focus attention on those scenarios with the highest likelihood of both initiating and propagating fires. Such an understanding is important since different mechanisms can lead to drastically different fires. Additionally, the FIPS approach can involve the development of nominal generic fire development scenarios that can then be tailored to the case-specific conditions. Due to the lack of clarity in the data which describes fires, this method relies upon inputs based upon expert judgement.

RES and EPRI are discussing how to apply this framework in Fire Risk Requantification Studies. We expect a more realistic characterization of the initial fire conditions for growth beyond the source component. The full application of a FIPS based approach at a detailed level appears to be beyond our current capability; however, the FIPS approach will lead us to think about scenarios more critically, and is expected to direct us to examine currently used severity factors, applying the supporting data in a more refined fashion.

Once a FIPS has been developed at an appropriate level of detail, the analyst must then decide how to more fully characterize the fire which challenges secondary fuels elements and the FRA damage targets. For example, for a particular electrical cabinet configuration, the heat release rate (HRR) must be determined in order to assess damage to cabling in the overhead. The IPEEEs typically used a point estimate to describe the HRR of a particular cabinet fire. This HRR was based loosely upon the internal configuration of cabling and components inside the cabinet. In particular, if cable bundles were separated such that fire propagation from one bundle to another could be dismissed, then a HRR of 69 KW was assumed. If no distinct bundles existed (or propagation could not be dismissed), then a HRR of 200 KW was assumed [11]. Very few IPEEEs considered panel fires of greater fire intensity.

The Fire Risk Requantification Studies will characterize fires more fully. First of all, a distribution of HRRs will be developed which will contain higher HRRs than typically assumed in the IPEEEs. Higher HRRs have been seen in electrical cabinet fire tests [12,13]. Also, for certain types of higher energy electrical cabinets, e.g. switchgear panels, energetic electrical faults have occurred. For example, an energetic electrical fault in a 4KV switchgear cabinet at a NPP [14,15] caused collateral damage. Assessing the extent of fire damage for energetic faults is very challenging. However, higher HRRs and consideration of energetic faults may very well impact the fire risk estimates for a plant.

There are other characteristics of fires besides HRR which could benefit from a more mechanistic view. For example, fire location with respect to transient fires could be refined beyond typical IPEEE treatment. Turbine buildings have experienced more transient fires than areas of the control building. The basis for this disparity seems to be reasonably understood and is based upon traffic, extent of occupancy, the types of work activities undertaken, and administrative controls. Another area which could benefit from a better mechanistic view is self-induced cable fires. Currently a fire is postulated to occur in a tray with a frequency based on the total combustible fuel loading of all cables in the plant, and equally weighted among cable fuel loading. A more improved approach could be based upon such factors as cable type/function, e.g., power cables, and cable pressure points such as bends, or locations of splices.

Follow up in the Fire Risk Research Program is definitely needed to better describe early fire effects. Initially we need better data which more completely, and more consistently, describes the fire scenario. Also, further examination of existing data may be helpful. The FIPS approach relies upon expert elicitation. Feedback from FIPS usefulness, and potential viability, from the Fire Risk Requantification Studies will help RES determine if pursuing the approach, and developing expert elicitation input, would be useful.

IV. Summary

In conclusion, the Fire Risk Research Program has made significant progress towards addressing important sources of uncertainty in FRA. The Program is improving our understanding of underlying factors in all key areas discussed in this paper. RES is also performing analyses, participating in tests, and reviewing the latest data in many areas, most prominently in circuit analysis. Groundwork is being performed to support the quantitative treatment of uncertainty. RES is collaborating with EPRI and international organizations.

RES has plans for improving our understanding of key uncertainties. The Fire Risk Requantification Studies will integrate much research, beyond those issues identified in this paper, and provide a more complete treatment of uncertainty. Not only will we be identifying significant sources of uncertainty across all of FRA, but we will be developing distributions for many parameters, and treating uncertainty more comprehensively in order to combine parametric and model uncertainty in the overall CDF quantification.

V. Acknowledgments

The author acknowledges the significant review and comments provided by Steve Nowlen, Distinguished Member of the Technical Staff, Sandia National Laboratory (SNL). Mr. Nowlen is the SNL program manager and technical lead for the RES Fire Risk Research Program.

VI. References

[1] N. Siu and H. Woods, "The U.S. Nuclear Regulatory Commission's Fire Risk Research Program - An Overview," Proceedings from International Workshop on Fire Risk Assessment, Helsinki, Finland, June 29 - July 2, 1999, NEA/CSNI/R(99)26, June 2000, pp. 32-44.

[2] U.S. Nuclear Regulatory Commission, "Fire Risk Analysis for Nuclear Power Plants," NUREG/CR-2258 (UCLA-ENG-8102), September 1981.

[3] LaChance, J., et. al., "Circuit Analysis - Failure Mode and Likelihood Analysis; A Letter Report to the USNRC," Sandia National Laboratories, May 8, 2000, available in the USNRC Public Document Room under USNRC cover memorandum, T.L. King to G.M. Holahan and M.E. Mayfield dated June 13, 2000, RES File Code RES-2C-1. Report being updated.

[4] Electric Power Research Institute, "Characterization of Fire-Induced Circuit Faults: Results of Cable Fire Testing," EPRI TR-1003326, Palo Alto, CA, 2002.

[5] U.S. Nuclear Regulatory Commission, "Cable Insulation Resistance Measurements Made During Cable Fire Tests," NUREG/CR-6776 (SAND2002-0447P), April 2002.

[6] Electric Power Research Institute, " Spurious Actuation of Electrical Circuits Due to Cable Fires: Results of an Expert Elicitation," EPRI TR-1006961, Palo Alto, CA, May 2002.

[7] U.S. Nuclear Regulatory Commission, "Technical Basis and Implementation Guidelines for a Technique for Human Event Analysis (ATHEANA)," NUREG-1624 Rev.1, April 2000.

[8] Electric Power Research Institute, " Fire PRA Implementation Guide," EPRI TR-105926, Los Altos, CA, December 1995.

[9] Electric Power Research Institute, "Fire Modeling Guide for Nuclear Power Plant Applications," EPRI TR-1002981, Palo Alto, CA, August 2002, p. 2-15.

[10] Dennis Bley et. al, "Improved Fire Risk Analysis Methodology for Determination of the Frequency of Challenging Fires," submitted by Buttonwood Consulting, draft report, March 2002.

[11] U.S. Nuclear Regulatory Commission, "Perspectives Gained From Individual Plant Examination of External Events (IPEEE) Program," NUREG-1742 Vol 1, April 2002, p. B-8.

[12] U.S. Nuclear Regulatory Commission, "An Experimental Investigation of Internally Ignited Fires in Nuclear Power Plant Control Cabinets, Part I - Cabinet Effects Tests," NUREG/CR-4527 Vol.1 (SAND86-0336), April 1987.

[13] U.S. Nuclear Regulatory Commission, "An Experimental Investigation of Internally Ignited Fires in Nuclear Power Plant Cabinets, Part II - Room Effects Tests," NUREG/CR-4527 Vol.2, (SAND86-0336), October 1988.

[14] U.S. Nuclear Regulatory Commission, "Operating Experience Assessment of Energetic Faults in 4.16KV to 13.8 KV Switchgear and Bus Ducts that Caused Fires in Nuclear Power Plants 1986-2001," Report Accession Number ML021290358, February 2002.

[15] U.S. Nuclear Regulatory Commission Information Notice 2002-27: Recent Fires at Commercial Nuclear Power Plants in the United States, September 20, 2002.

Narrowing the Uncertainties in Human Reliability Analysis

Erasmia Lois, N. Siu, M. Cunningham, E. Thornsbury, and J. Cai[1]

Office of Nuclear Regulatory Research
U.S. Nuclear Regulatory Commission

Abstract

Human reliability analysis (HRA) is performed as part of probabilistic risk analysis (PRA) to support risk-informed regulatory decision-making. Given the increasing importance of the role of PRA in regulatory decision-making, it is crucial to use HRA methods, tools, and data that can, for a given risk-informed decision, adequately assess the human contribution to risk. However, HRA is viewed by experts as one area that can contribute significantly to the uncertainties of PRA results. Therefore, one of the objectives of the U.S. Nuclear Regulatory Commission (NRC) HRA Research Program is to address the uncertainties in HRA.

Uncertainties are associated with the models used in HRA to quantify the significance of human failure events (HFEs), the quality of the data available to estimate the probabilities of these events, and the quality of the HRA. Modeling uncertainties are being addressed by research focused on (a) improving our understanding of human performance and, therefore, improving the models (and associated underlying theories) driving the quantification process and (b) model completeness, that is, addressing specific topics such as advanced control rooms, low-power and shutdown operations, long-term recovery, latent conditions, ex-control-room actions, team performance, and post-severe-accident performance. Data uncertainties are being addressed by developing methods and tools focusing on an effective use of existing information related to HFEs and on designing and performing experiments to generate data. Uncertainties associated with HRA quality are addressed by developing guidance for performing and reviewing HRAs and supporting the efforts of various professional organizations to develop HRA standards.

1. Background

As stated in the NRC's policy statement on the use of PRA [1], the NRC intends to increase the use of PRA technology in "all regulatory matters to the extent supported by the state of the art in PRA methods and data." Some of the ongoing regulatory activities potentially affected include efforts to make Part 50

[1] The opinions expressed in this paper are those of the authors and not of the U.S. Nuclear Regulatory Commission

of the Code of Federal Regulations more risk-informed [2][2], the updating of the general risk-informed framework for supporting licensee requests for changes to a plant's licensing basis, described in a revised version of Regulatory Guide (RG) 1.174 [4], the revision of the reactor oversight process to incorporate risk information [5], and the evaluation of the significance of operational events [6].

Human reliability analysis (HRA), a process for identifying potentially important human failure events (HFEs) and assessing their likelihood, is an essential component of PRA.[3] Previous analyses and past experience from operational events show that credible HFEs can usually be identified for most (if not all) of the safety functions treated in PRAs. It is therefore not surprising that HRA generally plays an important role in PRA (see, for example, a review of the results of Individual Plant Examinations [7]), and that uncertainties in HRA results are often an important contributor to the uncertainty in the overall results of the PRA. Given the increasingly important role of PRA in regulatory decision-making, therefore, it is important to have HRA methods, tools, and data that can, for a given risk-informed decision, adequately assess the human contribution to risk. These methods, tools, and data need to support the identification of potentially significant HFEs and the quantification of the likelihood of these HFEs. The quantification process should appropriately account for dependencies of the HFEs and the uncertainties in the probabilities of the HFEs. Depending on the particular decision, the analysis must be performed at a sufficient level of detail to support the identification of key causes of HFEs and their potential fixes.

The NRC has over the years supported the development of both PRA and HRA methods. Starting out with the development and use of PRA, the NRC supported the development of many of what we now call first generation HRA methods such as the well-known THERP [8] and SLIM-MAUD [9] HRA methods. As the recognition of the limitations of the first generation HRA methods and the importance of PRA in regulatory applications grew, the NRC supported the development of ATHEANA (A Technique for Human Event Analysis) [10], which along with several other recent HRA methods (for example MERMOS [11]) is referred to as second generation. ATHEANA (like most second generation HRA methods) is aimed at addressing the issue of scenario-specific context and a particularly challenging topic in HRA: the treatment of errors of commission, which was not treated (in general) by first generation methods. ATHEANA's underlying premise is that significant human errors occur as a result of a combination of influences associated with plant conditions and specific human-centered factors that trigger error mechanisms by plant personnel. This premise is based on the work of researchers investigating the causes of human error and is supported by reviews of operational events. It requires the identification of these combinations of influences, called the "error-forcing contexts" (EFCs), and the assessment of their influence.

ATHEANA has improved the NRC's capability to analyze and quantify control-room-related HFEs. However, there is a broad range of HRA application issues (involving a variety of EFCs) still remaining to be addressed. These issues and NRC plans to address the issues are described below. In addition, recognizing that first generation HRAs are widely used to identify important human actions and derive

[2]As stated in Ref. 3, risk-informed regulation is "an approach to regulatory decision making that uses risk insights as well as traditional considerations to focus regulatory and licensee attention on design and operational issues commensurate with their importance to health and safety."

[3]In this paper, the term "human failure event" is used instead of the more generic "human error" to avoid an implication of blame (e.g., for situations where operators follow their training, but the training is inappropriate for the situation) and to provide an explicit tie with the PRA.

important insights with respect to the role of human performance in plant safety, the paper also discusses NRC plans regarding the development of insights and guidance to support reviews of such HRAs.

2. HRA State of the Art

Numerous reports and papers have been written on this issue [12, 13, and 14]. Key sources of uncertainty raised in these reviews, as well as in many earlier reviews (e.g., the Lewis Commission's review of WASH-1400 [15]) include the adequacy of the data used to support HRA and the adequacy of models used to depict our current understanding of human behavior under accident conditions. Regarding the latter, one concern raised over the years by researchers is the lack of explicit treatment of one particular aspect of HFE context: post-initiator dynamic plant behavior (i.e., the evolution of plant conditions over time). The coupling of this behavior with the operators' training and procedures was a significant aspect of the Three Mile Island accident in 1979. Other scenario-specific complicating factors, including multiple equipment failures and faulty instrumentation readings, have been significant contributors in actual operational events and yet are, at best, treated as operator workload issues. Another issue raised with widely used HRA methods involves the role of organizational processes and factors (e.g., work processes and safety culture) as another contextual factor for multiple HFEs within an accident sequence and across multiple sequences [16]. Because of their pervasive influence (which affects the degree of dependency between HFEs and therefore the joint probability of their occurrence), these factors may have a significant impact on risk. A related issue, recently raised based on a review of core damage accident precursors [17], is the adequacy of current HRA methods for dealing with "latent errors," i.e., pre-initiator HFEs.

Numerous research efforts have been initiated over the last decade to provide improved HRA methods that address these issues. In particular, methods aimed at providing improved treatment of post-initiator accidents (including the NRC-supported ATHEANA method) have been developed and are starting to be used in trial applications. Many of these methods have been reviewed by a study on "errors of commission"[4] undertaken by the Committee on the Safety of Nuclear Installations (CSNI) [18], and some of these methods are now used to support decisions [19, 20]. Regarding the treatment of organizational factors, the state of the art is less advanced. A number of methods [21, 22] have been proposed and undergone some degree of testing, but it appears that further work is needed before these methods can be used to support decisions.

However, it appears that the HRA research community is moving towards achieving a reasonable degree of consensus on a number of issues. For example, there appears to be fairly broad agreement that more causally-based methods are needed to better identify, model, and quantify potentially risk-significant post-initiator HFEs to support current PRA structures, and that these methods should explicitly consider potential EFCs, i.e., combinations of plant conditions and other influences that make operator errors more likely. It is further generally recognized that treatment of plant conditions requires some consideration of the plant's dynamic behavior during the accident. Table 1 provides a summary of recommendations developed during international HRA workshops and collaborative efforts.

[4]References 13 and 18 define an error of commission as an inappropriate action, particularly one that might occur during the response to a transient or an accident, that places the plant in a situation of higher risk. Other definitions found in the literature are similar but not identical.

Table 1

Summary of Recommendations From a Sample of HRA Workshops and Collaborative Projects [5]

1994 Workshop on Human Reliability Models (recommendations for evolutionary models) [23]

1. Develop shared definitions, common language, common system of analysis.
2. Assess the reliability and validity of proposed tools, data, and information.
3. Improve task analysis methods so that they can systematically identify the context for a given action.
4. Address what the operator thinks.
5. Address the influence of teamwork and organizational factors.
6. Find better ways to use existing information (e.g., simulator experiment results).
7. Focus data collection programs on two levels: errors during normal operations and errors in near misses and actual accidents.

1998 OECD (Organization for Economic Cooperation and Development)/CSNI Report on Human Reliability Modeling and Data Issues [13]

1. Validate HRA methods.
2. Avoid standardizing HRA methods to the point that it stagnates the results.
3. Intensify data collection efforts.
4. For potential future use, pay attention to work on emerging HRA techniques.
5. For potential future use, pay attention to work on emerging dynamic PSA methods.
6. Increase cooperation.

2000 OECD/CSNI Report on Errors of Commission [18]

1. Work to better understand how operators work. Move towards "human-centered analysis" rather than "equipment-centered analysis."
2. Establish a database that includes qualitative aspects of errors of commission (EOCs).
3. Improve knowledge to support quantification.
4. Develop guidance for standardizing documentation of error opportunities/error forcing contexts.
5. Develop guidance on the role of traditional task analysis.
6. Improve the incorporation of knowledge from behavioral sciences to support human error identification, analysis, and quantification.
7. Improve guidance and procedures for identifying likely EOC opportunities and for screening important EOCs.

However, these efforts have not resulted yet in a consensus on how these issues should be addressed. Apparent areas of disagreement include:

- terminology and definition,
- appropriate levels of model decomposition,
- precise definition and treatment of the EFC for a given HFE (e.g., which contextual factors should be treated deterministically, which should be treated through the use of HFE probability modifiers, and which factors need not be explicitly addressed),

[5] The recommendations listed above are paraphrased from the source reports.

- the role of generic data (and generic HFE estimates) in HFE quantification, and
- the adequacy of the current (static) PRA framework for defining scenario context.

In spite of the disagreements, it appears that there is a reasonable degree of consensus within the HRA research community with respect to (a) the basic nature of the problem, (b) areas for research and development, and (c) the need for increased cooperation to accelerate progress.

Although most HRA research has been focused on strengthening the data and models used in HRA, the quality of an HRA, i.e., how well an HRA method is implemented, is another important source of uncertainty. For example, as shown in the staff evaluation reports, HRA was an area with important weaknesses in individual plant examinations (IPEs), not only because HRA has not reached the level of maturity of other PRA areas, but also because of deficiencies in implementing the HRA method chosen to do the analysis. As discussed in the IPE insights report [7], the broader issue of PRA quality is an important one, and several professional societies, e.g., American Society of Mechanical Engineers (ASME) [24], have undertaken initiatives to develop standards for performing PRAs (including HRAs). Currently, these standards provide an overall guidance on how to perform an HRA. However, it appears that for NRC applications, especially for reviewing licensee analyses regarding human performance, more detailed analysis is needed.

3. Purpose, Objective, and Scope

The purpose of the HRA Research Program is to support the NRC's Risk-Informed Regulation Implementation Plan (RIRIP) [25], which has been developed to implement the NRC's strategic plan. The general objective of the program is to develop improved HRA methods, tools, and data needed to support NRC regulatory activities, including the broad implementation of risk-informed regulation in the areas of rule development, licensing, and oversight.

The goal of the HRA Research Program is to improve the HRA state of the rt to the level of maturity needed for the HRA to have the degree of confidence of decision-makers achieved by other portions of the PRA. As discussed later in this paper, a key tactic for pursuing this goal is the use of experiments and observations, a tactic that has been used by other high-risk industries for developing predictive models of human performance.

The scope of the HRA Research Program is to develop the infrastructure needed to perform or review HRAs. HRA implementation activities are carried out by other NRC programs and are not part of the HRA Research Program. For example, HRA for pressurized thermal shock (PTS) is performed as part of the PTS PRA. However, if there is a need for expanding or modifying an HRA method to address the particular needs of a PRA effort, these developmental activities will become part of the HRA Research Program. For example, it is anticipated that, in order to perform an HRA for fire events, current methods will need to be expanded to better address ex-control-room human actions potentially dominating a fire PRA. This method development work is included in the HRA Research Program.

4. The Approach

The HRA Research Program has adopted an iterative approach. That is, it builds on relevant work performed by NRC and other organizations, and data, and tools developed by the HRA Research Program are fed back to associated NRC programs.

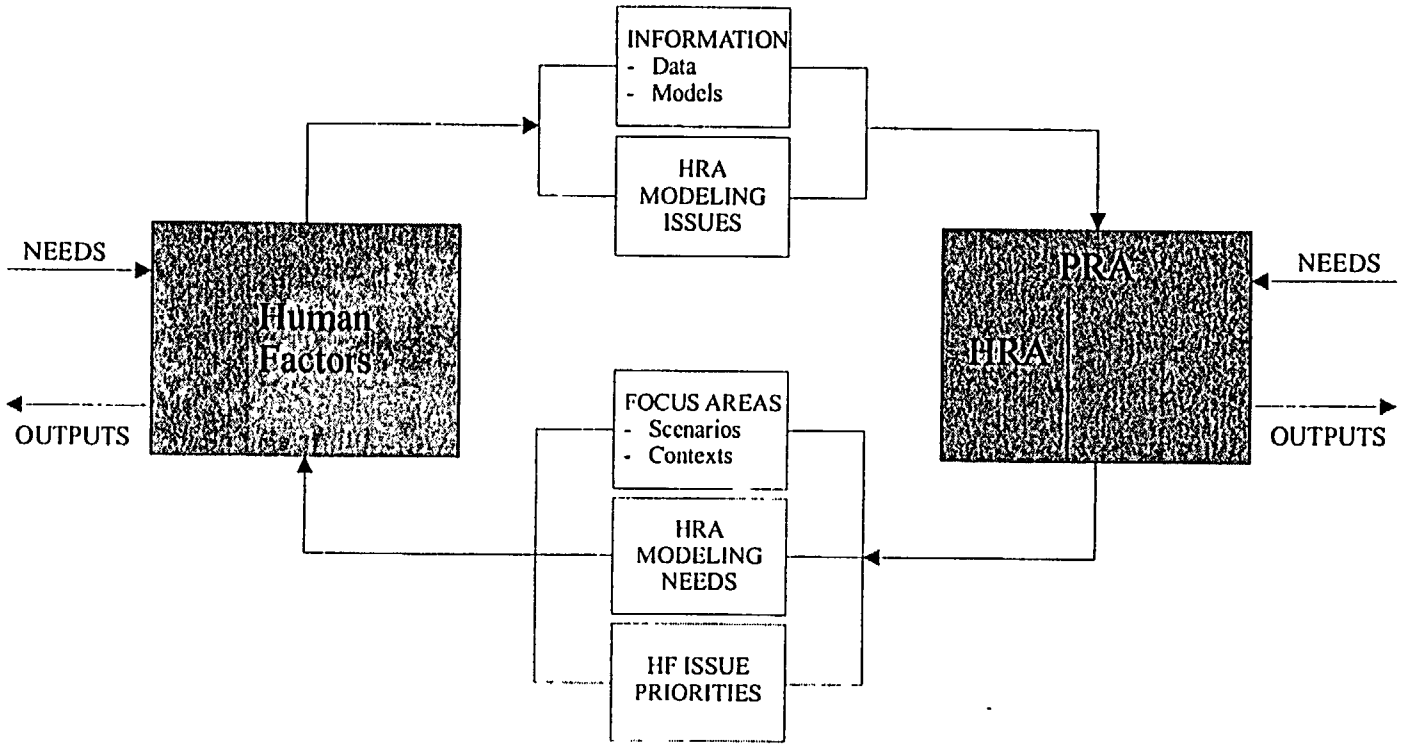

Figure 1. Relationship Between HRA and Human Factors (HF) Research Activities

Figure 1 illustrates the interface of the HRA Research Program with the NCR's human factors (HF) research activities. Through the work performed by HF research (and in general by the behavioral sciences community), we develop an understanding of the influences on human performance during abnormal events. Behavioral sciences develop the theories that explain the phenomenology of human behavior under accident conditions and, therefore, provide the basis for building the frameworks (i.e., logic models or mathematical expressions) needed to quantify the likelihood of HFEs. Also, HF work frequently identifies areas that should be addressed in HRA. For example, the issue of the adequacy of current HRA methods to treat "latent conditions," i.e., pre-initiator HFEs, was identified as a result of HF work on the "Human Performance Contribution to Risk in Operating Events" [17]. Similarly, HRA research and implementation efforts frequently result in identifying issues to be considered by HF research. For example, through the various PRA/HRA efforts a need was identified to better understand human performance under *specific* accident conditions (for example, steam generator tube rupture (SGTR)) rather than under accident conditions *in general*.

The interface of the HRA Research Program with other NRC activities is similar to the HRA/HF interface. For example, the HRA Research Program interfaces with the PRA efforts on PTS, fire and SGTR, the Standardized Plant Analysis Risk Model (SPAR) development, precursor analyses, and HRA reviews.

The following sections describe the work planned for HRA for Fiscal Year (FY) 03 through FY06. The program is focusing primarily on work related to reactor safety. However, risk analysis is also used for accidents initiated from radioactive sources other than the reactor itself, that is, for accidents initiated from radioactive materials and waste. Therefore, HRA needs for materials and waste are also included in the program. Chapter 5 outlines plans for reactor related HRAs and Chapter 6 outlines plans for materials and waste related work.

5. Reactor Applications

As mentioned in Section 2, the sources of uncertainties in HRA can be characterized in terms of adequacy and quality of data and models used and the quality of HRA method implementation The HRA Research Program includes activities in all three areas. These activities are discussed in the following sections. Table 2 shows the activities and an associated schedule[6]. The products of these efforts will be documented in letter or NUREG/CR reports.

5.1 Improve HRA Implementation

5.1.1 Develop HRA Guidance

As indicated earlier in this paper, PRA/HRA quality has become an important issue since the onset of the risk-informed regulation. Key questions faced by HRA analysts (and reviewers) today are the suitability of a method used to address a regulatory issue, the level of detail of the analysis needed, and the adequacy of method implementation in an application. For example, if a method provides data and guidance for

[6] The execution of the planned activities is highly dependent on budget and the staff's overall priorities. For example, the activities related to security and safeguards ("vulnerability study") took precedence over many of the activities of the HRA Research Program plan during for FY02 [26]. As a result many activities planned for FY02 did not take place.

estimating probabilities for HFEs only on the basis of time available to plant operators, it would not be suitable for applications related to human actions for which the available time does not have a significant influence. Also, although the use of improved methods (e.g., ATHEANA) has proved to be valuable for some risk-informed applications (e.g., PTS), it is recognized that not all applications need such a detailed analysis. A key question to be addressed is when the improved, more detailed methods are needed versus when the older, less detailed but widely used methods are sufficient. In addition, HRA practices vary significantly and, therefore, there is a need for more detailed guidance for the staff to ensure an appropriate review of the various methods (and associated data) and their capability to model human performance under the different conditions addressed in the various analyses. The objective of this work is to develop HRA guidance for the NRC's reviewers and analysts.

Therefore, this work involves the development of guidance for:

- reviewing/assessing the quality of an HRA,
- explaining the types of applications for which an HRA method is most appropriate, and
- explaining when a detailed, context-specific analysis, required by second generation methods (e.g., ATHEANA), is needed as opposed to the more traditional level of analysis required by first generation methods.

5.1.2 Support HRA Standards Development

A number of HRA standard activities have been completed or are underway. ASME has published a PRA standard [24] that includes a section on HRA. The Institute of Electrical and Electronics Engineers (IEEE) has also published a standard for HRA [27]. These standards are high level, and both societies have efforts underway to publish supporting documents with lower level (i.e., more detailed) guidance. Furthermore, the American Nuclear Society (ANS) has on going activities for developing standards for low-power and shutdown PRAs that include HRA. The NRC is supporting these efforts through NRC staff participation and, when necessary, through contractor support.

5.1.3 Support Lessons Learned Development

The NRC has underway several PRA activities:

- A PRA in support of the development of technical basis for modifying the Pressurized Thermal Shock (PTS). Rule screening criteria (specified in title 10 Part 50.61 of the U. S. Code of Federal Regulations) is near completion.
- A "fire requantification study" is currently underway to better assess the risk significance of fire initiators to plant risk.
- A study for SGTR-induced severe-accidents is planned to be performed in the near future [28].

At the completion of each study, a lessons learned report containing insights regarding the capability of ATHEANA (or other HRA method) used to address the key human performance issues in these PRAs will be developed. The HRA lessons learned document for the PTS HRA is due in April 2003. Related documents from the other studies will be developed when the studies are completed. These lessons will be used for improving the HRA guidance as well as to develop unique or supplemental guidance to support regulatory activities.

5.2 Improve HRA Data

The HRA Research Program includes efforts on data needs for estimating HEPs, for testing and validating models (or frameworks) driving the quantification process, and for supporting international activities.

5.2.1 Data Development

The strength of available data for HRA is one of the biggest concerns expressed by practitioners and decision-makers. Data are needed not only for the quantification of HFE probabilities, but also to support the development and validation of HRA models (which, for example, postulate that certain factors are part of the EFC, and that there are specific relationships between the EFC elements and the HFE probability).

Regarding HFE quantification, it should be noted that ATHEANA, like other advanced HRA methods, distinguishes between the occurrence of a particular EFC and the occurrence of an unsafe act (UA), given the EFC. Thus, information is needed to assess both the likelihood of an EFC (given the PRA scenario in which the HFE is embedded) and the conditional likelihood of a UA (or set of UAs) leading to the HFE, given the EFC. However, in general, the information available from reports on operational events is not of sufficient quality to directly address these two issues. Furthermore, the risk-significant HFEs for which probabilities are desired are typically events in accident scenarios that have not yet been observed. In these cases, classical statistical methods cannot be used to develop the HFE probabilities. It can be seen that the use of subjective judgment is unavoidable, and that the Bayesian framework for estimation, which directly addresses situations where data are sparse, provides an appropriate way to proceed.

This is an important point from the standpoint of a data collection program, because the Bayesian framework accommodates different forms of "evidence," including indirect observations, model predictions, and expert judgment, as well as actuarial data. The precise formalisms for employing these data in an HRA context are not yet developed. However, regardless of how the formalisms are developed, it is important to recognize that a wide variety of information can be used in a Bayesian analysis. Therefore, the data collection activity need not focus on one particular source of information (e.g., operational events, simulator experiments, or operator requantification tests) over another.

It is also important to recognize that the quantity and quality of HRA data has been a concern since the time of the landmark Reactor Safety Study [15] (see, for example [29]), and that this concern is not expected to be resolved quickly (given the issues mentioned above). Therefore, it can be expected that substantial improvements will require a sustained, long-term, and potentially resource-intensive effort.

This work is performed as a joint activity with HF research and involves the following steps:

- determine qualitative and quantitative data needs of HRA,
- develop a data search/collection tool, and
- identify data sources and use the tool to create a data repository for HRA use.

As seen in Table 2, some of these steps are pursued in parallel. The first step in the project is to determine HRA data needs and identify potential data sources. This step is near completion and the work performed is summarized in a draft INEEL (Idaho National Engineering and Environmental Laboratory) report (December 2002). For example, the use of information available in the open psychological literature has been examined and an approach on how such data can be used for HRA purposes has been proposed.

Regarding the second step, the development of a tool enabling HRA analysts to take advantage of information available from different types of sources, has been initiated. The use of the capabilities of today's information technology is being explored to develop a search tool that would allow an analyst to use information available from different sources and in different forms. The third step, the identification of data sources and the use of the tool to create a data repository for HRA is planed for FY04 and beyond. The Advisory Committee on Reactor Safety (ACRS) [30] has recommended as a potentially useful data source the information generated in support of the development of the industry's symptom-based emergency operating procedures. This source is likely to include the scenario variations considered by the procedure developers and the bases for addressing or not addressing these variations in the procedures. This and other human-performance-related sources would be examined in the future. Data collection efforts for creating an HRA data repository for HRA will be a multiyear effort and plans on this activity will be determined as the work evolves.

5.2.2 Support International Activities for Generating and Collecting Data

The use of experimental facilities for generating data supporting HRA is being pursued through collaborative efforts with international programs with which the NRC has cooperative agreements. Specifically, the Halden Human Machine Interaction Laboratory (HAMMLAB) has ongoing activities on designing and executing experiments aimed to generate data supporting HRA model testing and verification. HAMMLAB is also planning to review past experiments and extract HRA-relevant information potentially useful for both model testing and HEP estimation. The NRC supports the HAMMLAB through direct contribution and through direct NRC and contractor staff support. Strong collaboration is planned for the next few years through frequent communication, staff exchange, meetings, and report reviews.

In parallel, efforts are being made to collect information from international programs compiling human-related operational experience data and related sources. In particular, the NRC is supporting the CSNI efforts (led by the WGRISK HRA working group) on establishing a framework allowing sharing HRA data among the member countries.

5.2.3 Evaluate the Cost-effectiveness of a Domestic Research Simulator Devoted to Human Performance Research

The ACRS, in its letter on "Human Factors and Human Reliability Analysis Research Plans" [30] recommended that "The NRC should consider development of a control room simulator devoted to support research on human factors and human reliability." The staff in its response [39] committed to determine the feasibility of cooperating in this effort with the Department of Energy (DOE). Plans for this work will be developed in FY03.

5.3 Improve HRA Models

Key uncertainties related to models used in HRA are related to the quantification processes used to estimate HEPs and to the completeness of the models used. The HRA Research Program has activities to address both aspects of HRA modeling uncertainties. Section 5.3.1 discusses activities related to quantification and the remaining sections discuss issues related to model completeness.

5.3.1 HRA Quantification Including Uncertainty

In its 1999 review of ATHEANA as documented in NUREG-1624 Rev. 1 [10], the ACRS commented that the quantitative portion of the ATHEANA methodology "still needs significant development" [31]. One of the issues raised by the ACRS concerned whether the ATHEANA process for using expert judgment builds upon the body of work that has been developed on expert elicitation and the utilization of expert opinions (e.g., see NUREG/CR-6372 [32]).

A second and somewhat related issue has been identified during the course of the PTS HRA. In the PTS analysis, efforts are being made to distinguish between aleatory (sometimes called "random") and epistemic (sometimes called "state of knowledge") uncertainties. To make this distinction, the meaning of the model parameters has to be clear. For example, in the case of HRA, the question is whether the HFE probability, which is taken to be a measure of aleatory uncertainty, includes such things as variations in time of day at which the accident initiator occurs, or if these variations are to be included in the uncertainty about the HFE probability. It is not clear that the issue of uncertainty characterization and quantification has been seriously addressed in the HRA literature. This is an important point because, when eliciting expert judgments, it is necessary to be clear and consistent about the quantity being estimated.

A third quantification issue is that, as discussed in Section 5.2, the information available to support quantification may be in a variety of forms (e.g., operational events, model predictions, results of simulator experiments, expert judgments, tabulated generic error probabilities). It is widely recognized that Bayes' Theorem provides an appropriate formalism for dealing with these different forms of evidence. However, the specific implementations of Bayes' Theorem to address certain forms of evidence have not been developed.

Therefore, the HRA Research Program will develop a more formal approach to HFE quantification. This objective will be accomplish by developing a quantification framework that addresses uncertainties in a manner consistent with the PTS PRA philosophy [33], makes appropriate use of the various forms of available information, and appropriately accounts for potential biases in situations involving expert elicitation.

Progress on the first step has been accomplished by improving the ATHEANA quantification process [34]. The revised framework identifies explicit relationships between EFCs, UAs, and HFEs, identifies contextual elements that need to be addressed as part of a given EFC, identifies and classifies the uncertainties in the various contextual elements as being aleatory or epistemic, identifies and classifies the uncertainties in the estimation of the conditional probability of a UA (or set of UAs), given a particular EFC, and provides a detailed description of the general quantification process to be followed.

The second step, making more appropriate use of the various forms of available information, may be accomplished by characterizing the forms of evidence likely to be available to support quantification, and by developing appropriate likelihood functions for use in a Bayesian estimation process.

The third step, appropriately accounting for potential biases in situations involving expert elicitation, will be accomplished by reviewing the literature on elicitation processes, considering the quantification needs identified by the quantification framework, and then adapting a process suitable for use in future HRA analyses.

The overall improvement of the quantification process will be achieved by combining the results of the preceding steps into a unified quantification process, testing the process through a demonstration problem, and if needed, updating the process and developing recommendations for further research.

5.3.2 HRA for Upgraded and Advanced Control Rooms

The staff has developed an Advanced Reactors Research Plan [35] to support the NRC's advanced reactor licensing activities. One aspect of this plan is to address the operators' role and staffing levels in the new reactors, both of these are likely to be different from those of current generation plants. The proposed advanced reactor designs have a strong reliance on the premise that they will be free from human error, and that if an event occurs, human intervention will not be necessary for an extended period of time. Another issue is the applicability of HFE probabilities used in current HRAs developed to depict performance for relatively fast accident evolution (modeled in HRAs for current generation reactors at full power). When dealing with slowly evolving accidents, such as those expected to be dominant in some accident sequences, revision of HEF probabilities may be needed. Therefore, it is important to determine if (and what) modifications are warranted to appropriately incorporate the impact of human performance in advanced reactors. The issue of the impact on operator performance due to multiple modules will also be addressed. Further, the extensive use of digital instrumentation and control (I&C) (e.g., touch screens and different control designs) could impact the probability of human error and needs to be investigated.

In addition, current plants are gradually upgrading their control rooms by replacing their analog I&C systems with advanced digital systems. These changes are also likely to require improvements in current HRA methods and tools to support risk-informed regulatory applications [36].

Therefore, the objectives of this work are to identify key issues associated with HRA for upgraded and advanced control rooms, develop guidance for reviewers of HRAs involving upgraded and advanced control rooms, and develop improved HRA methods and tools to support PRAs for upgraded and advanced control rooms.

If funding becomes available, the work will be initiated in FY03 and it will involve a review of current trends in control room upgrades, of current proposals for advanced reactors, and of previous studies on the risk implications of advanced control room technology (e.g., see [37]). Based on these reviews, key HRA issues will be identified and the ability of existing methods (including ATHEANA) to address these issues (in light of the information available at a design stage) will be evaluated. Guidance for reviewers of HRAs for upgraded and advanced control rooms will be developed. It is expected that improved HRA methods will be also be developed and demonstrated in a limited test. It is anticipated that these methods will address a) interactions between the operators, digital protection and control systems, and the plant, and b) any changes in the roles of operators (as compared with current approaches). This work will be coordinated with activities conducted under the NCR's digital I&C PRA research [36].

5.3.3 Latent Conditions in HRA

As mentioned before, the results of the "Review of Findings for Human Performance Contribution to Risk in Operating Events" (NUREG/CR-6753 [17]) suggest that latent conditions, i.e., plant conditions caused by errors which occur prior to an initiating event but which are not revealed until some later point in time due to a triggering event (e.g., an accident scenario), may have more impact on plant risk than previously recognized, and that they may require improved treatment in HRAs.

Current PRA treatments of latent conditions are varied. Some studies address these conditions explicitly (as separate contributors to component, train, or system unavailability), while others treat them implicitly (through the failure probabilities assigned to the hardware). The modeling choice is generally dependent on the form of the data used to estimate unavailabilities (e.g., whether failures due to human error are distinguished from other failures).

A number of currently available HRA methods, e.g., THERP, appear to be capable of dealing with errors leading to individual latent conditions and their effect [40]. However, these methods do not deal with a potentially significant issue: systematic dependencies among latent conditions, e.g., due to such factors such as common work processes [41]. This issue may be important because, if the dependencies are significant, their cumulative impact on multiple HFEs and multiple sequences may alter a plant's risk profile.

The objectives of this work are to develop an improved understanding of latent conditions observed during operational events, determine where HRA improvements are needed to improve the treatment of latent conditions, and develop improved HRA methods to identify, model, and quantify latent conditions.

The first step of this project will involve the review and evaluation of the latent conditions identified in NUREG/CR-6753. The evaluation will consider the structure of current PRA component failure databases (to determine how the observed errors are addressed), and of current HRA methods (to determine the extent to which they can be used to model these errors. The evaluation is expected to result in recommendations regarding how current HRA methods can be best used, as well as regarding where improvements are needed.

The second step, which can be performed in parallel with the first, will involve an analysis of operational data for HFEs that were or may have been caused by latent conditions, to determine if there is evidence for dependencies between these failures. This analysis will consider but will not be limited to common cause failure data, as it will consider events involving different components and systems at different times.

The third step will develop improved methods for treating human-induced latent conditions. The thrust of this work will naturally depend on the results of the preceding tasks. However, it is currently anticipated that the issue of dependencies will need to be addressed, and that organizational considerations (e.g., work processes) will need to be treated in order to address these dependencies. It is also anticipated that results from ongoing international research efforts in this area (e.g., including the work of the International Cooperative Program on PRA Research (COOPRA) working group on organizational influences on risk) will be needed for this step.

The final step will involve an application of the improved methods. The application will revisit the conclusions of NUREG/CR-6753 and will provide insights regarding the risk significance of latent conditions as well as insights regarding the usability of the improved methods.

As noted by many researchers, the issue of latent conditions is strongly tied to the broader issue of culture and organizational influences on risk. The need and options for addressing these broader topics in the HRA Research Program will be assessed in FY03, in preparation of potential research activities.

5.3.4 HRA Extended Applications

To date, much of the emphasis of HRA methods development activities worldwide has been on the treatment of HFEs associated with control room actions taken to prevent core damage within a few hours after an initiating event. As many of these methods are based on a general understanding of human behavior and the sources of error, they should be broadly applicable when dealing with other situations (e.g., post-initiator actions outside of the control room, long term recovery actions, actions taken during severe accidents, and actions during low power and shutdown operation). However, these other situations provide challenges (e.g., regarding the treatment of teamwork, the interactions of multiple teams, the availability and quality of indications, the impact of the use of guidelines rather than specific procedures, the extended time available for actions) whose practical treatment may require additional developments.

The objectives of this project are to evaluate existing HRA methods, and develop, as needed, improved HRA methods and tools for the following situations:

- post-initiator actions outside of the control room,
- low-power and shutdown (LPSD) operation,
- mitigation of slow-moving accidents, and
- severe accidents.

For each topic, key features that need to be addressed will be identified and HRA methods (including both first and second generation methods) will be evaluated for their ability to practically address these features. Through this examination, needs for improving methods or tools (including guidance) will be determined.

If funding becomes available, it is currently expected that work related to ex-control room actions and LPSD operation will be initiated first and work on severe accidents will follow. Work on long-term recovery actions will be coordinated with similar work for advanced reactors, any unique issues will be addressed separately.

5.3.5 Formalized Methods: Screening, Individual and Crew Modeling

The ACRS review of ATHEANA [31] and the results of peer reviews have identified a number of specific areas where ATHEANA (as documented in NUREG-1624, Rev. 1 [10]) can be improved. One area, the process for quantifying HFE probabilities, is being currently addressed (see Section 5.3.1). This work addresses other areas identified, including the lack of a formal screening method, the lack of an explicit model of awarness for individual crew members (e.g., to provide more formal links between error forcing contexts, potential error mechanisms, and unsafe acts), and the lack of an explicit model for addressing interactions within a crew. Regarding the latter two issues, it is expected that the development of explicit models will improve the accuracy of HRA predictions, reduce the reliance of the analysis results on the judgment of the particular analysis team involved, and provide an improved means for incorporating experimental data into the analysis (e.g., to test implicit hypotheses built into the analysis and to the assess the strength of specific model factors).

This effort will be initiated in FY04 or later, in order to take advantage of the ongoing efforts (including the ATHEANA applications to various situations) and of anticipated input from ongoing cooperative research activities (e.g., work being conducted by the WGRISK of OECD/CSNI).

The objectives of this project are to develop a formal screening method for use in context-based HRA methods and to develop and test explicit models for addressing individual awareness and team issues for use in HRA.

Regarding the development of a formal screening method, the ATHEANA applications for PTS, fire, and SGTR will be reviewed. The purpose of the review will be to characterize how screening was done in those previous analyses, and to identify areas for improvements in the process. Based upon the results of this review, and upon an understanding of the information available at different stages of an HRA analysis, a more formal screening method will then be developed. This method will be tested in a limited application.

Regarding the explicit modeling of cognitive and team issues, it is recognized that ATHEANA has been developed to support a conventional (static) PRA model structure, whereas a detailed treatment of operator awareness and team effects may require a modeling approach that explicitly accounts for system dynamics. It is also recognized that there are a number of research activities looking at these effects (including the dynamic PRA work being performed at the University of Maryland [43]). In this effort, the results of these ongoing activities will be reviewed to determine how their results can be used within a context-based approach to HRA. The results of this review will be used to propose an improved HRA approach.

5.3.6 Fire HRA

As indicated in the NRC Fire Risk Research Program Plan [19], the current fire PRA/HRA treatment of the response of plant operations staff to fire events is relatively crude. Some fire PRAs increase human error probabilities to account for the additional "stress" induced by the fire and some do not take credit for ex-main-control-room actions in the affected fire area (due to heat and smoke). However, these adjustments may not adequately address such plant-specific issues as the complexity of fire response procedures or the role of fire brigade members in accident response nor are they universally agreed upon. Moreover, they are quite judgmental, there currently is no strong technical basis for the magnitude (or even direction) of the adjustments.

Another concern is that the effects of certain elements of context that may arise due to the effects of fire (e.g., fire-induced faulty instrumentation readings, spurious equipment actuation, progressive loss of equipment over time) on operator situation assessment and decision-making are not included. Further, current PRA/HRAs do not explicitly address incorrect operator actions stemming from incorrect decisions.

In principle, ATHEANA provides an appropriate approach for addressing these issues of task allocation, procedure complexity, and fire-induced EFCs. However, because response to fire events involves significant ex-control-room-human actions, it may be necessary to expand ATHEANA to address ex-control-room actions. The direct application of ATHEANA to the "fire risk requantification study" is part of the Fire Program and not the HRA Research Program. The HRA program will address only method development (or modification), if needed.

Therefore, the objective of this task is to modify or develop HRA methods, as needed, for addressing EFCs associated with fire effects (e.g., environmental effects, loss of instrumentation, spurious actuation, time-dependent equipment losses). This task will interface with other related work of this plan, for example the work planned for "Extended Applications" and "Formalized Methods."

5.3.7 Steam Generator Tube Rupture HRA

The Office of Nuclear Reactor Regulation has requested that the Office of Nuclear Regulatory Research to perform confirmatory research for steam generator tube integrity during postulated severe accidents in pressurized water reactors (PWRs) [28]. One of the desired outcomes is an "improvement of probabilistic safety assessment modeling of severe-accident-induced steam generator tube rupture (SGTR) scenarios, including the effects of operator actions." The adequacy of current HRA for post-core damage SGTR studies will be examined as part of this HRA Research Program.

The objective is to develop an improved HRA approach for post-severe accident SGTR scenarios. The actual PRA/HRA is not part of this plan and will be executed as part of the SGTR PRA. The need for developmental efforts will be determined when the SGTR PRA is initiated.

6. HRA for Materials and Waste Applications

As indicated in the RIRIP [25], The Office of Nuclear Material Safety and Safeguards (NMSS) is currently developing a risk-informed regulation framework to cover applications involving the NRC's nuclear materials safety and nuclear waste safety arenas. This development activity involves, among other things, the performance of case studies on specific topics. The objective of this work is to provide HRA support to these nuclear materials and waste risk assessment activities, as needed.

It is recognized that the wide variety of facilities and processes of concern to NMSS will likely require the development of a variety of PRA (and HRA) methods and tools. RES plans to initiate work in FY03 to, in concert with NMSS, to characterize the PRA methods, tools, and data needs for these facilities and processes.

For FY03, the need for developing guidance on how to apply first generation HRA methods for NMSS applications has been identified. For the longer term, activities regarding the development of methods, data, and tools (e.g., software) to more suitably address the various NMMS applications will be performed as part of the HRA Research Program.

Table 2

HRA RESEARCH PROGRAM PROPOSED MILESTONES AND SCHEDULE[7]

	FY03	FY04	FY05	FY06
Reactor Applications				
Improve HRA Implementation				
Guidance Development	Develop draft guidance	Finalize guidance	Revise guidance if needed	Revise guidance if needed
Support Standards	Ongoing: Schedule determined by the individual professional societies			
Develop Lessons' Learned	PTS HRA / Fire HRA		SGTR HRA	
Improve Data				
Data Development	• Develop draft data search prototype tool • Characterize data to be collected • Use tool to collect data	• Continue collecting data, create an HRA data repository • Improve search tool as needed	Continue collecting data	
	Support international and domestic activities on collecting data			
	Feasibility study on research simulator			
Improve Models				
HRA Quantification (including uncertainty)	Characterize forms of evidence	• Identify/develop an approach to incorporate evidence • Review expert elicitation processes	• Adopt a process for use in HRA • Combine results to create unified quantification framework	Test/revise quantification framework
HRA For Upgraded and Advanced Reactors	Identify issues	Develop guidance for HRA reviewers	Develop improved methods as needed	
Latent Conditions HRA	Develop an improved understanding of latent conditions (including issues related to safety culture of an organization)	Develop improved methods for incorporating latent conditions (including safety culture) in HRA	Revise methods, as needed	
Extended Applications	Improve methods to adress • LPSD • Mitigation of slowly-moving accidents	Improve methods to address ex-control-room actions	Improve methods to adress severe accidents	
Formalized Methods		Develop a screening method for ATHEANA	Develop and test models addressing individual and team awareness	
Fire HRA	Improve methods as needed	Perform additional work, if needed		
SGTR HRA	To be determined			
Materials and Waste Applications				
HRA for Materials and Waste	• Develop Guidance • Identify needs	Develop methods and tools as needed		

[7] Milestones and schedule are subject to management approval and funding availability

7. References

1. U.S. Nuclear Regulatory Commission, "Use of Probabilistic Risk Assessment Methods in Nuclear Activities: Final Policy Statement," Federal Register, Vol. 60, p. 42622 (60 FR 42622), August 16, 1995.

2. U.S. Nuclear Regulatory Commission, "Options for Risk-Informed Revisions to 10 CFR Part 50 - 'Domestic Licensing of Production and Utilization Facilities'," SECY-98-300, December 23, 1998.

3. U.S. Nuclear Regulatory Commission, "White Paper on Risk-Informed and Performance-Based Regulation," SECY-98-144, June 22, 1998.

4. U.S. Nuclear Regulatory Commission, "An Approach for Using Probabilistic Risk Assessment in Risk-Informed Decisions on Plant-Specific Changes to the Licensing Basis," Regulatory Guide 1.174, March 25, 1999.

5. U.S. Nuclear Regulatory Commission, "New NRC Reactor Inspection and Oversight Program," NUREG-1649, Rev. 1, 2000.

6. R.J. Belles, et al., "Precursors to Potential Severe Core Damage Accidents: 1998," U.S. Nuclear Regulatory Commission, NUREG/CR-4674, Vol. 27, 2000.

7. U.S. Nuclear Regulatory Commission, "Individual Plant Examination Program: Perspectives on Reactor Safety and Plant Performance," NUREG-1560, 1997.

8. A.D. Swain and H.E. Guttman, "Handbook of Human Reliability Analysis with Emphasis on Nuclear Power Plant Applications," U.S. Nuclear Regulatory Commission, NUREG/CR-1278, 1983.

9. D.E. Embrey, et al., "SLIM-MAUD: An Approach to Assessing Human Error Probabilities Using Structured Expert Judgment," U.S. Nuclear Regulatory Commission, NUREG/CR-3518, 1984.

10. U.S. Nuclear Regulatory Commission, "Technical Basis and Implementation Guidelines for A Technique for Human Event Analysis (ATHEANA)," U.S. Nuclear Regulatory Commission, NUREG-1624, Rev. 1, 2000.

11. C. Bieder, S. Vidal, P. Le Bot, "Feedback from the actual implementation of the MERMOS method," Proceedings of the 5th International Conference on Probabilistic Safety Assessment and Management (PSAM5), Osaka, Japan, November 27–December 1, 2000.

12. G. Parry, "The need for, and some suggested characteristics of, an improved HRA approach for use in PSAs," in Human Reliability Models: Theoretical and Practical Challenges, H. Blackman, N. Siu, and A. Mosleh, eds., Center for Reliability Engineering, University of Maryland, College Park, MD, pp. 13-29, 1998.

13. Nuclear Energy Agency Committee on the Safety of Nuclear Installations, "Critical Operator Actions: Human Reliability Modeling and Data Issues," NEA/CSNI/R (98) 1, 1998.

14. E. Dougherty, Guest Editor, Reliability Engineering and System Safety, 29, Special Issue on Human Reliability Analysis, 1990.

15. U.S. Nuclear Regulatory Commission, "Reactor Safety Study: An Assessment of Accident Risks in U.S. Commercial Nuclear Power Plants," WASH-1400 (NUREG-75/014), 1975.

16. T. Murley, Director, Office of Nuclear Reactor Regulation, memorandum to E. Beckjord, Director, Office of Nuclear Regulatory Research, "Organizational Factors Research," February 4, 1994.

17. D.I. Gertman, et al., "Review Findings For Human Performance Contribution to Risk in Operating Events," NUREG/CR-6753, March 2002.

18. Nuclear Energy Agency Committee on the Safety of Nuclear Installations, "Errors of Commission in Probabilistic Safety Assessment," NEA/CSNI/R (2000) 17, 2000.

19. N. Siu, H. Woods, M. Dey, "NRC Fire Risk Research Plan: Fiscal Years 2001-2002, U.S. Nuclear Regulatory Commission," Draft Report for Information, ADAMS Accession No:ML003773018, November 5, 2000

20. U.S. Nuclear Regulatory Commission, "Reevaluation of the Pressurized Thermal Shock Rule (10 CFR 50.61) Screening Criterion," SECY-00-0140, June 23, 2000.

21. S.B. Haber, et al., "Influence of Organizational Factors on Performance Based Reliability," U.S. Nuclear Regulatory Commission, NUREG/CR-5538, 1991.

22. D.M. Murphy and M.E. Pate-Cornell, "The SAM framework: modeling the effects of management factors on human behavior in risk analysis," Risk Analysis, 16, 510-515, 1996.

23. H. Blackman, N. Siu, and A. Mosleh, Human Reliability Models: Theoretical and Practical Challenges, Center for Reliability Engineering, University of Maryland, College Park, MD, 1998.

24. American Society of Mechanical Engineers, "Standard for Probabilistic Risk Assessment for Nuclear Power Plant Applications," ASME RS-S2002.

25. U.S. Nuclear Regulatory Commission, "Risk-Informed Regulation Implementation Plan," SECY-00-0213, October 26, 2000.

26. N. Siu, et al., "The NRC Human Reliability Research Program," OECD/NEA/CSNI Workshop, Rockville MD, May 2001.

27. IEEE Guide for Incorporating Action Reliability Analysis for Nuclear Power Plants, IEEE Std. 1082-1997, September 1997.

28. S.J. Collins, Director, Office of Nuclear Reactor Regulation, memorandum to A.C. Thadani, Director, Office of Nuclear Regulatory Research, "User Need Request Related to Steam Generator Severe Accident Response and Testing of Steam Generator Tubes During Severe Accident Conditions," February 8, 2000.

29. H.W. Lewis, et al., Risk Assessment Review Group Report to the U.S. Nuclear Regulatory Commission, NUREG/CR-0400, 1978.

30. G. Apostolakis, Chairman, Advisory Committee on Reactor Safety, letter to W. Travers, Executive Director Of Operations, "Human Factors and Human Reliability Research Plans," September 24, 2002.

31. D.A. Powers, Chairman, Advisory Committee on Reactor Safeguards, letter to W.D. Travers, Executive Director for Operations, "NUREG-1624, Rev. 1, 'Technical Basis and Implementation Guidelines for a Technique for Human Event Analysis (ATHEANA)'," December 15, 1999.

32. R.J. Budnitz, G. Apostolakis, D.M. Boore, L.S. Cluff, K.J. Coppersmith, C.A. Cornell, and P.A. Morris, "Recommendations for Probabilistic Seismic Hazard Analysis: Guidance on Uncertainty and Use of Experts," NUREG/CR-6372, April 1997.

33. N. Siu, "Uncertainty analysis and pressurized thermal shock: an opinion," white paper, U.S. Nuclear Regulatory Commission, September 3, 1999, ADAMS Accession No: ML992710064.

34. J. Forester, et al., "Quantification and Treatment of Uncertainty in Human Reliability Analysis Based on ATHEANA," 6th International Conference on Probabilistic Safety Assessment and Management, San Juan, Puerto Rico, June 23-28, 2002.

35. "Advanced Reactor Research Infrastructure Assessment," ADAMS Accession No ML023310540

36. U.S. Nuclear Regulatory Commission, NRC Research Plan for Digital Instrumentation and Control, draft SECY letter, November 20, 2000.

37. J. O'Hara, W. Stubler, and J. Higgins, "Hybrid Human-System Interfaces: Human Factors Considerations," BNL report J6012-T1-4/96, Brookhaven National Laboratory, 1996.

38. J.T. Larkins, Executive Director, Advisory Committee on Reactor Safeguards, memorandum to the Commission, "Draft Report to the U.S. Nuclear Regulatory Commission on Reactor Safety Research from the Advisory Committee on Reactor Safeguards," March 22, 2001.

39. W.D. Travers, Executive Director for Operations, "Human Factors and Human Reliability Research plans," letter to G. Apostolakis, Chairman, Advisory Committee on Reactors Safety, December 2002, ADAMS Accession No ML0231160012.

40. "Summary of Discussion Group I," in *Human Reliability Models: Theoretical and Practical Challenges*, H. Blackman, N. Siu, and A. Mosleh, eds., Center for Reliability Engineering, University of Maryland, College Park, MD, pp. 231-236, 1998.

41. G. Apostolakis, K. Davoudian, and J.S. Wu, "The Work Process Analysis Model (WPAM)," *Reliability Engineering and System Safety, 45*, 107-125, 1994.

42. C.L. Smith, V.N. Shah, T. Kao, G. Apostolakis, "Incorporating Aging Effects into Probabilistic Risk Assessment — A Feasibility Study Utilizing Reliability Physics Models," NUREG/CR-5632, November 2000.

43. Y. Chang and A. Mosleh, "ADS-IDACrew: dynamic probabilistic simulation of operating crew response to complex system accidents," Proceedings of the 5th International Conference on Probabilistic Safety Assessment and Management (PSAM5), Osaka, Japan, November 27–December 1, 2000.

This page left intentionally blank

STANDARDIZED PLANT ANALYSIS RISK (SPAR) MODEL DEVELOPMENT PROGRAM

Patrick O'Reilly
U.S Nuclear Regulatory Commission

Introduction

In order to provide the Nuclear Regulatory Commission (NRC) staff with analytical tools to use in performing their risk-informed regulatory activities, the Operating Experience Risk Analysis Branch (OERAB) in the Division of Risk Analysis and Applications (DRAA) of the Office of Nuclear Regulatory Research (RES) has developed Standardized Plant Analysis Risk (SPAR) models. These probabilistic risk assessment (PRA) models span the following areas: Level 1 - internal events, full power operation, (2) Level 1 - internal events, low power and shutdown operations, (3) Level 1 - external events (including fires, floods, and seismic events), and (4) Level 2/Large Early Release Frequency (LERF).

SPAR Model Users Group (SMUG)

In September 1999, OERAB formed the interoffice (staff from the Office of Nuclear Reactor Regulation, RES, and the four regional offices) SPAR Model Users Group (SMUG) to discuss, coordinate, and provide guidance on technical direction of methods and model development issues related to the Accident Sequence Precursor (ASP) Program and the routine assessment of events. The SMUG also supports the development of models for risk-informed regulatory activities performed by the members' organizations. They provide their organization's input to the type of models to be produced, the level of detail that the models require, the model QA review process, and model development schedule priority. As one of their first achievements, the SMUG prepared the Integrated Plan for Development of Standardized Plant Analysis Risk (SPAR) Models, and influenced its approval by the management of agency model user organizations in October 2000. This plan specifies the scope and approach to be taken in the efforts to develop the different types of SPAR models identified above.

SPAR Models and the NRC's Mission

The SPAR models support the NRC's strategic goals of: (1) maintaining safety, (2) improving staff regulatory effectiveness, efficiency and realism, (3) reducing unnecessary burden, and (4) increasing public confidence. These models consist of analytical tools for use by the NRC staff in the following regulatory activities undertaken in pursuit of these goals:

- To determine the risk significance of inspection findings (SDP Phase 3) or of events to decide: (a) the allocation and characterization of inspection resources, (b) the initiation of an inspection team, or (c) the need for further analysis or action by other agency organizations

- To determine the risk significance of events as input to enforcement severity evaluations and temporary enforcement discretion.

- To support risk-informed decisions on plant-specific changes to the licensing basis as proposed by licensees, and provide risk perspectives in support of the agency's reviews of licensees' submittals.

- To perform various studies performed in support of regulatory decisions as requested by the Commission and other NRR branches.

- To estimate the risk significance of events and/or conditions at operating plants so that the agency can analyze and evaluate the implications of plant operating experience in order to: (a) compare the operating experience with the results of the licensees' IPEs/PRAs, (b) identify risk conditions that need additional regulatory attention, (c) identify risk insignificant conditions that need less regulatory attention, and (d) evaluate the impact of regulatory or licensee programs on risk.

- To provide rigorous and peer reviewed evaluations of operating experience thereby demonstrating the agency's ability to analyze operating experience independently of licensees' risk assessments and enhancing the technical credibility of the agency.

- To screen and analyze operating experience data in a systematic manner in order to identify those events or conditions which are precursors to severe accident sequences.

- To provide the capability for resolution of generic/safety issues, both for screening (or prioritization) and more rigorous analysis to determine if licensees should be required to make a change to their plant or to assess if the agency should modify or eliminate an existing regulatory requirement.

- To assist in the identification of threshold values for exercises connected with the development of a Mitigating Systems Performance Index within the Reactor Oversight Program.

Level 1, Revision 3 SPAR Models

Evolution of Level 1 SPAR Models (Full Power Operation)

Background

The origin of the Level 1 SPAR models can be traced back to the beginning of the Accident Sequence Precursor (ASP) Program. In the early 1980s, when the ASP Program was first established, the program used two sets of event tree models in its precursor analyses [3], one set for PWRs and another set for BWRs. Each set contained four event trees: (1) loss of main feedwater, (2) loss of offsite power (LOOP), (3) loss-of-coolant accident (LOCA), and (4) main steam line break (MSLB) accident. Operational events that could not be modeled using these standardized event trees were analyzed using custom models specifically developed for the event.

In 1985, a categorization scheme for all U. S. light water reactors (LWRs) was developed that grouped plants with similar responses to transients and LOCAs at the system or functional level into eight classes of plant-class specific, train-based, event tree models. Each class contained

event trees for three initiating events: (1) non-specific reactor trip, (2) LOOP, and (3) small-break LOCA.

Beginning in 1994, the NRC staff started using the SPAR models for precursor analyses and for prompt assessments of operational events. These models consisted of system-based, plant-class event trees and plant-specific fault tree system models. These models described mitigation sequences for the following initiating events: a non-specific reactor trip (which explicitly includes loss of feedwater and ATWS), LOOP [and station blackout (SBO)], small break LOCA, and - for PWRs - steam generator tube rupture (SGTR).

Revision 0 SPAR Models

Development of the first generation of 75 simplified, plant-specific models (designated as Revision 0) was completed in June 1994. These models consisted of 75 plant-specific, linked event tree/fault tree models divided into nine event tree classes. There were six PWR classes and three BWR classes, based on similar plant response to transients and LOCAs. The plant-specific fault trees were based on data obtained from Updated Final Safety Analysis Reports (UFSARs), available plant PRAs, the NRC Plant Information Books, and Individual Plant Examinations (IPEs -secondary source of information only). They used supercomponents for basic events to make run time more efficient. Except for emergency a.c. power, support systems were not modeled. The Revision 0 SPAR models did not consider test and maintenance unavailabilities. Common cause failures (CCFs) and system/sequence recovery actions were included. Equipment performance data (point estimates only) were generally taken from the Accident Sequence Evaluation Program (ASEP).

Revision 1 SPAR Models

Ten Revision 0 SPAR models [models for the nine lead plants in each Revision 0 plant class plus one BWR with high pressure core spray (HPCS)] were subjected to a peer review by an NRC contractor. The entire set of models was then revised to address the comments generated by the peer review. The revised models, which were completed in June 1995, were designated the Revision 1 models.

Revision 2QA SPAR Models

The train level Revision 2 SPAR models were developed at Idaho National Engineering and Environmental Laboratory (INEEL) by improving the Revision 1 SPAR models. Some of the more significant improvements included: improvements to the emergency a.c. power model; revision of the models for the power conversion, feedwater, and condensate systems at BWRs; and a list of improvements based on plant information obtained from reviews of available PRAs, updated IPEs (secondary source of information only) and licensee responses to the station blackout rule. The Revision 2 SPAR models were completed in April 1996. RES then engaged two contractors to perform a systematic review of all 75 Revision 2 SPAR models. This review employed a standard set of procedural guidelines. The results of the review were documented in 75 individual review reports. The most significant key comments generated by this review were addressed by revising the Revision 2 SPAR models to create the Revision 2QA SPAR models. Addressing the remainder of the review comments was postponed for future revisions of the SPAR models.

The Revision 2QA SPAR models considered the following initiating events in the event trees: transients (with a transfer to an ATWS event tree); loss of offsite power (including station blackout); small loss-of-coolant accidents, and steam generator tube rupture (for PWRs only). Their event trees are smaller in size and less complex than the NUREG-1150 event trees.

The Revision 2QA SPAR models have a fault tree for every event tree branch point (results in 35-45 fault trees per plant model). The fault tree models were kept small through the use of supercomponents. For example, the supercomponent HPI Motor-Driven Pump (MDP) includes: HPI MDP fails to start; HPI MDP fails to run; HPI pump discharge valve fails to open; HPI suction MOV fails to remain open; and HPI discharge MOV fails to remain open. The system fault trees in the Revision 2QA SPAR models include: human actions required for the system to operate, common cause failures that render the system inoperable, and simplified dependencies on emergency a.c. power during a LOOP. The failure of support systems was specifically excluded for the purposes of keeping the models simple.

The basic event data for the Revision 2QA SPAR models were obtained from independent hardware failure data sources, such as the Accident Sequence Evaluation Program (ASEP) database, previous ASP data analyses of operational events, and plant-specific PRAs or updated IPEs (secondary source of information only). Probabilities associated with supercomponents were hand calculated. The common cause failure methodology used was the Multiple Greek Letter (MGL) Method, with the data obtained from various sources (NUREG/CR-5801, PRAs, and updated IPEs (secondary source of information only). Human error probabilities and recovery actions were based on analyses of operational events in the ASP Program. For performing model quantification, the initiating events were expressed on a per hour basis to facilitate the analysis of operational events. The default sequence cutset probability truncation was set at 1.0×10^{-15} per hour. The results of quantification were expressed in terms of point estimates only, since these models did not possess uncertainty propagation capability.

Revision 3/3i SPAR Models

For a number of reasons, use of the Revision 2QA models by staff analysts was somewhat limited. The most significant criticism received from users was that these models, with the notable exception of the emergency a.c. power system, do not include support systems. In addition, as mentioned above, they do not have uncertainty analysis capability. Further, the human reliability analysis methodology in the Revision 2QA SPAR models is very simplistic, and rather inflexible.

In response to expressed users' needs, the Revision 3/3i SPAR models are being developed by improving the Revision 2QA SPAR models as follows:

- Adding more support systems (e.g., service water, component cooling water, and d.c. power systems).

- Expanding the number of initiating events modeled to include: medium- and large-break LOCAs, inter-system LOCA, and on a plant-specific basis, risk significant support system initiators.

- Adding a new common cause failure analysis methodology - the Alpha Factor Method.

- Adding the capability to propagate uncertainty in equipment performance data.
- Modeling recovery at the cut set level.
- Adding an improved HRA methodology.
- Modeling the unavailability contributions from equipment test and maintenance activities.
- Breaking up most of the supercomponents.

After a Revision 2QA SPAR model has been improved as described above, the result is identified as a Revision 3i (the "I" stands for interim - the model has not yet undergone an onsite QA review) SPAR model. By their very nature (e.g., incorporation of support systems), the Revision 3i SPAR models are more complex than the Revision 2QA SPAR models.

At the recommendation of the SMUG, the following two-part (internal and external) QA process was developed that specified the review scope necessary for an acceptable SPAR model:

- Initiating events.
- Event tree structure (tree tops).
- System fault tree structure (frontline and support).
- Crossties.
- Equipment failure modes.
- Equipment operating alignment/status.
- Operator actions.
- Common cause events.
- Test/maintenance.
- Baseline importance measure results.

The in-house QA review of each completed Revision 3i SPAR model includes two basic parts:

- Review of the electronic model and associated documentation for consistency with each other and with the other plant models.
- Executing a suite of test analyses to verify operability and reasonableness of results.

The external portion of the QA review of each Revision 3i SPAR Model takes place at the plant site or, in the case of a multi-plant model review - at the licensee's headquarters facility - during a meeting with the respective plant PRA staff. At this meeting, the Revision 3i SPAR model for a specific plant is reviewed against the licensee's PRA model for that plant. The scope of this review includes the event tree structure, system success criteria, and dependencies. The baseline core damage frequency estimates are compared and the contributors to the dominant sequences are reviewed. In addition, the SPAR model is further benchmarked by comparing results obtained for selected postulated scenarios against those obtained using the licensee's PRA model. Differences between the results obtained with the Revision 3i SPAR model and those obtained with the licensee's PRA model are identified and discussed with the licensee's PRA staff to determine and understand the reasons for the differences. Currently these onsite QA reviews are being conducted in conjunction with NRR's benchmarking of the SDP Notebook for the plant.

Upon completion of the onsite QA review of a Revision 3i SPAR model and resolution of the comments generated by the review, the SPAR model is then revised to reflect the resolution of these comments. After discussion with the PRA analysts at our contractor at the Idaho National Engineering and Environmental Laboratory (INEEL), including a check to confirm that the specific model has no outstanding significant technical issues, the model is judged as having met the SPAR Model Development Program's QA acceptance criteria. It is then certified as a Revision 3 Model acceptable for general use by staff analysts.

Revision 3 SPAR Model Development Accomplishments

Production of the Revision 3i SPAR models began in late 1998, and will continue until all 72 models (since the Revision 1 SPAR models were developed, three operating plants have been shut down permanently, which reduced the complete set of SPAR models from 75 to 72) have been produced. As of October 25, 2002, 68 Revision 3i SPAR models had been produced. The project's goal is to complete the remaining four Revision 3i models by November 30, 2002. This effort is currently on schedule. The onsite QA reviews of the Revision 3i SPAR models are scheduled for completion by September 30, 2003. As of October 25, 2002, 43 onsite QA reviews of Revision 3i SPAR models had been conducted. Of these 43 models, 30 had been certified as Revision 3 SPAR models.

The Revision 3/3i SPAR models were recently reviewed against the requirements specified in the proposed ASME Standard on PRA. The results of this review indicated that the Revision 3/3i SPAR models do not fully comply with the proposed PRA Standard's requirements in two specific areas - human reliability analysis (HRA) and documentation. In addition to completing the production and QA review of the entire set of 72 Revision 3i SPAR models, FY 2003 development plans include an update of the SPAR model HRA methodology to add uncertainty analysis capability and to improve the documentation of the Revision 3i SPAR models. Once the production and onsite QA review of all 72 Revision 3/3i SPAR models has been completed, the effort will shift to maintaining and updating the models, on an as-needed basis, as indicated from user feedback.

Level 1, Low Power/Shutdown SPAR Models

Background

At the beginning of FY 2002, there were two low power/shutdown (LP/SD) SPAR models available for staff use. These models were based on the two detailed shutdown PRAs sponsored by the NRC - a PWR LP/SD SPAR model based on the detailed Surry Shutdown PRA performed by Brookhave National Laboratory (BNL) and documented in NUREG/CR-6144, and a BWR LP/SD SPAR model based on the detailed Grand Gulf Shutdown PRA performed by SNL and documented in NUREG/CR-6143. In addition, three prototype templates and associated guidelines had been produced and were available for use in developing other LP/SD SPAR models: (1) all PWRs, (2) BWR 5/6s, and (3) BWR 4s. These templates are basically working PRA models with all plant-specific system fault tree information removed and replaced with undeveloped events. These templates had received an internal peer review.

The LP/SD SPAR models use the same human reliability analysis (HRA) methodology that is used in the Revision 3 SPAR models. As originally developed, this methodology did not specifically

address human performance issues that are likely to be encountered during low power and shutdown operation. As mentioned above, the existing methodology does not include uncertainty analysis capability, and therefore it does not fully comply with the requirements of the proposed ASME Standard on PRA. Finally, the current documentation of this methodology consists of a draft INEEL report, which has never been subjected to Peer Review.

Working with INEEL, the SMUG prepared a program plan for developing LP/SD SPAR models, which is presented below.

Program Plan for Development of LP/SD Models

Expansion of Templates into LP/SD SPAR Models for Lead Plants

- Expand the appropriate existing LP/SD SPAR model template into a LP/SD SPAR model for the lead plant in each of the following plant classes as follows:

    - Millstone 3
    - Byron 1 & 2
    - Oconee 1, 2, and 3
    - Millstone 2
    - Palo Verde 1, 2, and 3
    - Peach Bottom 2 & 3

[NOTE: Surry and Grand Gulf, for which LP/SD SPAR models already exist, are also considered lead plants for their respective plant classes.]

- Starting with the appropriate LP/SD template, develop a LP/SD model for each of the above-identified lead plants in each plant class as summarized below:

    - Add all plant-specific system fault tree logic from the corresponding Revision 3 SPAR model.

    - Add all the basic event information from the Revision 3i SPAR model.

    - Revise the LOOP and emergency diesel-generator (EDG) recovery probabilities for the longer recovery times anticipated during LP/SD operation.

    - Modify the system logic so the system configuration is properly represented in each plant operating state (POS) group. Initially, this will be based on the detailed shutdown PRAs for Surry and Grand Gulf (NUREG/CR-6144 and -6143, respectively). Eventually, the system configurations should be based on input obtained from the plant licensee. This information should be available as a result of the peer review of the models.

    - Review the system success criteria. Initially these will be based on the two shutdown PRAs cited above. Eventually, they should be based on input received from the plant licensee during peer review.

- Add new test and maintenance basic events, and modify the associated probability values to reflect LP/SD conditions.

- Revise the recovery rules for the new test and maintenance combinations prohibited by Technical Specifications during LP/SD operation.

- Modify the human error probabilities (HEPs) to reflect longer recovery times (may depend on completion of HRA tasks specified below)

- Prepare and document guidance on using the LP/SD SPAR model for a lead plant in a plant class to develop LP/SD models for the other plants in the same plant class.

- Prepare a draft users' manual for each lead plant's LP/SD SPAR model, including: (1) a table of differences between the systems for the lead plant and those for the other plants in the same plant class, and (2) the development guidance identified above .

- Subject each LP/SD SPAR model and associated guidance to an onsite QA review against the licensee's low power/shutdown PRA model.

- Revise the LP/SD SPAR model and associated guidance to address review comments and issue the final model and guidance.

Update of HRA Methodology and Documentation

Update the HRA methodology currently used in the LP/SD SPAR models (and in the Level 1, Revision 3 SPAR models for full power operation) to. (1) add uncertainty analysis capability, (2) include specific application to the analysis of events/conditions occurring during LP/SD operation, and (3) improve the documentation of the methodology. The purpose of these enhancements is to ensure that the methodology and associated documentation will comply with the requirements of the proposed ASME Standard on PRA. This will be accomplished as follows:

- Determine the uncertainty distributions that will allow the propagation of uncertainties in the human error probability values for the existing SPAR model HRA methodology. This effort will consider both full power and low power/shutdown operation.

- Determine whether the range of performance shaping factors (PSFs) and the number of decrements within each PSF category in the current methodology are appropriate for application to LP/SD conditions. This will be done by benchmarking the HRA methodology against known LP/SD events. If the current PSFs are not applicable to LP/SD conditions, identify how they should be modified to produce more realistic probability values for the failure of operators to diagnose or take the appropriate action in response to events/conditions occurring during LP/SD operation.

- Document the results of the above work in a draft NUREG/CR report covering both full power and LP/SD operations. This report will include a separate section providing guidance on applying the methodology to the analysis of events/conditions occurring during LP/SD operations based on the results from the work identified above.

- Subject the draft report to internal and external Peer Review

- Revise report to address Peer Review comments and issue the final NUREG/CR report.

Implementation of Plan - Accomplishments

During the twelve-month period ending October 25, 2002, the LP/SD SPAR model development effort accomplished the following:

- Completed an internal peer review of the template for developing LP/SD SPAR models for all PWRs, revised the associated documentation to address the review comments, and issued the final template and documentation

- Using the LP/SD SPAR model template for all PWRs, produced draft LP/SD SPAR models for the lead plants in two plant classes: Byron 1 & 2 and Millstone 3.

- Conducted an onsite QA review of the LP/SD SPAR model for Surry 1 & 2 against the licensee's LP/SD PRA.

- Transmitted the LP/SD SPAR models for Byron 1 & 2 and Grand Gulf to the respective licensees in preparation for the onsite QA reviews of these models.

Level 2/LERF SPAR Models

Background

An important measure of risk used by the NRC to assess the safety of nuclear power plants is the large early release frequency (LERF) of radionuclides which can potentially result from a core damage accident. A definition of LERF can be found in Regulatory Guide 1.174 (July 1998). While a complete Level 2 probabilistic risk assessment (PRA) estimates the composition and frequency of all postulated releases, an estimate of LERF can be obtained with substantially less resources from a reduced Level 2 analysis. At the start of FY 2002, the situation regarding the capability for staff analysts to perform Level 2/LERF analyses of operational events/conditions/findings was as follows. NRC staff analysts had limited analysis tools for Level 2/LERF evaluations of risk associated with operating events/conditions in operating U.S. nuclear plants. The analysts had to either construct a custom model for each specific case to be analyzed, or rely on their assessment of the licensee's Level 2/LERF calculations.

There were eight existing plant class-specific, LERF models available at the time for staff use - six PWR models and two BWR models - which were completed for the ASP Program during FY 1999. These models had been developed for different priorities than those that were envisioned in FY 2002, and with limited time and resources. They had not been peer reviewed. The classification of the models was based on containment type. Limited user experience with these models indicated that improvements (e.g., such as simplifying the user interface, reducing the conservatism in basic assumptions, and enhancing the overall user-friendliness of the models) were needed to better serve user needs. There were no available fully detailed Level 2 models. The need for user-friendly Level 2/LERF models had been previously expressed by the SMUG, as well as by staff analysts who perform Level 2/LERF analyses, and was documented in the

Integrated SPAR Model Development Plan. The Integrated Plan outlined an approach for determining the usefulness of the existing SPAR LERF Models and for developing the kinds of models suitable for use in regulatory applications. This approach consisted of the following phases:

- Phase 1 - Determine the usefulness of currently available LERF models.
- Phase 2 - Considering the results obtained in Phase 1, prepare a detailed program plan for developing Level 2/LERF models that meet the needs of staff users.
- Phase 3 - Implement the plan after approval by the management of user organizations.

Phases 1 and 2 were successfully completed during FY 2002, as discussed below.

FY 2002 Accomplishments

Phase 1

In Phase 1, BNL reviewed the status of the six existing PWR LERF models and the two existing BWR LERF models. These models had been developed for use with the System Analysis Programs for Hands-on Integrated Reliability Evaluations (SAPHIRE) code. In conjunction with the review of the model descriptions documented in the model-specific reports, BNL also exercised the actual LERF models in order to fully understand their capabilities and limitations. This part of the effort allowed BNL to determine the user friendliness of the computer models, the length of the running times, the quality of the reports that can be generated, the graphics capabilities, etc.

Based on their review, BNL reached the following conclusions about all eight of the existing LERF models reviewed:

- Technical information in the existing models is outdated.
- The level of detail in the existing models is probably not justified given the users' needs..
- Extrapolation to other plants in the same class is not easily achievable.
- The models do not lend themselves to investigating precursor events.
- The existing models are not very user friendly, since they are long running, complicated to track, and have complicated, limited report generation capability.

Overall, BNL concluded that:

- The existing LERF SPAR models appeared to be a very thorough fitting of the NUREG-1150 data into the existing SPAR structure.

- The model generation did not employ engineering insights to achieve development of an optimum LERF analysis tool for current SPAR model user needs and therefore did not result in the creation of a new, user-friendly, computer model.

- Much of the complexity of the models arose from the uncertainty associated with Level 2 phenomena and did not enhance correlation of precursor events with LERF outcomes.

- The complexity of the LERF event trees could be simplified by deleting or consolidating Level 2-related questions to some degree without affecting the technical accuracy of the models.

- Incorporating results and insights from post-NUREG-1150 research could also help reduce the level of detail.

- The use of bridge event trees (BETs) should be retained.

- A better link between the Level 1 and Level 2 models is needed to allow real traceability of precursor events from Level 1 to Level 2.

    - Could link the Level 1, BET and simplified LERF trees directly, allowing the user to make a complete pass through the entire structure in a single run.

- BNL proposed construction of a database program:

    - To obtain high level results relatively quickly.
    - To store results from running a base case for each plant, plus a variety of results from variations from the base case.
    - Could use its data to construct a parametric model that can be used to quickly obtain overview results of sensitivity cases
    - Would also include data from more than one plant.

        - Could help with the extrapolation from the reference plant to other plants in the same class
        - Could obtain results for a group of plants for comparison using data from different plants.

Phase 2

With guidance from the SMUG, BNL developed a program plan for developing LERF SPAR models based on:

- The results of BNL's review and evaluation of the existing Level 2/LERF models.

- Comments received from the SMUG and key LERF model users.

- Experience with the existing models obtained by INEEL during their work on the development of LERF thresholds for the NRC's Risk-Based Performance Indicator (RBPI) Program.

- User needs expressed by staff analysts during individual interviews and the discussions held during a February 2002 meeting involving the SPAR Model Users Group (SMUG), key Level 2/LERF model users, and BNL staff.

This program plan consists of the following tasks:

Development of LERF SPAR Models

- Review of LERF-Related Literature
  - Review NRC and industry sources of technical information for information on LERF-related phenomena and Level 2 phenomenological models published since the issuance of NUREG-1150.
  - Obtain insights and data from this review that are applicable to the development of LERF models.
    - Initially use these insights to establish lead or reference plant categories.
    - Later apply these insights in the development of the bridge trees and LERF event trees for each of these lead plants.
- Establish Plant Categories and Priority
  - The plant categories will be established based on containment type (plus other plant features which could influence calculation of LERF) as follows:
    - Westinghouse-designed PWRs - three categories (large, dry; sub-atmospheric; and ice condenser containments).
    - Combustion Engineering-designed PWRs - two categories (those with PORVs and a large, dry containment; those without PORVs and a large, dry containment).
    - Babcock & Wilcox-designed PWRs - one category (large, dry containment).
    - BWRs with a Mark I containment - two categories (BWR/4s with RCIC; BWR/3s with isolation condenser).
    - BWRs with a Mark II containment.
    - BWRs with a Mark III containment.
- Development of Simplified Bridge Trees
  - Retain the bridge tree concepts from the existing LERF models.
  - Bridge trees may be simplified, depending on the level of event tree complexity finally chosen.
  - Bridge trees will be compatible with the Level 1, Revision 3 SPAR model logic.
- Development of Improved LERF Event Trees

  Develop improved LERF event trees for the lead plant in each plant category using information based on engineering judgement, BNL's previous experience with LERF issues, and the results of the literature search discussed above. These trees will have the following characteristics:

- The new, simplified LERF event trees will incorporate the updated information and insights obtained from NRC and industry research published since the NUREG-1150 studies were completed.

- The level of detail of these trees is expected to be greater than those of NUREG/CR-6595, but substantially less than those of the existing LERF models.

- These new trees should be more scrutable and useful for the analysis of operational events/conditions than those of the existing LERF models.

- The structure of these trees will be consistent with the concepts used in other NRC programs that involve LERF [i.e., results of the LERF SPAR models will be in agreement with the concepts in other NRC LERF-related programs, such as the Significance Determination Process (SDP)].

- The trees will be constructed in a manner which will allow future expansion to include late releases, if there is an expressed users' need to do so.

- Quantification of LERF SPAR Models for Lead Plants

  - Quantify the LERF SPAR model for the lead plant in each plant category using engineering judgement, past experience and the insights and data obtained from the literature review to estimate split fractions for the event tree branches. Address parameter and modeling uncertainty issues

- Preparation of SAPHIRE Input

  - Convert the finalized LERF SPAR model structure and data into the SAPHIRE format.

- Preparation of Guidance for LERF SPAR Models for Other Plants in the Same Lead Plant Category

  - Prepare guidance for developing LERF SPAR models for other plants in a plant category from the LERF SPAR model for the lead plant in that category.

    - Include a procedure for performing an efficient extrapolation from the LERF model for the lead plant to another plant in the same plant category.

    - The LERF SPAR Database could be useful in this process.

- Preparation of a Users Manual for the LERF SPAR Model for Each Lead Plant

  - Prepare a draft users manual for the LERF SPAR model for each lead plant in a plant category, documenting the methodology followed in the development of the LERF SPAR model, including:

- Selection of plant categories.
- Development of the bridge trees.
- Identification and binning of the plant damage states.
- Development and quantification of the improved LERF event trees.
- A separate section documenting analysis results obtained with the specific LERF SPAR model.
- A separate section consisting of the guidance specified above on how to develop a LERF SPAR model for another plant in the same plant category.

- Development of Specifications for SAPHIRE Improvements

  Provide specifications outlining improvements to the SAPHIRE suite of PRA codes which will be used with the LERF SPAR models that address expressed users' needs regarding user-friendliness of input and output formats and computer run time, such as the following:

  - Users of the improved LERF SPAR models need a post-processing capability that allows processing of the plant damage states (PDSs) to easily obtain initiating event and sequence contributions to the PDSs.

  - Staff analysts need a better link between Level 1 and LERF results that would also allow analysis of LERF results in terms of contributions from initiating events, sequences, etc.

  - To satisfy users' needs, the improved LERF SPAR models require a better user interface, which would include:

    - Default options to allow the user to exercise the model with a minimum of steps.
    - Improved summary reports.
    - The ability to easily export data to spreadsheet or word processor programs.

- Beta Testing of Draft LERF SPAR Models

  - Release a beta version of the models to a limited user distribution for user review and testing, and solicit user input on the model interface.
  - Revise the models as necessary to address comments from beta testing.

Development of a SPAR LERF Results Database

Development is contingent on sufficient user interest after LERF SPAR model development and review has been completed.

- Two-fold purpose:

  - To capture for future use relevant results from plant analyses as they are carried out, thus avoiding unnecessary repetition of analyses.

- To store information that a modeler would need to model a plant in the same plant category as a particular lead plant.

- Database features:
  - Must be user-friendly so that a user can easily query it to obtain results for individual plants, or to compare results among plants in the same or different plant categories.
  - Will initially be populated with the results obtained using LERF SPAR model for the lead plant in each plant category.
    - In the future, relevant results from LERF SPAR models for plants other than the lead plants in each plant category would be added as they are generated by SPAR LERF model users.
  - Will also be used to store relevant plant parameters needed to create a LERF SPAR model for a plant other than the lead plant in a plant category:
    - Those characteristics of the specific plant of interest that can affect the progression of an accident following the onset of core damage through early containment failure, and which differ from those of the lead plant in that category.

- Specification for Database
  - Develop a specification for a database that can be used to query LERF- related results previously calculated with the LERF SPAR models.
  - Should capture data in this database such as the following information regarding the Level 1, Revision 3 SPAR model for each lead plant:
    - Contributions to the baseline core damage frequency (CDF) from the various types of initiating events.
    - Details of the most dominant sequences for that plant.
    - The contribution to LERF for the lead plants from the following:

      Initiating event.
      Accident class (e.g., LOCAs, transients, ATWS).
      Plant damage state (PDS).
      How the initiating events contribute to the various PDSs.

- Creation of LERF SPAR Database and Population with Data
  - Database will also contain plant-specific information developed for non-lead plants.

- Preparation of LERF SPAR Database Users Manual

  Prepare a users manual that documents the steps that a user should follow to query the database for results of individual plants or groups of plants:

  - Manual will explain how to use the plant-specific information stored for non-lead plants in the creation of a LERF SPAR model for such a plant.

Development and Implementation of Internal Quality Assurance (QA) Procedures, and Response to External Peer Review Comments

- Development of Internal QA Procedure

  Develop an internal QA procedure appropriate for review of the various elements of the SPAR LERF models and the SPAR LERF Database outlined in this plan.

- Conduct Onsite QA Review

  - Subject the LERF SPAR model to an onsite QA review with the licensee's PRA staff and benchmark the model against the licensee's LERF model to verify treatment of the phenomenology and the logic in the models.
  - Revise the LERF SPAR model as necessary to address the comments obtained during the review.

- Maintenance/Updating of LERF SPAR Models and Database

  - Maintain/update the SPAR/LERF models as necessary to meet user needs.
  - Maintain/update the SPAR/LERF Database as necessary.
  - Provide technical assistance to LERF SPAR model users in a timely manner.

Development of External Events Methodology

Current Capability for Analyzing External Events/Conditions

Currently, there exists a methodology for assessing the risk associated with events/conditions involving external event initiators, which is basically a screening tool that was developed several years ago for the ASP Program. This is the methodology documented in the 1996 draft report, "Development of a Methodology for Analyzing Precursors to Earthquake-Initiated and Fire-Initiated Accident Sequences," by G. Apostolokis, R Budnitz, et al. This methodology has not been peer reviewed. However, it has been used by the staff a number of times, with mixed results, which are a direct result of a fundamental limitation. Its usefulness for a given application depends upon whether the licensee for the specific plant of interest performed a detailed fire or seismic PRA (whichever is applicable) for their plant's IPEEE, or whether they used one of the abbreviated methods developed by the industry to estimate the risk associated with a fire- or seismic-related event or condition (e.g., the FIVE Methodology developed for risk analysis of fires, the Seismic Margins Methodology developed for risk analysis of seismic-related events/conditions). In the latter case, the usefulness of the methodology may be limited because, in the FIVE Methodology and in the Seismic Margins approach, sequences which failed to reach a particular threshold were

discarded before the CDF contribution associated with fire or seismic events/conditions was estimated. For a given event or condition, one or more of these discarded sequences may become important, but the analyst has no way of knowing what the sequence(s) is(are), since it(they) does(do) not appear in the IPEEE documentation.

Plan for Developing External Events Methodology

The Integrated SPAR Model Development Plan contained the approach for developing external events methodology outlined below.

- Determine Usefulness of Current External Events Methodology for Use in Regulatory Applications.
  - Survey SMUG members and key analysts from the user organizations to establish criteria for acceptability of results of review/exercise of model.
  - Review/exercise "Development of a Methodology for Analyzing Precursors to Earthquake-Initiated and Fire Initiated Accident Sequences" to determine if the application of this methodology in conjunction with Level 1, Revision 3 SPAR models is sufficient to address internal fires and floods, and seismic event issues in conjunction with Regulatory Guide 1.174 and the external events SDP.
    - Provide feedback regarding results of evaluation to SMUG and key users.
    - Meet with R. Budnitz/G. Apostolakis to:

      Obtain overview of methodology
      Discuss results, address issues raised by review group.
      Discuss extension of methodology to other external (e.g., floods hurricanes) events.

    - Visit regional office/site to exercise methodology (expect site to be one for which a Level 1, Revision 3 SPAR model exists).
    - Exercise methodology in conjunction with Level 1, Rev 3 SPAR model, fire/flood/seismic related event or conditions analysis and also the external events SDP.
    - Discuss results, identify issues raised during exercise.
    - Formulate recommendations regarding methodology content, application for presentation to SMUG.
  - SMUG provides direction to RES/OERAB for acceptability of use of current external events methodology in regulatory applications.
  - SMUG determines necessity/extent of methodology development for assessment of non-fire, non-seismic, non-flood related event or conditions that could impact the risk due to fires, etc., in other areas of the plant.

- Determine if information from IPEEEs and the IPEEE reviews can be used to eliminate or support the need for a methodology to assess these types of events/conditions.

- SMUG decides to pursue or to drop development of methodology to address these external event issues.

- SMUG provides direction to RES/OERAB regarding development of methodology and associated QA process/peer review for assessment of non-fire, non-seismic, or non-flood-related events or conditions that could impact the risk due to fires, etc., in other areas of the plant.

Status of Effort

Prior to FY 2003, no development work on this effort had taken place. The FY 2003 RES budget does contain funding support for a limited effort. This will allow the evaluation of the currently available methodology to begin. The level of funding budgeted for FY 2004 will support a more extensive development effort.

NRC FORM 335 (2-89) NRCM 1102, 3201, 3202

U S NUCLEAR REGULATORY COMMISSION

BIBLIOGRAPHIC DATA SHEET

(See instructions on the reverse)

1 REPORT NUMBER (Assigned by NRC, Add Vol , Supp , Rev , and Addendum Numbers, if any)

NUREG/CP- 0180

2 TITLE AND SUBTITLE

Proceedings of the 2002 Nuclear Safety Research Conference

3 DATE REPORT PUBLISHED

MONTH: March YEAR: 2003

4 FIN OR GRANT NUMBER

A3988

5. AUTHOR(S)

Conference Papers by various authors;
Compiled by Susan Monteleone, BNL

6 TYPE OF REPORT

Proceedings of conference on safety research

7. PERIOD COVERED *(Inclusive Dates)*

October 28-30, 2002

8 PERFORMING ORGANIZATION - NAME AND ADDRESS *(if NRC, provide Division, Office or Region, U S Nuclear Regulatory Commission, and mailing address; if contractor, provide name and mailing address)*

Office of Nuclear Regulatory Research
U.S. Nuclear Regulatory Commission
Washington, DC 20555-0001

9 SPONSORING ORGANIZATION - NAME AND ADDRESS *(if NRC, type "Same as above"; if contractor, provide NRC Division, Office or Region, U S Nuclear Regulatory Commission, and mailing address)*

Same as Item 8 above.

10 SUPPLEMENTARY NOTES

S. Nesmith, NRC Project Manager; Proceedings prepared by Brookhaven National Laboratory

11 ABSTRACT *(200 words or less)*

This report contains papers on reactor safety research presented at the 2002 Nuclear Safety Research Conference (formerly titled the Water Reactor Safety Information Meeting) at the Marriott Hotel at Metro Center in Washington, DC, October 28-30, 2002.

The papers describe the programs and results of nuclear safety research sponsored by the U.S. Nuclear Regulatory Commission's Office of Nuclear Regulatory Research. Also included are invited papers concerning nuclear safety issues from U.S. government laboratories, the electric utilities, the nuclear industry, and from foreign governments and industry.

The papers compiled here are in the order of their presentation on each day of the meeting.

12 KEY WORDS/DESCRIPTORS *(List words or phrases that will assist researchers in locating the report)*

reactor safety research
nuclear safety research

13 AVAILABILITY STATEMENT

Unlimited

14 SECURITY CLASSIFICATION

(This Page) Unclassified

(This Report) Unclassified

15 NUMBER OF PAGES

16 PRICE

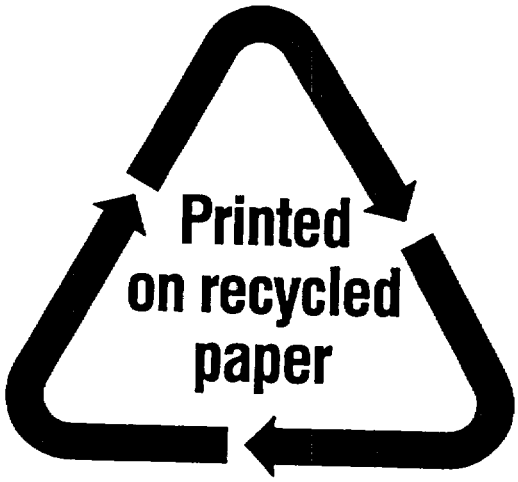

Federal Recycling Program

UNITED STATES
NUCLEAR REGULATORY COMMISSION
WASHINGTON, DC 20555-0001

OFFICIAL BUSINESS
PENALTY FOR PRIVATE USE, $300